Modeling the Sauter Mean Bubble Diameter in Mechanical, Forced-air Flotation Machines

Jan Edward Nesset

Department of Mining and Materials Engineering

McGill University

Montreal, Canada

A thesis submitted to the Faculty of Graduate Studies and Research in partial fulfillment of the requirements of the degree of Doctor of Philosophy

February, 2011

Dedication

To the women who are everything in my life,

My wife Valerie

And my daughters Ellen and Kirsten

This thesis is also dedicated to the memories of Professors Andre Laplante and Ralph Harris, who were members of the author's research proposal committee, and friends and colleagues for many years, and who passed away at far too young an age

ABSTRACT

The extraction of a mineral from an ore may involve separation processes using air or gas in flotation machines. The size of bubbles created in this process is of great importance to the efficiency of the mineral separation achieved. There currently exists no available model for predicting the *Sauter mean bubble diameter,* D_{32}, from the key process variables for mechanical flotation machines. This is seen as a significant shortcoming since flotation is a surface area (of bubbles) dependent process, the key metric being the bubble surface area flux, S_b, defined as $6\,J_g/\,D_{32}$, where J_g is the superficial gas velocity. Knowledge of how key variables affect the bubble size distribution (BSD), and hence S_b, is seen as an essential component of process understanding and optimization. The objective of this work was to develop a mathematical expression for D_{32} based on the key process variables of frother type and concentration, superficial gas velocity, power intensity (impeller tip speed), liquid viscosity, and altitude (elevation above sea level).

In order to effectively measure the BSD that links to the S_b leaving the pulp phase, a relatively large 700 liter cell, a Metso RCS™ 0.8 m^3 pilot unit, was selected. This unit, having an internal shelf baffle, produced separation of turbulent (near impeller) and quiescent (near froth) regions, ensuring that the measured BSD was truly reflective of the surface area flux leaving the pulp zone. Failure to adequately address this has been a shortcoming of work by others. The Metso unit was powered by a variable speed drive that permitted an 8-fold increase in power intensity covering the full range of industrial impeller tip speed (4.6 to 9.2 m/s). Five frothers were tested, covering a broad range in types including alcohols and polyglycols, Viscosity was modeled by varying water temperature between 4 and 40 ^oC. Altitude was modeled by varying gas density, an air-helium mixture fed to a smaller 5.5 liter laboratory Denver cell. The McGill gas dispersion sensors; bubble viewer and J_g probe, were used for measurement.

The work showed that the effect on D_{32} for all frothers can be normalized to the same set of curves when dividing concentration by a frother's $CCC95$ value. The notion of $CCC95$ is introduced and is equivalent to Laskowski's CCC (critical coalescence concentration) but more suitable for mathematical analysis and model development. It represents the frother concentration (ppm) for which 95% reduction in D_{32} has been achieved. Frother concentration was found to be the variable with the largest impact on D_{32} and is modeled with an exponential decay function that reaches a limiting bubble size at frother concentration exceeding the $CCC95$ value. Higher $CCC95$ results in a lower limiting bubble size. It appears that the $CCC95$ value for a frother may be predicted from its' basic molecular structure using the *Hydrophile-Lipophile Balance/Mol. Wt.* parameter. It was also found that the $CCC95$ value for a frother increases with increasing J_g.

D_{32} was found to depend on $J_g^{0.5}$ with a notional "bubble creation size" at J_g = 0 cm/s. The dependence on viscosity relative to that at 20 ^oC was a power relationship having an exponent of 0.776, while similarly, that for simulated altitude (gas density relative to air density at sea level)) showed less dependency with an exponent of -0.132. Surprisingly,

impeller speed was found not to have any significant effect on D_{32} across the range representing an 8-fold increase in power intensity and a doubling of impeller tip speed. It is postulated that the hydrodynamic conditions within the impeller/stator region are ones where the high degree of free-stream turbulence and high void fraction (gas hold-up) result in a lower and non-constant drag coefficient on individual bubbles meaning a (disruptive) drag force with less dependence on relative fluid velocity and more effect of viscosity.

The overall D_{32} model, developed in a 2-phase air-water system, shows very good agreement with measured plant data from 5 operating sites worldwide, representing 3-phase (air-water-solids) flotation systems. The S_b- J_g curves produced by the model can be used as a “road-map” to benchmark plant operation as illustrated by a case study from the Lac des Iles palladium mine in Ontario. This approach is seen as a significant development for process understanding and optimization.

RÉSUMÉ

L'extraction de minéral d'un minerai peut impliquer des processus utilisant de l'air ou du gas dans des machines de flottation. La taille des bulles formées dans ce processus est de grande importance à l'efficacité de la séparation minéral obtenue.Présentement aucun modèle ne permet de prédire le *diamètre moyen de Sauter d'une bulle*, D_{32}, dans une cellule mécanique de flottation à partir des variables clés de ce même procédé. Cette lacune est significative puisque la flottation est un procédé dépendant de l'aire surfacique (des bulles), le paramètre clé étant le flux d'aire surfacique de bulles, S_b, défini comme étant $6\,J_g/D_{32}$ où J_g est la vélocité superficielle du gaz. La façon dont les variables clés influencent la distribution des tailles de bulles (DTB) et par conséquent S_b est une confirmation essentielle pour comprendre et optimiser le procédé.

L'objectif de travaux de recherche de cette thèse est de développer une expression mathématique pour la détermination du D_{32} basée sur des variables clés : type et concentration du moussant, vélocité superficielle du gaz, puissance d'agitation, viscosité du liquide et l'altitude (élévation au-dessus du niveau de la mer).

Afin de mesurer efficacement la DTB en lien avec le S_b des bulles quittant la phase de pulpe, une cellule relativement grande (700 litres) soit une unité pilote Metso RCS^{TM} de 0,8 m^3, a été choisie. Cette unité, qui a un plateau déflecteur interne, produit une séparation des zones de turbulence (près de l'agitateur) et de quiescence (près de l'écume) assurant ainsi que la DTB mesurée est le reflet exact de flux surfacique de bulles quittant la pulpe. Cette démarche constitue en soit une contribution importante car elle rectifie une mauvaise interprétation souvent retrouvée dans les travaux d'autres chercheurs.

L'unité Metso, qui a un variateur de vitesse, permet une augmentation de l'intensité de la puissance de l'ordre de 8 fois couvrant ainsi l'étendu complète des vitesses de bout de l'agitateur industriel (4,6 à 9,2 m/s). Une large sélection de types de moussant (5) incluant les alcools et les polyglycoles ont été testés. La viscosité a été modélisée en variant la température de l'eau entre 4 et 40 ºC. L'altitude a été modélisée en variant la densité de gaz par un mélange air-hélium alimentant une cellule ''Denver'' laboratoire de 5,5 litres. Les capteurs de dispersion de gaz de l'Université McGill sont le visionneur de bulles et la sonde J_g.

Les travaux montrent que l'effet sur le D_{32}, de tous les moussants testés, peut être normalisé à la même série de courbes en divisant la concentration par la valeur $CCC95$ d'un moussant. La notion de $CCC95$ introduite est équivalente à la CCC (concentration critique de la coalescence) de Laskowski, mais mieux adaptée pour l'analyse mathématique et le développement de modèle. Elle représente la concentration de moussant (ppm) à laquelle 95 % de réduction du D_{32} est atteinte. Les résultats obtenus permettent d'affirmer que la concentration de moussant est la variable qui a le plus grand impact sur le D_{32} et peut être modélisée par avec une fonction décroissance exponentielle qui atteint la taille limite de bulle à une concentration en moussant près de la valeur de CCC. Plus la valeur de $CCC95$

est élevée plus la taille limite de bulle est basse. Il semble également que la valeur de $CCC95$ pour le moussant peut être prédite par sa structure moléculaire en utilisant le paramètre HLB/MW et que la valeur de $CCC95$ d'un moussant augmente avec le J_g.

Les travaux entrepris ont aussi permis de découvrir que le D_{32} est fonction du $J_g^{0,5}$ avec une notion de « création de la taille de bulle » à J_g = 0 cm/s. Le D_{32} est également fonction de la viscosité à 20 ºC par une relation de puissance avec un exposant de 0,776, alors quelle a moins de dépendance à (densité de gaz) avec un exposant de -0,132.

De façon surprenante, il a été découvert que la vitesse de l'agitateur n'avait pas un effet significatif sur le D_{32} dans la plage testée, soit une augmentation de l'intensité de puissance de l'ordre de 8 fois et le doublement de la vitesse en bout de l'agitateur. Il est postulé que les conditions hydrodynamiques à l'intérieur de la zone agitateur/stator sont celles où le niveau élevé de turbulence à écoulement libre et la fraction de vide élevée (taux de rétention de gaz) résultent en un coefficient de traînée non constant plus bas pour les bulles individuelles, signifiant une force (perturbatrice) de traînée moins dépendante de la vélocité relative des fluides mais avec plus d'effet de viscosité.

Finalement, le modèle D_{32} développé pour un système biphasé (air-eau) montre une bonne concordance avec les données mesurées en usine dans 5 sites industriels, représentant des systèmes de flottation à 3 phases (air-eau-solides). Les courbes S_b-J_g produites par le modèle peuvent être utilisées comme un abaque pour étalonner les opérations en usine tel qu'illustré par l'étude de cas de la mine de palladium du Lac des Îles en Ontario confirmant ainsi l'utilité du modèle, une avancé en soit pour la compréhension et l'optimisation du procédé de flottation.

ACKNOWLEDGEMENTS

The author expresses his sincerest and deepest thanks to Wei Zhang, who, while an undergraduate student, was employed as a technician to perform the many tests and measurements associated with this work. His dedication to the task and enthusiasm for the work were unparalleled.

Thanks are due to my many fellow graduate students and colleagues at McGill, in particular Dr Cesar Gomez, Dr Ram Rao, Dr Peter Radziszewski, Frank Rosenblum, Ray Langlois, Barbara Hanley, Dr Claudio Acuna, Jason Doucet, Davin Knuutila, Dr Jose Hernandez-Aguilar, Dr Luis Calzado, Rodrigo Araya-Ledezma, Dr Willy Kracht, Helin Girgin, Marta Bailey, Dr Jorge Torrealba, Rebecca Payant, Mayeli Alvarez-Silva, Ryan Cunningham, Azin Zangooi, Hope Tan, Dr Mitra Mirnezami, Dr Barnabe Ngabe, Dr Stephanie Somot, Edwin van Der Spuy and Annie Wang. A special thanks to Frank Cappuccitti of Flottec whose enthusiasm and insatiable interest in our work continues to fuel our research passion. Each of you has contributed to the great pleasure I have had being a student, and a teacher, again.

Thanks are also due to Metso Minerals, Dr Brian Flintoff and Richard Peaker who made it possible to obtain the necessary flotation equipment. An NSERC (Natural Sciences and Engineering Research Council) IS2 (industrial scholarship) was provided to the author, sponsored by SGS Lakefield Research, and is very gratefully acknowledged. The financial support of two NSERC CRD (Collaborative Research and Development) grants were made possible; one from a consortium of companies (Vale Inco, Xstrata Process Support, Teck Corporation, COREM, Agnico Eagle, SGS Lakefield Research, Shell Canada and Flottec), the other from the AMIRA International P9 project. Many discussions were held and data were kindly supplied by engineers at FL Smidth and Outotec, as well as plant personnel at sites worldwide where we have been making measurements and having great fun over the past 7 years. Your cooperation and help has been invaluable.

A special thanks to my good friend and colleague over many years and now my thesis supervisor once again, Professor Jim Finch. It has been a wonderful, fruitful collaboration for us both, may it continue.

I also wish to thank our daughters Ellen and Kirsten who have put up with an old man trying to regain some of his youth, and who delight in telling their friends their dad is “bubble-man”.

And finally, I will be eternally grateful to my beloved wife, Valerie, who was my inspiration, through her own PhD, to begin this work, and who has encouraged and made it possible for me to complete it.

“There are none so blind as those who will not see”

John Heywood, 1546

TABLE OF CONTENTS

NOMENCLATURE

$A, a, a_o, a_l, a_{max}, B, b, C, c, D_{o\,l}, D_{o\,max}, d_l, n$		Various constants and parameters in the D_{32} model
J_g	cm/s	Superficial gas velocity, superficial gas flow rate divided by the cross sectional area of the flotation cell
d, d_i	mm	Individual bubble diameter
D	m	Impeller diameter
D_{32}	mm	Sauter mean diameter of the BSD, total volume of bubbles divided by total surface are of bubbles assuming spherical shape
D_{10}	mm	Arithmetic mean diameter of the BSD, total diameter of bubbles divided by total number of bubbles
D_o	mm	"Creation" bubble size at J_g = 0 cm/s
D_l	mm	Limiting bubble size
S_b	1/s, s^{-1}	Bubble surface area flux, total surface area of bubbles per unit area of cell per unit of time
Q_g	m^3/s	Volumetric flow rate of gas
A_{cell}	m^2	Cross-sectional area of the cell
Vg	m^3	Volume of gas in cell
V_{cell}	m^3	Volume of cell
K, K_{pulp}	1/s, s^{-1}	Flotation rate constant, overall and in pulp
R_f	fraction	Froth phase recovery factor
BSD		Bubble size distribution
HLB		Hydrophile -Lipophile Balance, empirical relationship measuring contribution of polar and non-polar groups for a frother in aqueous solution
$RCS™$		Reactor Cell System, Metso Minerals patented cell design separating turbulent from quiescent zones
MW, mw	g/mole	Molecular weight

N	rpm	Impeller rotational speed
N_{Re}		Reynolds number, ratio between inertial and viscous forces
N_{We}		Weber number, ratio between inertial and surface tension forces
P	Pa	Pressure
P, P_{net}	W	Power input
P_I	W/m^3	Power intensity or specific power, net power divided by the cell or liquid volume
S	m/s	Impeller tip speed
CCC	ppm	Critical coalescence concentration
$CCC95$	ppm	Concentration for which 95% reduction in D_{32} has been reached
$CCCX$	ppm	Concentration for which X% reduction in D_{32} has been reached
PPM, ppm	g/t	Parts per million
f_v		Viscosity correction factor in D_{32} model
f_d		Altitude (gas density) correction factor in D_{32} model
f_l		Limiting bubble size correction factor in D_{32} model
f_h		Hydrostatic pressure correction factor in D_{32} model
C_{bulk}	ppm	Frother concentration in the bulk aqueous phase
C_{froth}	ppm	Frother concentration in the froth phase
$C_{interface}$	ppm	Frother concentration at the bubble air/water interface

Greek Letters

σ	N/m	Surface tension
ρ	kg/m^3	Density
μ	Pa-s	Dynamic viscosity
φ		Symbol for mathematical function in D_{32} model
ε_g	%, fraction	Gas hold-up or void fraction of gas

LIST OF FIGURES

LIST OF TABLES

CHAPTER 1: Introduction

The separation process known as froth flotation emerged in the early 20th century and revolutionized the mining industry; providing the world with a ready supply of sought after metals at a time of rapid industrial expansion. This spurred the growth of companies that became mining giants, many that are still with us today; examples are BHP (BHP Billiton), Zinc Corporation (Rio Tinto), Phelps Dodge (Freeport McMoRan), Kennecott (Rio Tinto), Magma Copper, Cominco (Teck Resources) and Inco (Vale). In the view of technology historian Jeremy Mouat (Mouat, 1996), froth flotation was "the greatest single metallurgical improvement of the modern era". Mouat goes on to state that: "flotation was of central importance to the smooth functioning of the global economy". Investment in large mining ventures could be safely made because flotation, able to better process variable and lower grade ore deposits at higher throughput rates than existing methods, assured mine operators of predictable extraction efficiencies and low cost, and investors of good financial returns. Metals such as copper, zinc, nickel and lead became available at a price and quantity that met the rapidly increasing demand of the emerging automobile, electrical distribution and home appliance industries.

Prior to the advent of froth flotation (hereafter referred to simply as flotation), reliance on the mineral separation techniques that had prevailed for more than 400 years, such as hand sorting and gravity methods (jigs, vanners and riffled tables) (Hoover, 1914), would have made impossible the availability of these metals in sufficient quantity and suitable cost. The low-cost, efficient and higher capacity flotation process allowed mining to become a mechanized and (almost) continuous process rather than the labour-intensive industry it had been (Mouat, 1996; Menghetti, 2005) and forced smelters to create new technologies such as multi-hearth roasters and large reverberatory furnaces to accommodate the much finer sized concentrate feeds (Laist, 1933).

What emerged in the early 20th century, therefore, was a revolutionary mineral separation method of great industrial significance, but which was rather poorly understood in terms of fundamentals. There was an understanding (Rickard, 1916) that a "collector" hydrocarbon (simply called *oil* in those early days) was required in very minute quantities (grams/tonne of ore) and mixed into the *pulp* (ground ore-water mixture or *slurry*) in order to selectively coat the desired mineral particles. This oily coating made the target particles *hydrophobic* (water hating) and able to attach to air bubbles introduced into the pulp. Sulphide minerals have a natural affinity for hydrocarbons while non-sulphides such as silicates and carbonates (*gangue* minerals) tend to remain *hydrophilic* (water loving) and do not attach to the bubbles. Bubbles with attached hydrophobic particles will rise to the pulp surface, due to their buoyancy in water, and form a *froth* of enriched concentration (of the desired mineral) which can then be removed separately as a *concentrate*. A separate stream, depleted in the desired mineral, also exits the flotation process and is called the *tailing*.

Bubbles were initially created naturally by adding acid to react with minerals in the ore (Everson patent, 1885; Delprat patent, 1904), by applying a vacuum to the separation vessel (Elmore patent, 1898), or by violent mechanical agitation of the pulp (Sulman et al patent, 1906). None of these initial methods afforded close control of gas addition or bubble production, and the introduction of hydrocarbon collector (the oil) was often what was residually in the ore (from the mining process) or far in excess of what was actually required for true froth flotation. Excess use of hydrocarbon resulted in less effective processes better described as *bulk oil flotation* and *skim flotation*. In fact, it was first Froment (1902) who made the link that the essential combination of a very minute quantity of hydrocarbon combined with separate introduction of small gas bubbles were the two key elements to froth flotation. The pneumatic mechanically-agitated sub-aeration cells that became the industry standard, were introduced around 1915 (Lynch et al, 2007) and were quickly adopted. About this time it was also realized that the froth could be better controlled independently by the addition of a separate group of hydrocarbons, called *frothers*, designed to stabilize the froth in the flotation cell and permit it to break down (*de-gas*) following concentrate removal. Typically, these frothers were creosote based (cresylic acids), pine tar based (terpineols) or based on other natural oils such as eucalyptus (Rickard, 1916). References of the era (Rickard, 1916) suggest frother selection was based on froth stability relating to ore type, with little appreciation for their impact on bubble size in the pulp. MIBC (methyl isobutyl carbinol) (1930's) and polypropylene glycols (1950's) were subsequently added to the suite of frothers widely used in base metals processing (Fuerstenau, 2007). This suite of frothers has remained largely the same for a period of 70 years. Understanding the key role played by frothers and their relation to bubbles in the flotation process has been equally slow to emerge; one reason being the lack of appropriate measurement sensors (Finch and Gomez, 2001).

During the period of roughly 1930 to 1960, science made great strides in describing the fundamentals behind the chemistry and physics of flotation (Fuerstenau, 2007), notably through single-particle and single-bubble studies that established the importance of contact angle and zeta potential measurements, detailed micro-flotation testing using devices such as the Hallimond tube to establish the importance of pH and electrochemical potential (Eh), and theoretical approaches to the particle-bubble attachment processes that helped predict an optimum bubble size range. New groups of collectors, such as amines, were found to selectively float non-sulphide minerals, and flotation advanced from sulphide base metals to industrial minerals such as potash, phosphates, and to oxides such as titanium and iron ores. There appears to be little research during this period attempting to establish direct relationships between flotation performance and air flow rate or bubble size.

The important relationship between bubble size and particle size in flotation was investigated by a number of workers in the 60's and 70's. Reay and Ratcliff (1975) showed, through manipulation of the relevant flow equations, that collection efficiency of particles by bubbles would strongly depend on the bubble to particle size ratio. They concluded that, within practical constraints, there was a powerful incentive to make bubble size as small as possible. Anfruns and Kitchener (1976) demonstrated, through elegant single bubble and particle size experiments, the strong dependence of particle collection efficiency on this

ratio, and the need for small, minus 1 mm, bubbles in collecting sub-40 μm particles. In a major review of the physical factors affecting flotation, Jameson et al (1977) concluded that bubble size is an important variable that is almost never controlled in plants, in large part because it is difficult to accurately measure. They offered the opinion that sub-500 μm (<0.5 mm) bubbles would be required to significantly improve the collection efficiency of very fine particles. They lamented that bubbles of this size were generally not produced by conventional mechanical flotation machines. Although the importance of matching bubble to particle size was established by the late 1970's, there were no bubble-sizing methods suitable for industrial measurements.

The study of machine scale-up criteria and the desire to better understand flotation kinetics seems to have been spurred by the rapid increase in size of flotation cells that began in the 1970's, as illustrated in Figure 1.1(adapted from Lynch et al, 2007). Many cell designs of the day were *self-aerating* (e.g. Wemco, Denver Sub-A) where air is drawn into the cell due to the low pressure created by the rapidly rotating impeller, as compared to *forced-air* (Dorr-Oliver, Outokumpu, Denver D-R) machines where the air is introduced into the impeller region by low-pressure blowers (Taggart, 1954). Many cell designs had mechanically-driven *froth paddles* to physically pull the froth from the cell into the discharge launders. Arbiter, Harris and co-workers (Arbiter et al, 1976; Harris, 1974l) studied scale-up of commercial cells examining key *hydrodynamic* relationships. They concluded that froth removal rate and bubble-particle interaction/attachment were key recovery drivers and that increased air flow alone could lead to a decrease in recovery of coarser particles. Regarding frothers, Arbiter et al note that as frother was increased, a decrease in bubble size, an increase in entrained air, and a decrease in air flow occurred in a self-aerating cell. With the benefit of hindsight, it would now appear that studying both forced-air and self-aerating machines as a single group, and the predominance at the time of mechanical froth removal, helped to confound the key relationships that these researchers were looking for on the industrial scale. A lack of suitable sensors for measuring the hydrodynamic variables *in-situ* in the industrial environment was clearly of need.

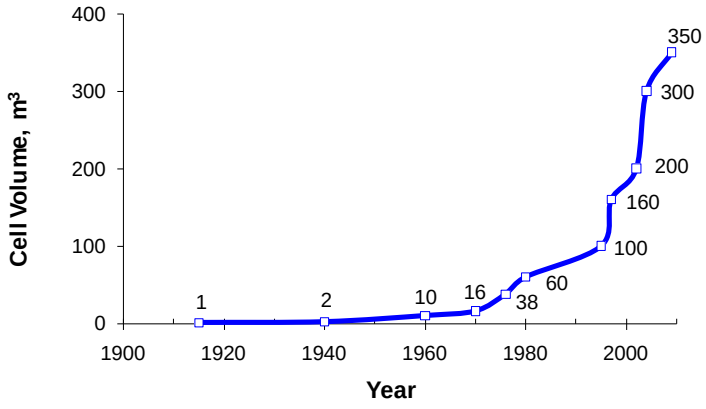

Figure 1.1 Increase in maximum flotation cell size over the past 100 years (adapted from Lynch et al, 2007)

King (1972, 1973) was among the first to propose a flotation model that linked kinetics (i.e. the flotation rate constant) to the bubble surface area per unit volume of pulp. This relationship incorporated the notion of volumetric air rate and specific surface area of bubbles present (m^2/m^3) plus a constant that represented the proportion of total particles eligible to float. Laplante et al (1983) built on this approach and that of Pogorely (1962) to refine and validate, on a laboratory batch scale, a flotation-rate model incorporating air rate and measured bubble size as a function of air rate and frother concentration. Not until the later 1980's and early 90's was the link established on an industrial scale between flotation kinetics and the key hydrodynamic or *gas dispersion* variables, through the work at McGill University (Dobby and Finch, 1986; Xu and Finch, 1989; Finch and Dobby, 1990) and the Julius Kruttschnitt Mineral Research Centre (JKMRC, University of Queensland) (Gorain et al, 1997, 1999). The initial McGill work was based on study of flotation columns and was subsequently adapted to mechanical flotation machines (Cooper et al, 2004). These workers established the key relationship linking flotation kinetics to the air flow rate and bubble size, developed the necessary industrially-robust sensors and measurement protocols, and validated the relationships through multiple surveys in industrial environments. Since the 2000's, in combination with other modeling techniques such as CFD (computational fluid dynamics) (Koh et al, 2000; Koh and Schwarz, 2007) population balance (Harris et al, 2002) and probabilistic models incorporating the physics of particle-bubble collision, attachment, detachment (Herbst and Harris, 2007) and recovery through the froth (Cilliers, 2007), flotation practitioners are now able to scale and optimize the flotation plants based on fundamental measurements and process understanding.

During the later 1990's, Finch and co-workers (Gomez and Finch, 2002; Hernandez-Aguilar et al, 2002; Gomez et al, 2003) established the techniques and robust sensors to measure the gas dispersion metrics; Superficial gas velocity (J_g) representing the volumetric gas flow (Q_g) exiting the pulp per unit cross-sectional area of the cell (A_{cell}) per unit of time; the Sauter mean bubble size (D_{32}) representing the bubble size distribution (of measured individual size d_i) for use in calculating the bubble surface area flux (S_b), the total surface area of bubbles exiting the cell per unit cross-sectional area of the cell per unit of time. These parameters are linked by the following relationships:

$$J_g = \frac{Q_g}{A_{cell}} \qquad 1.1$$

$$d_{32} = \frac{\sum d_i^3}{\sum d_i^2} \qquad 1.2$$

$$S_b = \frac{6J_g}{D_{32}} \qquad 1.3$$

A third measured variable, the volumetric gas hold-up ($\mathcal{E}_g$), expressed as a fraction or %, also forms one of the gas dispersion metrics and relates the volume of gas (V_g) to the volume of the cell (V_{cell}):

$$\varepsilon_g = \frac{V_g}{V_{cell}} \quad 1.4$$

Gorain and co-workers (1997, 1999) showed that bubble surface area flux (S_b) is a key driver of flotation recovery through the k-S_b relationship,

$$k_{Pulp} = PS_b \quad 1.5$$

$$k = PS_bR_f \quad 1.6$$

where k_{Pulp} represents the rate constant in the pulp phase, k represents the overall flotation rate constant (pulp and froth), P is a floatability parameter for the mineral particles to be floated, and R_f is recovery of floated particles across the froth phase. Observing that S_b is inversely proportional to D_{32} it is seen that the rate of flotation, and hence recovery, is inversely linked to bubble size and directly proportional to the volumetric flow of gas, Q_g. Studies of flotation performances therefore require accurate and precise measurements of both these key parameters. These needs were fulfilled by the breakthrough developments in sensor technology and process measurement of McGill and the JKMRC. Interestingly, the work of Laplante et al (1983) predicted the same relationship as Equation 1.6 for what they termed the “free-floating mode”, that is, the condition where particles are free to collect on the bubble surface as opposed to their “hindered floating mode” where the bubble surface becomes loaded with collected particles. The majority of base metal rougher and scavenger flotation can be considered to be in the free-floating mode.

What has emerged over this almost century of studying flotation is an understanding of the key role played by the bubbles themselves; their size and their total combined surface area available for collecting hydrophobic particles. Reliable models (i.e. understanding) for predicting bubble size as a function of the key process variables (e.g. frother, J_g, viscosity, rotor speed, solids, air density) are lacking. Models of bubble size have been developed for aerated stirred tank reactors (*CSTR's*) used in chemical engineering applications (Parthasarathy et al, 1991; Machon et al, 1997), however, these models loose applicability in flotation reactor systems having impeller/stator designs where turbulence and energy dissipation rates in the narrow regions between impeller and stator are orders of magnitude greater than in conventional CSTR's (Al Taweel and Cheng, 1995). The high energy intensity available in flotation cells also permits air (or gas) to be injected at a considerably higher rate than in conventional CSTR's. Models predicting bubble size specifically for flotation systems are clearly required. There has been some work on modeling bubble size using laboratory-sized cells, however, these studies have been inadequate in accounting for the effect of many key variables (e.g. frother) and limitations occur when using small cells (4-10 liters) to model behavior in larger tanks where there are distinct regions of turbulence and quiescent behavior.

The aim of this research is, therefore, to model bubble size as a function of the key variables affecting the flotation process. The study will be performed using pilot scale equipment (0.8 m^3) that is up to two orders of magnitude larger than equipment used for studies performed to date by others (Grau and Heiskanen, 2003, 2005), and will incorporate the key process variables of superficial gas velocity, frother type and concentration, power input (impeller speed), gas density and pulp viscosity. Key interaction effects between the most important variables will also be investigated. The study will restrict itself to the 2-phase air-water system. Understanding the 2-phase behavior prior to tackling the inclusion of solids seems logical and also avoids the logistical problems of handling solids on this scale in a university laboratory. Comparisons of the developed model with plant measurements taken from operations worldwide will also be performed in order to validate the approach.

1.1 Thesis Objectives

The overall goal of the research was to develop and validate a model for predicting bubble size in a gas-water (i.e. 2-phase) system in mechanical, forced-air, flotation machines. This required the following sub-objectives to be met:

1. Development of an experimental set-up and test program involving both a pilot plant and a laboratory flotation cell capable of investigating the five (5) variables to be examined
    a. Characterization of the pilot cell and gas dispersion measurement sensors
    b. Conducting the test program on the pilot unit to investigate the effect of power input, gas rate, viscosity, and frother type and concentration
    c. Developing a sub-testing program on a laboratory cell to investigate the effect of gas density, since this variable could not be investigated safely or cost effectively on the large pilot unit
    d. Performing the mathematical analysis required to produce a robust model with acceptable levels of statistical significance
2. Conduct in-plant measurements at a variety of operations worldwide to produce validation data for the developed model
    a. Develop a plant testing methodology that would produce a sufficiently broad range of results
    b. Develop a method for comparison of the model to the plant data
3. Demonstrate, through in-plant metallurgical testing and gas dispersion measurements, the links between flotation performance and the variables of bubble size and air rate.

1.2 Thesis Scope

Previous work on bubble size modeling in flotation has been limited to testing on laboratory sized equipment and with a relatively incomplete suite of the important operating variables. Some modeling has been on forced air machines (Gomez et al, 2006) while other has been on self-aerated units (Koh and Schwarz, 2007). The results have not always been in agreement, for example, the importance of power input on bubble siz (Grano, 2006). Those researchers using modeling techniques (such as CFD and population balance models) that require bubble size as an input variable have therefore tended to input constant values (Koh and Schwarz, 2007, Cilliers, 2007) or very simplified models as in JKSimFloat™ (Harris et al, 2002). This work aims to provide both practitioners and modelers with a reliable tool for prediction of bubble size. As a starting point, this work will focus on forced-air machines having stator-impeller mechanisms for liquid circulation and air distribution (the most prevalent type). The choice of an industrial, pilot-sized, cell avoids several of the shortcomings of measurements made on small laboratory units and will make the results more credible for practitioners and researchers alike.

The choice to model the 2-phase system is not seen as a deficiency; rather it is seen as a logical progression to first understand gas-liquid behavior before introducing solids into the analysis. The variables selected for study are those considered the main manipulated variables (gas rate, frother type and concentration, impeller speed) and "situational" variables (gas/air density and liquid viscosity). While the operational variables are self-evident, the choice of the situational variables, viscosity and gas density, may be less so. Flotation plants operate at elevations from sea level to about 5,000 meters above sea level where the air density is about half that at sea level. Plants also operate in conditions where the pulp temperatures can vary from near 0 ^{o}C to near 70 ^{o}C, and with a wide range in both particle size and solids content, both of which will impact pulp viscosity. As a result, the effective viscosity of the liquid/solid phase can vary greatly. An attempt was therefore made to include the effect of viscosity on bubble size, by varying liquid viscosity only at this stage of 2-phase testing, recognizing that solids content and size are also likely factors in 3-phase systems. The ranges selected for all the variables can be considered representative of industrial practice, with some extension above and below typical operating range for frother concentration, and below normal for gas rate (J_g), in order to more fully define relationships. The model can be considered to be empirical in that parameters are fitted from the data obtained to suitable equations. As such, their use is limited to the range of data collected, but given that these ranges represent industrial conditions rather well, this limitation is not seen as a serious one.

The inclusion of gas dispersion and metallurgical data from operational plants also introduces a greater amount of variability than laboratory data, since all process factors in a plant cannot be controlled and measurements are performed under feed conditions varying over time. Nevertheless, including some plant data is seen as a worthwhile contribution to the work, as it represents the first time such links have been made.

1.3 Thesis Structure

The thesis is organized in eight (8) chapters and three (3) appendices. The details of the structure are as follows:

Chapter 1: Introduction

The flotation process is introduced, with an emphasis on understanding the role of bubbles spanning the century since the inception of flotation in the early 1900's. The thesis objectives and the scope of the work are presented.

Chapter 2: Literature Review

The literature review covers bubble size modeling in stirred tank reactors and flotation, and the link to the bubble surface area flux (S_b); the gas dispersion parameter that connects bubble size to flotation kinetics and hence, particle recovery.

Chapter 3: Materials, Methods and Measurement

The experimental set-up for the pilot and laboratory flotation cells is described, as are the measurement methods, and the data validation and measures of reproducibility (i.e. precision). Correction factors are developed to account for the changes in measured bubble size and gas rate that occur as a result of differences in hydrostatic pressure and frother concentration (bubble size only).

Chapter 4: Experimental Results and Analysis: Laboratory Testing

Results are presented for the four variables tested on the large 800 liter pilot cell; frother, air rate, impeller speed and liquid viscosity, and for gas density which was tested on the small, 5.5 liter, laboratory cell. Interaction effects between the two most important variables, gas rate and frother concentration, were tested on the 800 liter cell. Some analysis of results is introduced.

Chapter 5: Building the Bubble Size Model

The results from test work on the 800 liter pilot cell and 5.5 liter laboratory cell, described in Chapter 4, are combined into a comprehensive model (single equation) for prediction of bubble size (D_{32}) and bubble surface area flux (S_b). The precision of the model in predicting D_{32} and S_b is presented.

Chapter 6: Model Comparison to Laboratory and Plant Results (Validation) and Model Predictions

The model is used to predict the effect of the key variables on D_{32} and S_b, leading to new understandings of how the flotation variables impact recovery. Gas dispersion data from five plants (3-phase system) are presented and used to validate the developed D_{32} and S_b models. Case study data from the Lac des Iles palladium mine/mill in Ontario is combined

with the model output in order to demonstrate how the model can be used as a benchmarking and optimization tool.

Chapter 7: Discussion of Results

Discussion of the model in detail, including some of the key findings, implications, relationships and potential uses are made.

Chapter 8: Conclusions and Claims to Original Research

Conclusions and claims to original research and contributions to knowledge are covered, and suggestions made for future research directions.

Appendix A: Gas Dispersion Measurements and Correction Factors

Detailed description of the methodology for making the gas dispersion measurements (BSD, J_g and ε_g), and calculations for establishing the various correction factors (CF's) that account for hydrostatic pressure difference between the sensor measurement location and the reference location.

Appendix B: Method for Correcting Initial D_{32} and CCCX Measurements

This section details the calculations required for establishing corrected D_{32} and CCCX values from initial CCCX values for *Correction Factor for Bubble Coalescence in Bubble Viewer* found in Section 3.4.

Appendix C: Experimental Data from the Laboratory Studies

Data from test work on the 800 and 5.5 liter cells are presented on a CD.

CHAPTER 2: Literature Review

This literature review is divided into three elements that are important to the study, and ultimately the prediction of bubble size; the role of frothers, modeling bubble size, and measurement of bubble size.

2.1 The Role of Frother in Bubble Break-up and Coalescence

Bubble properties are strongly impacted by frother, both concentration and type (Pugh, 2007; Cho and Laskowski, 2002; Finch et al, 2008). It is also recognized that frother plays more than one role in flotation (Wills and Napier-Munn, 2007). In addition to creating stable froth that serves to increase gangue removal from the collected minerals via water drainage from the inter-bubble spaces (*Plateau borders*) in the froth (Cilliers, 2007), frother also influences the size and hence number and surface area of bubbles created in the pulp. Within the pulp the mechanism appears to have at least 2 components; bubble *break-up* and bubble *coalescence*. Given an initial bubble in water subjected to some level of turbulence, the presence of frother will contribute to the bubble's ability to break into smaller bubbles (break-up), and will also affect the ability of the resulting daughter bubbles to re-combine into larger bubbles (coalescence). Frothers, being surface active agents or *surfactants*, will concentrate at the air-water interface and impact the interfacial and near-interfacial properties of the bubble. Having a hetero-polar molecular structure the frother molecule will tend to orient itself with its hydrophilic end (OH or similar group) on the water side and its hydrophobic, non-polar, hydrocarbon end on the air side. Coalescence prevention by surfactants (frothers) is a combination of stabilization of a water layer on the bubble surface and an increase in bubble rigidity. The discussion of coalescence depends on what process is the focus, what prevents coalescence at bubble formation seems easier to explain by the 'water layer' idea but coalescence prevention in the foam can be explained by the rigidity idea (and the action of particles). The role of frothers in facilitating bubble break-up is even less well understood. Even the most recent literature and textbooks (Gupta and Yan, 2006; Wills and Napier-Munn, 2007) erroneously report that bubble size reduction by frother is due to the reduction in air-water surface tension (i.e. surface energy). Yet salt solutions (e.g. NaCl), which are known to increase surface tension, have been shown to be equally effective at reducing bubble size (Quinn et al, 2007). The explanation, proposed by some (Finch et al, 2009), may lie in the dynamic nature of the surface forces caused by uneven concentration of surfactant over the bubble surface at the moment of air injection into the solution where frother is randomly distributed. It is thought that the force resulting from the *surface tension gradients,* rather than an overall decrease in surface tension itself, would produce surface instabilities that result in bubble break-up when sufficient mechanical energy (turbulence) is introduced to the system.

When frother is introduced to a gas-liquid mixture the characteristic bubble size (e.g. D_{10}, D_{32}) will decrease to a limiting value as more frother is added. In addition, it has been shown (Nesset et al, 2007) that the shape of the frequency distribution of the bubble size population (BSD) will also change; from a bi-modal distribution at zero frother to a much

narrower BSD and overall smaller average bubble size at higher concentrations as evident in Figure 2.1. A selection of bubble images corresponding to the BSD's of Figure 2.1 are shown in Figure 2.2. It is clear that viewing an image is illustrative but does not capture the information gained from collecting 10,000 bubble images and displaying as a frequency distribution.

Laskowski (2003) termed the concentration beyond which the bubble size is no longer reduced the *critical coalescence concentration*, or *CCC*. This is a concept that will be used and extended with this work. The difficulty with extracting the CCC value for a given frother from experimental data is pinpointing the precise location of the CCC from an exponentially limiting curve. Laskowski provided a graphical method that intersects two lines tangent to the upper and lower portions of the bubble size vs. concentration curve, but the method is somewhat impractical and does not lend itself to mathematical analysis. The notion of CCC95 was therefore introduced by Nesset et al (2007), adapting the exponential decay equation of Hernandez-Aguilar et al (2005b), defining the concentration for which the bubble size has been reduced to within 5% (i.e. 95% reduction) of its limiting value. This approach is mathematically straightforward and has been extended to define other levels of frother concentration relative to the CCC, generically referred to as CCCX such as CCC75, CCC50 and even CCC150 (representing 2X the CCC75 concentration).

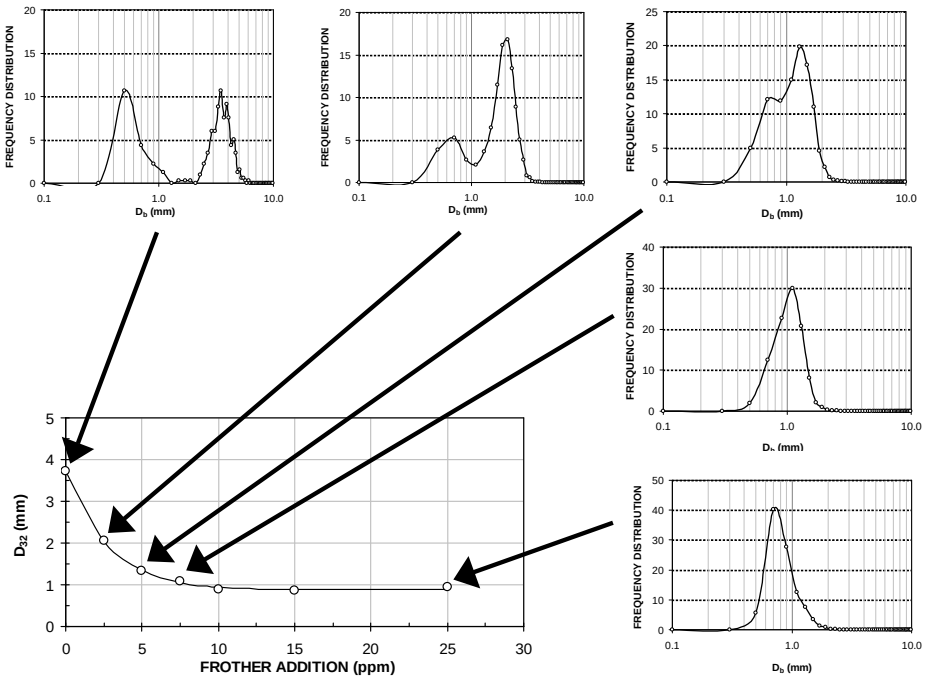

Figure 2.1 Changes in bubble size distribution (inset frequency distributions) as frother concentration is increased (Nesset et al, 2007) (DF250, mechanical forced-air machine)

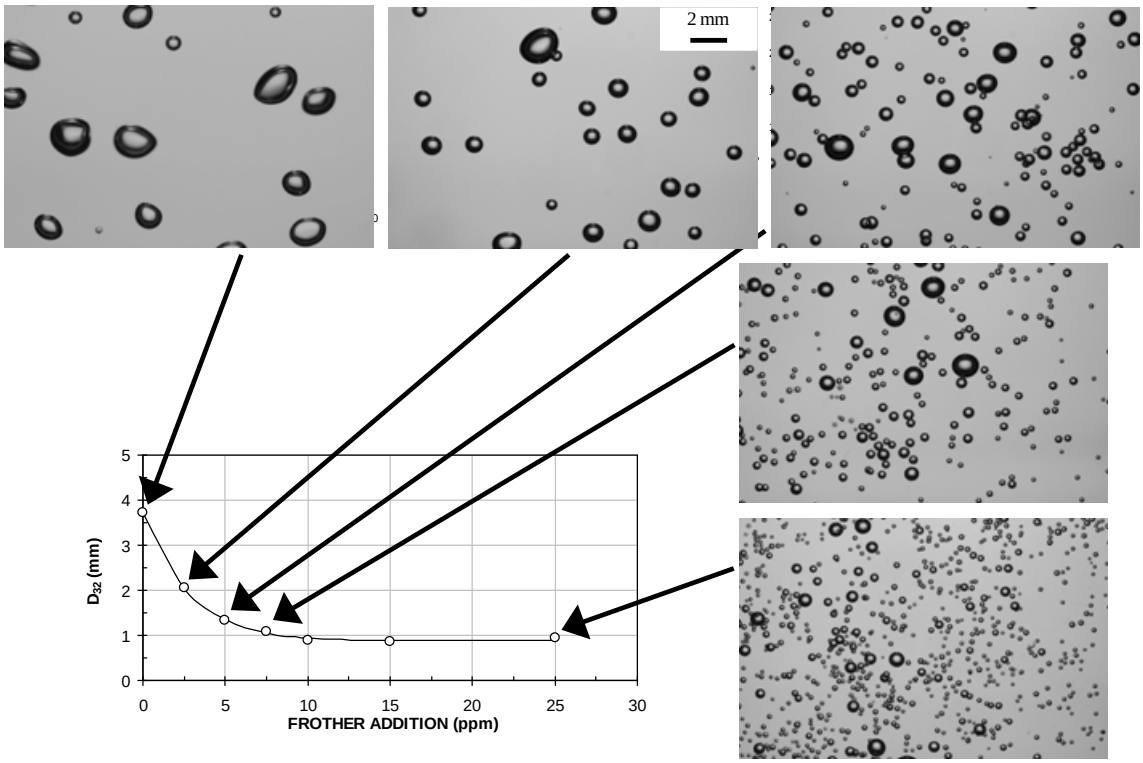

Figure 2.2 Images of bubble size as frother concentration is increased. Images correspond to BSD's in Figure 2.1 (DF250, mechanical forced-air machine)

2.2 Bubble Size Models

As noted in the Introduction, the ability to predict and model bubble size, and more specifically D_{32}, based on the main flotation variables would clearly be advantageous in terms of process understanding and optimization. At the commencement of this research there existed no adequate model for D_{32} for the key variables used in industrial flotation; however, relationships have been developed for the aerated stirred tank reactors commonly used in the chemical process industries. These reactors differ in some significant ways from flotation machines, so the models developed for their use may not be applicable. As a starting point, however, a review will be made of these models.

The analysis presented by Hinze (1955), based on droplets in liquid-liquid suspensions, forms the basis for most of the subsequent work and is based on a balance between inertial (disruptive, i.e. turbulent) forces and stabilizing (surface tension) forces as expressed by the *Weber Number* (N_{We});

$$N_{We} = \frac{\rho N^2 D^3}{\sigma} \qquad 2.1$$

where ρ and σ are fluid density and surface tension and N and D are impeller rpm and diameter. There exists, the analysis surmises, a critical bubble size below which a bubble will remain stable. It has since been shown (Martinez-Bazan et al, 2000) that the D_{32} is directly related to this critical diameter. Making the extension that the critical diameter is proportional to D_{32}, the expression established by Hinze becomes;

$$D_{32} \propto \left[\frac{\sigma^{0.6}}{\left(\frac{P}{V_L}\right)^{0.4} \rho^{0.2}} \right] \qquad 2.2$$

The P/V_L term represents the specific energy dissipation rate (Kolmogorov's theory of turbulence, 1949) and relates to the turbulence in the system; P represents the power input while V_L is typically taken as the volume of liquid, but, alternatively, could be the volume swept by the impeller.

The analysis was further refined by Calderbank (1958) who incorporated gas holdup and viscosity into Equation 2.2 to give;

$$D_{32} \propto \left[\frac{\sigma^{0.6}}{\left(\frac{P}{V_L}\right)^{0.4} \rho^{0.2}} \right] \left(\varepsilon_g\right)^{\alpha} \left(\frac{\mu_G}{\mu_L}\right)^{0.25} \qquad 2.3$$

where ε_g is the gas holdup and μ_L and μ_G are the liquid and gas viscosities respectively. The fitted α parameter was found to be 0.65 for an aliphatic alcohol and 0.4 for an electrolyte solution. More recently gas holdup, ε_g, has been found to be linearly related to the superficial gas velocity, J_g , over a limited range, which often defines the operating range of a flotation cell, for columns (Finch and Dobby; 1990) and mechanical flotation machines (Dahlke et al; 2005, Nesset et al; 2006). Thus Equation 2.3 indirectly links D_{32} to the superficial gas velocity raised to a power (α) between 0.4 and 0.65.

The analogous parameter in aerated stirred tank reactors (Machon et al, 1997) to the S_b parameter in flotation cells (Equation 1.3) is the specific interfacial area, a, the surface area of gas per unit volume of the occupied liquid volume in the vessel, given by:

$$a = \frac{6\varepsilon_g}{D_{32}} \qquad 2.4$$

In an effort to avoid issues of bubble coalescence that had been a factor in many of the earlier studies, Sridhar and Potter (1980) found that in the (non-coalescing) cyclohexane-air system, across a wide range of pressure, temperature and surface tension, the following relationship could be fitted for a, the specific interfacial area:

$$a \propto \left[\frac{\sigma^{0.6}}{\left(\frac{P_N}{V_L}\right)^{0.4} \rho^{0.2}} \right]^{-1} \left(\frac{J_g}{U_B}\right)^{0.5} \left(\frac{\rho_G}{\rho_A}\right)^{0.16} \left(\frac{P_T}{P_N}\right) \qquad 2.5$$

Note the introduction of the ratio terms, J_g and U_B (bubble rise velocity), ρ_G and ρ_A (density of gas and air at operating conditions), and P_N and P_T (net and total power input) in order to maintain dimensional coherence for the overall relationship. If one assumes $\mathcal{E}_G \propto J_g$ (as referenced previously) then Equation 2.5 can be inverted to give an expression for D_{32} using Equation 2.4. In this case, D_{32} becomes proportional to $J_g^{0.5}$, $(\rho_o/\rho_G)^{0.16}$, $P_N^{0.4}$ and $\sigma^{0.6}$.

All of this work (Equations 2.2, 2.3, 2.5) is based on the assumption of a critical Weber number and has maintained that a strong relationship (exponent 0.6) exists between the D_{32} and the surface tension at the liquid gas interface. More recent workers have disputed that these relationships apply in systems where a chemical environment exists that strongly opposes bubble coalescence after initial formation (Parthasarathy et al, 1991). Machon et al (1997) concluded that there was no correlation between surface tension and bubble size based on tests in an aerated stirred reactor for aqueous electrolyte and alcohol solutions, and that the critical Weber number approach to the analysis of these systems was inappropriate. They further concluded that both bubble break-up and coalescence are important processes in establishing bubble size in non-coalescing systems, and that it is interfacial *surface tension gradients* and not decreased surface tension that leads to bubble break-up. In later work by Alves et al (2002) they concluded that there is a clear difference between coalescing and non-coalescing systems (addition of electrolyte and surfactant), and that the non-coalescing systems tested exhibited a strong D_{32} dependence on P/V_L having an exponent from –0.52 to –0.37, depending on location relative to the turbine impeller. This agrees roughly with the theoretically derived exponent of –0.4 of Equation 2.2. They also found a similar exponent for coalescing systems at very low J_g values (0.2 cm/s) and concluded that the addition of surfactant or electrolyte did not alter the formation size of bubbles, only the subsequent coalescence process. They also concluded that the effect of P/V (i.e. turbulence) on bubble size is significantly lower for the non-coalescing systems. Furthermore, they could find no relationship between bubble size and gas rate for the non-coalescing system (due to the dominating influence of electrolyte/surfactant), however they did find a good correlation between gas rate and D_{32} for coalescing systems.

In summary, these studies on aerated stirred tank reactors provide some valuable information about the importance of electrolyte and surfactant additions in preventing bubble coalescence, and as a consequence strongly influencing bubble size. They also serve to point out that, once sufficient surfactant or electrolyte are in the aqueous system, surface tension is no longer the counter force in stabilizing the bubble, and that the classical analysis considering turbulence and surface tension may no longer be valid. The implication may be that for pure liquids surface tension will play a role whereas in aqueous solutions with surfactant, it may be surface tension gradients, as pointed out by Parthasarathy et al (1991), that are the driver. There is a clear need to differentiate between coalescing and non-coalescing systems. The review has also suggested that in non-coalescing systems, the effect of power intensity (turbulence dissipation rate) and gas density on the resulting bubble size is greatly diminished over coalescing systems, due, it is suggested, to the over-riding effect of the surfactant/electrolyte. Although many studies have shown the importance

of the power intensity, P/V_L, and to a lesser extent, liquid viscosity and gas density, there is not consistent agreement between studies. This may be due to large difference in size of reactors studied (note: most are rather small with diameters well below 0.5 m), methods of bubble visualization, and impeller design and measurement locations within the reactor volume, as described in a review by Alves et al (2002). In comparison to flotation machines, these aerated stirred tanks tend to operate at higher superficial gas velocities (typically of the order 10 cm/s) and with lower power intensity (typically below 1W/kg or 1 kW/m^3). Given these differences plus the absence of stators surrounding the impellers, the direct applicability of these aerated stirred tank reactor studies and models to flotation machines must not be assumed. Al Taweel and Cheng (1995) note a much greater energy dissipation rate within the very narrow impeller/stator gap of flotation machines compared with the remainder of the cell volume which is typically of the order of 1-2 kW/m^3. In flotation there is almost always a significant concentration of frother, electrolyte or both, so the general conclusions regarding non-coalescing systems should likely be heeded. The review of aerated stirred-tank models has served to illustrate the need for models developed specifically for flotation machines.

Modeling D_{32} in flotation machines

In his classic review of the early work on flotation machine scale-up, Harris (1976) noted that frother had a greater influence on bubble size than any of the machine variables under manipulation. At the time there was no adequate method for measuring bubble size in industrial machines and the comment went largely unnoticed. With the advent of flotation column technology in the 1970's and 80's, much work was done by the group at McGill and the University of Toronto (Dobby and Finch; 1986) on characterization of gas-sparged flotation columns. The method of establishing bubble size was by *drift flux analysis*, an inferred method that relies on measurement of gas holdup to calculate the bubble size (Banisi and Finch, 1994). In the water-air system with frother added, Finch and Dobby (1990) proposed an equation for bubble size (D_b) as a function of superficial gas velocity (J_g);

$$D_b = C \cdot J_g^n \qquad 2.6$$

The exponent n was found to be 0.25 for most porous sparger types, while the C parameter depends primarily on frother concentration as well as correcting for the effective active area of the sparger. Equation 2.6 suggests that for infinitely low J_g there will be an infinitely small bubble size, a notion that was not tested in their work. At the University of Cape Town a photometric device for measuring bubble size by extracting slurry samples through a narrow capillary tube (the UCT bubble size analyzer, Randall et al, 1989) was used to measure bubble size in a laboratory column as a function of different variables, including air rate, temperature, particle size and pulp viscosity and density (O'Connor et al, 1990). The data were fitted to power-law relationships similar to Equation 2.6. The exponent, n, for bubble size versus gas rate, was 0.4 and 0.47 respectively for air-water and air-water-solids, and n = 0.26 for the effect of viscosity in the air-water system. These tests were conducted in a coalescing system (i.e. no frother). In another series of tests reported in the same reference,

the authors note the overwhelming effect of frother on bubble size, and that various xanthate collectors, alone or in combination with frother, had no additional effect on bubble size.

Several workers attempted to model the hydrodynamic performance of particular laboratory flotation machines, including Sawant et al (1981), Nonaka et al (1982), O'Connor et al (1990), and Al Taweel and Cheng (1995). They all found that the power intensity (manipulated by varying the impeller rotational speed) had a measurable effect on gas holdup and/or measured bubble size (O'Connor et al, 1990). It is suspected that these small laboratory machines do not scale well to the larger machines since measurements are made in close proximity (a few cm) to the highly turbulent impeller/stator region where high recirculation of both liquid and gas bubbles back into the high-shear impeller region may occur. By contrast, in larger industrial units the impeller-stator region is distinctly separate in terms of distance from the greater proportion of the cell volume which is more quiescent. Hernandez-Aguilar et al (2002) have shown the sensitivity between sampling location and measured bubble size distribution in a Denver laboratory machine. This is a demonstrated limitation of making such measurements on small, laboratory-sized units.

Laplante et al (1983) recognized this limitation and constructed a 5.5 liter laboratory unit having a higher than normal height to width ratio that served to create a quiescent zone above the impeller region where bubble size measurements were made. Using a flash-and-camera technique and defining bubble size as the mean size of the population (D_{10}), they developed a relationship including both gas rate and frother concentration:

$$Ln\left[\frac{D_{10}}{2}\right] = a_1 Q_a - a_2 C_f + a_3 C_f^2 \qquad 2.7$$

The a terms are constants, Q_a is air flow rate and C_f is the concentration of frother. This was the first attempt known to the author to link bubble size, a machine variable (air flow rate), and the effect of frother concentration. Note the strong non-linear effect of the frother. Within the industrial environment, one of the first attempts at modeling the multiple effects of process and flotation machine variables in mechanical forced-air machines was performed by Gorain et al (1997, 1999).They employed a large pilot-scale machine (3 m^3) and direct measurement of bubble size (D_{32}, using the UCT method) and superficial gas velocity (J_g, using a manual JKMRC technique), as well as the impeller peripheral speed (S) and volumetric air flow rate (Q_a) in different plants. The slurry was characterized by its 80% passing size (P_{80}). Their work related the calculated bubble surface area flux ($S_b=6J_g/D_{32}$) to the measured and machine variables tested on the pilot unit, which had interchangeable impeller/stator parts. Gas dispersion measurements (D_{32} and J_g) were averaged from six readings, three near the top and three near the bottom, of the pilot cell. This seminal work confirmed the k-S_b relationship as presented in Equations 1.5 and 1.6. The resulting regression model for S_b showed (Gorain et al, 1999);

$$S_b \propto S^b \cdot \left(\frac{Q_a}{A_c}\right)^c \cdot A_s^d \cdot P_{80}^e \qquad 2.8$$

where b, c, d and e are fitted constants, A_c is the cell cross-sectional area, and A_s is the aspect ratio of impeller diameter to height. Their data fitting for 64 data points resulted in an

acceptable R^2 of 0.81 and yielded the following parameters; b = 0.44, c = 0.75, d = -0.10 and e = -0.43.

Examination of Equation 2.8 reveals that the J_g measured to yield S_b (left side of equation) and Q_a/A_c (right side) can be considered the same variable, measured independently, of air rate per unit of surface cross-sectional area of the cell (Note: while J_g is measured at specific locations, Q_a/A_c is an average for the cell, and there may be some difference). By substituting J_g for Q_a/A_c, and $6J_g/D_{32}$ for S_b (Equation 1.3), Equation 2.8 can be rearranged to solve for D_{32} giving;

$$D_{32} \propto \left[\frac{J_g^{0.25}}{S^{0.44} \cdot A_S^{0.1} \cdot P_{80}^{-0.43}}\right] \qquad 2\text{-}9$$

Gorain et al (1999) recognized that frother concentration plays the largest role in establishing bubble size, although it does not appear in their equation. They concluded that given the good correlation of the data fitting, the frother concentration must have been sufficiently high (i.e. near the CCC value to prevent coalescence), and the variation sufficiently small between plants, so as not to impart significantly on the measured bubble size due to frother concentration. Although not specifically designed as a model for bubble size, the re-arranged Gorain relationship is the only one that can be used to predict D_{32} for air rate and some key variables in industrial mechanical flotation machines. Note that P_{80} can be considered a measure of pulp viscosity and S relates to power intensity. By comparison, the 0.25 exponent for J_g is the same as that suggested by Finch and Dobby (1990) for column spargers, but differs from that of Sridhar and Potter (1980) who found the exponent to be 0.5 for aerated stirred tanks, both for coalescing and non-coalescing systems. O'Connor et al (1990) found the exponent to be 0.4 and 0.47, respectively, for air-water and air-water-solids in laboratory column tests without frother. The Gorain exponent relating D_{32} to S, the peripheral impeller speed, has a value of -0.44 and suggests a very low dependency on power intensity, about 1/3 of this value (0.11), since $P \propto N^3D^5$, $S = \pi ND$, hence $P \propto S^3D^2$.

Recent investigations by Grau and Heiskanen (2005) on (somewhat larger than typical laboratory units) 50 and 70 liter laboratory flotation machines in air-water, determined that D_{32} was dependent on impeller tip speed (S) to the power -0.41 and -0.55 for 2 different impeller/stator designs for the 50 liter unit, for an S range of 2 to 7 m/s. Similar tests on the 70 liter unit showed no significant relationship, although for a narrower range of S, 3.4 to 4.4 m/s, which the authors point to as a possible reason for the lack of a similar dependency. It is important to note that the range of impeller tip speeds in these tests is largely below those typically used in industrial units, 5 to 7 m/s (Fallenius, 1976; Arbiter, 1999; Deglon et al, 2000). The study is significant since it employed a rigorous visualization method for bubble size distribution measurement developed at the Helsinki University of Technology (HUT) that produces statistically precise measurement of D_{10} and D_{32} (Grau and Heiskanen, 2002) and is similar to the McGill method. This group has also characterized the effect of gas rate, frother type and concentration, and solids content but did not extend the analysis to

producing mathematical relationships for predicting bubble size (Grau and Heiskanen, 2003, 2005).

This review of the literature has highlighted that there is currently no generally accepted model incorporating the important process variables for prediction of bubble size in forced-air, mechanical flotation machines. At best, there are models from aerated stirred tank designs that can give an indication. These systems, however, differ in some important aspects; the absence of stators, they operate at different levels of gas rate and power intensity, and (typically) do not adequately account for the most significant variable, surfactant concentration. Bubble size models developed specifically for flotation systems are incomplete and have not gained acceptance as evidenced by the observation that flotation modeling still relies on assumed constant values or assumed relationships for inputting of bubble size (Koh and Schwarz, 2008; Cilliers,2007; JKSimFloat™). This work attempts to address this shortcoming.

2.3 Scale-up Numbers in Flotation

In order to complete the review of parameters that influence flotation and flotation machine design, a short description of the relevant scale-up numbers will be presented. Some of these have been introduced in previous sections and they are essentially those of fluid mixing and gas-liquid reactor design in chemical engineering (Oldshue, 1983). Their applicability to flotation has been reviewed by Arbiter, Harris and co-workers (Arbiter and Steininger, 1965; Arbiter et al, 1976) (Harris, 1974, 1976) (Arbiter, 1999) and Deglon et al (2000). They note large variation in numerical value between manufacturers but concluded that these still formed the basis for manufacturers' equipment scale-up at the time. The typical ranges quoted below are from their work.

Power intensity. The net power per unit volume of the cell, or sometimes the volume swept by the mechanism impeller. Still widely quoted by manufacturers; typical ranges are 1-3 kW/m^3 but can have a range of 0.8 to 9.5 (Deglon et al, 2000)

$$P_I = \frac{P_{net}}{V} \qquad 2.10$$

Power number. The ratio between actual (net) power and the theoretical power. Typical ranges in flotation are 3.4-6.6 with 5 being average. N_P is analogous to the drag coefficient for bodies moving through fluids and the friction factor in pipe flow (Arbiter and Steininger, 1965; Massey, 1975) and so becomes constant at higher N_{Re}, typical of the turbulent conditions present in mechanical flotation cells. Note that the introduction of air/gas lowers the effective fluid density and also the P_{net} for a given N_P.

$$N_P = \frac{P_{net}}{\rho N^3 D^5} \qquad 2.11$$

Impeller tip speed. Tip speed is considered important since blade velocity affects pulp circulation rate, fluid/gas shear and therefore gas dispersion. Typical values are 5-7 m/s but values as high as 9 m/s have been reported by Deglon et al (2000). Note that consumed power will increase as N^3 so cost and motor size increase very rapidly with increasing S.

$$S = \pi ND \tag{2.12}$$

Air flow number. The ratio between the air flow rate and the theoretical impeller pumping rate. Reported ranges are from 0.01 to 0.25, a factor of 25x. It is therefore considered more of a guide than an important scale-up criterion.

$$N_Q = \frac{Q}{ND^3} \tag{2.13}$$

Air flow velocity. This number represents the ability of an impeller of diameter, D, to accommodate a volumetric flow rate of gas. Industry values vary greatly, from 0.02 – 0.5 m/s, so, like N_Q, it is more of a guide than a scale-up criterion. It is linked to the superficial gas velocity (J_g) since there is typically a relationship between impeller size and cell size.

$$U_Q = \frac{Q}{D^2} \tag{2.14}$$

Mixing Reynolds number. The ratio of inertial (or centrifugal) to viscous force and is an indicator of the level of turbulence in the impeller region. Typically N_{Re} are > 10^5, well into the turbulent region of flow. Note that N_{Re} will decrease as Q is increased ("effective" ρ deceases due to gas hold-up) or as N is decreased. The lower limit of turbulent N_{Re} is considered to be about 10^3, however certain high-shear impeller designs (e.g. Rushton turbines) may be as low as 10^2 (Oldshue, 1983). Figure 2.3 illustrates the N_P - N_{Re} relationship for a selection of impeller types. Flotation impellers are high-shear and would likely fall somewhere between R-1 (Rushton turbine) and R-2 in the figure. It would be reasonable to expect that modern flotation impeller designs would have their transition to turbulent behavior between N_{Re} 10^2 and 10^3. Within the turbulent region, changes to viscosity, rotational speed or impeller size will not change the value of N_P.

$$N_{Re} = \frac{ND^2\rho}{\mu_o} \tag{2.15}$$

Froude number. The ratio of inertial (or centrifugal) to gravitational force. Similar Froude numbers imply similar hydrodynamic conditions in cells of different sizes, and has proven useful in the analysis of solids suspension and gas injection into liquids (Wraith et al, 1995) Typically, N_{Fr} are in the range 0.5 – 1.0, and is considered a useful scale-up criterion for flotation.

$$N_{Fr} = \frac{DN^2}{g} \tag{2.16}$$

Weber number. Ratio of inertial (or centrifugal) to surface tension force. It is useful in the study of liquid droplet dispersion but may be less applicable to flotation systems since surface tension has been shown to be of less importance in such non-coalescing systems.

$$N_{We} = \frac{\rho N^2 D^3}{\gamma} \qquad 2.17$$

In the 1960's, 70's and 80's there was considerable effort placed in investigation of such scaling parameters in the hope that consistencies would be revealed that would enable designers to scale equipment effectively, as the demand for larger cells grew. To a large extent this has been successful as the key parameters of P_I, S, N_P, N_Q, N_{Re} and N_{Fr} continue to play a role. To these have been added the gas dispersion parameters (introduced earlier and which have highlighted the importance of bubble size), and flotation modeling. The goal here being to provide new process analysis and design tools that will help improve equipment design, lower costs and improve metallurgical performance. A quantitative understanding of bubble size will be key to the success of these objectives.

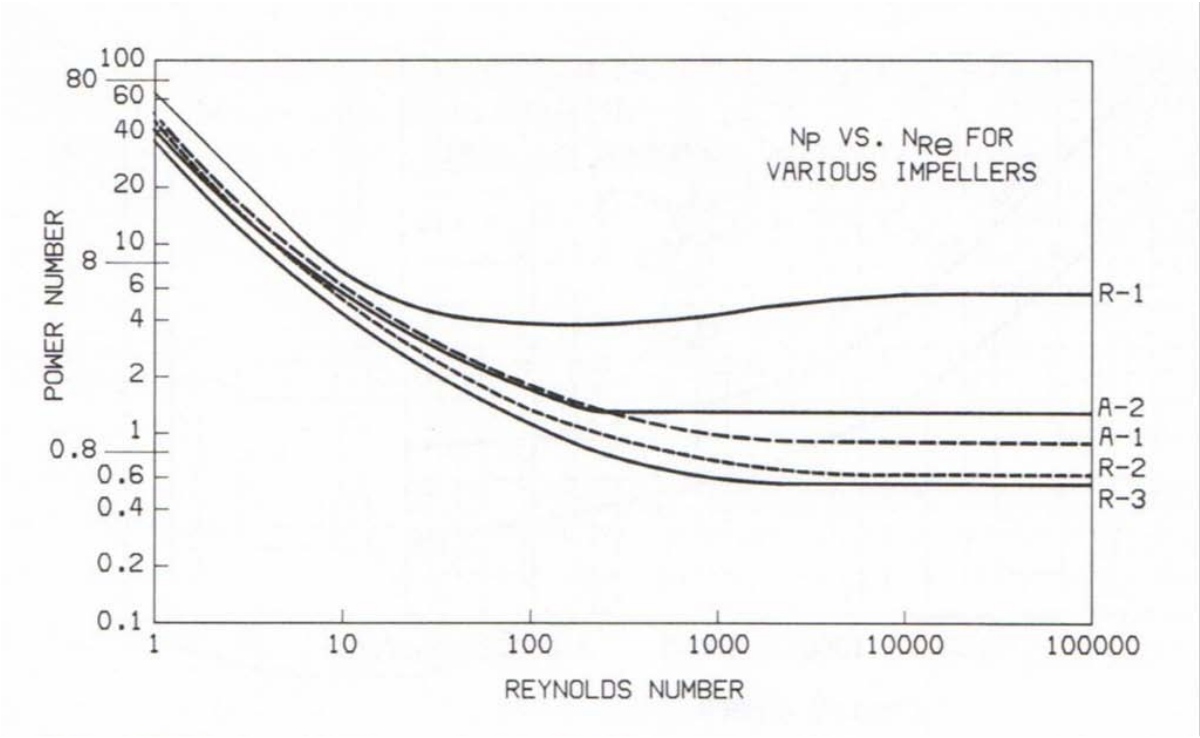

Figure 2.3 Power number (N_P) versus Reynolds number (N_{Re}) for various impeller types in stirred tanks: R-1, flat blade turbine (Rushton); R-2, 6-blade bar turbine; R-3, 2-blade anchor; A-1, marine 3-blade propeller, A-2, 4-blade axial flow turbine (from *Fluid Mixing Technology*, 1983, Oldshue)

2.4 Measurement of Bubble Size

The measure of bubble size is, by its very nature, an inexact science. The reality is that a distribution of shapes and sizes is present, and this distribution can be bimodal, normal, log-normal, or any combination of these in a broad or narrow format (Bailey et al, 2005; Hernandez-Aguilar and Finch, 2005). This is illustrated by the variety of distribution shapes presented in Figure 2.1, where the only change is frother concentration. The matter is further complicated by the fact that industrial measurements currently cannot be made in-situ since bubbles need to be removed from the sampling location in order to be analyzed. Representative sampling becomes a concern, particularly for bubbles approaching the dimensions of the sampling device (i.e. sampling tube diameter), or very small bubbles that have slow rising velocities, or simply because bubbles may be moving in a direction that does not permit entry into the sampler. Once removed, the issues of pressure (hence volume) changes, opportunities for coalescence, even opportunities for break-up in certain capillary-tube systems, are introduced. If photography and imaging techniques are employed, there are issues of resolution, individual bubble discrimination (currently about 200 µm using the McGill BV method), shape identification, the number of bubble images required to maintain statistically representative values. There are ample opportunities to lose measurement precision and introduce bias. Fortunately, the methods have evolved and most of these issues have been resolved to an acceptable level, at least for making engineering decisions (Grau and Heiskanen, 2002; Hernandez-Aguilar et al, 2002). The earlier method for sampling the BSD in plant environments, the UCT analyzer (University of Cape Town) (Randall et al, 1989), has been shown to have limitations in reproducing the BSD. This capillary tube/optical method misses the larger bubbles due to the small capillary size and may rupture bubbles into smaller ones if the vacuum/pumping system is improperly operated (Grau and Heiskanen, 2005; Hernandez-Aguilar et al, 2004). The McGill BV (Gomez and Finch, 2002) captures bubbles through a sampling tube into a viewing chamber and uses video and imaging software to count a large number of bubbles (>5000) to give statistically robust measures of the BSD. The McGill device has gained wide industrial acceptance and is the instrument used in the work reported here. Similar devices are in use at Helsinki University of Technology (HUT) (Grau and Heiskanen, 2002), the University of Newcastle (Jameson and Allum, 1984) and the University of Santa Maria (Yianatos et al, 2001).

The entire bubble size distribution (BSD) is very cumbersome to deal with in gas dispersion calculations and so representative descriptors are introduced to represent the BSD. The D_{32} (Sauter mean) (Equation 1.2) and D_{10} (arithmetic mean) diameters are the most appropriate measures for this work. D_{32} represents the inverse of the *specific surface area* (i.e. total surface area/ total volume) of bubbles and so is appropriate in studies involving surface area calculations for volumetric gas flow rates. It is not overly influenced by small numbers of the largest bubbles, nor large numbers of very small bubbles, since neither of these contribute significantly to the total surface area of the BSD. It is, therefore, a measure that is impacted less by sampling errors that may occur at the upper and lower ends of the BSD. For a given distribution, the value of D_{32} will always exceed that of D_{10}, as illustrated for the BSD shown

in Figure 2.4. As the BSD approaches a mono-sized distribution the ratio of D_{32} / D_{10} will approach unity (Hernandez-Aguilar et al, 2005; Nesset et al, 2005). Understanding where the volume of gas is distributed in a BSD is important, particularly if sizes exceed 2 mm, as is often the case for jetting spargers (Bailey et al, 2005), since this volume fraction is large but contributes little to flotation recovery.

The typical range of bubbles present in mechanical flotation cells is well represented by Figure 2.4, being in the range 0.5 to 4 mm. Accounting for bubbles of 1mm and below is not well represented by the D_{32} however, and it has been argued this bubble size range is important for collection of small particles (<10 µm) (Jameson et al, 1977; Nesset et al, 2006). Nesset et al showed D_{10} to be a better indicator of small bubbles in the BSD than D_{32}, and it therefore becomes an important descriptor of the BSD, making up for this deficiency of the D_{32}. Figure 2.5 illustrates the difference between the D_{32} and D_{10} in describing the % of minus 1mm bubbles in the BSD for 3 different plants including measures in the laboratory and pilot cells of one plant (Lac des Iles).

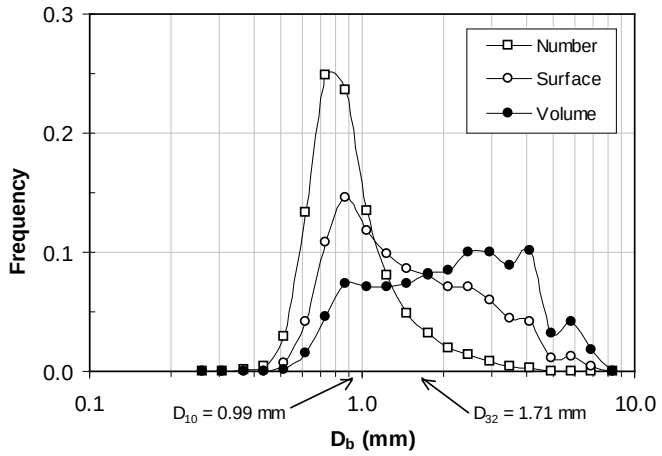

Figure 2.4 Bubble frequency distributions for number, surface area and volume showing the corresponding D_{10} and D_{32} values

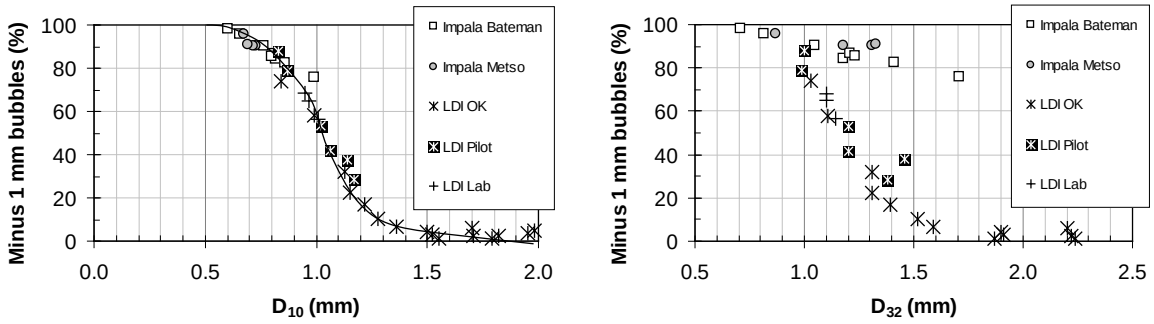

Figure 2.5 Plant measurement data illustrating that D_{10} is a better predictor of % minus 1 mm bubbles in the BSD than is D_{32} (Nesset et al, 2006)

CHAPTER 3: Materials, Methods and Measurement

The general objective of this work was to build a model of bubble size, D_{32}, as a function of five key variables within the water-gas flotation system, viz. frother type and concentration, power intensity (impeller speed), gas rate (superficial gas velocity), gas density (to simulate elevation above sea level) and fluid viscosity (by varying water temperature). To this end a test unit (flotation cell) was sought that would meet the following criteria:

- Sufficiently large volume (of the order of 1 m^3) to provide for distinctive *turbulent* (near impeller) and *quiescent* (near froth) zones
- Able to vary the rotational speed of the impeller to represent an industrially-appropriate range of power intensity
- Accessible for use of the three gas dispersion sensors simultaneously
- Fit the available space within the laboratory (approx. 2.5 m x 2.5 m x 2.5 m)

A Metso Minerals 0.8 m^3 RCS™ (Reactor Cell System) pilot-scale flotation cell was made available by the supplier that met the criteria. All variables, with the exception of gas density, were tested on this unit. Testing gas density (i.e. effect of altitude) involved blending air and helium to achieve reduced gas densities. The large quantity of helium required, and hence decreased oxygen content in the area of the cell, precluded the use of the Metso cell. Instead, a smaller Denver laboratory flotation machine, fitted with a 5.5 liter cell, was used. This represented a compromise; balancing safety, cost and quality of results since measurements with the Denver machine were unavoidably made closer to the turbulent region of the impeller.

3.1 The Metso 0.8 m^3 RCS™ Pilot-Scale and Denver Laboratory Flotation Machines

Photographs of the installed Metso 0.8 m^3 unit and internal views of the stator and impeller are shown in Figures 3.1 and 3.2. Figure 3.3 shows the installed gas dispersion sensors; gas holdup, gas velocity and bubble size. The arrangement is schematically illustrated in Figure 3.4. Note the positioning of all sensors at the same cross-sectional vertical reference plane located 0.2 m below the liquid surface, 0.12 m above the shelf baffle and approximately 0.25m above the stator/impeller assembly. The testing protocol (Gomez and Finch, 2002, 2007) calls for all measurements to be taken at a location sufficiently above the turbulent impeller/stator region but somewhat below the froth interface, thereby representing conditions of the bubble surface area flux (and therefore linking to pulp phase mineral recovery) exiting the liquid (pulp) phase into the froth phase. As shown in Figure 3.5, all three sensors were positioned as symmetrically as possible on the same radius (average 18.6 cm from the wall representing 68% of the distance from the center of the cell), a location that had been selected through testing as giving consistent J_g and D_{32} values, and which will be detailed in the following section.

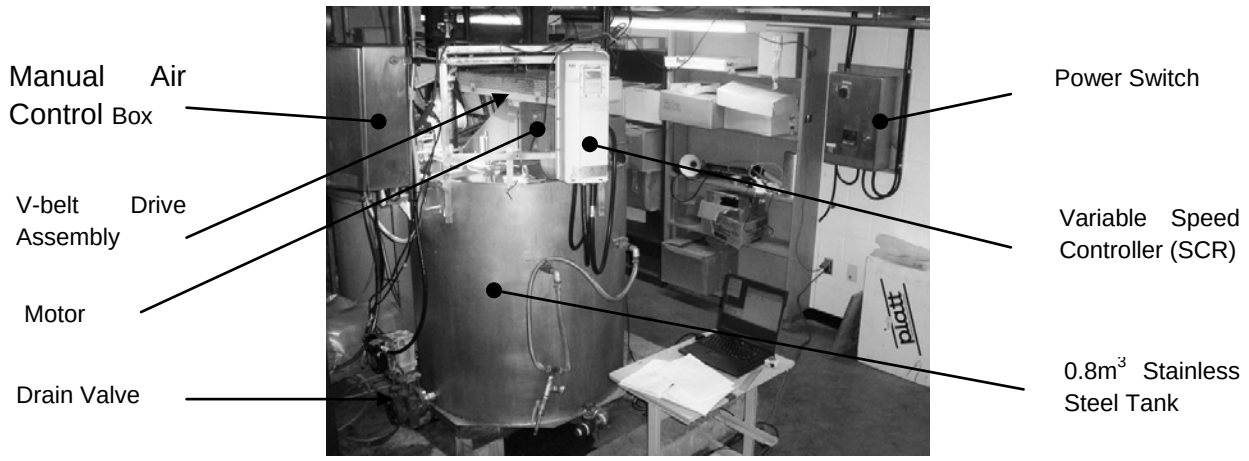

Figure 3.1 Metso 0.8 m^3 RCS™ cell assembly in McGill laboratory

Figure 3.2 View of impeller/stator located at bottom of shaft near cell bottom (left image). Close-up of impeller/stator. Note air slot located between impeller vanes (right image)

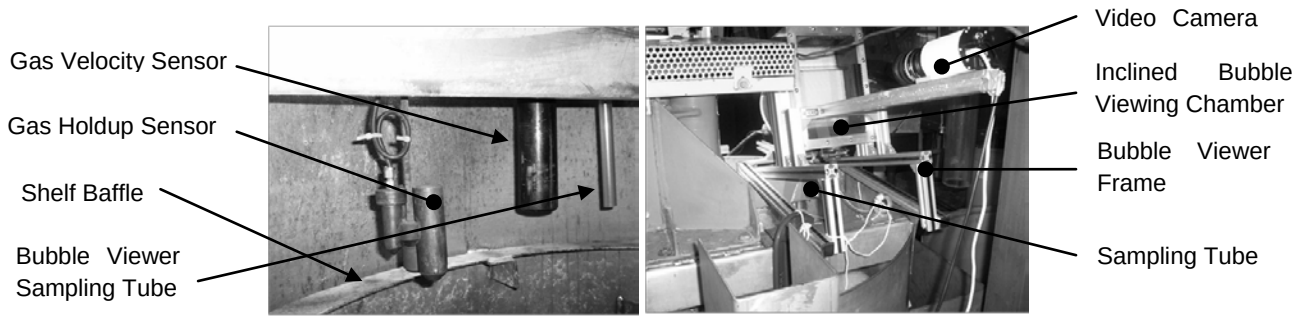

Figure 3.3 Gas dispersion sensor locations. Gas holdup, gas velocity and bubble viewer sampling tubes (left image). McGill Bubble Viewer clamped on cell beams (right image). Note that sensor measurements are made at the same elevation in the cell in the quiescent zone, above the shelf baffle

Figure 3.4 Schematic of the Metso RCS™ 0.8 m^3 cell showing arrangement of the gas dispersion sensors, manipulated and measured machine variables, and dimensions

Figure 3.5 Plan view of gas dispersion sensor locations in the Metso cell. Note that the sensors were located as close to the same radial distance from the center of the cell as possible, averaging 68% of the distance to the wall

Figure 3.6 shows the Denver flotation machine setup with the bubble viewer assembly located above the flotation cell, and the bubble sampling tube extending down into the corner of the cell. Gas flow to the unit was controlled via mass flow meters. A constant cell level was maintained by re-circulating the froth/water overflow back into the cell. Direct superficial gas velocity (J_g) measurement by sensor was not possible due to the small size of the cell, so a calculated value based on gas flow rate and cell cross-sectional area (minus the "obstructions") was used.

Figure 3.6 Arrangement of the Denver flotation machine and McGill Bubble Viewer positioned on stand above the cell. Note the bubble sampling tube extending down into the corner of the cell

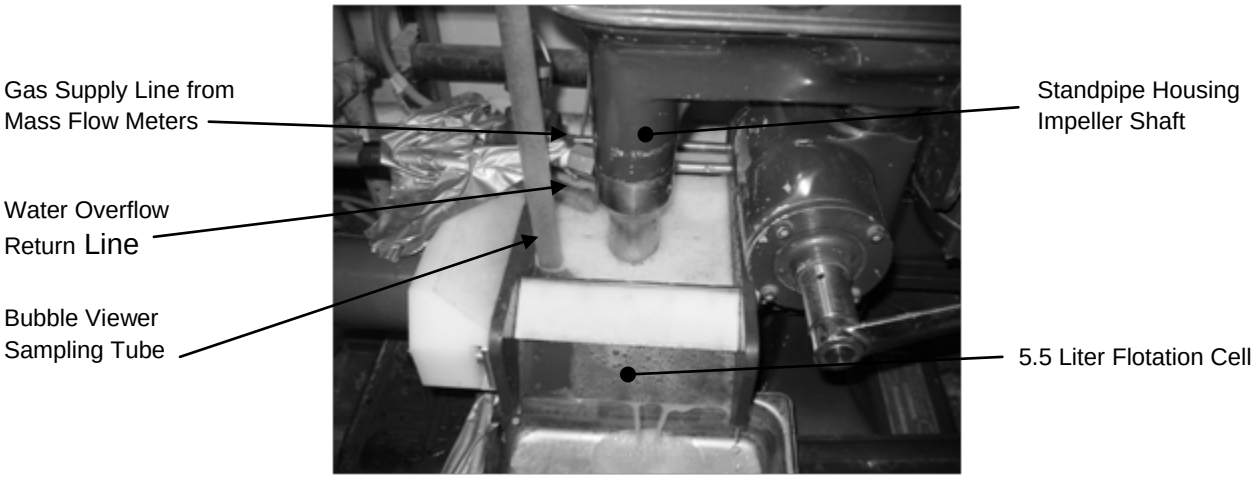

Figure 3.7 Close-up of Denver flotation machine and cell showing bubble sampling tube location in corner of cell

A schematic of the Denver cell setup appears in Figure 3.8 and shows the cell dimensions and bubble sampling tube location in the cell corner, the only location possible given the equipment dimensions. Since there is no quiescent zone in such a small volume cell, the sampling location represented a compromise between distance below the froth interface and above the impeller. The default position was approximately half-way between the two. Gas flow was controlled by two mass flow meters, one for air and a second for helium during the variable gas density testing simulating the effect of altitude. Impeller rotational speed could be manually controlled. A value of 1600 RPM, corresponding to an impeller tip speed of 5.86 m/s, was chosen as the default setting as it is typical of industrial values (Deglon et al, 2000; Arbiter and Steininger, 1965), and similar to the default value for the Metso cell at 5.73 m/s corresponding to a motor frequency of 50 Hz.

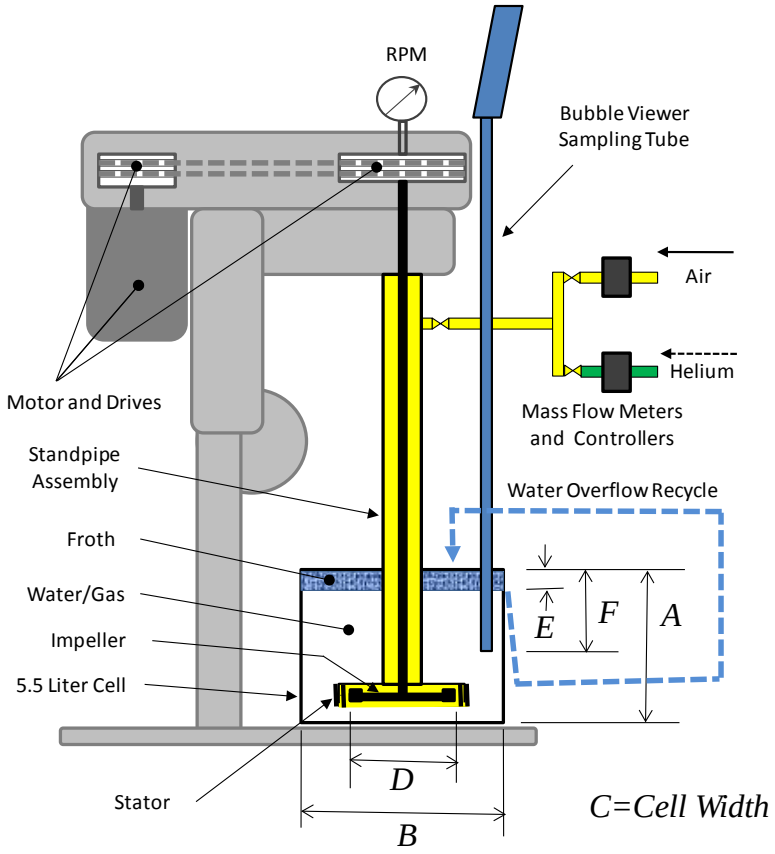

A	*B*	*C*	*D*	*E*	*F*
19.5 cm	17.5 cm	16.8 cm	7 cm	~3.5 cm	9.5 cm

Note: Drawing Not to Scale

Figure 3.8 Schematic drawing of the Denver flotation machine, cell dimensions, gas delivery system and bubble sampling location

3.2 Gas Dispersion Measurements and Sensors

Gas dispersion measurements using the McGill-developed sensors for superficial gas velocity (J_g), bubble size distribution (D_b) and gas hold-up ($\mathcal{E}_g$) has become an industry standard (Harbort and Schwarz, 2010) used worldwide by major mining companies and flotation cell manufacturers. Their method of operation have been well documented (Gomez and Finch, 2002, 2007; Hernandez-Aguilar, 2005; Gomez et al, 2006) and will only be reviewed here.

The measurement of J_g relies on sensing volumetric change of accumulating gas in a closed tube (of known cross-sectional area) through a pressure sensor, thus giving a slope of pressure versus time ($\Delta P/\Delta t$). This slope measurement is repeated several times in order to obtain sufficiently precise average values, since individual measurements can differ considerably due to random process variability. A schematic representation of the J_g sensor is shown in Figure 3.9. A correction to the measured pressure is required to compensate for the difference in hydrostatic pressure inside the tube and the reference location.

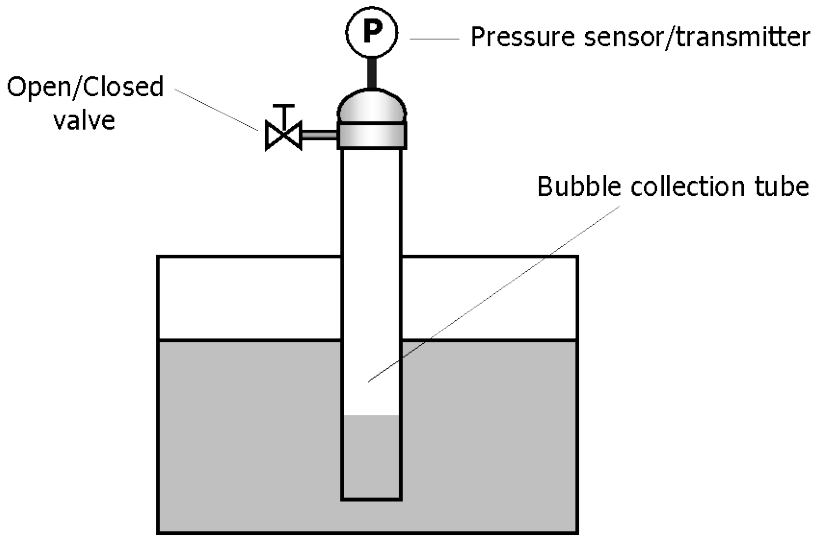

Figure 3.9 Schematic representation of sensor for measuring J_g, the superficial gas velocity

Bubble size distribution (BSD) is measured using a sampling tube and visualization chamber with backlighting from which a video camera captures bubble images. A schematic of the McGill Bubble Viewer (BV) is shown in Figure 3.10. Typically, for each reported measured BSD, 10,000 individual bubble images were processed by the commercial software (Northern Eclipse, Empix Imaging) and deposited into an Excel file in order to generate the number frequency BSD. As with the J_g measurement, correction factors are

required to bring the bubble diameters measured in the viewer (under vacuum) back to the actual pressure at the measurement location.

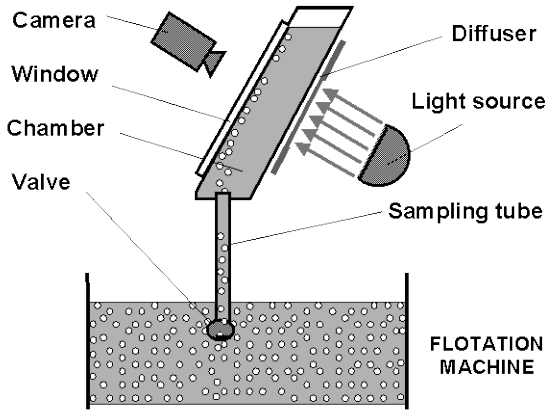

Figure 3.10 Schematic representation of the McGill Bubble Viewer for determining bubble size distribution by image analysis

The gas holdup ($\mathcal{E}_g$) sensor, shown schematically in Figure 3.11, is comprised of 2 tubes cells) that measure internal cell conductivity. One tube is open at both ends (*open cell*) and reports conductivity for the aerated liquid while the second tube (*siphon cell*) is partly restricted at the bottom and reports conductivity for gas-free liquid; the ratio of the readings permits the void fraction to be calculated using a relationship derived by Maxwell in 1892 for conductivity of a dispersion with a non-conducting phase (the bubbles), known as "Maxwell's equation". Both J_g and $\mathcal{E}_g$ measurement data were captured using commercial software (iFix, GE Fanuc Automation). The convention is to report measured values of J_g, D_b and $\mathcal{E}_g$ corrected to the same cross-sectional reference plane in the cell, in this case, 20 cm below the froth-liquid interface as shown in Figure 3.4. Details of the $\mathcal{E}_g$ measurements are not presented in the thesis as gas holdup was not a modeled variable for predicting D_{32}.

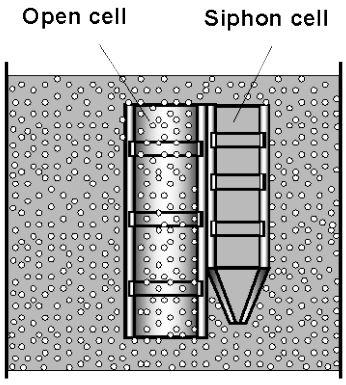

Figure 3.11 Schematic drawing of the gas holdup sensor which measures differences in conductivity between the open and siphon cells to determine $\mathcal{E}_g$

3.3 Characterizing the Metso 0,8m^3 Pilot Cell

Metso cell volume calibration

Prior to testing on the Metso cell, a standard volume of liquid was specified as 700 liters based on the volumetric calibration shown in Figure 3.12. This was established by successively adding approximately 8600 gm lots (each pail precisely weighed) of water to the cell and recording the water level from the cell bottom. Mass was converted to volume based on water temperature. The practical limit of the tank is slightly more than 700 liters, less than the nominal faceplate value of 800 liters, due to the presence of internal launders. Every test was therefore conducted with the water level (non-aerated) at 71.6 cm from the tank bottom (internal measurement).

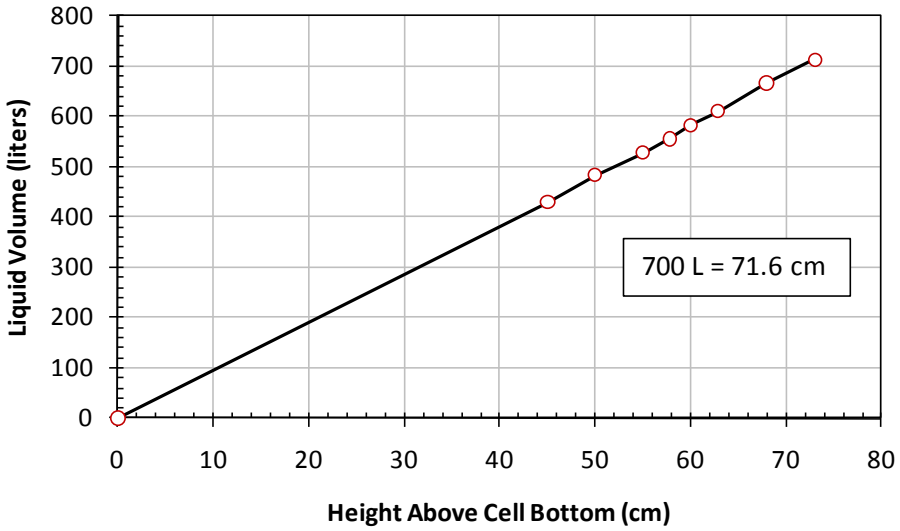

Figure 3.12 Volume versus height calibration for the Metso 0,8m^3 cell. Although nominally an 800 liter cell, the standard for this work was 700 liters (non-aerated)

Metso cell power calibration

A useful feature of the Metso cell is the variable frequency motor drive (SCR) which permits the adjustment of the impeller rotational speed over more than a 2-fold range. Of interest are the net power input and the impeller tip speed. Calibrations were therefore required linking these desired parameters to the manipulated variables of the unit; viz. SCR frequency, gas rate and frother concentration. Conditions of *no-load* (cell empty) and *full-load* (700 liters of water in cell, no air) were tested in both the clockwise and anti-clockwise impeller rotational direction. Results for clockwise and anti-clockwise were virtually identical (difference 0.01%) so only clockwise results are reported. Figure 3.13 shows three of the calibration curves. The upper curve shows there is an almost perfect linear relationship between the motor SCR frequency setting (Hz) and motor RPM: viz. $RPM = 29.7 \cdot Hz$. The relationship was the same for both full-load and no-load conditions.

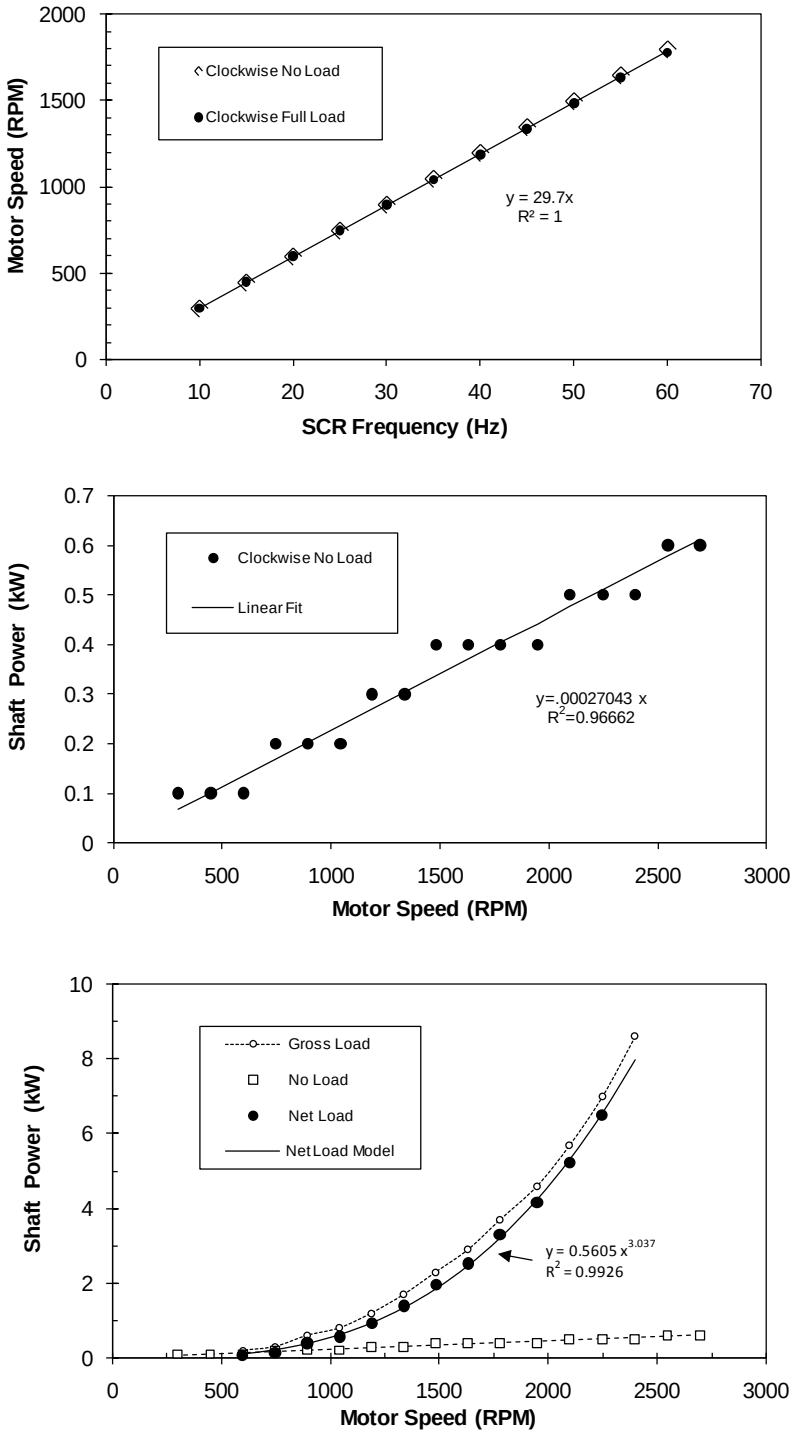

Figure 3.13 Metso cell calibration curves. Top: Motor speed (RPM) shows a linear relationship with SCR drive frequency (Hz). Middle: No- load calibration of shaft power (kW) as a function of motor speed (RPM). Bottom: Gross and net shaft power versus motor speed for full-load. Note the fitted exponent is 3.037 versus a theoretical value of 3

The center plot shows the no-load relationship between motor RPM and shaft power (measured by motor torque and speed sensors). This calibration is required in order to determine the motor RPM versus net load relationship, based on *Net Power = Gross Power – No Load*. The fit is linear with an R^2 of 0.967. The bottom curve shows the calculated Net Power versus motor RPM relationship for the full-load condition (i.e. 700 L water, no air). The theoretical relationship is $Net\ Power \propto RPM^3$ for fluid mixing impellers (Oldshue, 1983). The best-fit power relationship for the data yields an exponent of 3.037 and an R^2 better than 0.99. Net Power can therefore be reliably determined from the relationship; $Net\ Power\ (kW) = 0.5605 \cdot RPM^{3.037}$.

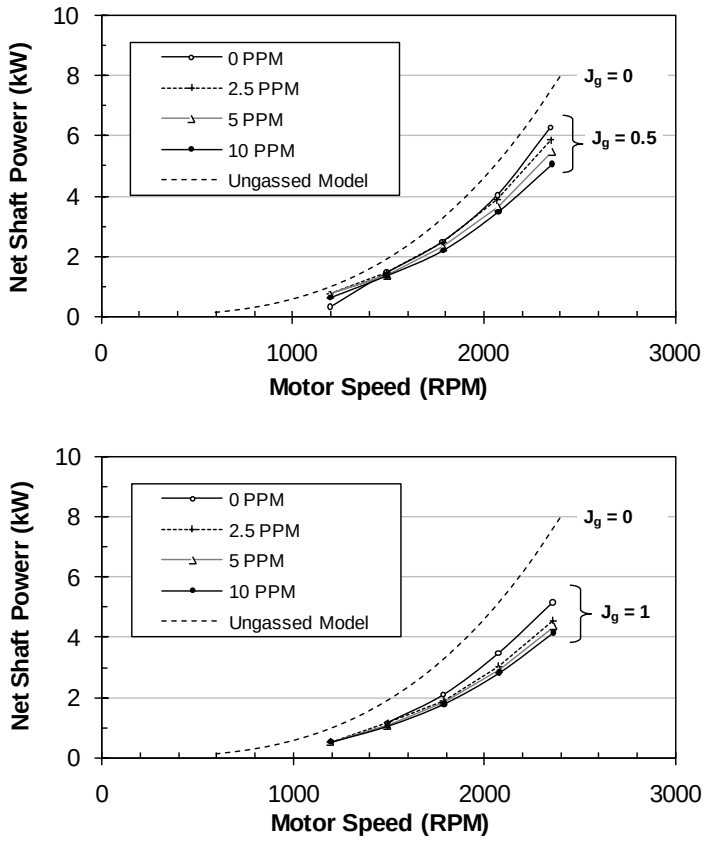

Figure 3.14 The effect of air rate (J_g) and frother addition (DowFroth 250) on net power versus motor speed compared to the ungassed (J_g =0) condition of Figure 3.13

Of obvious interest in flotation is the effect of air and frother addition on net power draw. Power versus motor RPM curves were generated for J_g of 0.5 and 1 cm/s for frother additions (DowFroth 250) of 0, 2.5, 5 and 10 ppm. These are compared to the *ungassed* condition (J_g =0 cm/s) in Figure 3.14. Adding air at J_g = 0.5 cm/s reduces net power by 21% at 0 ppm frother and a further 15% at 10 ppm frother for a total power reduction of 36%. At J_g = 1 cm/s the corresponding power reductions were 35% and 13% for a total decrease of 48%.

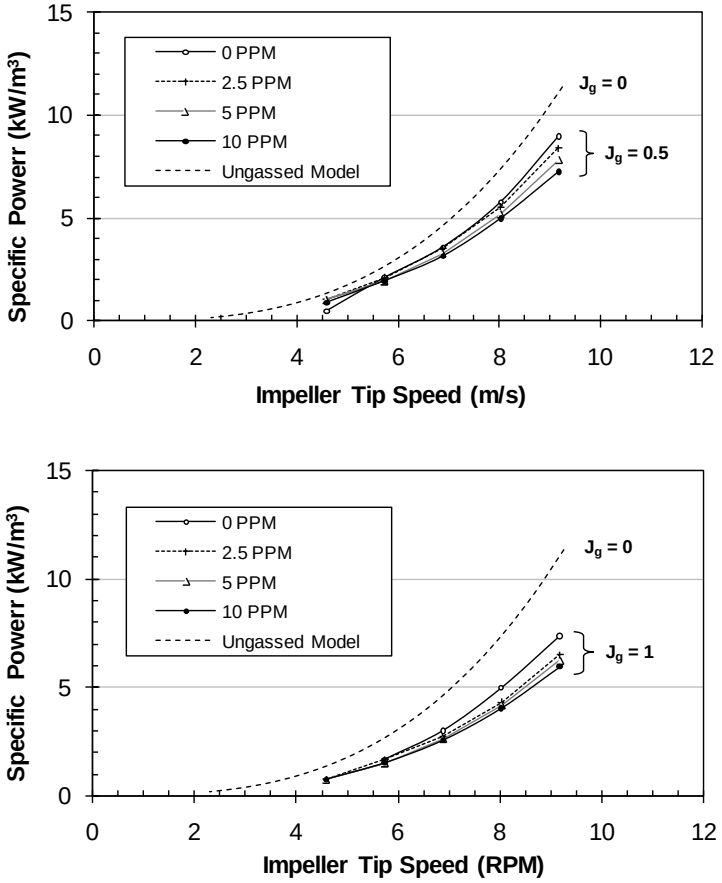

Figure 3.15 The equivalent plots to Figure 3.14 converted to impeller tip speed (m/s) versus specific power (kW/m^3)

The data of Figure 3.14 are more usefully presented in terms of specific power (kW/m^3 of liquid) and impeller tip speed (m/s) since these are the metrics more commonly used by engineers. The plots of Figure 3.14 are converted and re-presented in Figure 3.15 on this basis. Since power draw is directly proportional to the fluid density (Oldshue, 1983), these measurements also serve to indicate an "effective density" and therefore an indication of volumetric air content (gas holdup) in the impeller region. For example, at J_g = 1 cm/s and 10 ppm frother, the net power reduction is 48% from the water-only condition (density = 1). The "effective density" can therefore be interpreted to be 0.52 with equivalent air content (gas holdup) of 48%, if air density is considered negligible relative to water.

The specific power is determined by dividing net power by 0.7 m^3 of water in the cell. To calculate the impeller tip speed from the motor speed one needs the ratio of motor sheave (dia = 0.125 m) to mechanism sheave (dia = 0.356 m) and the impeller diameter (0.21 m).

$$Impeller\ Tip\ Speed\ (ms^{-1}) = \frac{Motor\ \ Speed\ (rpm\ )}{60} \cdot \left[\frac{Motor\ \ Sheave\ \ Dia}{Mechanism\ \ Sheave\ \ Dia}\right] \cdot \pi \cdot Impeller\ Dia \qquad 3.1$$

Measurement of superficial gas velocity, J_g

Ideally, in order to obtain a fully averaged and representative measure of the gas dispersion parameters within a flotation cell, surveys should be conducted in both a horizontal and vertical plane and then weighted based on some criterion such as the J_g of the annular area for that given point. Surveys on industrial units have been conducted by Dahlke et al (2001) and Araya et al (2009) suggesting that single representative locations can be identified that will adequately serve to reflect the overall average in J_g behaviour. Araya et al found, by noting that the J_g profile across the cell was parabolic, that a position r/R of 0.71 represented the area-integrated average for the cell cross-section. The process of selecting the most suitable elevation of the vertical sampling plane is somewhat simplified by the bubble surface area flux measurement protocol, which measures the flux across a horizontal plane not far below the froth interface (typically 0.5 m industrially but less on smaller cells). The selection exercise therefore reduces to one of identifying the most suitable depth of this plane for the specific Metso cell and confirming the position of the radial (r/R) measurement.

As explained in Section 3.2, J_g is determined by measuring pressure change versus time ($\Delta P/\Delta t$) in the sensor tube as the valve is closed (Figure 3.9). This is done over a sequence of valve opening and closing. Tests were run to establish the required number of slope measurements to minimize variability. Two depths (71 and 76 cm below the cell lip) and two radial distances (15.7 and 19 cm from the cell wall) were selected for either 20 or 30 repeat slope measurements. Figure 3.16 shows plots of the cumulative average mean and standard deviation versus increasing measurement number in the calculation. The upper plot is for nominal J_g = 0.5 cm/s while the middle and lower plots are for nominal J_g = 1 cm/s. All three plots show that a limiting value of mean and standard deviation are approached as the number of measurements included in the average approaches ten. This is in agreement with the Central Limit Theorem which suggests that far fewer than 30 measurements are required to establish a representative mean value if variation in the parent population is normally distributed. The number of individual slope measurements used to calculate J_g was therefore established at ten.

Depth and radial J_g measurements were conducted to establish a single, representative measurement location for the Metso cell. Radial positions of 3.5, 15.7 and 19 cm from the cell wall were the only positions accessible for measurement. Depth measurements were made at 66, 68.5, 71, 73.5 and 76 cm from the top edge of the cell. Each reported J_g value represents the average of ten measured $\Delta P/\Delta t$ slopes. The results are (Figure 3.17) show good repeatability of the measurements. The error bars indicate relative standard error of the mean to be about 2.5% for J_g = 0.5 cm/s and 3.6% for J_g = 1 cm/s. The trend of the error to be proportional to the J_g value was evident throughout the test work and may be linked to the wider bubble size distribution (i.e. larger standard deviation about the mean) at higher J_g. With depth, J_g is seen to be consistent for 71 cm and higher at both levels of gas rate. With radial position, J_g decreased at 3.5 cm from the wall for low J_g, and at 19 cm for the higher J_g. A depth of 71 cm and a radial position of 15.7 cm were therefore selected as being most suitable for single position testing. These positions correspond to relative liquid depth (z/H) of 0.712 and relative radial position of (r/R) of 0.726. This radial position is similar to the

optimum position of r/R = 0.71 identified by Araya et al (2009). Table 3.1 summarizes the precision of the J_g measurements. At the 95% confidence level (t-statistic of 1.99 for 90 data points) the J_g measurements have a precision (relative standard error of the mean) of ± 4.9% at J_g = 0.5 and ± 7.2% at J_g = 1 cm/s based on 90 measurements each (9 points x 10 measures per point).

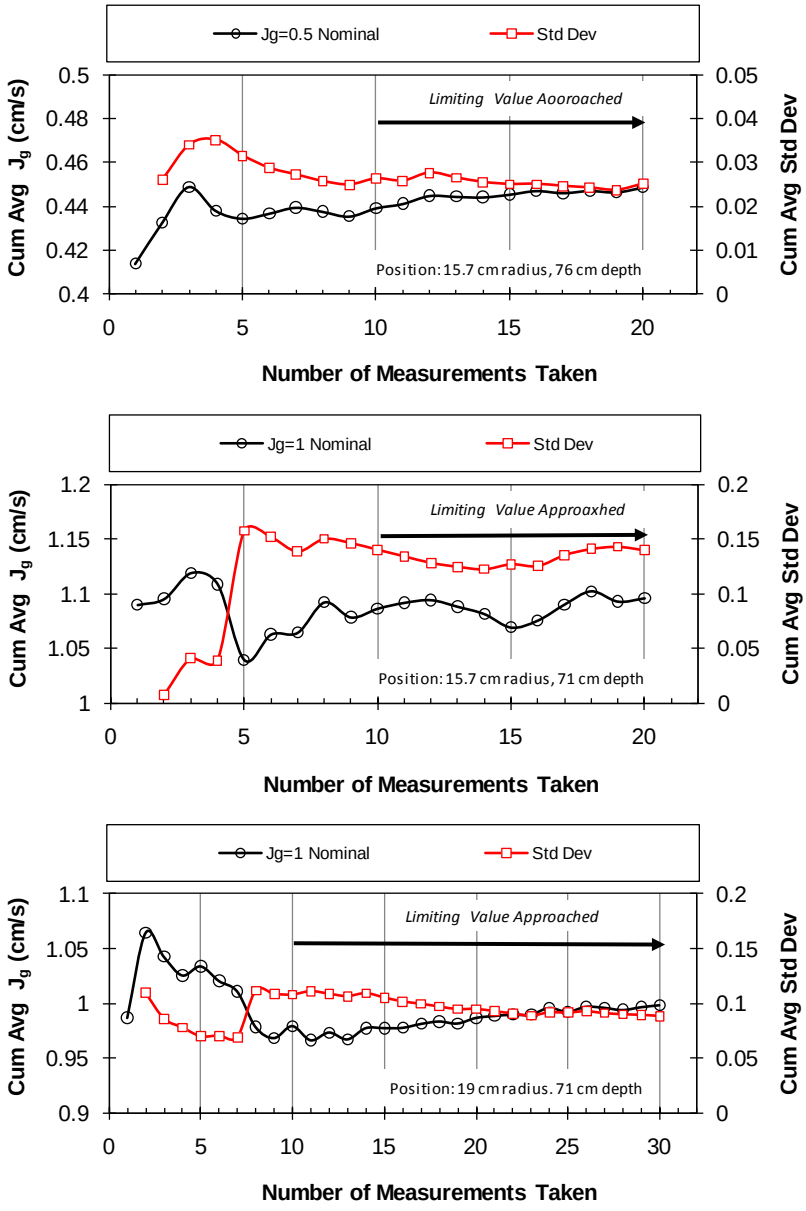

Figure 3.16 Statistical indicators for J_g (cumulative average and cumulative standard deviation) with increasing number of slope ($\Delta P/\Delta t$) measurements

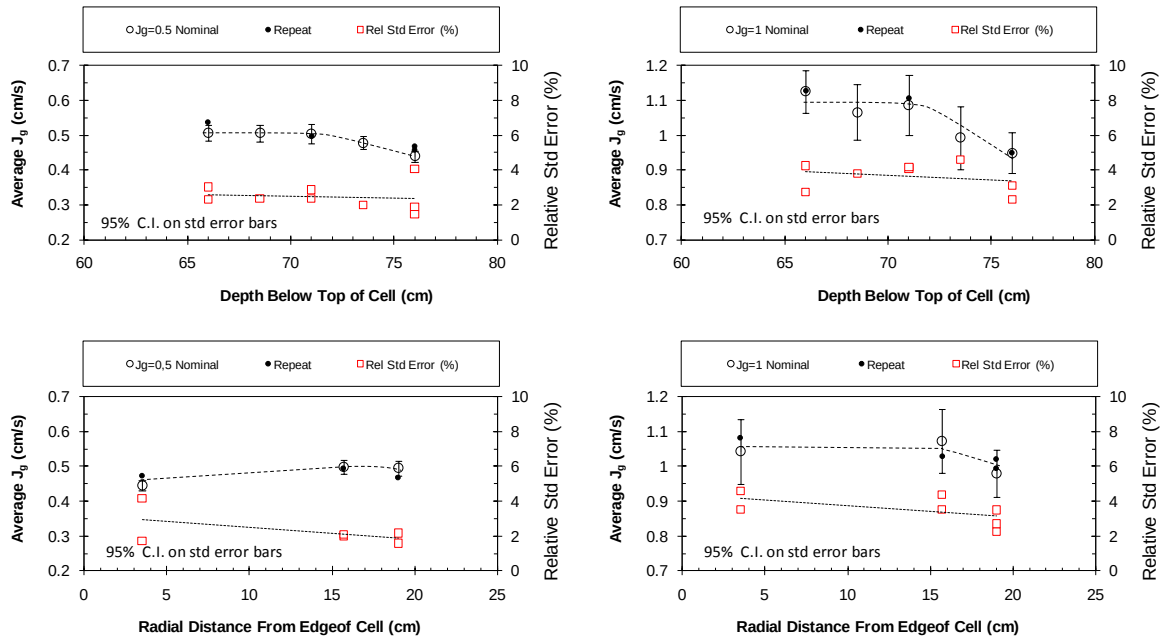

Figure 3.17 Statistical indicators for J_g at 0.5 cm/s and 1 cm/s (average and % relative standard error) for measurements taken with depth (upper figures) and radial position (lower figures). Each point represents the average for ten measurements. Error bars are for the 95% confidence limits on the standard error of the mean. Left figures are for J_g = 0.5 cm/s, right figures are for J_g = 1 cm/s

Table 3.1 Precision of J_g measurements for J_g values of 0.5 and 1 cm/s for data of Figure 3.17 (data set nine points x ten measurements per point for each J_g)

Measure	***Nominal J_g (cm/s)***	
	0.5	***1.0***
Standard Deviation	0.0385	0.1213
Relative Standard Deviation (%)	7.84	11.49
Standard Error of Mean	0.0122	0.0384
Relative Standard Error (%)	2.48	3.64
95% Confidence Limits (%)	± 4.93	± 7.23

Validation of the selected measurement location

The selected location for the single position gas dispersion measurements, as described in the previous section, represents a trade-off between time, cost and suitability of the results for the intended purpose. An appreciation of the fluid flow pattern within the cell would be a useful gauge for additional validation of the selected location. Fortunately, such information was available through the AMIRA P9 project (joint funders of this research) from the work of

Koh and Schwarz (2001, 2004) and Zhu et al (2001) of CSIRO (Australia). They modeled a Metso RCS™ 0.8 m^3 cell, using CFD (computational fluid dynamics) methods, and through direct velocity measurements using LCV (laser-Doppler velocimetry) techniques. Figure 3.18 shows their results for a standard water test (no air) giving both measured (left side) and modeled (right side) velocity vectors. Note the occurrence of three major flow vortices, two in the lower turbulent region and one in the upper quiescent region of the cell. The location of the gas dispersion measurements is shown as a black rectangle (z/H=0.73, r/R=0.63-0.73) in an area of very low velocity, just to the left of the upper vortex. Low fluid velocities would provide for vertically-rising bubble swarms suitable for sampling by the gas dispersion sensors. This corroborating data helps support the selection of the measurement location.

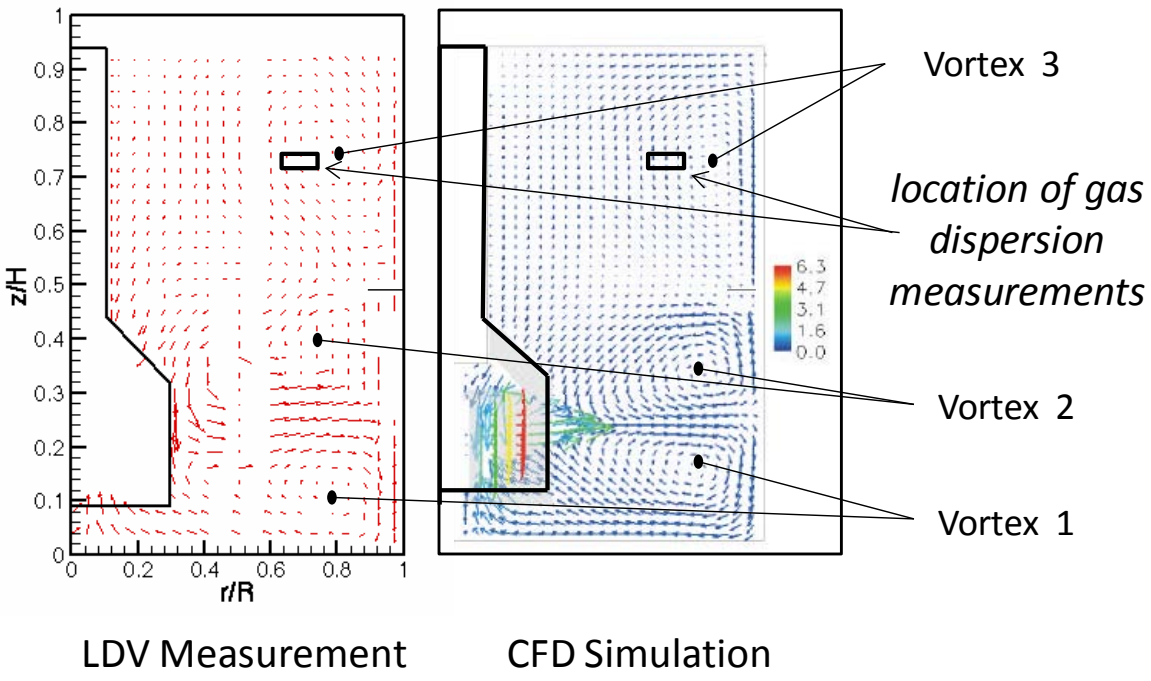

Figure 3.18 Comparison of liquid velocity vectors in a vertical plane for the Metso RCS™ 0.8m^3 cell (Koh and Schwarz, 2001, 2004). The rectangle indicates the location of the gas dispersion measurements for this study; located in the quiescent zone near Vortex 3. The length of the arrow indicates the relative velocity of the fluid at that location

Measurement of bubble size, D_{32}

The determination of a single bubble size distribution (BSD) using the McGill Bubble Viewer (BV) required considerably more time for set-up and measurement than did a set of J_g measurements. Typically, one BSD measurement was completed in one hour compared to less than 15 minutes for a set of ten J_g slopes (giving one data point). Single BSD measurements were therefore reported in most cases, while multiple measurements taken

under different conditions of frother concentration and J_g were used to establish estimates of precision. A total of 19 pairs of either two or three repeats were analyzed to establish relative standard deviation for D_{32} and D_{10}. The results covered a wide range of frother concentration (0 to 16 ppm) and gas velocity (0.05 to 1.25 cm/s) as shown in Figure 3.19. There is a clear indication that relative standard deviations for both D_{32} and D_{10} decrease with increasing frother concentration (DowFroth 250), but have no apparent relationship to J_g. The relative standard deviation values for D_{32} and D_{10} show an almost identical value, 1.86% and 1.87% respectively. Figure 3.20 (upper) shows a histogram frequency distribution of relative standard deviation for D_{32} and D_{10} which further highlights this similarity. When D_{32} and D_{10} data are combined and then analyzed on the basis of frother and no frother (24 and 14 data sets respectively), the resulting frequency histogram of relative standard deviations appears as in Figure 3.20 (lower). Relative standard deviation for D_{32} and D_{10} measurement with frother is therefore 1.45%, and without frother, 2.56%. Table 3.2 summarizes the precision of D_b measurement. At the 95% confidence level, D_b values are ± 3.9% overall, breaking down to ± 3% with frother and ± 5.5% without.

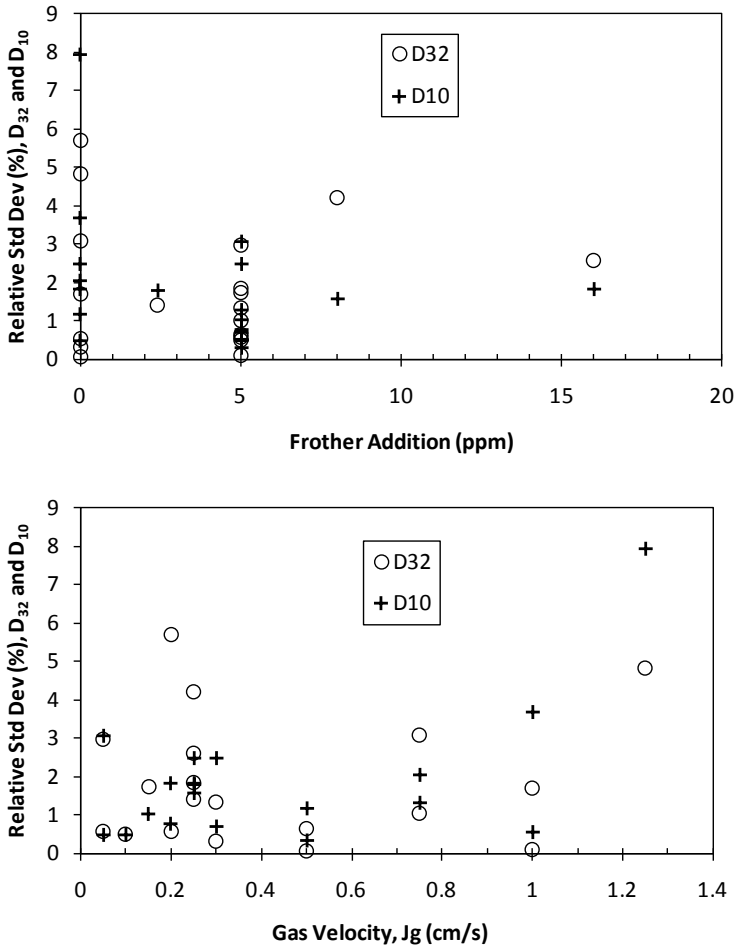

Figure 3.19 The relative standard deviation (%) of D_{32} and D_{10} measurement versus frother concentration (DowFroth 250) (upper) and gas velocity (J_g) (lower) for 19 pairs of data

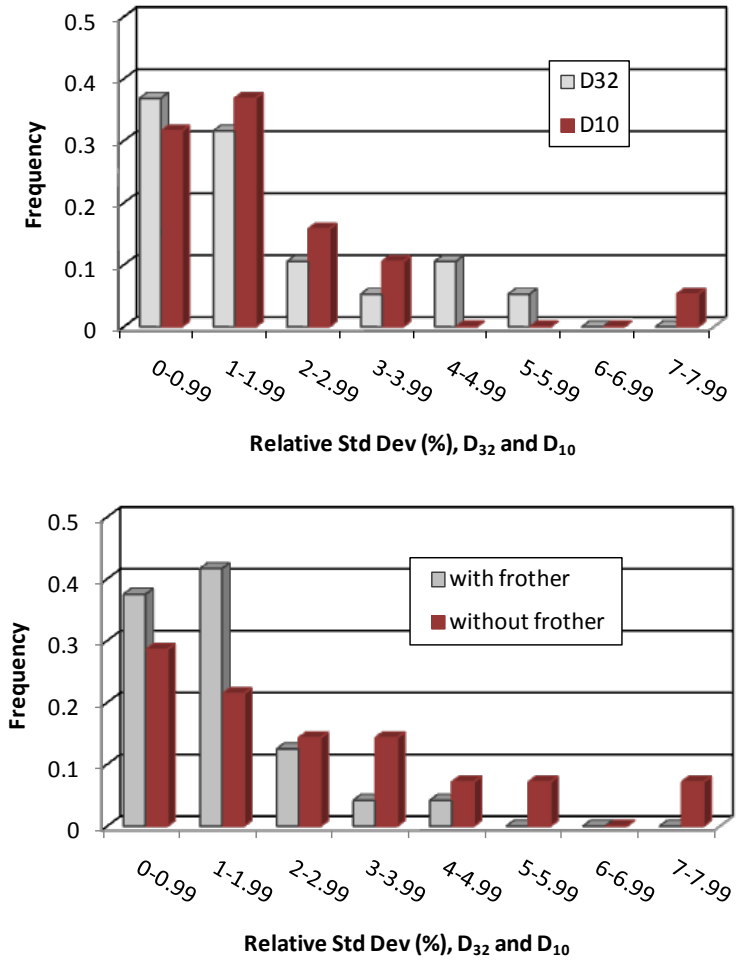

Figure 3.20 Frequency histogram for relative standard deviation (%) comparing D_{32} and D_{10} (upper), with and without frother (lower)

Table 3.2 Precision of D_b measurements for data of Figures 3.19 and 3.20

Measure	***Data Sets***			
	D_{32}	***D_{10}***	***With Frother***	***Without Frother***
Data Pairs, number	19	19	24	14
t-statistic for α = 0.975	2.093	2.093	2.064	2.145
Relative Standard Deviation (%)	1.86	1.87	1.45	2.56
95% Confidence Limits (%)	± 3.88	± 3.91	± 3.00	± 5.49

As an example, using the Confidence Limits from Table 3.2, a measured D_{32} of 4.0 mm at no frother would have a 95% Confidence Range of 3.78 – 4.22 mm. Similarly, a measured D_{32} of 1.5 mm with frother would have a 95% Confidence Range of 1.46 – 1.54 mm.

3.4 Measurement Correction Factors

As briefly discussed in Section 3.2 on Gas Dispersion Sensors and Measurement, correction factors need to be determined for both bubble size and superficial gas velocity to account for pressure and temperature differences between the sensor measurement position (the measurement reference plane shown for the Metso cell in Figure 3.4) and the position of the sensing device (pressure transducer or bubble imaging camera). There is also a second correction required for the bubble size to account for some degree of coalescence occurring in the bubble viewer if the frother concentration within the viewer is not sufficiently high to suppress bubble coalescence after sampling. The protocol for this work was to use the liquid in the cell (water plus frother) to also fill the bubble viewer, thus there were conditions of low or no frother for which some coalescence would occur and measured D_b's would be larger than at the sampling location.

The method of establishing the pressure-temperature correction factors have been well documented (Gomez and Finch, 2002; 2007; Hernandez-Aguilar, 2005; Gomez et al; 2006) and an adapted version of the McGill Manual on Gas Dispersion Measurements is included in Appendix A. Experiments designed to establish the correction factors required to account for bubble coalescence in the bubble viewer will also be summarized here (Zhang et al, 2009). These factors have been applied to the measured D_b and J_g values used for model development.

Pressure and temperature correction factors

The details of the methods are found in Appendix A. Only a summary of the applicable measurements and factors will be presented. Figure 3.21 illustrates the relevant physical measurements in the context of a typical set-up of gas dispersion sensors in a flotation cell. The relevant values for these experiments are found in Table 3.3. The absolute atmospheric pressure (P_A) is that for McGill's elevation. The relevant equations are:

$$J_g = \frac{P_A + \rho_b H_L}{P_A + \rho_b (H_L - H_O)} \cdot \frac{dP}{dt} \qquad 3.2$$

where

$$\rho_b = \frac{P_2 - P_3}{H_{BD}} \qquad 3.3$$

$$Correction\ Factor\ for\ d_b = \frac{d_1}{d_2} \sqrt[3]{\frac{P_{abs\,1}}{P_{abs\,2}}} = \sqrt[2]{\frac{P_A + P_4 + \rho_w H_1}{P_A + P_2 + \rho_b H_E}} \qquad 3.4$$

and

$$P_4 = P_2 - \rho_w (H_1 + H_2 + H_3) \qquad 3.5$$

Note that an additional pressure-sensing tube, P3 in Figure 3.21, was inserted in the Metso cell to enable calculation of bulk density by using the J_g tube to provide pressure P2. The iFix/Excel software was programmed to automatically correct J_g from dP/dt readings. Bubble size corrections for the Metso and Denver cell measurements were calculated to be:

Metso Cell = 0.9838 (- 1.6%), Denver Cell = 0.9999 (- 0.01%)

The Metso cell correction of -1.6% is within the precision for D_{32} and D_{10} (relative std dev 1.9%) as discussed in Section 3.3 and shown in Table 3.2.

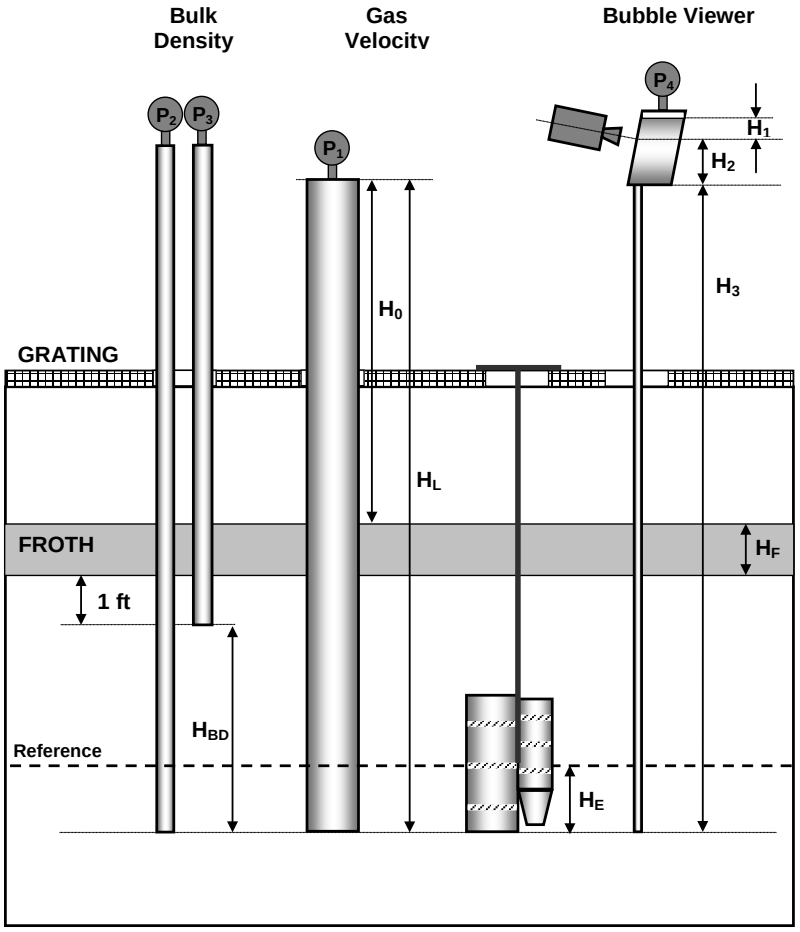

Figure 3.21 Schematic showing relevant physical parameters for gas dispersion sensors in a typical flotation cell. Values specific to these experiments are found in Table 3.3

Table 3.3 Relevant physical parameters for gas dispersion sensor set-up

Cell	***Physical Measure (cgs units)***									
	P_{A**}	P_2	H_L	H_1	H_2	H_3	H_{BD}	H_E	ρ_w	ρ_b
Metso	1026	1044-1049	114.5	6	13	86.5	14.5	0	0.9982*	$P_w(1-\varepsilon_g)$
Denver	1026	1032	-	6	13	48.5	-	0	0.9982*	$P_w(1-\varepsilon_g)$

**20 °C ** McGill elevation-atmospheric pressure*

Correction factor for bubble coalescence in bubble viewer

The natural tendency for bubbles, once formed, is to coalesce with other bubbles in order to lower the overall surface energy of the "system" (Finch et al, 2008). This process can be slowed, and even prevented entirely, by the presence of surfactants, or particulate solids on the bubbles, that prevent the rapid *film-thinning* of fluid between approaching bubbles required for coalescence to occur (Rao and Leja, 2004). This adds the requirement that the sampling system have sufficient surfactant in solution to preserve the bubble size once captured at the sampling point. However, this must occur without the liquid-plus-surfactant that is displaced from the bubble viewer (as it fills with air) influencing the bulk solution in the cell being sampled. Given that the volume of the bubble viewer and sampling tube are of the order of 5-6 liters, half of which may exit during the sampling period, an unintended influence on cell frother concentration may occur if the cell being sampled is not large compared to the bubble viewer volume. With the Denver cell at 5.5 liters (the Metso cell is 700 liters) there would clearly be an issue with the Denver cell if frother were added to suppress coalescence in the BV. Having, say, a maximum 10 ppm in the BV would result in up to +3 ppm in the Denver cell and only +.04 ppm in the Metso cell at the end of a measurement. Clearly, this precludes the use of additional frother in the BV when measuring bubble size in the Denver cell. Using pure water in the BV is equally unacceptable for reasons of dilution in the small cell volume, and the subsequent loss of preservation of bubble size once entering the viewer. The obvious resolution was to use the same water as in the cell to fill the BV for both Denver and Metso cell testing, and to develop a correction factor for those conditions (zero and low frother concentrations) where some bubble coalescence in the BV occurs. An additional question arises: what minimum frother concentration in the BV will adequately suppress coalescence in cases where the cell being measured is sufficiently large to accept BV solution containing frother?

The task was to develop a correction factor to be applied to the measured D_{32} in the bubble viewer filled with the same frother concentration as in the cell. Four levels of cell frother concentration were used. These concentrations were based on the CCC concept described by Cho and Laskowski (2002) and refined by Nesset et al (2007). Recall the CCC (critical coalescence concentration) represents the concentration beyond which no further reduction in bubble size, or more precisely D_{32}, occurs. The notion of CCCX was introduced by Nesset et al (2007) to represent the frother concentration for which x% of the maximum bubble size reduction has occurred relative to zero frother concentration. For example, the CCC95 represents the amount of frother for 95% reduction in D_{32} from the bubble size at zero frother. Nesset et al introduced a 3-parameter exponential expression that can be used to establish the CCC95, or any other CCCX value, from experimental data. That work forms part of this thesis and will be described in detail in Chapter 4. To summarize, once the characteristic CCC95 for any frother has been established, the D_{32} can be determined for any ppm level of that frother from the expression;

$$D_{32} = d_l + a \cdot exp\left[-b \cdot \frac{ppm}{CCC95}\right] \qquad 3.5$$

For J_g in the range 0.5 to 1 cm/s:

d_l is the limiting bubble size as concentration → ∞ (d_l = 0.907 mm)

a is the difference between D_{32} at zero frother and D_l (a= 3.133 mm)

b is the decay constant (b = 3.071)

Testing was conducted using DowFroth 250 at a J_g setting of 0.5 cm/s for which the characteristic CCC95 (uncorrected) had been established as 8.35 ppm. Frother levels in the Metso cell were selected at CCC0 (0 ppm), CCC50 (1.88 ppm), CCC85 (5.16 ppm) and 2x CCC99 (25.0 ppm). The bubble size was measured 8-10 times for each CCC level at increasing frother concentration in the bubble viewer. The results are shown in Figure 3.22. All curves exhibit an exponential decay reaching a limiting value and so can be characterized by an equation similar to Equation 3.5 having D_l, A and B parameters but without the CCC95 term. The parameters are listed in Table 3.4 and the model curves in Figure 3.22 reflect the goodness of the data-model fits. As a check on the CCCX levels in the Metso cell, the span between D_l values (Table 3.4) for CCC50 and CCC85 versus overall span (D_l for 2xCCC99 minus D_l for CCC0) are shown to be 47.7% and 83.3% respectively, close to the target concentrations set for CCCX levels in the Metso cell.

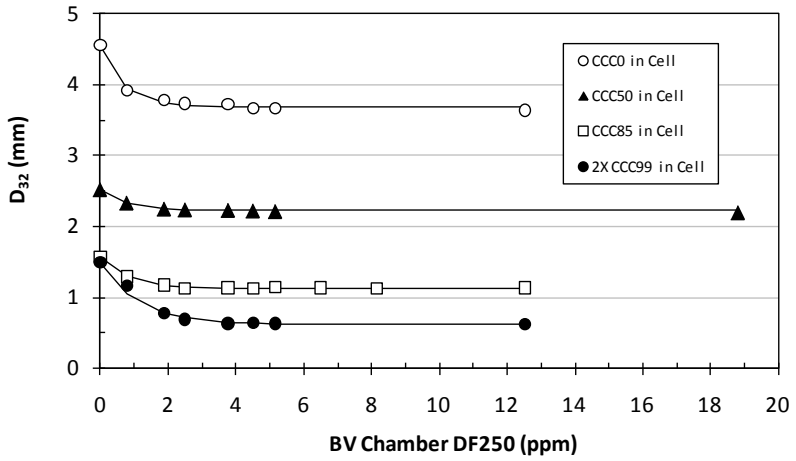

Figure 3.22 Behaviour of D_{32} as measured in the McGill BV as frother concentration is increased for four different CCCX levels in the cell (frother: DowFroth 250, J_g = 0.5 cm/s) (Note these are uncorrected CCCX values)

Table 3.4 Values for 3-parameter model used to fit data in Figure 3.22

Frother CCCX Level in Cell	**Model Parameter**			**% Distance Between D_l for CCC0 and 2xCCC99**
	D_l	A	B	
CCC0	3.69	0.8602	1.551	0
CCC50	2.226	0.2954	1.263	47.7
CCC85	1.134	0.4339	1.259	83.3
2xCCC99	0.6234	0.8719	0.9167	100

The parameters of Table 3.4 can be used to establish the required correction factors for D_{32} for the case when frother concentrations in the cell and bubble viewer are the same. For the bubble viewer at a specified CCCX in the flotation cell:

$$D_{32} = D_l + A \cdot exp[-B \cdot ppm] \quad 3.6$$

Defining X as the % of the CCC (for the flotation cell) and equating to the exponential term in Equation 3.5, one can write:

$$1 - {}^{X}/_{100} = exp\left[\frac{-b}{CCC95} \cdot ppm\right] \quad 3.7$$

Re-arranging to solve for ppm in the cell gives:

$$ppm = \left(\frac{CCC95}{-b}\right) \cdot ln\left[1 - {}^{X}/_{100}\right] \quad 3.8$$

Since ppm values are the same in both the cell and BV, one can substitute Equation 3.8 for ppm into Equation 3.6 giving D_{32} for the bubble viewer:

$$D_{32} = D_l + A \cdot exp\left\{-B \cdot \left(\frac{CCC95}{-b}\right) \cdot ln\left[1 - {}^{X}/_{100}\right]\right\} \quad 3.9$$

The correction factor for D_{32} measured in the BV can be defined as;

$$Correction\ Factor = \frac{D_l}{D_{32}} \quad 3.10$$

where D_{32} is obtained from Equation 3.9 for which all parameters are known for each of the four CCCX tests (Table 3.4). This data set provides four “measured” points (CCC0, CCC50, CCC85 and 2xCCC99), however, additional points can be generated for other CCCX values from simple models for D_l, A and B parameters. These relationships are shown in Figure 3.23 and were used to determine correction factors for CCC10, CCC20, CCC30 and CCC40, for a total of 8 measured plus modeled points.

The astute reader will have realized that once the calculated correction factors are applied to the original measured D_{32} values, the determination of the overall D_{32} model and parameters expressed by Equation 3.5 to establish these factors will themselves change as will the reported CCC95 values, in fact all CCCX values will change. This requires an iterative procedure be applied until convergence of model parameters and CCCX values is achieved. The details are described in Appendix B and required the adjustment of the CCCX values for the tests (not the numerical value of the corrections themselves from Equations 3.9 and 3.10). The corrected parameters for Equation 3.5 therefore become, after iteration:

d_l = 0.901 mm, the limiting bubble size as concentration → ∞

a = 2.41 mm, the difference between D_{32} at zero frother and D_l

b = 2.995, the exponential decay constant

The main difference being that *a* has decreased from 3.13 mm to 2.41 mm.

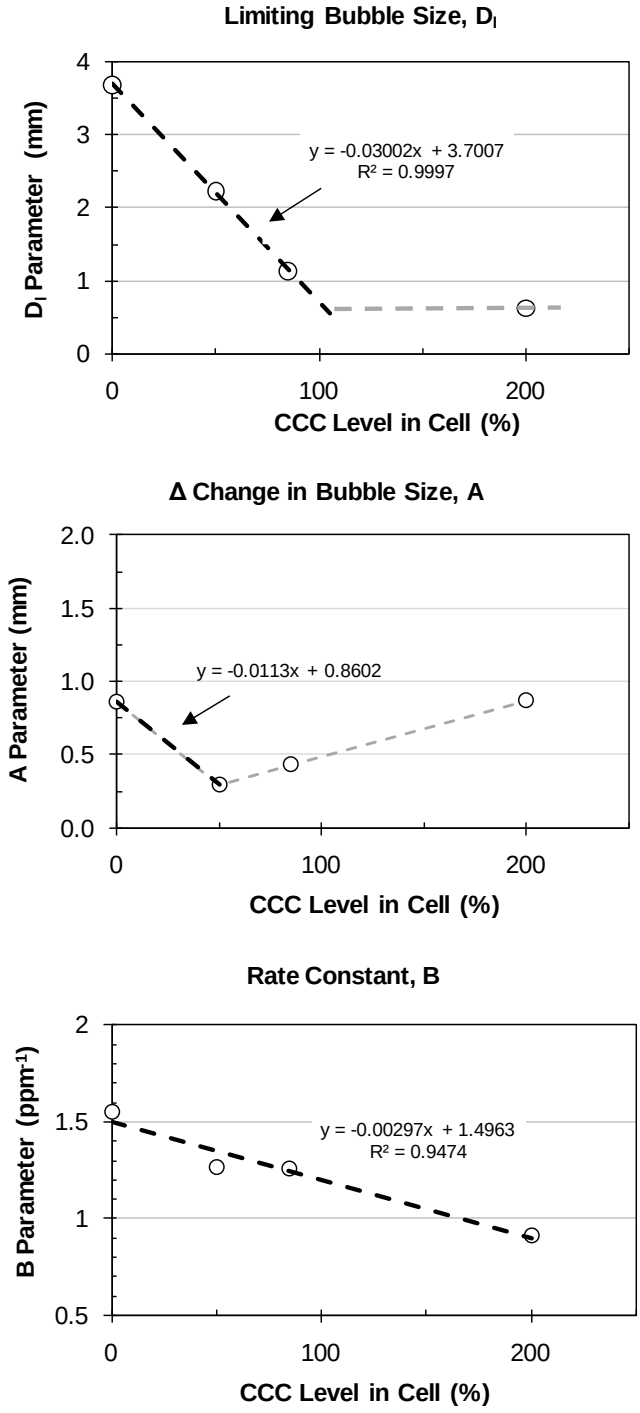

Figure 3.23 Models for D_l, A and B parameters from curves in Figure 3.22. The indicated linear equations were used to determine correction factors for original (uncorrected) CCC10, CCC20, CCC30 and CCC40 used in Figure 3.24

The adjustment of the initial CCCX levels (%) to those achieved at convergence is given by;

$$CCCX_{Revised} = 100 \cdot [1 - (1 - CCCX_o/100)^e] \quad 3.11$$

where

$$e = \frac{CCC95_o \cdot b}{CCC95 \cdot b_o} \quad 3.12$$

and the subscript o refers to the original D_{32} model and CCC95 values for DowFroth 250 ($CCC95_o$ = 8.35 ppm, $CCC95$ = 10.06 ppm, b_o = 3.071, b = 3.0). Figure 3.24 is a plot of the corrections made to the initial CCCX values and that were applied to uncorrected D_{32}'s.

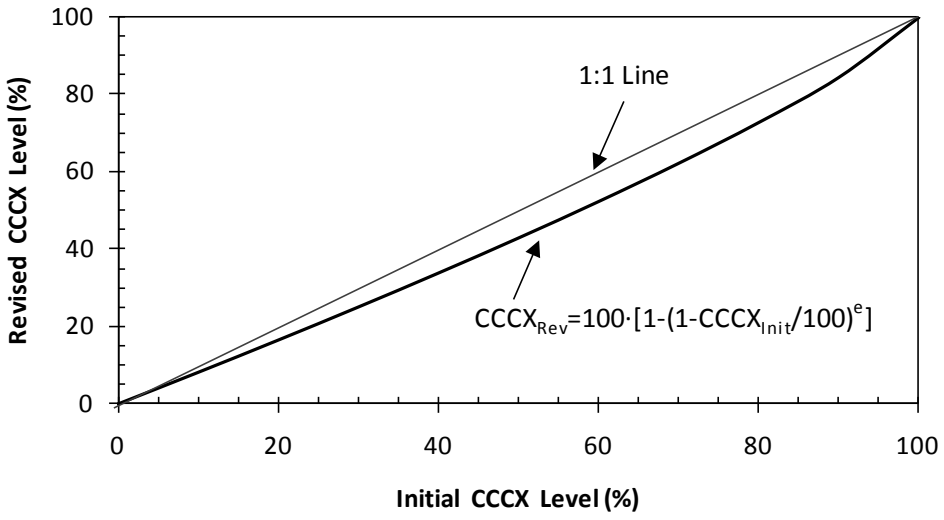

Figure 3.24 Corrections to the initial CCCX values applied to uncorrected D_{32}. (The derivation is found in Appendix B.2)

Figure 3.25 shows the D_{32} correction factor as a function of CCCX level (%), and a best-fit exponential curve having an R^2 of 0.998. The final fitted equation for a frother concentration (any frother) of CCCX (as %) is therefore:

$$Correction\ Factor = 1.00363 - 0.195298 \cdot exp[-0.054163 \cdot CCCX] \quad 3.13$$

This expression is valid for the full range of CCCX, and since concentration is expressed in terms of CCCX and not ppm for a specific frother, it will be applicable for any frother whose CCC95 is known. Note that for zero frother in the system, the correction factor is 0.81, but increases rapidly at low frother concentrations, reaching 0.95 by CCC24 and 0.99 by CCC49. Table 3.5 has been prepared specifically for DowFroth 250 (CCC95 = 10.06 ppm

for J_g = 0.5 cm/s) illustrating that for as little as 2 ppm in the BV, the correction factor is between 0.98 and 0.99. This bodes well for plant survey work where the process water used to fill the BV invariably contains significant residual frother (Gelinas and Finch, 2005). These factors will prove particularly useful for research work where smaller flotation cells or columns, fresh water, or water from the cell are often used. For the current work, Equation 3.13 was applied to the collected data. Note that these factors apply to D_{32} only and not D_{10}, which produced less predictable relationships not reported here.

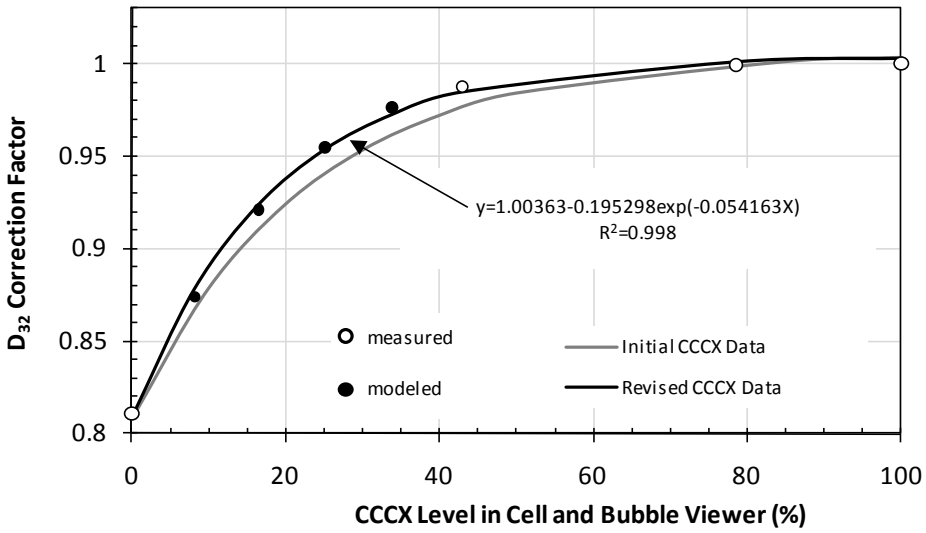

Figure 3.25 The D_{32} correction factor to be applied when the McGill BV and cell frother concentrations are at the same CCCX level

Table 3.5 Frother CCCX levels required in the McGill BV to achieve specific D_{32} correction factor tolerances (From model curve in Figure 3.25 and DowFroth 250 CCC95 = 10.06 ppm)

Bubble Viewer Frother to Achieve Correction Factor	***D_{32} Correction Factor***			
	0.95	***0.98***	***0.99***	***0.999***
Required CCCX Level (%)	24	39	49	69
Required PPM DF250	0.92	1.7	2.3	3.9

An interesting outcome of this bubble viewer characterization work is the opportunity to observe the evolution of the BSD as it is sampled in the cell and is exposed to different frother concentrations in the BV. Figure 3.26 shows a sequence of distributions for the case of low frother in the cell (1.88 ppm DowFroth 250 = CCC43, upper graph) as well as high frother in the cell (25.0 ppm DowFroth 250 = CCC99.9, lower graph). Note that high concentration in the bubble viewer preserves the BSD sampled from the cell. At low cell concentration, the BSD is bimodal and remains so within the bubble viewer as concentration is decreased, with coalescence resulting in larger bubbles in one mode (~2 mm dia) and a

greater population of smaller (daughter) bubbles (~0.35 mm dia) in the other mode. At high concentration in the cell, a tight, single mode BSD results but will become bi-modal for very low frother concentration in the BV. The resulting coalesced bubbles are smaller (~1.2 mm dia) and appear not to produce an increase in daughter bubbles as evident from the lower graph in Figure 3.26. It appears that the ability to produce smaller daughter bubbles may depend on the size of the coalesced bubble, and that 1.2 mm dia may be too small but that 2 mm dia is sufficiently large.

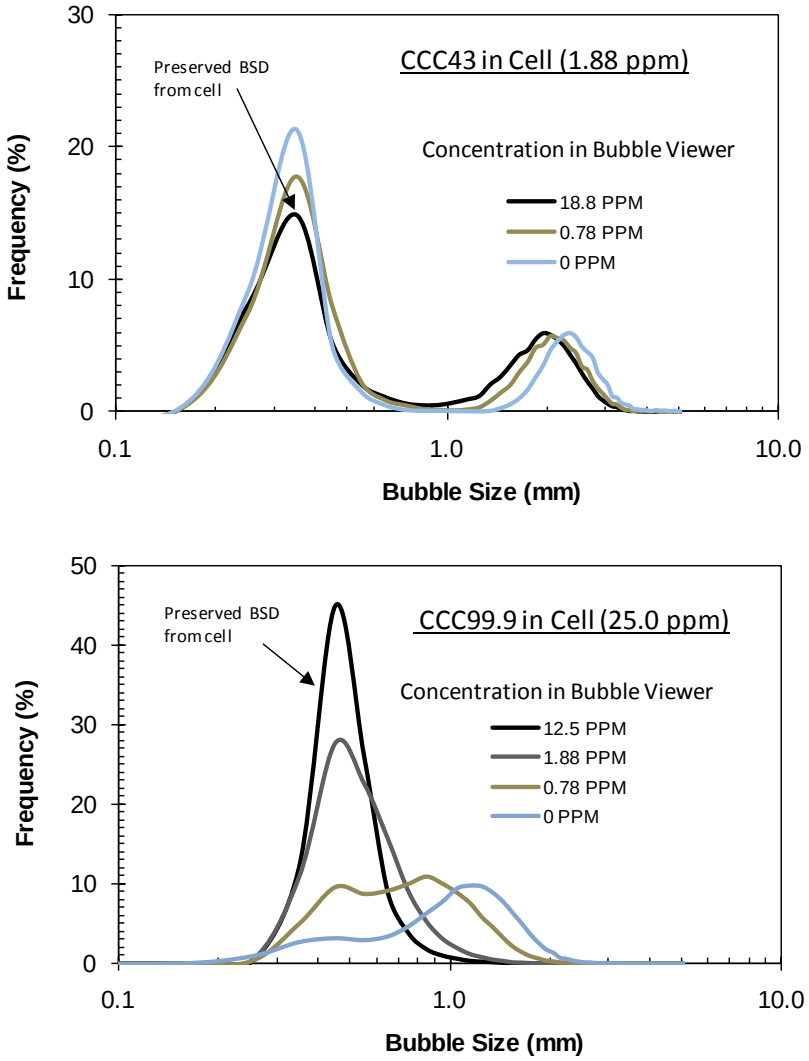

Figure 3.26 Effect of McGill BV frother concentration on the BSD as sampled in the cell. Upper: low concentration (1.88 ppm) in cell. Lower: High concentration (25.0 ppm) in cell. (DowFroth 250, J_g = 0.5 cm/s)

Frother selection

Table 3.6 lists the five frother types used for this work, and their sources. These represent four of the major chemical types of frothers; methyl isobutyl carbinol (MIBC, an aliphatic

alcohol), polypropylene glycol alkyl ether (DowFroth 250), polypropylene glycol (F150), and a popular blended mixture of aldehydes and ketones (F140). Pentanol was added to the list of four commercially available products to extend the range of molecular weight and carbon-chain length. Plant surveys have also indicated that short chain alcohols can enter process water streams as impurities in commercial xanthate supplies (Gélinas and Finch; 2005). Recent studies have indicated there may well be a role for short chain alcohols as frothers, either individually or as blends (Cappuccitti and Finch, 2008; Cappuccitti and Nesset, 2009). The long-time industry standards have been MIBC and DowFroth 250 and so these benchmark surfactants were selected for the phase of work investigating gas rate. Some inconsistencies with MIBC were noted during this work so "decay" tests were conducted for all 5 frothers.

In these decay tests, bubble size was measured at time intervals over a 3.5 hour period in the cell in order to observe changes to D_{32} and D_{10}. Frother concentrations representing CCC93 (at J_g =1 cm/s) were selected for all five frothers to provide equivalency of concentration, as well as an appropriately sensitive operating region. Figure 3.27 shows that four of the frothers maintained reasonably consistent bubble size (both D_{32} and D_{10}) over the 3.5-hour period, with the exception of MIBC (CCC93 = 12.5 ppm) which is seen to steadily increase in size with time. Increasing MIBC to 1.5x the CCC93 (i.e. 19.2 ppm) resulted in bubble size remaining constant for five hours. A plausible explanation is that MIBC is stripped from solution by the air blown into the cell, later confirmed by Azgomi et al (2009). This results in an increase in bubble size when starting at the CCC93 concentration level, but does not impact bubble size when starting at excess concentration since it is well above the CCC. Subsequent testing was therefore conducted primarily with DowFroth 250 to avoid potential issues with changes to bubble size over time using MIBC. This tendency of MIBC to lose effectiveness over time may be both a beneficial as well as detrimental characteristic. It would be beneficial in terms of reduced tendency to build up concentration in process circuits and recycle water in a plant, however, it could be detrimental in single flotation circuits with long retention times or high gas rates. It did introduce inconsistencies into this work for long tests in which frother (MIBC) was added incrementally and for long test series with increasing gas rates.

Table 3.6 The five frother types used in this work

Frother	***Description***	***Supplier***	***Molecular Weight***
Pentanol	Simple alcohol	Fisher	88
MIBC	Methyl isobutyl carbinol	Dow	102
DowFroth 250	Polypropylene glycol alkyl ether	Dow	235-265
F140	Blend of aldehydes and ketones	Flottec	Mixture C8-C22: typical 200-250
F150	Polypropylene glycol	Flottec	410-440

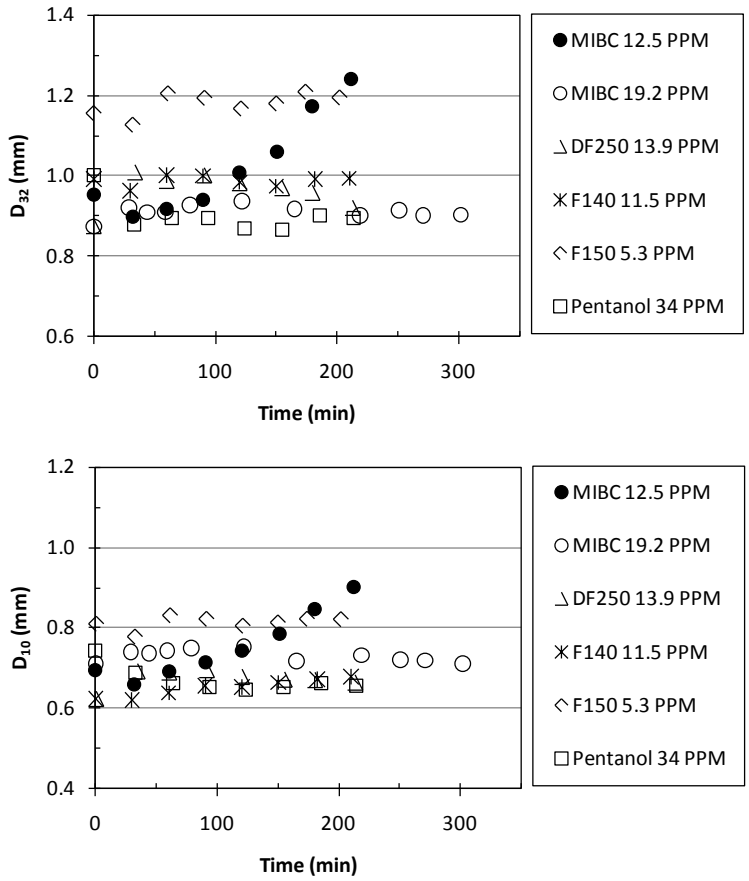

Figure 3.27 Frother decay tests measuring D_{32} and D_{10} over time. All ppm levels represent CCC93 concentrations except for MIBC 19.2 ppm which is 1.5xCCC93 (J_g = 1 cm/s, water temperature 24-26 ^{o}C)

Testing methodology

A brief review of the standard testing methodology for the Metso cell follows. Montreal tap water was used to fill the cell to a total volume of 700 liters and allowed to reach room temperature (16-18 ^{o}C) overnight. Frother, if added, was weighed and premixed (2 min agitation) in a pail before being transferred to the Metso cell. Approximately ten minutes of agitation without air ensured good frother dissolution. This was likely unnecessary for highly soluble frothers such as DowFroth 250, but was required for the F140 and MIBC. F140 had a tendency to stick to the cell walls when draining the cell and so scrubbing of the cell was required following each F140 test. Unless otherwise noted, tests were conducted under standard conditions of impeller speed 1485 RPM (50 Hz), equivalent to 5.73 m/s tip speed. Cell water was transferred via a Masterflex pump to fill the bubble viewer chamber. Note that there was some variation in the quality of Montreal tap water over extended time (weeks/months) which led to some variation in the measured bubble size at zero frother.

Blocks of tests were therefore conducted over as short a time-period as possible to minimize the effect of this uncontrolled variable.

Coarse adjustment of air rate was via a rotameter followed by fine adjustment with a needle valve to reach the target J_g value. As discussed in Section 3.3, ten measured slopes ($\Delta P/\Delta t$) were averaged for each reported J_g. Each bubble size measurement involved the collection of 500 independent images representing 10,000 individual bubbles. A 10-bit digital camera driven by a commercial software package (Northern Eclipse from Empix Imaging) was used. Data processing involved two steps: first digitizing individual images, followed by counting and sizing of individual objects (bubbles) according to shape factor criteria and threshold settings to discriminate bubble edges from background. Correction factors as described in Section 3.4 were then applied to the calculated values of D_{32} and D_{10}.

Testing on the Denver cell was similar; however, there was no independent measurement of J_g, simply a calculation of gas flow rate divided by the effective cell cross-sectional area. Control was via mass flow meters for air and helium. Impeller speed was 1600 RPM providing an impeller tip speed of 5.86 m/s, similar to that for the Metso cell (5.73 m/s). Bubble size measurement was conducted using the same equipment and protocol as for the Metso cell. A Masterflex pump was used to return the water overflow to the cell in order to maintain constant cell level.

The tests varying impeller speed were designed to establish the effect of power intensity on bubble size. It was confirmed that power (P) increase on the Metso cell did follow the expected cubic power-law relationship as a function of impeller rotational speed, N, (i.e. $P \propto N^3$, non-aerated and aerated). A doubling of impeller speed was possible on the unit, thereby covering impeller tip speeds from 4.6 to 9.2 m/s, providing an almost 8-fold increase in power intensity. Typical operating impeller tip speeds on industrial machines are from 5-7 m/s, however values up to 10 m/s have been reported (Deglon et al, 2002; Forman, 2010) The impeller speed tests were run at 2 levels of J_g, 0.5 and 1 cm/s.

Tests varying gas density were included in the attempt to simulate elevation, since many plants are located well above 3000 m, some approaching 5000 m in Bolivia, Chile and Peru. Mixing air and helium (He) proved a convenient means of obtaining gas mixtures with the desired density representing different altitudes. Individual mass flow meters and controllers for air and He were used to feed the mixture through an in-line mixer before being introduced to the Denver flotation machine. Mixtures between 0% and 100% He were tested, however, only a mixture of 60% He - 40% air is required to simulate an altitude of 5000 m where air density is about half that at sea level. Only data for J_g values of 0.25 and 0.3 cm/s were used as the ability of the Denver machine to fully disperse the gas at higher gas rates (above 0.5 cm/s) was suspect. Other test conditions were DowFroth 250 at 5 ppm and impeller speed of 1600 rpm (5.86 m/s).

The tests to establish the effect of water temperature served a dual purpose as the range of water temperature (3 to 41 ^{o}C) introduced a correspondingly significant change in the (dynamic) water viscosity (1619 to 641 µPa-s). The changes in both water density (999.9 to 991.8 kg/m3) and surface tension (0.07522 to 0.06943 N/m) over this range are small in

comparison, so the test became, de-facto, an investigation of the effect of viscosity over a temperature range that is representative of what flotation plants in many parts of the world experience. These tests were run at J_g of 1 cm/s (at 5 ppm of DowFroth 250), and temperature was allowed to either increase (if starting below room temperature) or decrease (if starting above room temperature). Hot water was used for the warmer tests and the naturally cold Montreal tap water of April/May was used for the colder tests. In total, four series of tests were conducted varying temperature and the results combined.

CHAPTER 4: Experimental Results and Analysis: Laboratory Testing

This chapter covers the bulk of experimental work relating to the development of the model for prediction of Sauter mean diameter, D_{32}, from the five main process variables selected: frother type and concentration, gas rate, impeller speed, liquid viscosity and gas density (to simulate altitude). Where available, the relationships for the arithmetic mean, D_{10}, are also reported, however, developing a model for D_{10} was not an objective of this work. Flotation is primarily a surface area (of bubbles) dependent process and as such, D_{32} is the parameter of interest. As noted in the Introduction, D_{10} can be important as a measure of the very small bubbles in the bubble size distribution (BSD), and there are clearly instances where small bubbles and the recovery of very fine particles are linked (Nesset et al, 2005, 2007). However, the primary driver of flotation kinetics is surface area flux ($S_b = 6\, J_g / D_{32}$) and so modeling the D_{32}, and not D_{10}, is the main interest.

4.1 Effect of Frother Concentration and Frother Type

Developing correlations

Five frother types were selected (Table 3.6) to cover the range of commercial frother groups as well as pentanol, a short chain, low molecular weight alcohol. Tests were conducted on the Metso 0.8 m^3 unit at two gas rates, J_g = 0.5 and 1 cm/s. Frother concentration is reported as frother *addition* since in some cases, as noted for MIBC, the concentration may change over time. Testing was conducted by incrementally adding frother and performing the bubble size measurement. Gas rate, gas holdup and power were also measured for each test. Results are presented in Figure 4.1 and suggest that the D_{32} versus ppm frother addition curves follow an exponential decay relationship reaching a limiting value beyond which no further reduction in bubble size takes place. This is consistent with the findings of Laskowski (2003)) who also found the curves reach a limiting value for D_{32}; however these data show more consistency in the exponential shape of the curves. These findings have been previously reported (Nesset et al, 2007) using a model of the form proposed by Hernandez-Aguilar (2005b) to fit the data;

$$D_{32} = D_l + A \cdot exp[-B \cdot ppm] \qquad 4.1$$

where D_l (mm) is the limiting D_{32} size as ppm$\rightarrow \infty$, A (mm) is the change in bubble size between zero frother and infinite frother, and B (ppm^{-1}) is the decay constant in the exponential equation. The Laskowski notion of the CCC (critical coalescence concentration of frother) beyond which no further reduction in bubble size takes place, can be handled as a % of A, the bubble size reduction achieved, and has been called CCCX, where X is the % reduction in A. For example, CCC95 represents the frother ppm addition for which the D_{32} size has been reduced to within 95% of its limiting value D_l. Figure 4.2 illustrates the concept. The CCC95 values are also indicated in Figure 4.1 for each frother test. Once the parameter B has been established for a frother, the conversion between CCCX and frother ppm can be found by re-arranging Equation 4.1:

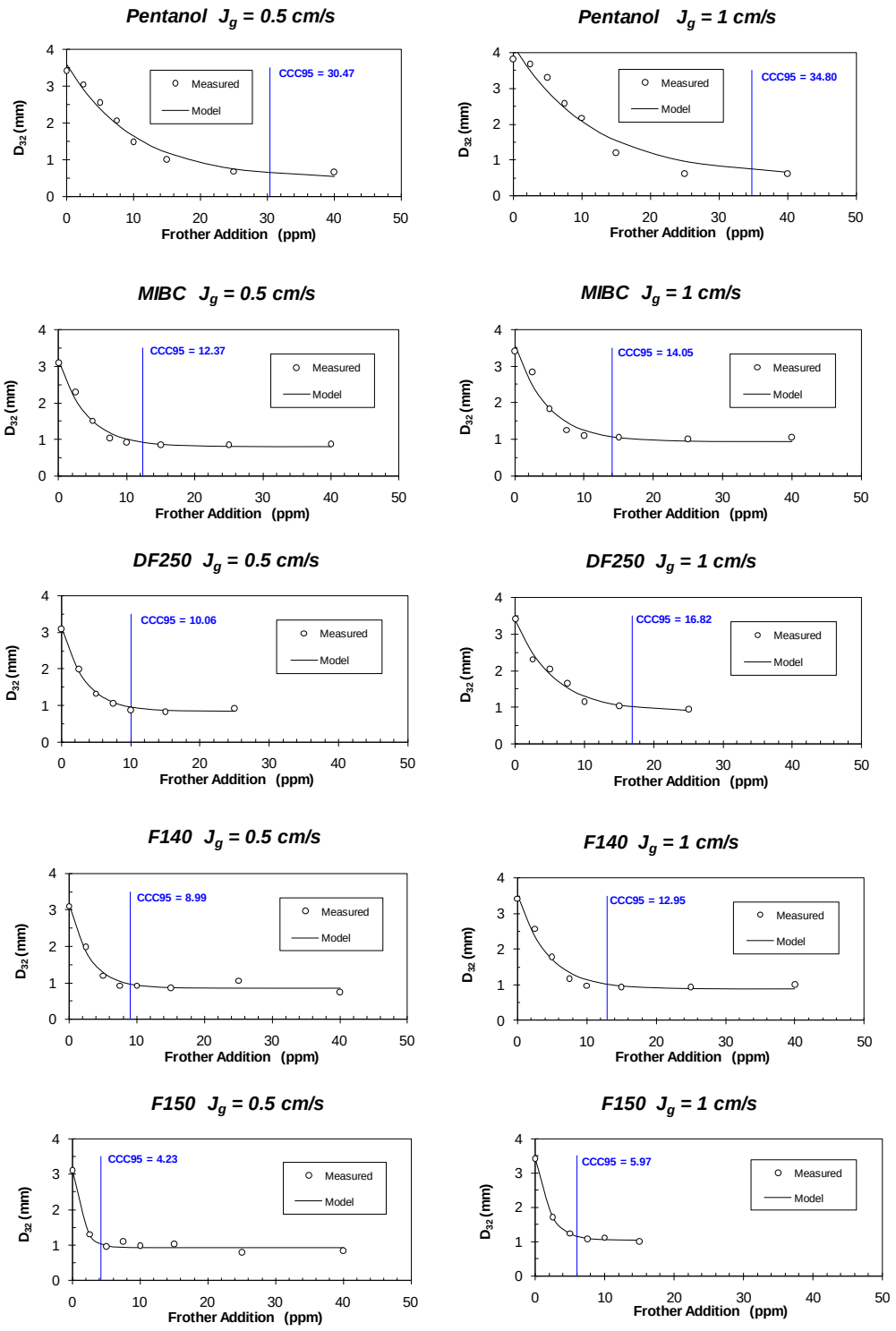

Figure 4.1 The effect of frother addition on D_{32} for the five frother types for J_g 0.5 and 1 cm/s. $CCC95$ values are indicated for the modeled curves. Model parameters and goodness-of-fit indicators are listed in Table 4.1. Error bars for 95% CL are within the data circles

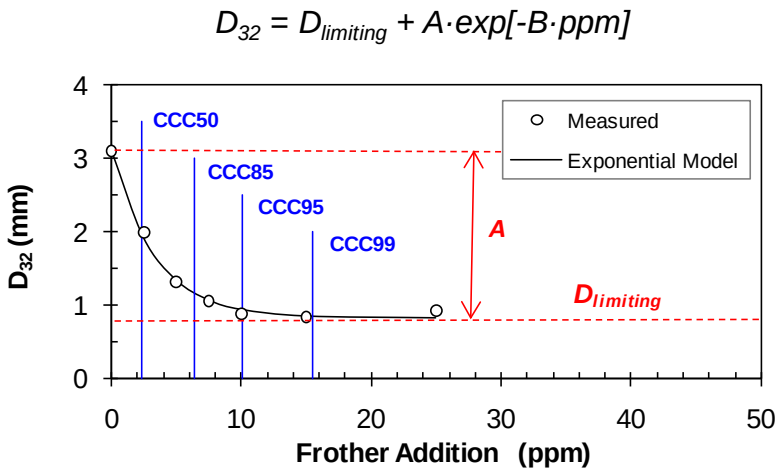

Figure 4.2 Illustration showing the exponential model used to fit the D_{32} versus ppm frother data. The CCCX lines indicate the ppm levels for X% reduction in A

Table 4.1 Model and goodness-of-fit parameters established from data of Figure 4.1. (MW = molecular weight, HLB = hydrophile-lipophile balance), *estimated value

Model Parameters		***Frother Type***				
		Pentanol (MW=88) (HLB=6.52)	*MIBC* (MW=102) (HLB=6.1)	*DF250* (MW=250) (HLB=8.0)	*F140* (MW=225) (HLB=5.8*)	*F150* (MW=425 (HLB=7.83)
J_g = 0.5 cm/s	D_I (mm)	0.4788	0.8024	0.8373	0.8514	0.9411
	A (mm)	3.113	2.376	2.289	2.289	2.162
	B (ppm^{-1})	0.09833	0.2423	0.2979	0.3331	0.7083
CCCX (ppm)	85%	19.29	7.83	6.37	5.70	2.68
	95%	30.47	12.37	10.06	8.99	4.23
	99%	46.83	19.01	15.46	13.83	6.50
J_g = 1 cm/s	D_I (mm)	0.5500	0.9458	0.8911	0.8829	1.0453
	A (mm)	3.643	2.617	2.485	2.631	2.374
	B (ppm^{-1})	0.08608	0.2132	0.1781	0.2313	0.5016
CCCX (ppm)	85%	22.04	8.90	10.65	8.20	3.78
	95%	34.80	14.05	16.82	12.95	5.97
	99%	53.50	21.60	25.86	19.91	9.18
R^2	J_g=0.5	0.979	0.983	0.997	0.979	0.984
	J_g=1	0.951	0.962	0.989	0.977	0.999
$R^2_{Adjusted}$	J_g=0.5	0.962	0.970	0.993	0.962	0.972
	J_g=1	0.914	0.933	0.977	0.960	0.997

$$ppm = \left[\frac{ln\left(1-\frac{X}{100}\right)}{-B}\right] \qquad 4.2$$

A summary of model parameters (from Equation 4.1) and measures of goodness-of-fit appear in Table 4.1 along with selected CCCX values for 85%, 95% and 99% as determined from Equation 4.2. The R^2 and R^2_{Adj} show excellent model fits with all R^2_{Adj} values above 0.96 except for MIBC and Pentanol at J_g = 1 cm/s having, still acceptable, R^2_{Adj} of 0.93 and 0.91 respectively.

The ability to predict some of the model parameters, such as D_l, B and CCC95 from fundamental properties of the frothers would be a useful development since the measurement of bubble size to establish values is a time-consuming and, therefore, costly process. The molecular weight (in some cases estimated or averaged) and the HLB values for each frother have therefore been included in Table 4.1. The HLB, the hydrophile-lipophile balance, is a measure of the solubility of a frother in water, and is an empirical measure based on the number of hydrophile (mixes with water, polar groups) and lipophile (does not mix with water, non-polar groups) groups in the molecule (Laskowski, 1993, 1998). HLB values can be calculated if the molecular structure is known (Pugh, 2007) and have been reported in the literature for many frother types (Laskowski, 2003; Rao and Leja, 2004). The exception here is F140, a blend of aldehydes and ketones of carbon chain length 8 to 22 (Cappuccitti, 2007), however, an estimated value has been indicated for F140 (HLB = 5.8) since its solubility is known to be considerably less than MIBC (HLB = 6.1).

Figures 4.3 and 4.4 have been prepared from the data of Table 4.1 to examine relationships between model parameters and the frother properties. It is seen from the left hand side plots in Figure 4.3 that, in general, D_l, and the decay constant B, increase as the molecular weight of the frother increases, while CCC95 decreases with increasing frother molecular weight (MW). A better indicator may be the ratio of *HLB/molecular weight* as shown in the right hand side plots which, arguably, produce somewhat better relationships than molecular weight alone. HLB/molecular weight would essentially indicate the degree of solubility per unit of molecular weight. Plots of HLB alone as the ordinate produced wide scatter. Others (Laskowski, 2003; Pugh, 2007) have noted the significance of the HLB but it is believed this is the first time the HLB/MW ratio has been shown to be linked directly to frother behaviour. Note that there is an effect of gas rate, J_g, on all parameters. Laskowski (2003) assumed no effect of J_g on CCC from his data, although close examination of his plots suggests one may exist. There is insufficient data here for definitive relationships to be claimed, however, the link between CCC95 and the HLB/MW ratio appears promising.

The 2 plots of Figure 4.4 show that a strong link exists between CCC95 and the limiting bubble size, D_l (left plot). It appears that higher molecular weight and less soluble frothers result in larger limiting bubble size. It is not felt that these correlations are simply an artifact of the model data fitting or by chance. The right hand plot of the decay constant, B, versus CCC95 is one of essentially the same parameter compared to itself since CCC95 is the ppm value for which the exponential decay has been reduced by 95%. The plot does serve to illustrate that CCC95 is very sensitive at low values of B, such as for Pentanol. The most significant plots from Figures 4.3 and 4.4 for D_{32} model-development purposes are likely the ones linking D_l to the CCC95 and also J_g.

Replicate tests were performed some weeks later for Pentanol and are shown in Figure 4.5. The reproducibility was not as good as for other repeats, possibly due to a suspected issue relating to changes in the quality of Montreal tap water over time. Tests replicated immediately produced very similar results, however those repeated after some time had (typically weeks), invariable produced differences in zero frother and limiting value bubble size. Since 700 liters were required for each test run, the only practical source was Montreal tap water and care was taken to run test series as close together in time as possible. As noted in Figure 4.4, due to its small decay constant B, Pentanol CCC95 determination is very sensitive to small differences in B.

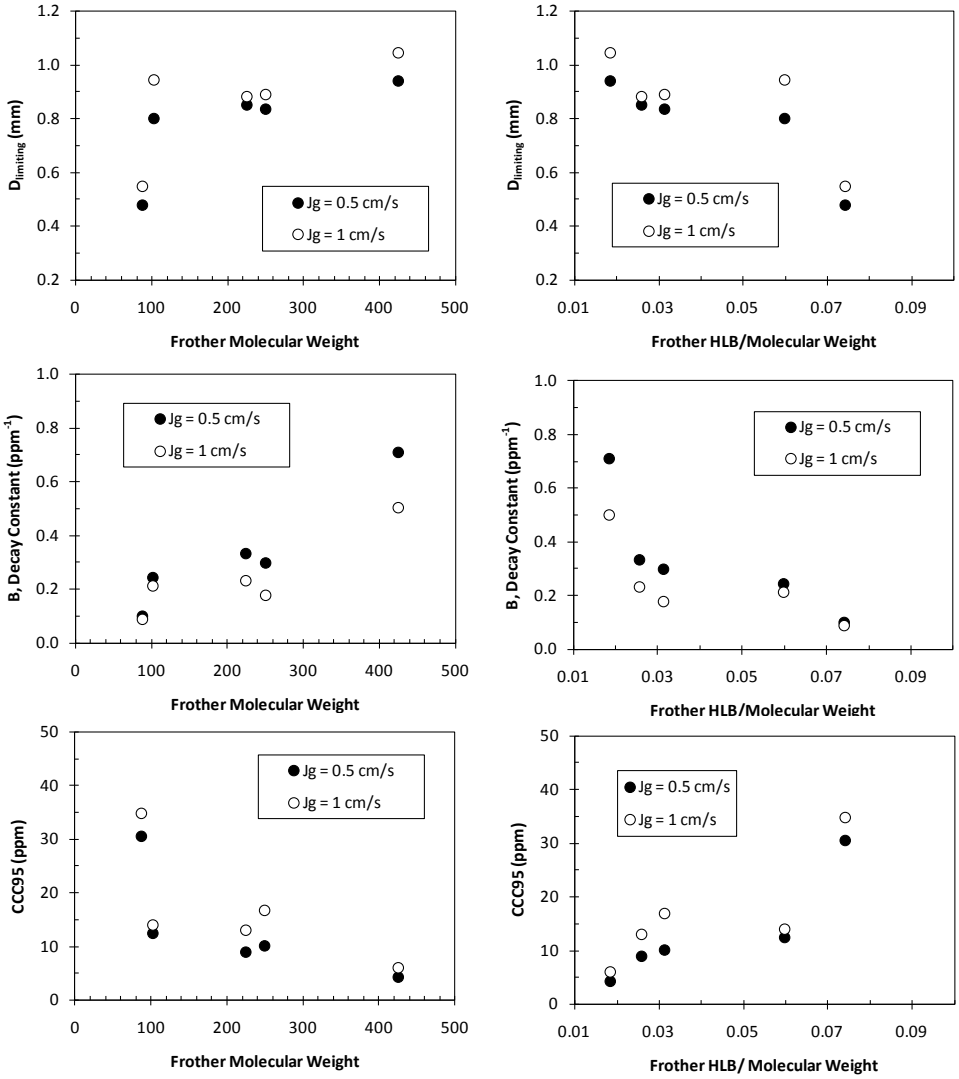

Figure 4.3 Comparisons of the model parameters $D_{limiting}$, B, and $CCC95$ for the five frothers versus frother molecular weight (left side plots) and HLB/molecular weight (right side plots)

Combined data for four frothers

The fact that the data for all frothers as shown in Figure 4.1 is well represented by a simple exponential decay equation, and following the example of Laskowski (2003), suggested a normalization procedure using CCC95 as the parameter to reduce all data to a single curve. The analysis has previously been presented in the literature (Nesset et al, 2007) and earlier in this thesis as Equation 3.5 in Section 3.4 on development of correction factors. It is presented again as;

$$D_{32} = d_l + a_o \cdot exp\left[-b \cdot \frac{ppm}{CCC95}\right] \qquad 4.3$$

where lower case d_l, and a_o are equivalent to D_l and A of Equation 4.1 and b is a modified decay constant, reflecting that the exponential relationship has been normalized by dividing ppm levels by the CCC95 for a particular frother and gas rate (J_g). The results for the four frother types, not including Pentanol, are shown in Figure 4.6, with an expanded view of the range from 0-2 ppm/CCC95 appearing in the lower plot. Pentanol was not included due to the uncertainties noted previously, although the issue is not major since the models with the inclusion of Pentanol were only marginally different. The parameters for the fitted models in Figure 4.6 are given in Table 4.2 and are for 3 data sets: All Data (combined data for J_g = 0.5 and 1 cm/s), and separately for J_g = 0.5 and 1 cm/s. The data fits are good having R^2 values of 0.97 to 0.98. The model parameters presented here are for corrected D_{32} values and replace those reported previously in the literature (Nesset et al, 2007). The differences between the previously reported model parameters and those reported here are small, but most notable to the value of a, the difference between D_{32} at zero frother and d_l since the largest correction to D_{32} is for the zero frother condition. The iterative correction factor approach detailed in Section 3.4 and Appendix B utilized the All Data model; however, there would have been no significant difference if either of the other models had been selected. Figure 4.6 supports the notion of a limiting value for D_{32} as frother concentration is increased given that the curves flatten for frother ppm exceeding 9x the CCC95.

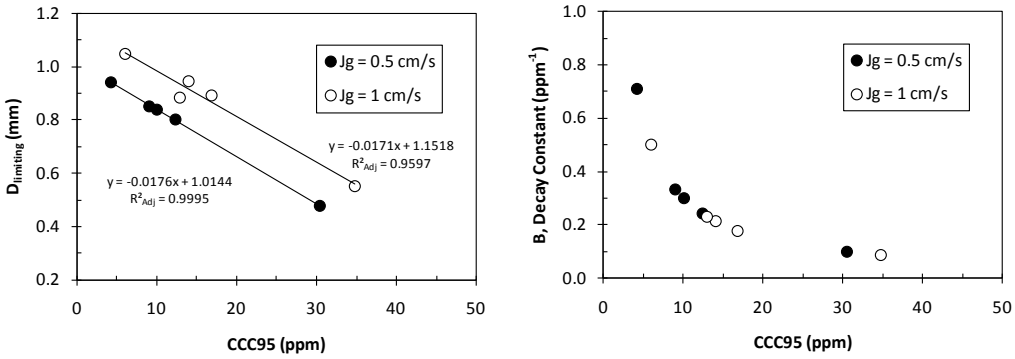

Figure 4.4 The relationship between CCC95 and D_l(left) and the decay constant, B (right)

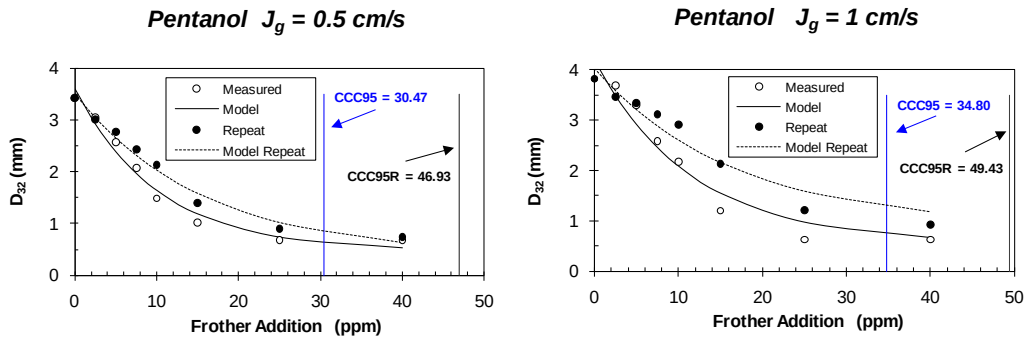

Figure 4.5 Replicate tests for Pentanol performed several weeks later highlight a possible issue with changing quality of Montreal tap water over time

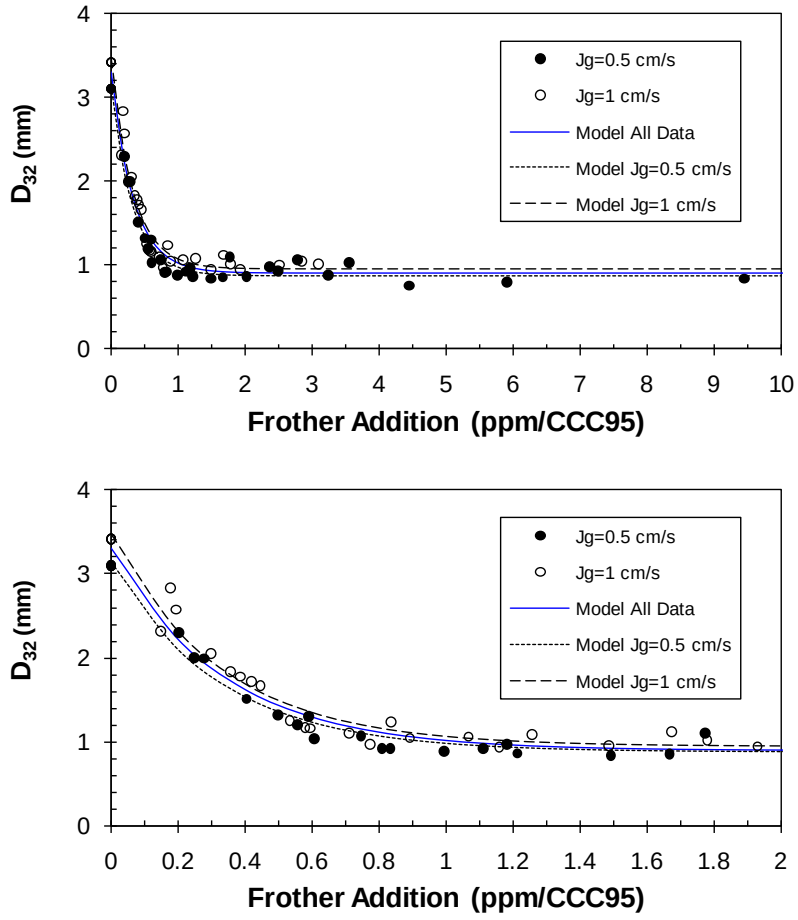

Figure 4.6 The normalized plots of D_{32} versus ppm/CCC95 for four frothers (not including Pentanol). The model parameters and goodness of fit values appear in Table 4.2. Note the bottom plot is an expanded view of the 0-2 ppm/CCC95 range and that the model fits are slightly different for J_g = 0.5 and 1 cm/s

The standard deviation data from Table 4.2 allow the 95% confidence intervals (CI) to be determined for modeled D_{32} values using Equation4.3. The All Data and J_g = 1 cm/s models have 95% CI of ±0.24 and ±0.22 mm respectively, while the J_g = 0.5 cm/s model has better precision at ±0.12 mm. The differences between the two J_g models fall within these tolerances since the difference in limiting values is only 0.08 mm. This is evident from Figure 4.7 which shows the 95% confidence limits for the All Data Model (upper plot) and J_g= 0.5 cm/s Model (lower plot). These models will form the basis for the overall D_{32} model which will be developed within this chapter and the next.

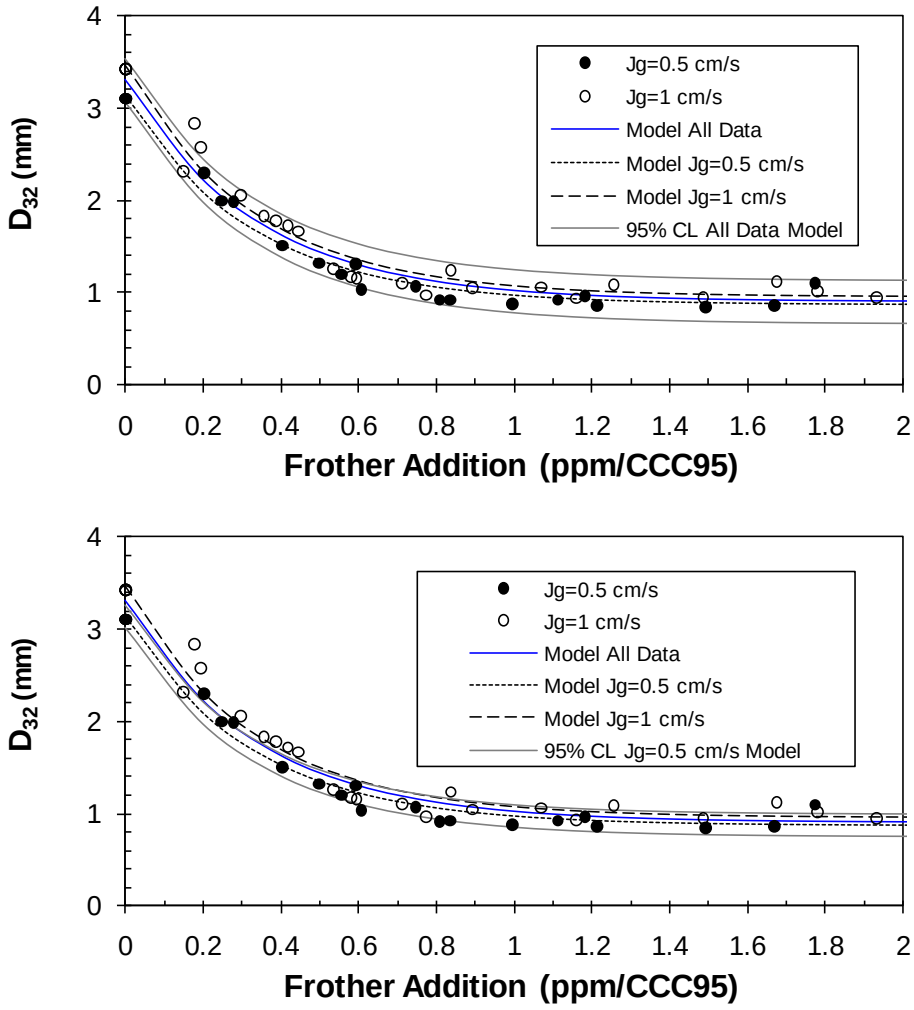

Figure 4.7 95% Confidence Limits for the All Data Model (upper plot) and J_g = 0.5 cm/s Model (lower plot)

Table 4.2 Model parameters and goodness-of-fit relationships for the data for four frothers shown in Figure 4.6. (Pentanol not included)

Model Parameter	***All Data***	***Model*** J_g ***= 0.5 cm/s***	J_g ***= 1 cm/s***
d_l (mm)	0.9012	0.8740	0.9515
a_o (mm)	2.408	2.264	2.515
b	2.995	3.090	3.054
Precision			
R^2	0.968	0.982	0.973
Std Dev (mm)	0.1173	0.0596	0.1086
Data Points, N	58	30	28
t-statistic	2	2.042	2.048
95% CI (± mm)	0.235	0.122	0.222

4.2 Effect of Superficial Gas Velocity (Gas Rate), J_g

Control of distribution of gas (usually air) flow rate to banks of flotation machines, and banks is increasingly being used to control grade and recovery of minerals, and therefore the economics of flotation performance (Cooper et al, 2004; Hernandez-Aguilar et al, 2006; Doucet et al, 2006), In terms of relative cost, supply of air is inexpensive compared to flotation chemicals since excess air is always produced (forced-air machines) and vented if unused. Understanding this key variable and its role in determining bubble size was therefore an important component of developing a model for D_{32}. Testing was conducted on the Metso unit using two frothers; DowFroth 250 and MIBC, as they (or equivalents) are widely used industrially and so have become industry "standards". A range in frother concentration, CCC99 to CCC0, was tested over a range of superficial gas velocity (J_g), from 0.05 to 1.5 cm/s. Water temperature was maintained in the 18-20 ^oC range, and testing was conducted covering lower and higher J_g ranges separately so as to avoid excessive temperature rise and frother removal due to long testing times, as could be a problem with MIBC.

Earlier plant studies by the author and co-workers (Nesset et al, 2006, 2007) had introduced a relationship for D_{32} versus J_g of the form;

$$D_{32} = D_o + C \cdot J_g^n \qquad 4.4$$

where

D_o - bubble size at J_g= 0 cm/s

n - constant exponent

C - parameter that is system (i.e. bubble generator and J_g) and chemistry dependent.

Figure 4.8 illustrates the data from three different plants and four cell manufacturers. These studies pointed to the notion of a bubble "creation size", D_o, at J_g = 0 cm/s, and a value for n of the order 0.55. To a significant extent, these plant studies prompted the current research involving a more controlled environment to better define the observed D_{32}-J_g relationship and the notion of a creation bubble size (D_o).

The results of the testing appear in Figure 4.9 showing D_{32}, as well as the bubble surface area flux ($S_b=6\ J_g/D_{32}$), versus J_g. The fitted lines correspond to relationships of the form shown in Equation 4.4. A summary of the fitted parameters for both DowFroth 250 and MIBC appear in Tables 4.3 and 4.4. Here the parameter C in Equation 4.4 has been replaced by the parameter a. In fact, a will turn out to be the more general expression of the a_o parameter introduced in Equation 4.3 relating D_{32} to frother concentration.

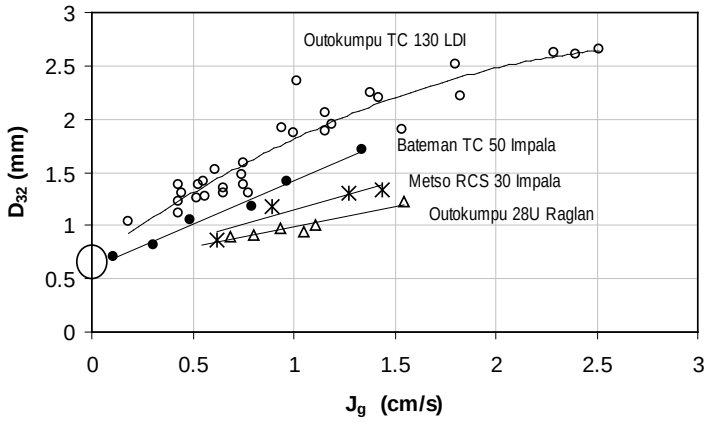

Figure 4.8 The D_{32}-J_g relationship for three plants and four cell manufacturers (Nesset et al, 2007). The circle on the ordinate axis indicates the notion of an intercept at J_g = 0 cm/s

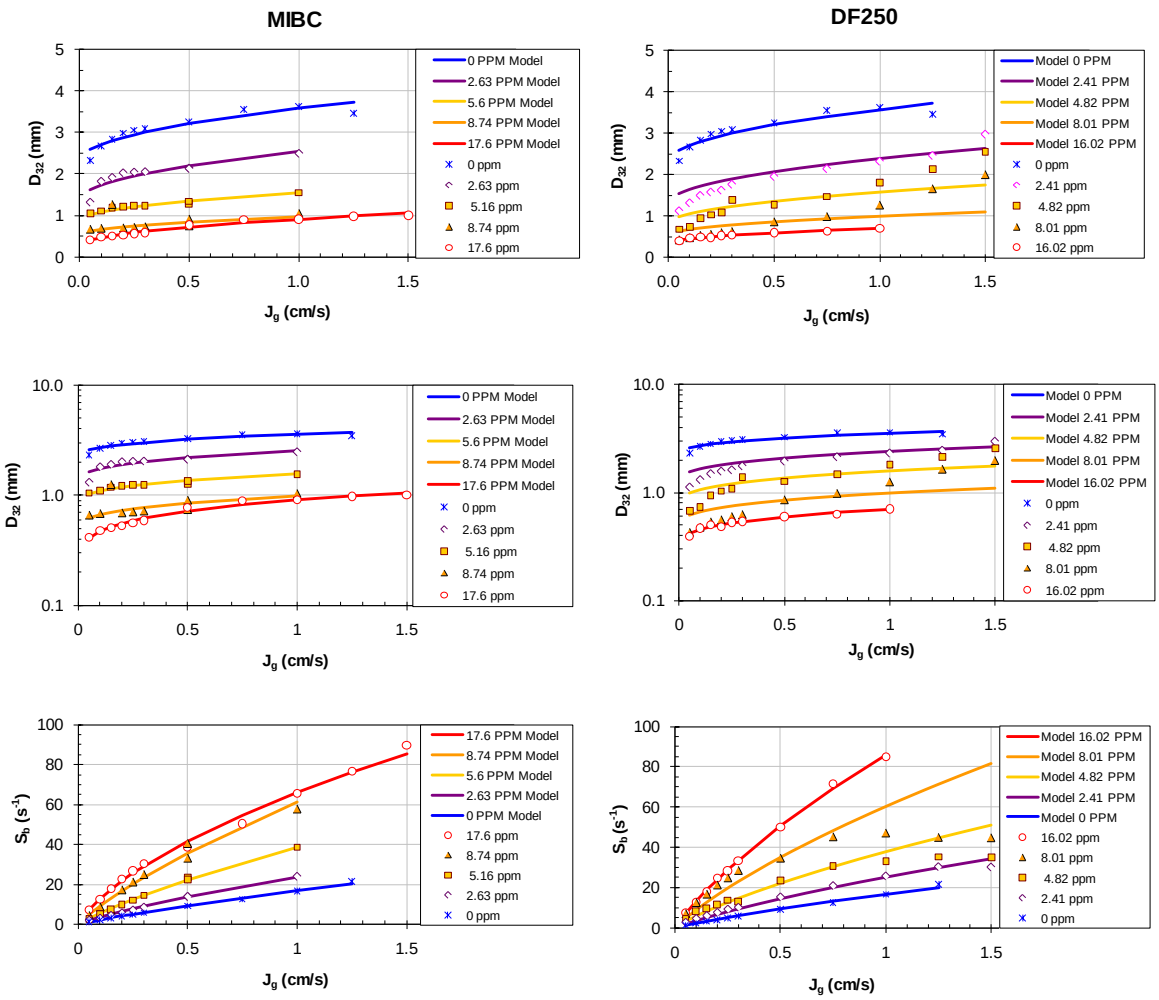

Figure 4.9 The D_{32}-J_g relationship (upper and middle plots) and D_{32}-S_b relationship (lower plots) for MIBC (left side) and DowFroth 250 (right side) established using the Metso cell for the air-water system. The fitted parameters used to establish the lines, plus measures of precision and fit, are found in Tables 4.3 and 4.4

The method used to fit curves (Equation 4.4) to the data was not simply one of allowing all three parameters to be simultaneously adjusted by a least-squares method. This was the first step which produced a range in values for n from 0.4 to 0.6. By then fixing n at successive values over this range and least-squares fitting the other two parameters, it was found that n = 0.5 minimized the error (discussion of why D_{32} is proportional to the square root of J_g will be explored in the Discussion chapter). It is evident from the upper plots in Figure 4.9 that D_o (the notional D_{32} at J_g = 0 cm/s) decreases with increasing frother addition and the question becomes “in what manner does D_o decrease”? There is a clue from the plots of Figure 4.1 showing that D_{32} decreases in an exponential fashion for J_g at 0.5 and 1 cm/s. This was also the case for D_{32} at J_g = 0.05 cm/s (i.e. very close to 0 cm/s, see Figure 5.1). It can therefore be argued that D_o will also follow the same exponential decay with increasing frother concentration. To simplify, the exponential relationship can be linearized by using the frother CCCX value rather than ppm (or ppm/CCC95) directly. Once the D_o

values at the limiting conditions of CCC0 and CCC99 have been established by least-squares fitting (with n = 0.5), the remaining $D_o|_{CCCX}$ values can be determined from:

$$D_o]_{CCCX} = D_o]_{CCC99} + (D_o]_{CCC0} - D_o]_{CCC99}) \cdot \left(1 - \frac{CCCX}{100}\right) \qquad 4.5$$

Values of $D_o|_{CCC0}$ and $D_o|_{CCC99}$ as determined from the data fitting are listed in Table 4.3 along with the values calculated from Equation 4.5. Once n and the D_o values were established, a was determined for each level of frother by a final least-squares regression of the data.

Table 4.3 Fitted parameters for the D_{32}-J_g relationship and measures of precision and fit for the plots shown in Figure 4.9

	Frother Addition Level in Cell				
DF250	**Min**	**Max**	**Intermediate Levels**		
PPM	0	16.02	2.41	4.82	8.01
CCCX at J_g = 0.5 cm/s	0	99	51	76	91
Fitted Parameters					
D_o (mm)	2.316	0.340	1.3081	0.8141	0.5177
a (mm)	0.126	0.036	0.108	0.0772	0.0478
n (exponent)	0.5	0.5	0.5	0.5	0.5
Precision					
R^2	0.864	0.968	0.813	0.688	0.595
R^2 Adjusted	0.797	0.949	0.733	0.501	0.352
Std Dev (± mm)	0.150	0.017	0.235	0.204	0.176
Rel Std Dev (%)	4.86	3.10	12.44	17.65	24.91
N	10	9	11	9	9
t statistic	2.262	2.306	2.201	2.306	2.306
95% CI (± mm)	0.339	0.039	0.518	0.472	0.407
MIBC	**Min**	**Max**	**Intermediate Levels**		
PPM	0	17.6	2.63	5.16	8.74
CCCX at J_g = 0.5 cm/s	0	99	47	71	88
Fitted Parameters					
D_o (mm)	2.316	0.267	1.3531	0.8615	0.5132
a (mm)	0.126	0.0640	0.1192	0.0696	0.0465
n (exponent)	0.5	0.5	0.5	0.5	0.5
Precision					
R^2	0.864	0.974	0.809	0.918	0.800
R^2 Adjusted	0.797	0.962	0.694	0.869	0.649
Std Dev (± mm)	0.150	0.036	0.138	0.041	0.060
Rel Std Dev (%)	4.86	5.15	6.92	3.32	7.76
N	10	11	9	9	8
t statistic	2.262	2.201	2.306	2.306	2.365
95% CI (± mm)	0.339	0.079	0.318	0.095	0.141

Figure 4.10 shows the D_o and a parameters versus frother ppm levels as determined by this method. There is close similarity between the parameter values for both frothers, and both follow a reasonable exponential decay as frother concentration is increased.

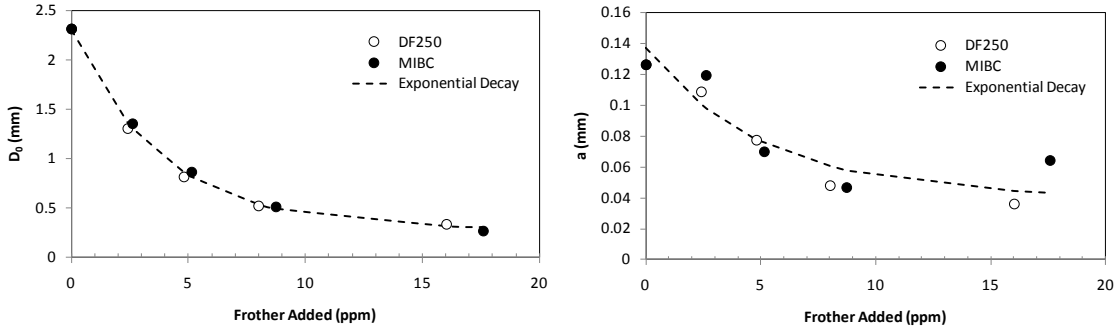

Figure 4.10 The D_o and a values determined for the data in Figure 4.9 and Table 4.3. The dashed line indicates that both parameters follow an exponential decay with increasing frother concentration

Table 4.3 also presents various measures of precision and goodness-of-fit for the data and fitted curves. For the *no frother* condition, the R^2_{Adj} is an acceptable 0.80. Overall, the MIBC and DowFroth 250 data have similar and good values of R^2_{Adj} for CCC99 (maximum concentration tested in order to establish the limiting bubble size) being 0.96 and 0.95 respectively. At the intermediate frother levels the MIBC data show a better fit than the DowFroth 250 having R^2_{Adj} values of 0.69, 0.87 and 0.65 for MIBC and 0.73, 0.50 and 0.35 respectively for DowFroth 250.The R^2_{Adj} are affected by poorer fits at low values of J_g, < 0.2 cm/s, particularly for DowFroth 250. There were also some suspect data points at the intermediate values of 4.82 and 8.01 ppm for DowFroth 250 that contributed significantly to the low R^2_{Adj}. Overall, In terms of the 95% confidence intervals for D_{32}, the *no frother* condition (largest bubbles) had limits of ±0.3 mm while the maximum frother condition at CCC99 (smallest bubbles) had limits of <±0.1 mm for both frothers. At the intermediate frother levels, MIBC had limits of ±0.1 - 0.3 mm compared to DowFroth 250 limits of ±0.4 - 0.5 mm. The data fits are acceptable for MIBC and less so for DowFroth 250, however, it needs to be pointed out that this analysis is for data covering a limited size range at each level of frother addition and is sensitive to small differences in measured bubble size. On the larger scale of D_{32} covering the entire range of frother concentration the fitting can be expected to be better. The following discussion on residual analysis will highlight this.

Residuals are defined as the difference between the actual data (y) and the model-predicted values ($\hat{y}$) from the fitted parameters listed in Table 4.3. These residuals can be used to provide an estimate of the precision and confidence limits for the entire data set, and therefore provide a better overall indication of the quality of the data fitting. Table 4.4 summarizes the residuals analysis and Figure 4.11 plots measured versus predicted values for D_{32} and S_b along with the 1:1 line indicating perfect prediction. The deviation from the 1:1 line on the y-axis represents the residual. The sum of squares of the residuals can be used to determine the residual standard deviation (=SUMSQ/[N-1])$^{0.5}$, and from this confidence

limits can be established. The R^2 is an indicator of how evenly the data is spread about the 1:1 line. Note that 4 outliers as indicated in Figure 4.11 were removed from the data analysis (but not the plots) on the basis of having Z values beyond the 99% confidence limit (Z value > 2.57); i.e. there is less than a 1% probability that we are wrong by excluding the data points.

Table 4.4 Residuals (y-ŷ) analysis for D_{32}-J_g and D_{32}-S_b data of Figure 4.9

	D_{32} Models				S_b Models			
Residuals (y-ŷ)	**DF250**	**MIBC**	**No Frother**	**All Data**	**DF250**	**MIBC**	**No Frother**	**All Data**
Sum Squared	1.139	0.203	0.202	1.545	359.96	99.97	2.828	462.76
N	38	37	10	85	38	37	10	85
Std Dev (± mm)	0.1755	0.0752	0.1499	0.1356	3.119	1.666	0.561	2.347
t statistic	2.03	2.03	2.262	1.99	2.03	2.03	2.262	1.99
95% CI (± mm)	0.356	0.153	0.339	0.270	6.33	3.38	1.27	4.67
R^2	0.928	0.982	1.000	0.975	0.970	0.994	0.993	0.985

It is evident from the plots and table that the MIBC, DowFroth 250, No Frother and All Data models provide good D_{32} and S_b predictions, all having R^2 values between 0.93 and 1.00. The 95% confidence intervals for MIBC, DowFroth, No Frother and All Data were ±0.15, ±0.36, ±0.34 and ±0.27 mm respectively. This compares well with the 95% confidence intervals reported in Table 4.1 for the All Data D_{32} versus $PPM/CCC95$ model of ±0.24 mm. Consistent with the data of Table 4.3, the MIBC fits are somewhat better than DowFroth 250. Comparable 95% confidence intervals (Table 4.4) for S_b are ±3.4, ±6.3, ±1.3 and ±4.7 s^{-1} respectively for MIBC, DowFroth, No Frother and All Data. Figure 4.11 shows that while the residuals for the D_{32} data (upper plots) are relatively consistent across the range, those for S_b increase for larger S_b (lower plots). The indicated 95% confidence limits and log plots are used to highlight this. The reason is that S_b is inversely dependent on D_{32}, so the poorer DowFroth 250 fit for small D_{32} will have an inversely large effect on S_b for the DowFroth data in the upper range. Overall, however, the fitted data parameters do provide a good prediction of D_{32} and S_b.

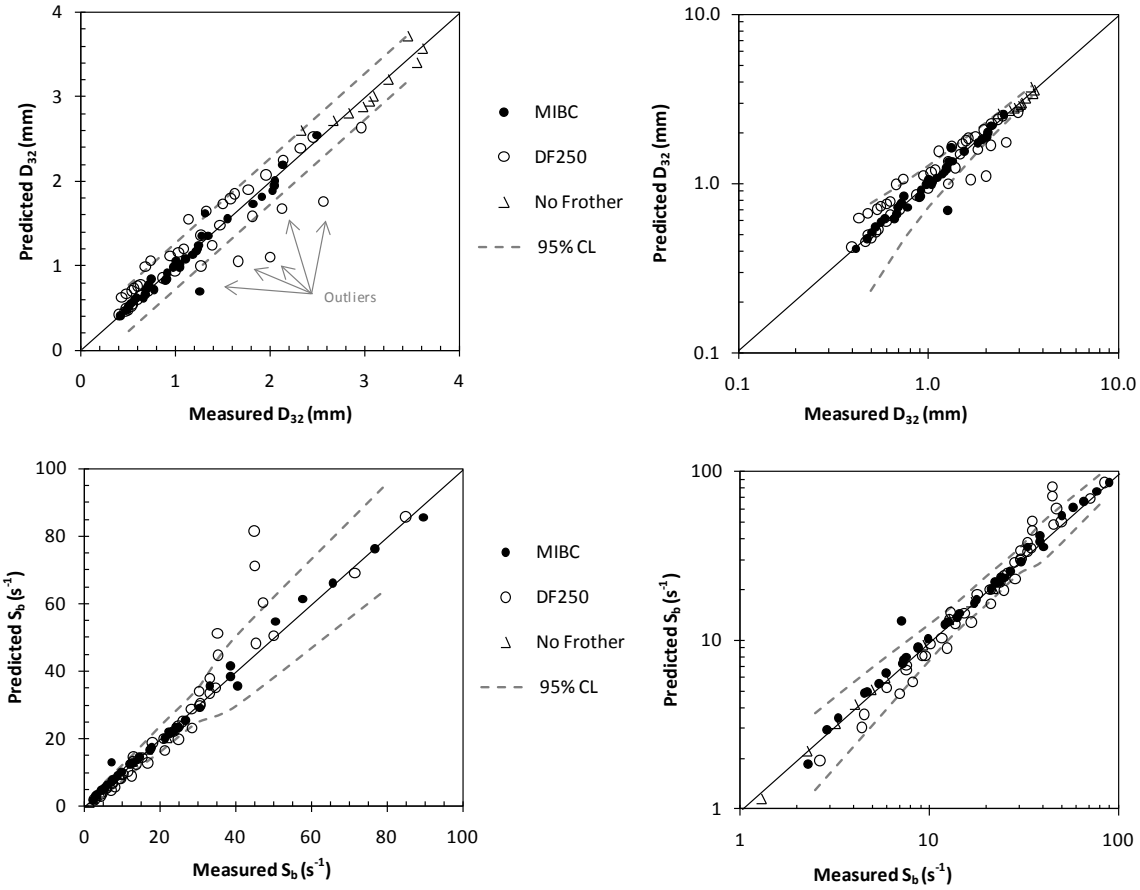

Figure 4.11 Measured versus predicted plots for D_{32} and S_b for the data of Table 4.3. The outliers were not included in the data analysis

The foregoing analysis has served to confirm the validity of a modified version of the previously introduced Equation 4.4 for determining D_{32} as a function of J_g, viz;;

$$D_{32} = D_o + a \cdot \left(100 \cdot J_g\right)^{0.5} \qquad 4.6$$

where D_o is as previously defined (the notional "creation" bubble size at J_g = 0 cm/s) and a is a parameter dependent on the frother concentration and the bubble generation method (in this case, forced-air mechanical flotation mechanism). The introduction of 100 in front of the J_g term is a means of avoiding the mathematical inconsistency which occurs during data fitting when J_g passes from less than a value of 1 to greater than 1. Mathematically at least, Equation 4.6 is applicable for J_g >0.01 cm/s. In the truest sense therefore, a is 10x the value indicated in Table 4.3 and Figure 4.10. Both D_o and a have been shown to behave in an exponentially decreasing manner with increasing frother addition, a feature which will be exploited in the subsequent chapter on model development.

4.3 Effect of Impeller Speed

Plant operators often consider the impeller rotational speed of the flotation machine as an adjustment that can be used to change the pumping rate of slurry, impact particle suspension and bubble-particle contact, or change bubble-size. It was therefore deemed an important variable for the study.

On the Metso unit, impeller rotational speed is controlled via the frequency setting (Hz) of the motor's silicon controlled rectifier (SCR) according to the relationship established in Figure 3.13 (motor *RPM= 29.7·Hz*), and Equation 3.1 that calculates the impeller tip speed (m/s) from the motor speed. The range of the SCR frequency on the unit was 30 to 80 Hz providing a range of impeller RPM from 313 to 834, equivalent to tip speed variation from 3.44 to 9.17 m/s. This 2.67x increase in rotational speed meant a net power increase of 19.7x was possible. This range extends well-beyond the typical industry range of 5 to 7 m/s, although impeller speeds up to 10 m/s have been reported for some applications, such as the South African platinum industry (Deglon et al, 2000, Forman, 2010).

The testing was done at 0, 2.5, 5 and 10 ppm DowFroth 250 at J_g levels of 0.5 and 1 cm/s. These concentrations represent CCCX levels of 0, 52, 77 and 95%. The range was selected so as to maintain reasonable sensitivity to bubble size change (i.e. avoiding very high levels of frother addition). At higher RPM, the water in the cell tended to heat more rapidly so care was taken to run these first and quickly to ensure minimum increase in water temperature, which typically was maintained in the range 18 to 22 ^{o}C, a sufficiently narrow range so no temperature correction was required.

Results of D_{32} versus impeller tip speed for all test conditions are shown in Figure 4.12 with 95% confidence limits indicated as established in the section on bubble size measurement in Chapter 3 (with frother ±3% CI, no frother ±5.5% CI; values from Table 3.2). Note that in some cases the confidence limit bars are of the same size or smaller than the data markers so are not very visible in the plots. Also indicated is the typical operating range for industrial flotation machines, as well as the lower operating limit of the Metso unit, below which air distribution in the cell deteriorated markedly. The most striking feature of the plots is the apparent uniformity of bubble size across the full range of frother addition and gas rates. The expanded scale (right hand plot of Figure 4.12) does suggest that for D_{32} above 1.5 mm there is a slight decrease in size with increasing impeller speed. The effect, however, is small and negligible across the range of 4.5 to 9 m/s (8x power increase). The representation of the full bubble size distributions (BSD) for the case of J_g = 0.5 cm/s at the four frother levels tested is shown in Figure 4.13, and serves to confirm that there is no appreciable change in the BSD, and therefore of D_{32}, across this wide range of impeller tip speed and power input.

Taking the given impeller diameter (Metso cell, 0.21 m) plus water viscosity and density at 20 ^{o}C, the impeller rotational speed (N) can be converted to an impeller Reynolds number ($N_{Re} = ND^2\rho/\mu_o$, the ratio of inertial to viscous forces). This is illustrated in Figure 4.14

showing that N_{Re} falls in the range 2.3 to 6.1 x 10^5, well into the turbulent range for impellers as illustrated in Figure 2.3. For Rushton-type (R-1) impellers, which would be similar to flotation impellers, the turbulent region occurs for N_{Re} >10^2 and the power number (N_P) becomes constant for N_{Re} >10^4. In the highly-turbulent range of N_{Re} > 10^5, as is the case here, net power becomes independent of fluid viscosity. Note that for the calculation of N_{Re}, the density of water alone has been used, not an adjusted density incorporating air content. If included, this would, at most, decrease the reported N_{Re} by ½ (at 50% air content) and the conclusions regarding highly turbulent conditions and constant N_P would remain the same.

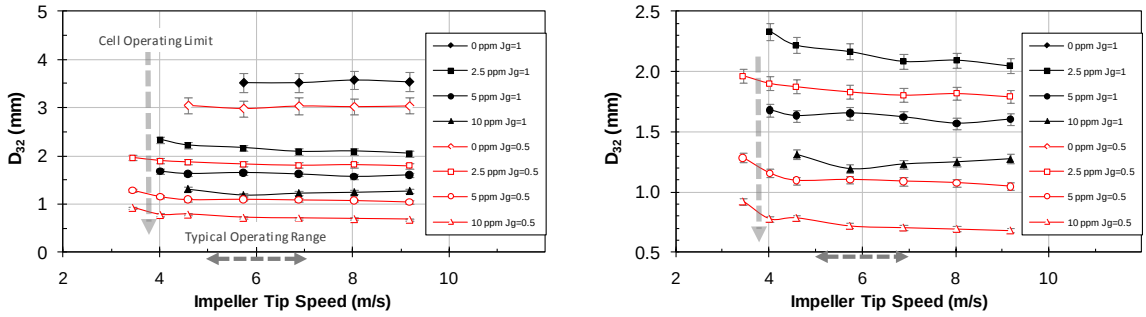

Figure 4.12 D_{32} versus impeller tip speed for four frother levels and J_g at 0.5 and 1 cm/s. The right hand plot shows an expanded D_{32} scale without the 0 ppm frother data (DowFroth 250, temperature 18 – 22 °C)

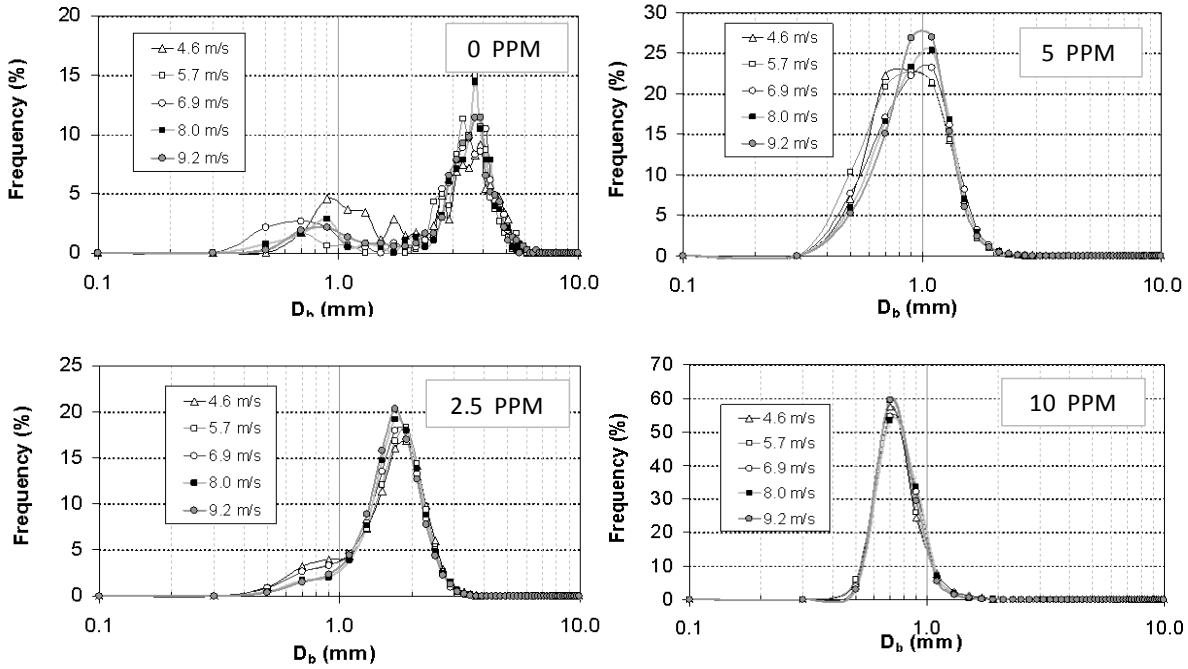

Figure 4.13 The BSD's for the J_g = 0.5 cm/s data shown in Figure 4.12. Note that impeller speed doubles from 4.6 to 9.2 m/s

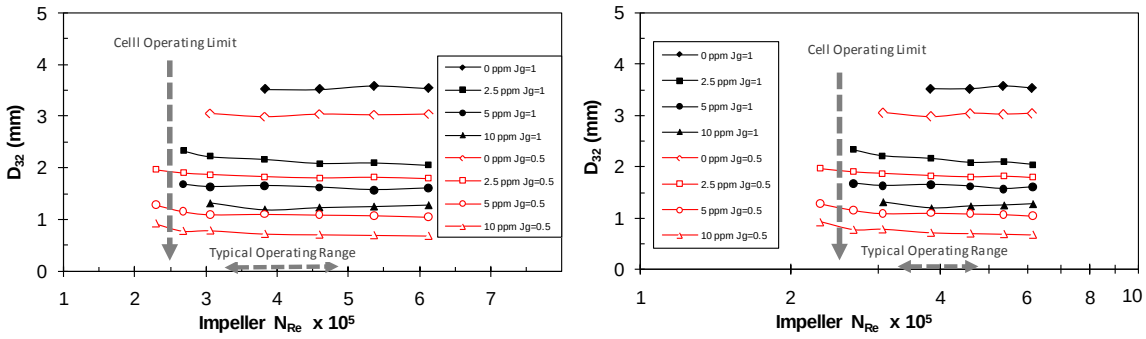

Figure 4.14 D_{32} versus impeller N_{Re} assuming liquid density = 1
(arithmetic scale on the left, logarithmic scale on the right)

In summary, it is evident that the conditions in the impeller region are highly turbulent and that bubble size and BSD are unaffected by significant changes in impeller speed (and resulting power input) within the full operating region of 4.6 to 9.2 m/s tip speed, corresponding to N_{Re} of 3.1 to 6.1 x 10^5. Below this, as the cell approaches its lower operating limit, at N_{Re} = 2.5 x 10^5 or impeller speed of 3.7 m/s, bubble size does begin to increase.

4.4 Effect of Viscosity (water temperature)

In operating flotation plants, the viscosity of the pulp can vary significantly as a result of changes in temperature, solids concentration and particle size. Consequently, the resulting impact on bubble size is of interest as many plants experience seasonal changes in water temperature (as much as Δ35 ^{o}C in Canadian plants), or particle size changes as ore hardness, mineralogy and throughput fluctuate. Testing for the effect of viscosity change is not straightforward, since it is not known if changing water temperature will impact the BSD in the same manner as, for example, a viscosity change due to smaller particle size or higher concentration of solids. The plan of work did not involve solids so the reference here to the effect of viscosity must be strictly that resulting from changes in water temperature.

Early experiments focused on finding a suitable additive to alter the water viscosity without impacting the other properties. Two materials were tried: sucrose (sugar) solution and polyacrylamide (PAC), a well-know thickening and flocculating agent. The sucrose proved to have some frothing properties and so was rejected on the basis it could impact bubble size apart from viscosity effects. The PAC seemed promising initially, having a wide range in viscosity possible (1 - 5 x 10^3 µPa-s), until at higher concentrations (0.15 wt% and above) its impact on the D_{32} proved to be inversely dependent on time and concentration. It is speculated that the long, cross-linked acrylamide chains were being broken apart by the high shear in the impeller region of the Denver cell where the initial testing occurred.

The decision was taken to vary water temperature in the Metso cell as a means of altering viscosity. Fortuitously, the testing period was in winter (March) and a test range of 3 to 40 ^{o}C was possible by varying proportions of cold and warmer water and by running the cell at the highest possible rpm to generate additional heating. A total of five test series were run to cover the full temperature range; four of them were judged to be successful. DowFroth 250 was added at 5 ppm (CCCX of 59%) at J_g = 1 cm/s and an impeller tip speed of 5.73 m/s (50 Hz). The CCCX was set at a level where changes to D_{32} would be evident. In all, a total of 32 tests were performed. The point could be argued that other properties of water that are temperature-dependent could be impacting the BSD, such as surface tension, density or contained enthalpy. These are plotted versus temperature, in Figure 4.15, as a function of their relative values at 20 ^{o}C. Also plotted is the measured D_{32} value relative to its value at 20 ^{o}C. The trends suggest that neither density nor surface tension contribute significantly to D_{32} changes since they remain virtually unchanged on a relative scale. Inverse enthalpy appears overly sensitive to temperature and could be a variable affecting viscosity through molecular excitation. The relative change in viscosity does seem to trend well with relative D_{32}. It is proposed that one can reasonably conclude that viscosity is the water property most closely correlated with D_{32} with changing temperature.

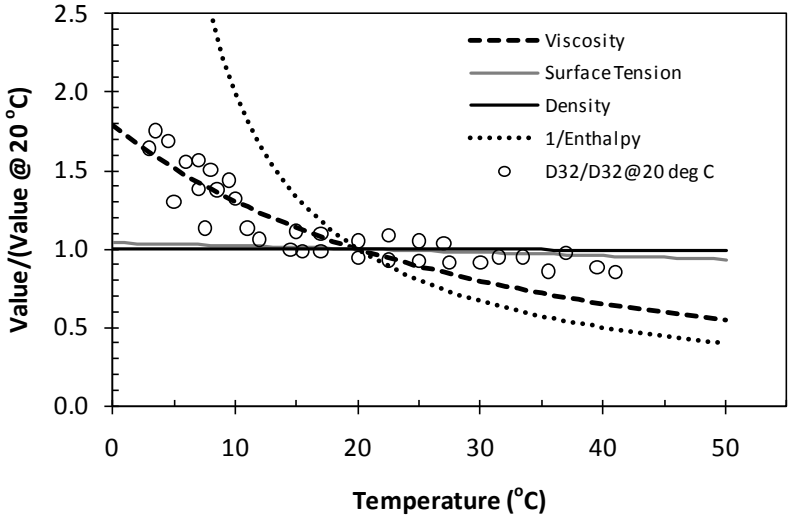

Figure 4.15 The relative values for water of density, surface tension, viscosity and inverse enthalpy to their values at 20 ^{o}C as a function of temperature. Also plotted are the measured relative D_{32} test data

Figure 4.16 presents dynamic viscosity, μ, versus temperature in absolute and relative measure (μ/μ_{20}) on the left and right ordinates respectively, along with a curve and equation fitted to standard reference data for viscosity versus temperature. D_{32} data were fitted to the relative viscosity term, μ/μ_{20}, by a simple power relationship which yielded;

$$D_{32} = 1.662 \cdot \left(\frac{\mu}{\mu_{20}}\right)^{0.776} \qquad 4.7$$

where

μ - the dynamic viscosity at the temperature of interest

μ_{20} - the dynamic viscosity at 20 ^{o}C (=1000 µPa-s)

and μ can be determined for temperature (T, ^{o}C) from (fitted from standard reference data):

$$\mu = 1774.8 - 55.458 \cdot T + 0.9779 \cdot T^2 - 0.0073 \cdot T^3 \qquad 4.8$$

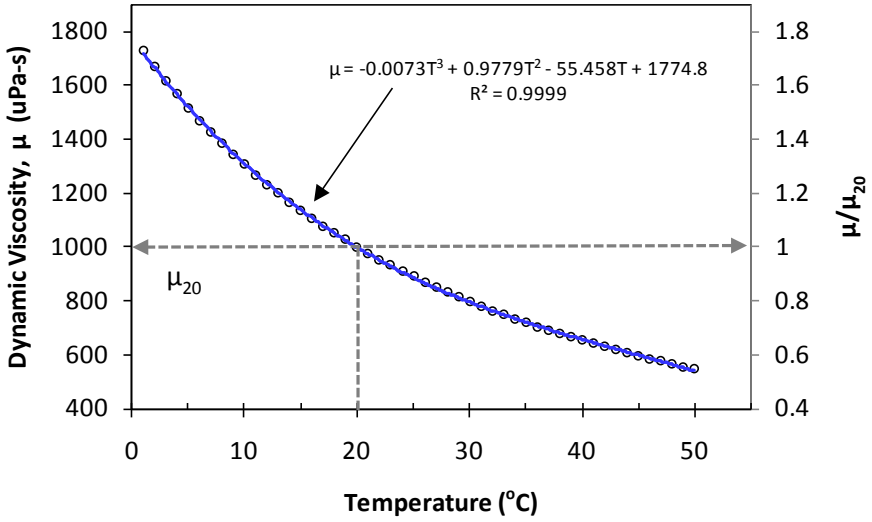

Figure 4.16 The relationship between temperature and dynamic viscosity, μ, in absolute measure (left ordinate) and relative measure to μ at 20 ^{o}C (right ordinate)

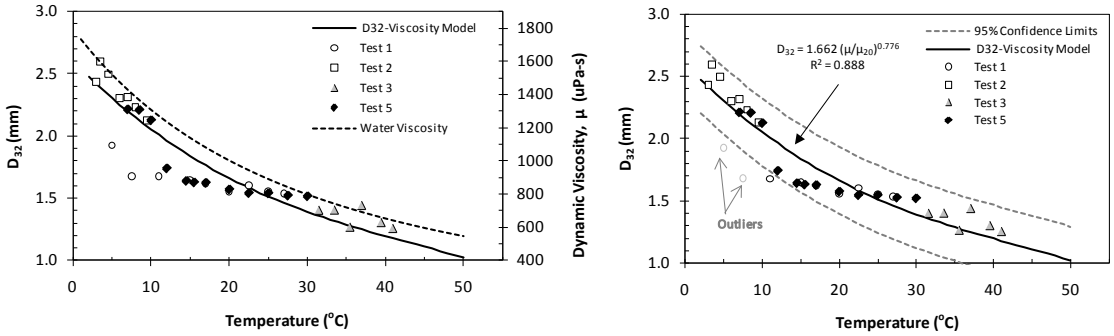

Figure 4.17 D_{32} versus temperature (left plot) and the corresponding best-fit equation. The same data and best-fit line showing the 95% confidence limits (right plot)

Table 4.5 indicates the measures of precision and goodness-of-fit for Equation 4.7. An R^2_{Adj} of 0.88 is acceptable for model-fitting; however the 95% confidence interval of ± 0.27 mm is higher than the precision for the other variables tested. The data and equation along with upper and lower 95% confidence limits are show in Figure 4.17. Overall, Equation 4.7 for D_{32} mirrors the viscosity change with temperature reasonably well, however the data does

flatten in the 10 to 20 ^{o}C range, contributing to the poorer overall precision of the data fit. Note that two data points well outside the 95% confidence limits were excluded from the data analysis. The effect of higher temperature on frother activity is not known and it could well be that some effectiveness is lost due to volatilization as temperatures climb into the 30's and above. The 1.662 mm value in Equation 4.7 represents the data-fit value for D_{32} at 20 ^{o}C. The viscosity-ratio term and exponent can be used in building the overall D_{32} model to account for viscosity effects on D_{32} at other than 20 ^{o}C conditions.

Table 4.5 Measures of precision and goodness-of-fit for D_{32}-viscosity model

Parameter	***Value***
Residual Sum of Squares	0.5428
N, data points	32
Std Dev (mm)	0.1323
t-statistic	2.039
95% Confidence Interval (± mm)	0.270
R^2	0.888
R^2 $_{Adjusted}$	0.880

4.5 Effect of Simulated Altitude (gas density)

The highest mines in the world operate at altitudes between four and five km above sea level; the Antamina Cu-Zn mine in Peru at 4.2 km and the Collahuasi Cu-Mo mine in Chile at 4.1 km being examples of large operations utilizing flotation. At these elevations the air density is approximately half that at sea level and the question has been raised as to the impact on flotation performance (Hales, 1998), specifically change in bubble size and its impact on mineral recovery. If significant, altitude would therefore become an important design variable, albeit not an operating one once equipment is in place. In order to *simulate the effect of altitude*, a low-density gas, in this case helium (density 0.1786 kg/m^3 at STP), mixed with air (density 1.293 kg/m^3) in different proportions to simulate different altitudes, was fed to the 5.5 Denver laboratory cell. As mentioned previously, the Metso cell was the preferred choice but, for reasons of cost and safety when using helium in a confined space, this small scale alternate was selected. The assumption being the type of gas used, in this case helium and air, will not affect the bubble creation process other than due to density. Others studying aerated bio-reactors at pressures from one to 20 atmospheres (0.1 to 2 MPa) have shown this assumption to be valid for a variety of gasses (Wilkinson and van Dierendonck, 1990). Keeping the J_g the same for the range of gas densities tested assures that density, and by extension simulated altitude, is the effect being tested for.

The experimental set-up is illustrated in Figures 3.6 to 3.8 with helium and airflow controlled independently via mass flow controllers. Two controllers were employed for different flow

ranges: 0-5 l/min (MKS Instruments Inc., Model #: 100B) and 0-30 l/min (MKS Instruments Inc., Model #: 1162B). Each was calibrated for both air and helium using a water displacement column, with collected gas volume corrected to STP (20 ^{o}C, 1 atm.) for temperature and pressure. An in-line static mixer (linked chain in a plastic tube), as shown in Figure 4.18, was used to ensure that both gasses were fully mixed prior to introduction to the cell. The average relationship between helium and air flow rates was then determined from these calibrations. This was required since the meters mass-controlled on the basis of air (or nitrogen) even though helium was being added through one of the meters. The final relationship determined for the meters was:

$$Volumetric\ Flow\ Rate\ \frac{He}{Air} = 1.4973\ \pm 0.0473 \qquad 4.9$$

Test conditions were 5 ppm DowFroth 250, equivalent to a CCCX of approximately 79%, and an impeller speed of 1600 RPM, equivalent to a tip speed 5.86 m/s. Water level in the cell was kept constant by recirculation of overflow via a peristaltic pump. Water temperature remained constant at about 18-22 ^{o}C. Consistency of bubble size measurement was an issue with the Denver cell, particularly with respect to J_g at values above 0.5 cm/s.

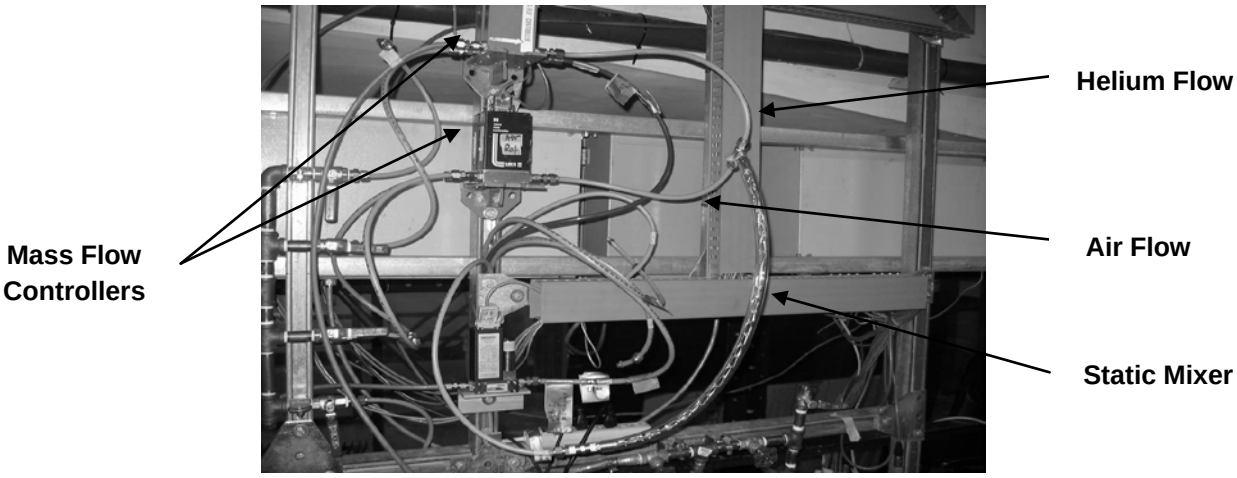

Figure 4.18 The mass flow controllers and static mixer (linked chain in tube) set-up for combining air and helium flows prior to feeding the Denver flotation machine (not in picture)

This is evident from Figure 4.19, showing variability of D_{32} and D_{10} data above 1 cm/s. It was later confirmed that the impeller was quite worn thus contributing to poor gas dispersion/distribution and variability of results at higher gas rates. Consequently, meaningful results were only obtained for values of J_g, below 1 cm/s. It is evident from Figure 4.19 that D_{32} for 100% helium is consistently larger than for 100% air for the "acceptable range" of J_g. For $J_g \leq 1$ cm/s, D_{32} and D_{10} for helium averaged 16.3% and 11.2% larger than for air. This difference is significant at greater than 99% Confidence Level (paired t-test).

Also indicated in Figure 4.19 is the J_g data range that was selected for comparison of gas density effects on bubble size, viz; 0.25 and 0.3 cm/s. For this range of J_g the relationships were consistent and a clear response was obtained. Two tests were performed at each J_g level and for 6 gas density combinations of air and helium, representing 0, 20, 40, 60, 80

and 100 % mixtures (volumetric flow rate). Table 4.6 lists the air-helium mixtures, and the corresponding gas density and equivalent altitude (km above sea level) based on density. The indicated region of interest is an air-helium ratio of 40:60 and greater, representing altitudes from sea level to 5.5 km.

Table 4.6 The range of air-helium mixtures and corresponding gas density and altitude above sea level (dry gas assumed). The shaded values in the table were the mixtures tested (* kilometers over sea level)

	Gas Ratio (%)		Density of Mixture (STP) (kg/m^3)	Equivalent Altitude (km.o.s.l.)*
	Air	***Helium***		
Region of Interest	100	0	1.293	0
	90	10	1.182	0.68
	80	20	1.070	1.43
	70	30	0.959	2.26
	60	40	0.847	3.19
	50	50	0.736	4.25
	40	60	0.624	5.49
	30	70	0.513	6.97
	20	80	0.401	8.82
	10	90	0.290	11.27
	0	100	0.179	14.93

Results are presented in Figure 4.20 (upper plot) and indicate an increase in D_{32} and D_{10} with decreasing density. The data presented in Figure 4.20, showing D_{32} versus gas density (ρ_g, air-helium mixture) relative to 100% air (ρ_o, at STP, 20 ^{o}C, 1 atm), were fitted to a power relationship yielding the result:

$$D_{32} = 1.06 \cdot \left(\frac{\rho_o}{\rho_g}\right)^{0.132} \qquad 4.10$$

Note that the data for 100% helium were excluded from the data fit to simplify the model and realizing that this density is well outside any region of practical interest, corresponding to a simulated elevation in excess of 10 km.

Of note in this relationship is the relatively weak dependency of D_{32} on the gas density ratio, exponent 0.132, corresponding to a 10% increase in D_{32} at simulated 5 km elevation, the maximum elevation of practical interest, relative to sea-level. The bottom plot of Figure 4.20 shows the (same) D_{32} data and model with equivalent altitude plotted on the main axis. The relationship of D_{32} versus altitude then becomes linear, corresponding to a +2% increase in D_{32} per km of altitude increase. The inverse of this, a 2% decrease/km, would be the case for the change in S_b ($=6J_g/D_{32}$) with altitude, yielding a practical maximum of 10% decrease in S_b at 5 km (simulated) altitude relative to sea level.

The question comes to mind as to the effect of lower density gas not only on D_{32}, but on the bubble size distribution itself. One method for assessing changes to the BSD is to examine D_{32} versus D_{10}. Data will group in different locations on such a plot if their BSD's are

different. Figure 4.21 shows the relationship for the data presented in Figures 4.19 and 4.20 for the case of 100% air and 100% helium only (in order to highlight any difference). Data beyond a J_g of 1 cm/s has not been plotted (but had no effect on the conclusion). It is evident that the data fall on top of each other indicating no measurable difference in the BSD as gas density changes. The data points move away from the 1:1 line (indicative of a mono-sized distribution) as J_g is increased, which is the expected trend (i.e. the distribution becomes wider). Since D_{32} and D_{10} are larger for helium than for air, the BSD is slightly broader but fall on the same trend line as for air alone.

The parameters describing the precision and goodness-of-fit for the model and data of Equation 4.10 are presented in Table 4.7. Note that the data are for J_g of 0.25 – 0.3 cm/s, however the density ratio and exponent term correction should be applicable for the full range of D_{32}. The model is judged a very good fit having an R^2_{Adj} of 0.835 and 95% confidence interval of ± 0.055 mm representing a relative standard deviation of only ± 2.3%. Recall that data for 100% helium were not included in the data-fitting analysis, being well outside the region of interest, so the limit of applicability for Equation 4.10 is for density ratios of 1 to 0.25, well beyond the practical range of interest for the simulated effect of elevation.

This completes the presentation of results and preliminary analysis and discussion that will be used to develop the overall prediction model for D_{32} in the following chapter.

Table 4.7 Precision and goodness-of-fit parameters for the D_{32}-gas density model presented in Figure 4.20 and Equation 4.10

Parameter	***Value***
Residual Sum of Squares	0.01247
N, data points	19
Std Dev (mm)	0.0263
Relative Std Dev (%)	2.31
t-statistic	2.101
R^2	0.853
$R^2_{Adjusted}$	0.835
95% Confidence Interval (± mm)	0.055

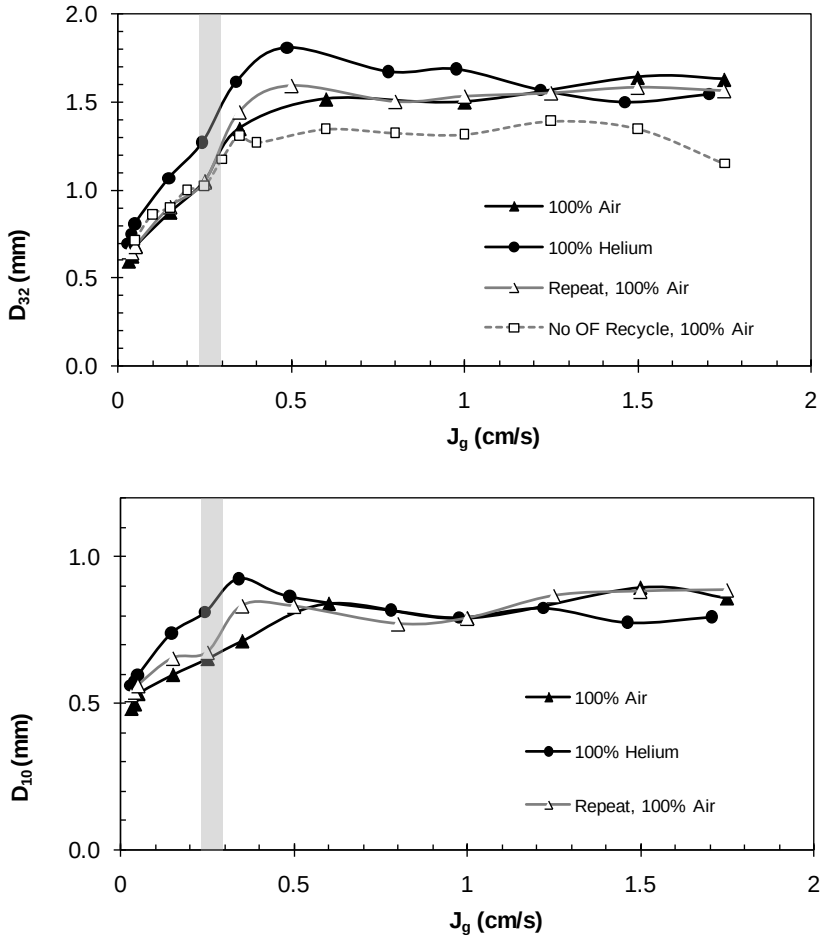

Figure 4.19 D_{32} (upper plot) and D_{10} (lower plot) versus J_g for initial tests on Denver cell comparing air and helium as well as repeatability of testing. Shaded area represents the J_g range (0.25 and 0.3 cm/s) selected for detailed comparison of gas density effect

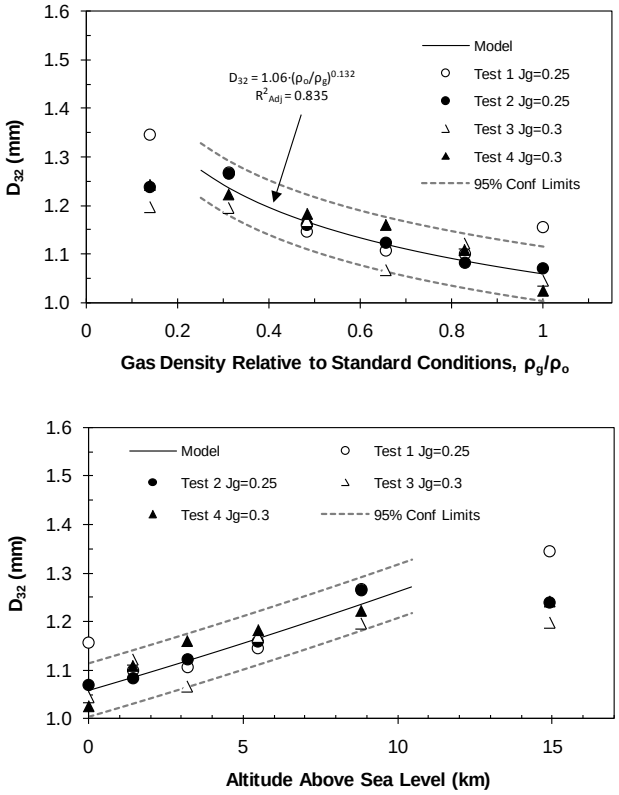

Figure 4.20 D_{32} as a function of gas density ratio, ρ_g/ρ_o (upper plot), and simulated altitude above sea level (lower plot) (5 ppm DowFroth 250, J_g = 0.25 - 0.3 cm/s)

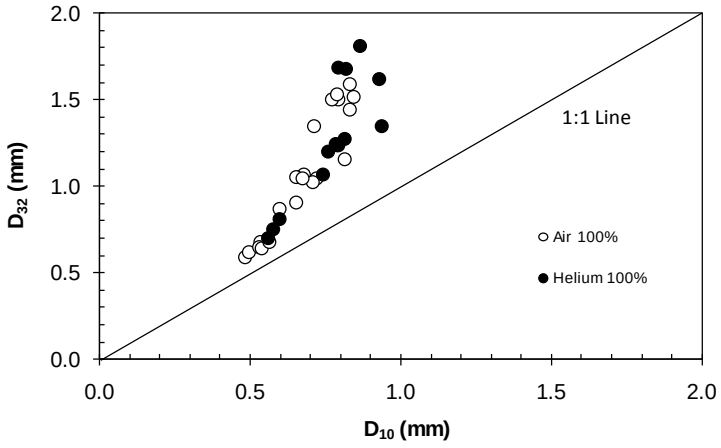

Figure 4.21 D_{32} versus D_{10} showing similar BSD's for both 100% air and 100% helium for the data of Figures 4.19 and 4.20 having J_g up to 1 cm/s. The 1:1 line indicates a population of mono-sized bubbles

CHAPTER 5: Building the Bubble Size Model

The development of a single expression for predicting D_{32} from key variables is the main objective of the thesis. To do so, requires that the individual relationships developed in Chapter 4 be combined in a manner that will permit compatibility between the individual relationships developed in terms of calculating D_{32}.

5.1 The Individual D_{32} Relationships

The following relationships were developed in Chapter 4:

Frother concentration and type

Re-stating Equation 4.3;

$$D_{32} = d_l + a_o \cdot exp\left[-b \cdot \frac{ppm}{CCC95}\right] \quad 5.1$$

where

- d_l (mm) is the limiting bubble size as frother ppm $\rightarrow \infty$
- a_o (mm) is a constant at 0 ppm frother
- b is the exponential decay constant
- $ppm/CCC95$ is the frother concentration (ppm) normalized by the specified frother CCC95 value (ppm) which is dependent on J_g

Superficial gas velocity (J_g)

Re-stating Equation 4.6;

$$D_{32} = D_o + a \cdot \left(100 \cdot J_g\right)^{0.5} \quad 5.2$$

where

- D_o (mm) is the bubble size at J_g = 0 cm/s (notional “creation size”)
- a is a constant (mm/10)/(cm/s)$^{0.5}$
- J_g (cm/s) is the superficial gas velocity

Impeller speed (power)

The analysis in Section 4.3 showed that, for practical purposes, within the range of impeller tip speed, 4.6 to 9.2 m/s, there was no effect on D_{32} measured in the quiescent zone beneath the froth (the reference plane of interest for gas dispersion measurements). No term will therefore be required to reflect power or impeller speed in the D_{32} equation.

Liquid viscosity (temperature effect)

Re-stating Equation 4.7 In terms of proportionality;

$$D_{32} \propto \left(\frac{\mu}{\mu_{20}}\right)^{0.776} \quad 5.3$$

where

- μ (Pa-s) is dynamic viscosity (of water in the test case) at the temperature of interest
- μ_{20} is the dynamic viscosity of water at 20 ^{o}C (STP)

Altitude (gas density)

Re-stating Equation 4.10 in terms of proportionality;

$$D_{32} \propto \left(\frac{\rho_o}{\rho_g}\right)^{0.132} \quad 5.4$$

where

- ρ_o (kg/m^3) is density of dry air at 20 ^{o}C and 1 atmosphere (STP)
- ρ_g is the density of gas/air at the conditions of temperature and pressure of interest

5.2 Assembling the D_{32} Equation

The four individual relationships cited above need to be incorporated into one expression. Those for viscosity (Equation 5.3) and altitude (Equation 5.4) are readily handled by factors that are proportional to these expressions since they are in dimensionless form. The product of these factors is multiplied by a function, φ, incorporating the J_g, ppm and $CCC95$ variables according to the expression:

$$D_{32} = f_v \cdot f_d \cdot \varphi\left[J_g, \frac{ppm}{CCC95}\right] \quad 5.5$$

where f_v and f_d are factors given by Equations 5.3 and 5.4.

To establish φ, use is made of Equation 5.1 to establish a general relationship:

$$D_{32} = d_l + a_o \cdot \exp[-b \cdot \frac{ppm}{CCC95}] \quad 5.6$$

Since this expression is valid for a unique value of J_g, the "constants" d_l and a_o need to be expressed in terms of their relationship to J_g in order to make the expression a general one. This can be done by considering the two limiting cases; the maximum D_{32} at frother concentration 0 ppm, and the smallest or limiting D_{32} at frother concentration CCC,

approximated by CCC99 for practical purposes. The limiting bubble size (i.e. at the CCC99 value), d_l, is the limiting case for Equation 5.2 expressed as;

$$d_l = D_{ol} + a_l \cdot \left(100 \cdot J_g\right)^{0.5} \quad 5.7$$

where D_{ol} is the D_o (i.e. for J_g = 0 cm/s) and a_l the value of a , both at the limiting case of CCC99.

In order to define a_o, a second relationship can be established for the maximum bubble size case of 0 ppm frother. Equating D_{32} for Equations 5.1 and 5.2 at this condition (i.e. 0 ppm) the exponential term becomes unity, hence:

$$d_l + a_o = D_{o\,max} + a_{max} \cdot \left(100 \cdot J_g\right)^{0.5} \quad 5.8$$

Re-arranging, results in an expression for a_o;

$$a_o = D_{o\,max} + a_{max} \cdot \left(100 \cdot J_g\right)^{0.5} - d_l \quad 5.9$$

These expressions for d_l (Equation 5.7) and a_o (Equation 5.9) describe their relationship to J_g and can be inserted into Equation 5.6 to obtain an overall expression for D_{32} as a function of J_g, ppm and $CCC95$. After re-arranging and gathering of terms one obtains:

$$\varphi = D_{o\,l} + a_l \cdot (100 \cdot J_g)^{0.5} + \left[(D_{o\,max} - D_{o\,l}) + (a_{max} - a_l) \cdot \left(100 \cdot J_g\right)^{0.5}\right] \cdot exp\left[-b \cdot \frac{ppm}{CCC95}\right] \quad 5.10$$

This is the equation for D_{32} without the corrections for altitude and viscosity. Note that the first two terms reflect the limiting case of minimum bubble size reached at the CCC. The first part of the third term (in square brackets) corresponds to the maximum bubble size at 0 ppm frother (when added to the first two terms). The exponential term is the driving function that accounts for the effect of frother between these two limiting cases. (Note that the exponential acts only on the “0 ppm” (square brackets) term)

The D and a constants in Equation 5.10 are determined from plots of D_{32} versus J_g for CCC0 and CCC99 frother concentration, such as Figure 4.9, and are the same for all frothers if one assumes the limiting bubble size remains the same for all frothers (a simplification for the moment to aid in the derivation). Figure 4.4 suggests that there may be some effect of frother type on the limiting D_{32} and this will subsequently be incorporated as a factor that may be added.

Equations 5.5 and 5.10 form the basis for the overall D_{32} model. Two additional factors require resolution; establishing the CCC95, and incorporating the possibility of different limiting bubble size for different frothers.

CCC95 as a function of superficial gas velocity, J_g

As described in Section 4.1, and summarized in Table 4.1, each frother exhibited a unique value for CCC95, one that also appears dependent on J_g. A relationship linking the two, and that could be incorporated into Equation 5.10, was sought. The DowFroth 250 data obtained from the D_{32} versus J_g tests for various frother concentrations (Section 4.2) was re-plotted as D_{32} versus frother concentration (ppm) and fitted to exponential decay curves (Equation 4.1) in order to extract CCC95 values. The results, showing CCC95 versus J_g for DowFroth 250, are plotted in Figures 5.1 and 5.2. The relationship proved a good linear fit, R^2_{Adj} = 0.903, having a standard deviation for CCC95 of ± 0.92 ppm and 95% confidence limits of ± 2.08 ppm.

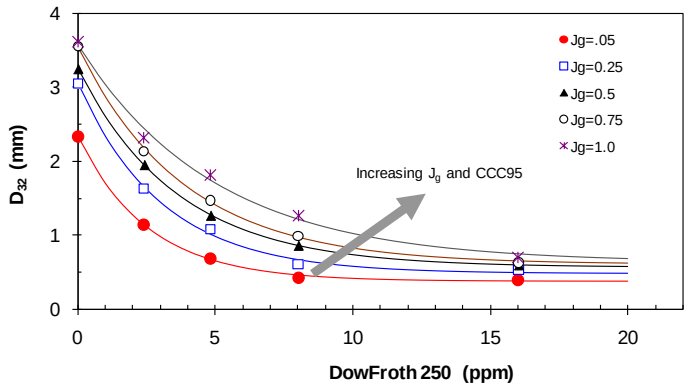

Figure 5.1 D_{32} versus ppm of DowFroth for increasing J_g. Fitted curves (Equation 4.1) were used to determine the CCC95 values shown in Figure 5.2

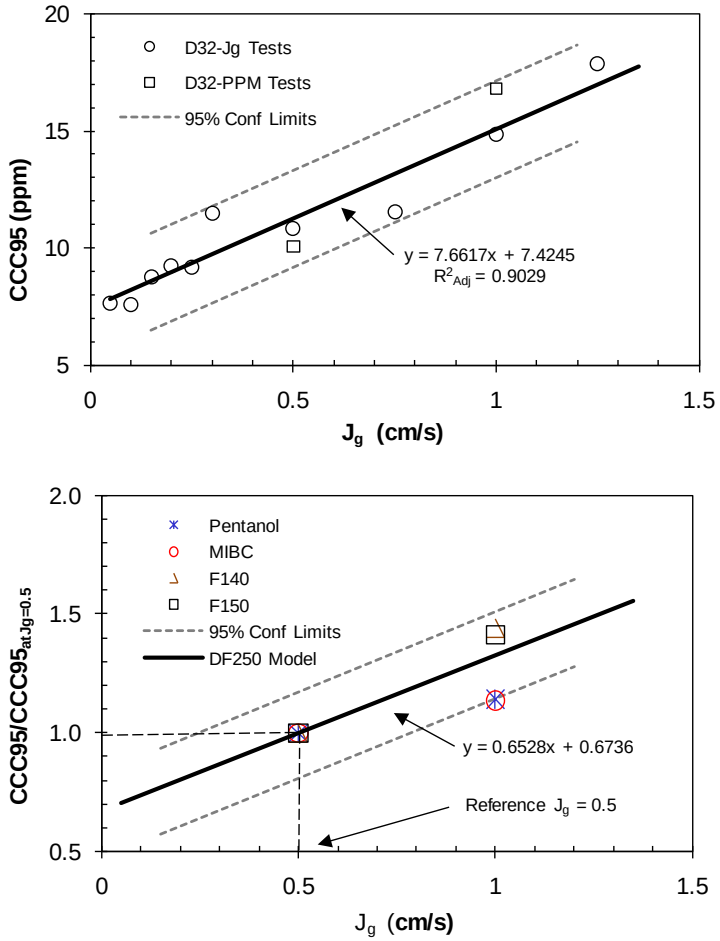

Figure 5.2 CCC95 versus J_g for DowFroth 250 (upper plot). Comparison with other frothers for CCC95 normalized by CCC95 at J_g = 0.5 cm/s (lower plot)

In order to incorporate J_g into the CCC95 relationship, values were normalized by dividing CCC95 values by CCC95 at J_g = 0.5 cm/s as shown in the bottom plot of Figure 5.2. This yielded the linear relationship:

$$CCC95 = CCC95_{Jg=0.5} \cdot \left(0.6736 + 0.6528 \cdot J_g\right) \qquad 5.11$$

The metric for frother type therefore becomes its CCC95 *measured at a standard J_g of 0.5 cm/s*. Once established, this value can be used to calculate CCC95 for any J_g using Equation 5.11 and inserting the resulting CCC95 into Equation 5.10. It is possible that different J_g – CCC95/CCC95$_{Jg=0.5}$ relationships exists for different frother types. The values for Pentanol, MIBC, F140 and F150 from Table 4.1 are also plotted in Figure 5.2 (bottom) and all fall within the 95% confidence limits for the DowFroth 230 equation. However, it is noted that Pentanol and MBC data (the alcohols) fall together right on the lower confidence limit boundary, and so a “weaker” relationship may exist for these alcohols over the polyglycols (and blends such as F140) tested.

The limiting D_{32} as a function of CCC95

The initial impression was that the limiting D_{32} bubble size was similar among frother types tested, and primarily governed by the J_g value as illustrated in Figure 5.1. The overall D_{32} model accounts for this effect of J_g. However, the excellent linear correlations shown in Figure 4.4 of $D_{limiting}$ versus $CCC95_{Jg=0.5}$ and $CCC95_{Jg=1}$ are sufficiently compelling to include in the overall model the option of a frother-type dependency on the limiting bubble size. Again, using the DowFroth 250 $CCC95_{Jg=0.5}$ (=10.06 ppm) as the base-case metric, and taking the slope of the $D_{limiting}$ versus $CCC95_{Jg=0.5}$ line equal to 0.0176 mm/ppm from Figure 4.4, the following factor, f_l, can be developed:

$$f_l = 0.0176 \cdot \left(10.06 - CCC95_{Jg=0.5\ cm/s}\right) \qquad 5.12$$

This limiting bubble size factor, f_l, represents the increase or decrease in limiting D_{32} that can be added to $D_{o\,l}$ in Equation 5.10 for frothers other than DowFroth 250, the base case. The adjustments are not large, typically less than ±0.1 mm, except in the case of Pentanol with a significantly higher value of CCC95 (30.47 ppm at J_g = 0.5 cm/s). The CCC95 values for Pentanol are not as precise since the D_{32} versus PPM curves had not fully reached limiting values (Figure 4.1). The f_l factor should therefore be used with caution for the case of Pentanol.

Selection of numerical values for the equation constants

In order to finalize the overall D_{32} equation, numerical values need to be assigned for the constants in Equation 5.10. These are taken from Table 4.2 for the rate constant in the exponential decay expression, and Table 4.3 for the maximum and minimum limiting conditions at CCC0 (0 ppm) and CCC99 (i.e. the CCC). One issue is the large difference between the limiting D_{32} values for MIBC and DowFroth 250 at high frother addition (16 ppm DowFroth 250 and 17.6 ppm MIBC) as seen in Figure 5.3. This difference seemed at odds with other tests showing fairly close limiting values. Additional data at high frother concentration were sought to help clarify the issue, and are also plotted in Figure 5.3. These additional data points for both MIBC and DowFroth 250 (from their D_{32} versus frother concentration tests) suggest that the MIBC values are correct ones since they agree with the previous data while the DowFroth 250 tests are significantly different from the previous values. Although not the ideal choice, the MIBC data were selected for the final model constants presented in Table 5.1since the DowFroth 250 values were judged to be uncertain.

The expression of Equation 5.10 with numerical values in-place then becomes;

$$\varphi = 0.267 + f_l + 0.064 \cdot (100 \cdot J_g)^{0.5} + \left[2.316 - (f_l + 0.267) + 0.0619 \cdot \left(100 \cdot J_g\right)^{0.5}\right] \cdot exp\left[-3.09 \cdot \frac{ppm}{CCC95}\right] \qquad 5.13$$

where $CCC95$ and f_l are determined from Equations 5.11 and 5.12 respectively.

The overall model for D_{32} has therefore been reduced to a single expression with the following input variables required:

Air rate - superficial gas velocity, J_g

Frother concentration – ppm in solution

Frother type – $CCC95$ at J_g = 0.5 cm/s, and f_1

Viscosity – viscosity relative to viscosity of water at 20 ^oC, f_v

Altitude – air density relative to density at 20 ^oC and 1 atmosphere pressure, f_d

The three factors, f_1, f_v and f_d can be included as required. Their default values are 0, 1 and 1 respectively.

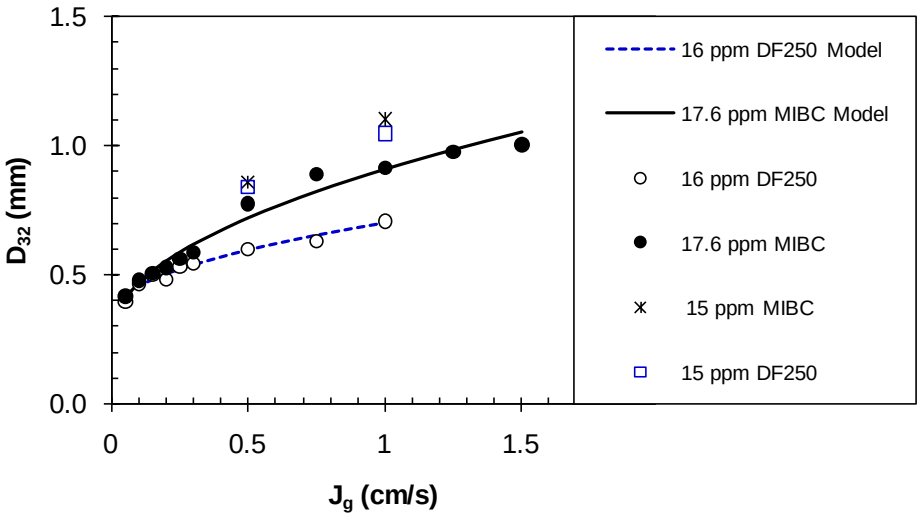

Figure 5.3 D_{32} versus J_g for MIBC and DowFroth 250 for the case of frother concentration at high CCCX levels, i.e. the D_{32} limiting condition. Model fits and data are the same as in Figure 4.9 and Table 4.3

Table 5.1 The numerical values for the constants in Equation 5.10; the overall D_{32} model

	Constant in Equation 5.10				
	$D_{o\,max}$	$D_{o\,lim}$	a_{max}	a_{lim}	b
Value	2.3158	0.2674	0.1260	0.0640	3.09

In the next section the overall model will be compared to the measured values used in its development, while in Chapter 6 the model predictions will be validated by comparing with plan data as well as exploring its predictive capabilities.

5.3 Model Prediction, Precision and Goodness-of-fit

One test of the overall model is to compare the measured values for all data sets used in its development, to the model predictions. Eight data sets for a total of 215 points were compared. The few outliers (noted in earlier sections) were not included. The data sets were DowFroth 250 and MIBC (ppm and J_g versus D_{32} tests), F140, F150, Pentanol, "zero frother", viscosity/temperature and altitude/density.

Using the $CCC95$- J_g relationship established for DowFroth 250 (Equation 5.11, Figure 5.2) for all frothers resulted in a poor data-fit for MIBC. This was corrected by providing MIBC with its own $CCC95$- J_g relationship determined from the data in the same figure. This relationship was also applied to Pentanol, the other alcohol-based frother in the group, since it had virtually the same slope as MIBC for $CCC95$ versus J_g (Figure 5.2). The "new" relationship for these two frothers to be used in place of Equation 5.11 therefore becomes:

$$CCC95 = CCC95_{Jg=0.5} \cdot \left(0.8639 + 0.2723 \cdot J_g\right) \qquad 5.14$$

The comparison between measured D_{32} and model predicted for each of the eight data sets is shown in Figure 5.4. In general, the comparisons are good across the full range, with some tendency to under-predict for Pentanol at higher D_{32} values. The altitude/density data, produced on the laboratory Denver machine, exhibited a bias (i.e. an "offset") which was corrected by increasing J_g by 13% when entering the data into the model. Some adjustment was expected since J_g on the Denver cell was calculated (gas flow rate/cell area) thus giving an overall average J_g, while the values from the Metso cell were from a single location and likely were higher than the average J_g (as noted previously).

The comparison of measured versus model prediction for the full data set (215 values) is shown in Figure 5.5 (upper plot) with the middle plot showing the same data with Pentanol removed. It is suggested Pentanol data has more variability since D_{32} did not reach its limiting value during the testing, and the initial D_{32} at 0 ppm was higher than for the other frothers that had been tested earlier. The precision and goodness-of-fit parameters were generated by *residuals analysis* (measured minus model prediction) and are presented in Table 5.2 and the bottom plot of Figure 5.5.

The precision of the model predictions had a standard deviation of ± 0.16 mm for the full data set (without Pentanol) yielding 95% confidence limits of ± 0.3 mm. The residuals analysis shown in Figure 5.5 (bottom plot) indicates that the error was uniformly distributed across the range of D_{32}. Table 5.2 indicates that, individually, DowFroth had a somewhat better fit (95% CI of ± 0.28 mm) than the average, while Pentanol was the poorest (95% CI of ±0.81 mm), likely the result of the reasons already noted. The viscosity/temperature and altitude/density data were surprisingly good considering the relative simplicity of their power models. The R^2 measure is an indication of the sample distribution about the 1:1 line, and at 0.956 it shows that data are normally distributed.

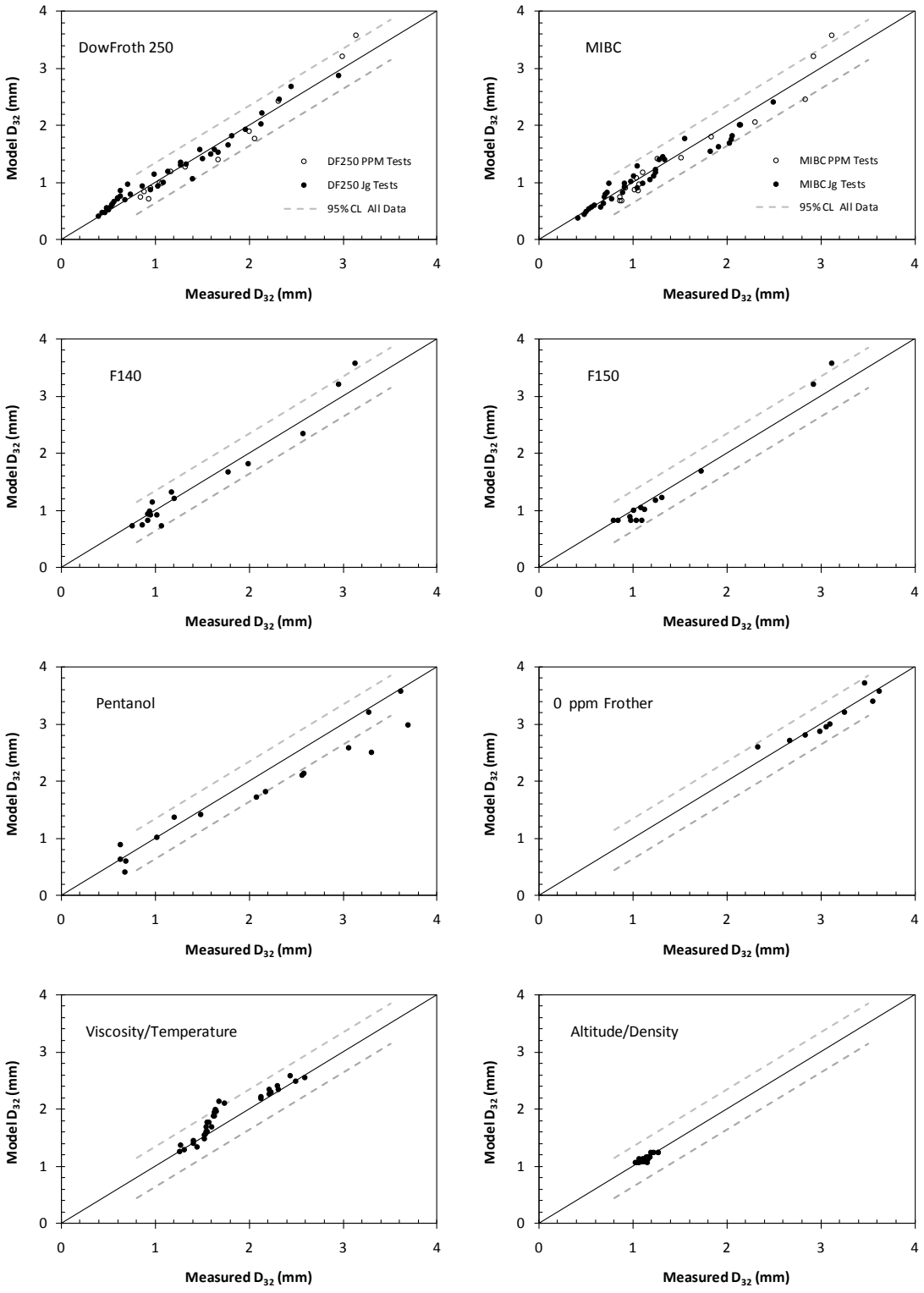

Figure 5.4 Measured versus modeled D_{32} for the individual data sets: five frother types, 0 ppm frother, viscosity/temperature and altitude/density. The residual 95% Confidence Limit lines are for the full (215) data set

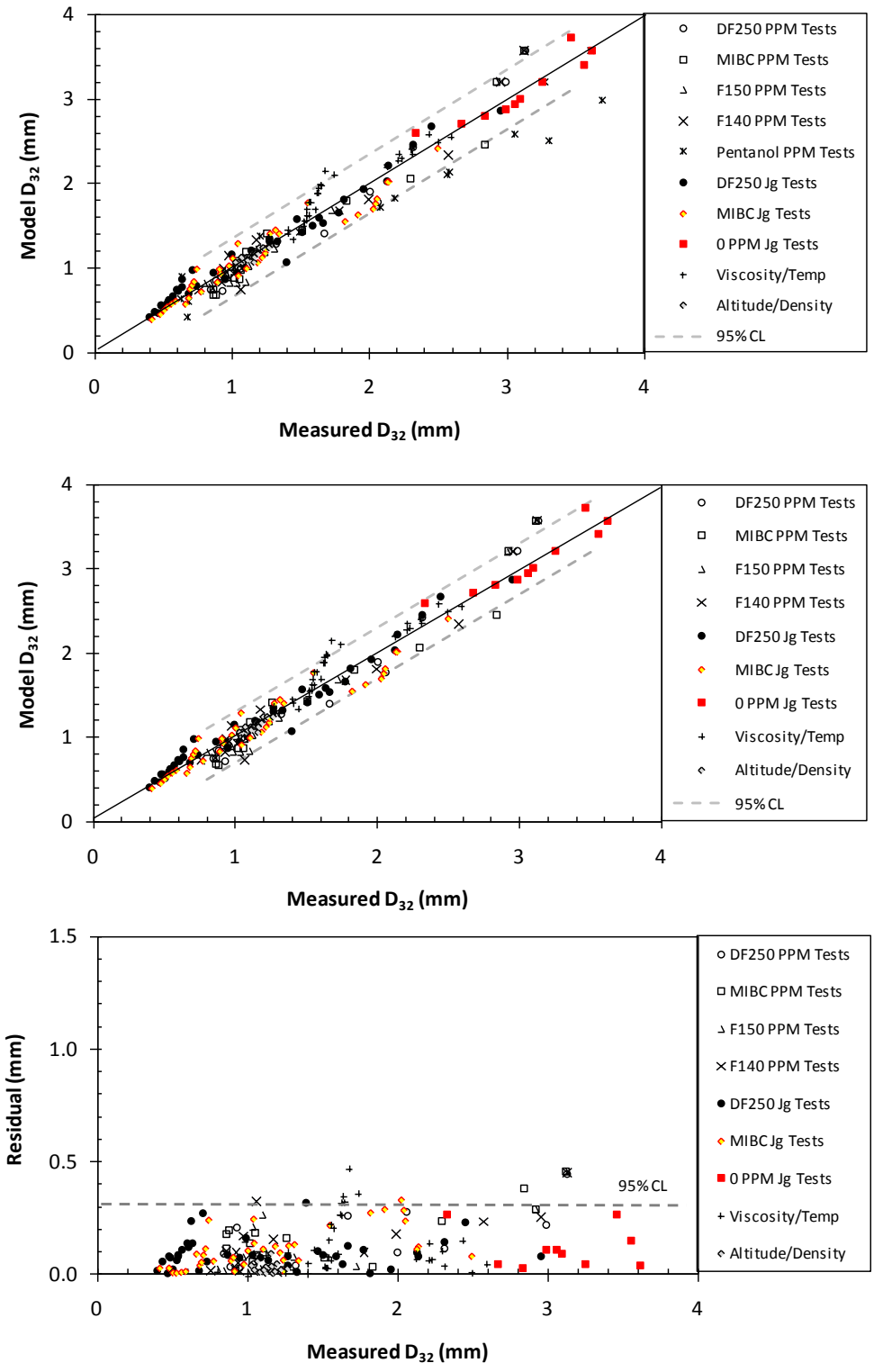

Figure 5.5 Measured versus modeled D_{32} for all data sets including Pentanol (upper plot) and without Pentanol (middle plot). Residuals of measured minus modeled are shown in the bottom plot

Recalling that the precision of the actual D_{32} measurements is ± 3% with frother and ± 5.5% without frother (Table 3.2), an estimate can be made (using the additive nature of variance) of the relative contributions to overall error provided by both the D_{32} measurement and the model. For a 1 mm bubble (frother case) the model contributes 98% of the error in the predicted D_{32}, while at 3 mm the model contribution is reduced to 83% of total error. At this stage, one can conclude the model is not likely to be improved significantly by improving the precision of bubble size measurement. The case of Pentanol is somewhat different as noted. Overall the model appears to be robust and a good predictor of D_{32} for a broad range of conditions.

Table 5.2 Precision and goodness-of-fit parameters for the overall D_{32} model based on residuals analysis (measured – modeled predicted values)

	Data Sets									
Parameter	All	All w/o Pentanol	DF250	MIBC	F150	F140	Pentanol	Zero Frother	Viscosity	Altitude (Density)
Sum Squared	6.953	4.765	1.027	1.449	0.460	0.552	2.188	0.479	1.037	0.0215
N, data points	215	199	54	53	14	16	16	14	32	20
Std Dev (± mm)	0.180	0.155	0.139	0.167	0.188	0.192	0.382	0.192	0.183	0.034
t-statistic	1.96	1.96	2.01	2.01	2.16	2.131	2.131	2.16	2.03	2.093
95% CI (± mm)	0.353	0.304	0.280	0.336	0.406	0.409	0.814	0.415	0.371	0.070
R^2	0.948	0.956	-	-	-	-	-	-	-	-

Predicting bubble size is the key step toward predicting bubble surface area flux, S_b, calculated from J_g and D_{32} ($S_b = 60\ J_g / D_{32}$ for the units used here). Figure 5.6 shows the corresponding measured versus predicted S_b (top and middle plots) and the residuals analysis, presented on a % basis (bottom plot). The absolute residuals increased with S_b as evident from the upper plot, while on a % basis the maximum residual values remained relatively constant (bottom plot). The residuals analysis for S_b presented in Table 5.3 shows a relative standard deviation of ± 11%, and a 95% confidence interval of ± 22%. In absolute terms, at the 95% confidence level, the model predicts to ± 8.8 s^{-1} at a typical S_b of 40 s^{-1}.

The overall model is judged to be robust and adequate for predicting both D_{32} and S_b across their full ranges. The analysis has highlighted the importance of the dependence of CCC95 on J_g for different frother types, as well as the need to fully define the D_{32} versus PPM curves for weaker frothers such as Pentanol.

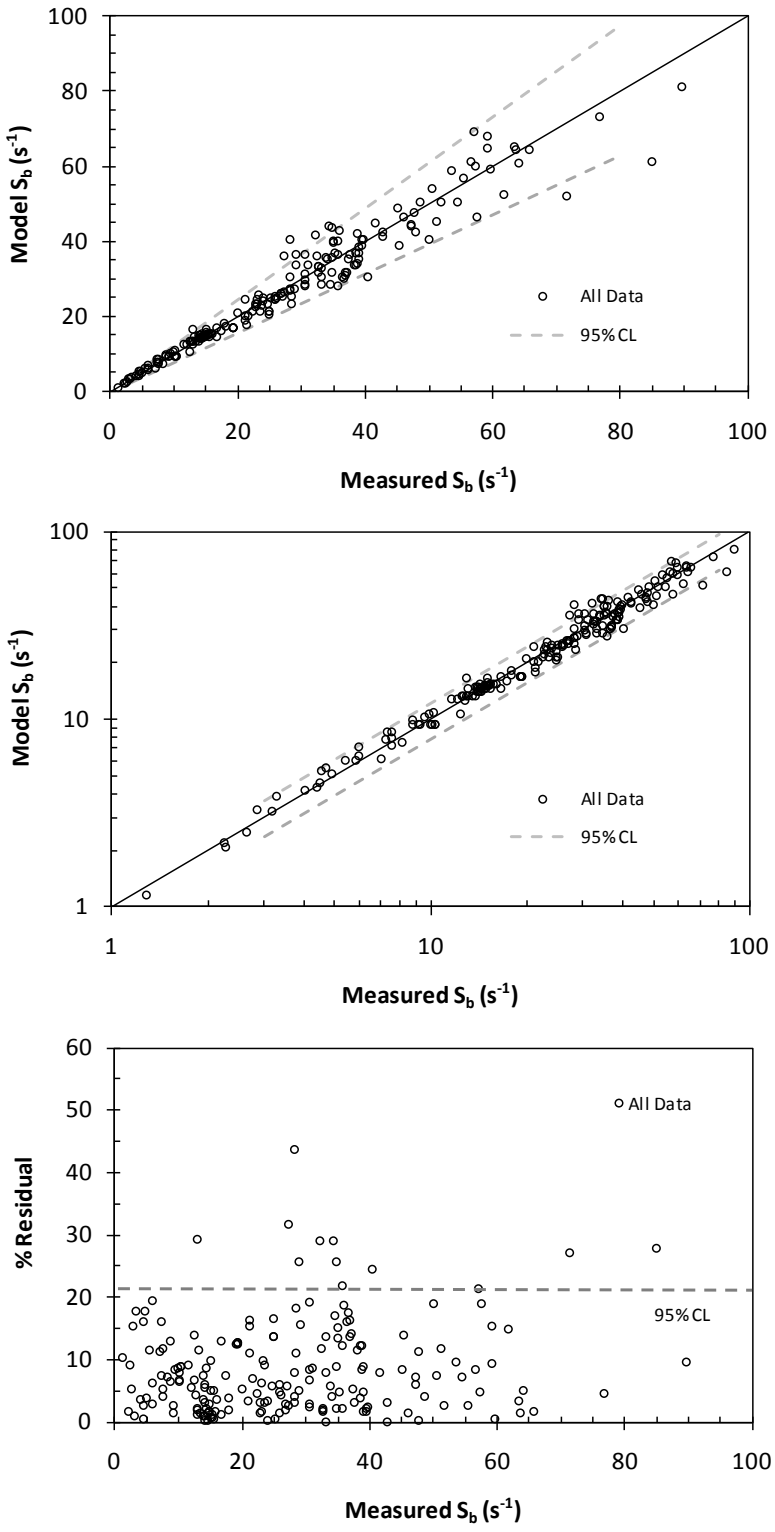

Figure 5.6 Measured versus modeled S_b for all data sets (excluding Pentanol) (top plot). The middle plot shows the same data on a logarithmic scale. Residuals on a % basis (measured minus modeled) are shown in the bottom plot

Table 5.3 Precision parameters for the S_b calculated from overall D_{32} model. Upper data is for residual analysis (measured – modeled), while lower data is for analysis of % Residual

	Data Sets	
Parameter	All Data	All Data w/o Pentanol
Residual Sum Squared	5090	3328
N, data points	215	199
Std Dev (± s^{-1})	4.88	4.10
t-statistic	1.96	1.96
95% CI (± s^{-1})	9.56	8.04
% Residual Sum Squared	32982	24273
Std Dev (± %)	12.41	11.07
95% CI (± %)	24.33	21.70

CHAPTER 6: Model Comparison to Laboratory and Plant Results (Validation) and Model Predictions

The final step of model development is to compare the capability of the model in predicting the correct behaviour of the dependent variables, in this case the D_{32} and the S_b, based on variation of the independent variables, in this case frother type, concentration, superficial gas velocity, viscosity and altitude. Data available for comparison included the laboratory tests themselves and measurements from five plants worldwide by McGill's gas dispersion research teams, four of these five having involved the author. There were no specific data available from the literature to correlate with the effects of altitude or viscosity, so predictions of the effect of these two variables were generated by using a simple flotation model and relating the variable effect to change in recovery through the flotation rate constant (k).

6.1 The Effect of Frother Type and Concentration

The modeled effect of increasing frother concentration on the D_{32} is the, now well-established, exponential decay relationship reaching a limiting value as shown in the left side plots of Figure 6.1. The corresponding effect on S_b is also shown in Figure 6.1 (right side plots) and indicates that frother has an effective, but limited, range over which it influences S_b. Within the variability of the measurements, the model and data show very good agreement, including no effect of frother on S_b at very low concentration. The fact the data follow the S-shape of the modeled S_b curve attests to the validity of the model in predicting the effect of frother type and concentration. As noted earlier, the Pentanol data show greater variation between model and data, recalling also that these data were not used to generate the model parameters.

6.2 The Effect of Superficial Gas velocity, J_g

Similar plots to those illustrating the effect of frother concentration (previous) were used to show the effect of J_g on D_{32} and S_b, and are presented in Figure 6.2. The data fit the modeled curves well, with a few noted exceptions. The DowFroth 250 S_b data are higher than the model curve for the 16 ppm condition. As discussed in Section 5.2 and shown in Figure 5.3, calculation of S_b is sensitive to the measurement of limiting bubble size since D_{32} appears in the denominator of the S_b equation. The inconsistencies in the DowFroth 250 D_{32} versus J_g data have been noted, however the model-data comparison is shown here nonetheless. The validity of the model is supported by the good agreement shown for the other frothers and the DowFroth 250 model-data comparison of Figure 6.1.

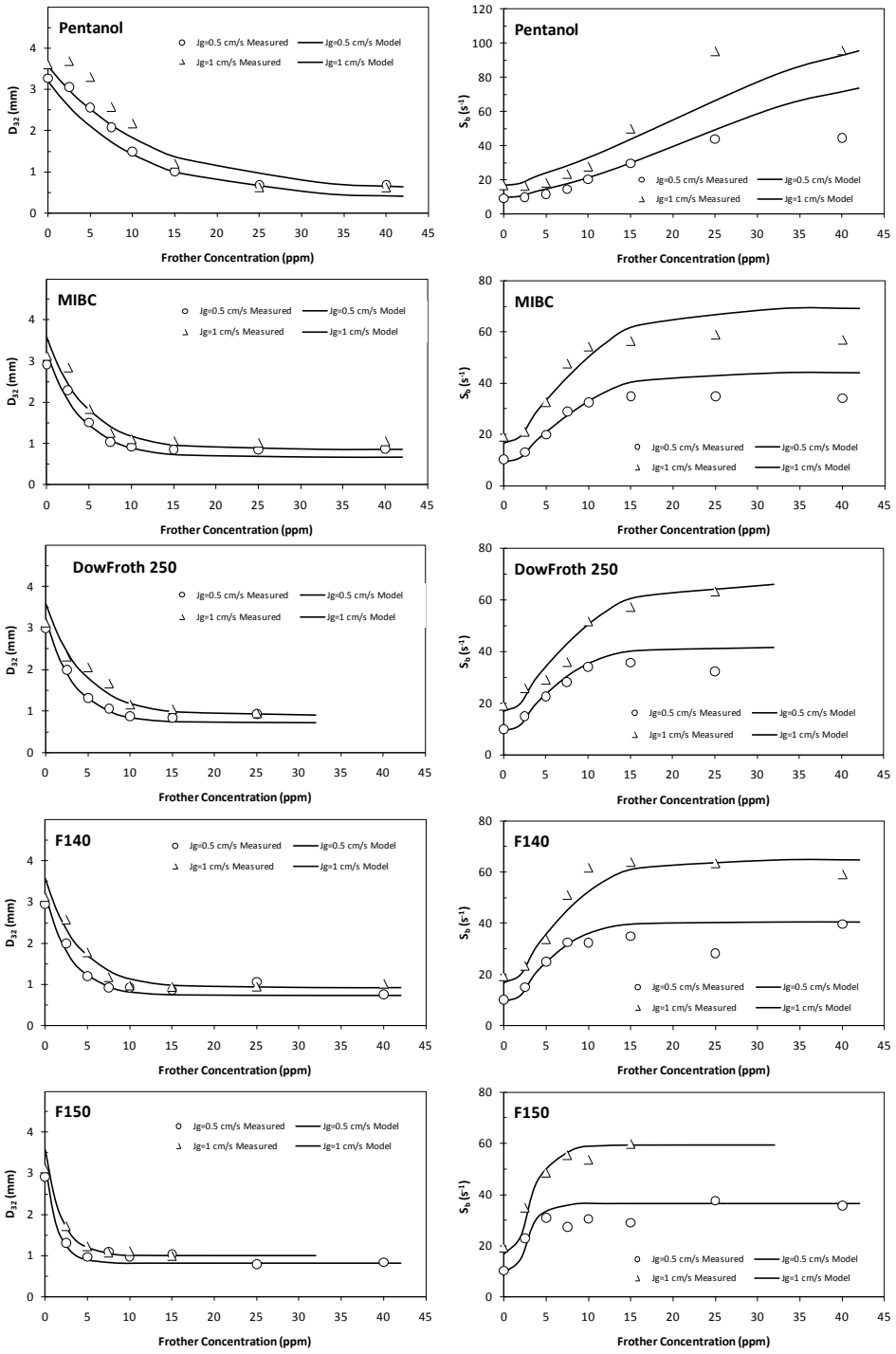

Figure 6.1 Model versus data comparison of the effect of frother concentration and type on D_{32} (left plots) and S_b (right plots).

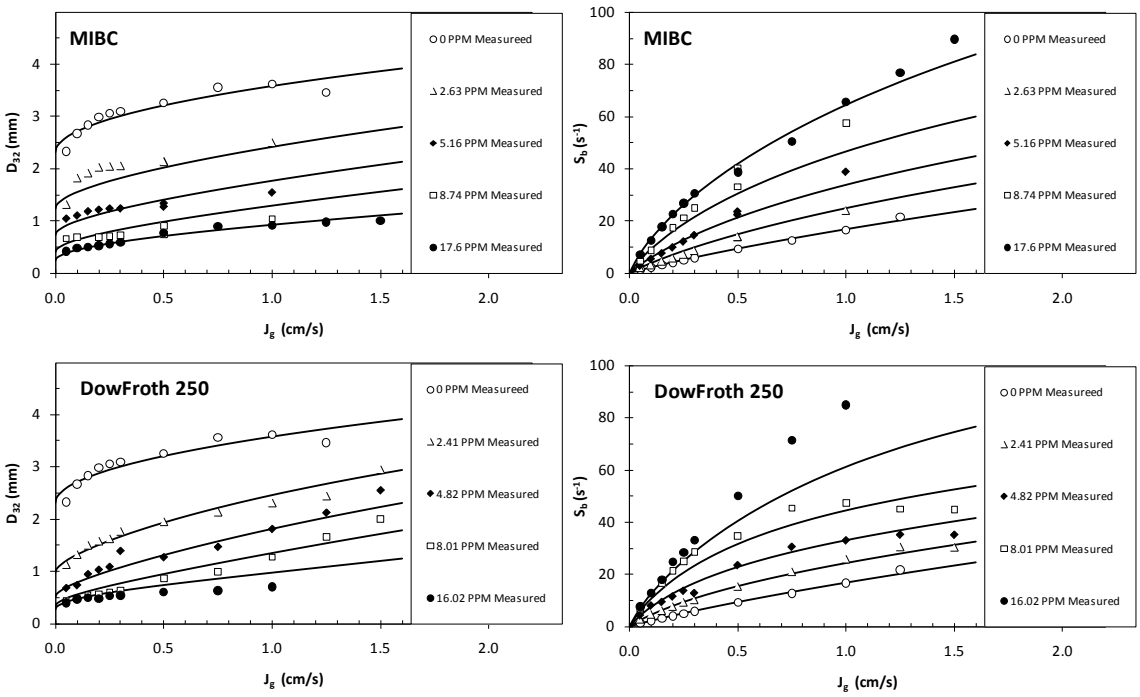

Figure 6.2 Model versus data comparison for the effect of J_g on D_{32} (left plots) and S_b (right plots)

6.3 Comparison to Plant Data

The ultimate goal of having a robust D_{32} model is to predict plant performance and the effect of key variables on flotation recovery. The work reported here has been developed within the 2-phase air-water system, a necessary starting point but missing the effect of solids content. The author and colleagues have been involved in many plant surveys using the McGill gas dispersion sensors and so a sizeable data base exists from which to compare the relationships developed in this work to those found in actual plants.

Data for *down-the-bank* measurements from five operations employing forced-air mechanical flotation machines are plotted in Figure 6.3 along with the D_{32} model predictions using DowFroth 250 parameters, this being the reference base case. Details of the five operations are found in Table 6.1 and indicate the broad spectrum of plant data; nickel, copper, platinum, palladium, cell sizes from 16 m^3 to 130 m^3, cells from three manufacturers and plants on four continents in varying environments. What is striking is that all data fall within the maximum and minimum boundaries of the developed model without exception; in terms of both D_{32} and S_b as a function of J_g. Equally notable is that the data groupings for each of the plants show D_{32} versus J_g following the slopes of the modeled curves. Perhaps surprising since these plants use a variety of frother types, frother concentration may change down the banks of cells in some cases, solids content will also tend to decrease down the banks, and the mechanical condition of cells may vary. The goodness of the model in defining the limits and the slopes of the curves suggests that solids effects are

likely secondary to the key variables of frother concentration and gas rate in determining D_{32} and S_b. All data fall within an "equivalent DowFroth 250" concentration range of 4 ppm (minimum) up to the limiting CCC value, with 2 plants (Lac des Iles and Los Colorados) operating at surprisingly low concentration levels of 4-5 ppm equivalent DowFroth 250. Two plants (Leinster and Raglan) operate at close to the CCC (minimum bubble size) and, hence, maximum S_b. The Impala UG2 plant falls between the others at an equivalent 8 ppm of DowFroth 250. The two plants having smallest D_{32} and highest S_b operate in a pulp environment having high dissolved salt content; the Leinster Ni plant having water salinity of 60 gpl, about twice that of sea water, while the Raglan Ni plant is at 30-35 gpl total dissolved solids. It is well established that salt solutions have a similar effect to frother in reducing bubble size (Quinn et al, 2007). Essentially these two plants are operating at high equivalent frother concentrations and achieving close to minimum bubble size due to their highly saline process water, in fact, the Raglan plant adds no frother at all.

Table 6.1 Flotation cell and circuit data for the five plants used to compare with the 2-phase D_{32} model shown in Figure 6.3 (TC = tank cell, U = U-shaped-bottom rectangular cells, R = rougher circuit, R/S = rougher/scavenger circuit, C = cleaner circuit) (*now BHP-Billiton)

	5 Operating Plants				
Company →	***NA Palladium***	***WMC****	***Xstrata Ni***	***Escondida***	***Impala Platinum***
Operating Plant Site	***Lac des Iles***	***Leinster***	***Raglan***	***Los Colorados***	***UG2***
Cell Manufacturer	Outotec TC	Outotec 16U	Outotec 28U	Outotec TC	Bateman TC, Metso TC
Cell Size (vol) (m^3)	130	16	28	100	50, 30
Circuit Duty	R/S	R/S	R/S	R	R, C
Site Location	Ontario	Australia	Quebec	Chile	South Africa
Metal/mineral floated	Palladium	Nickel	Nickel	Copper	Platinum

Lac des Iles case study

The gas dispersion study by a McGill team at the Lac des Iles palladium (Pd) operation in 2003 (Nesset et al, 2005) and a follow-up study by one of the team members as an SGS-Lakefield employee in 2005 (Hernandez-Aguilar et al, 2006) afforded unique data for validation of the bubble size model presented here. The 2003 study, comparing plant performance to a parallel pilot plant study, had shown that the D_{32} measurements in the pilot cells were significantly smaller than in the plant, and the investigators speculated that this difference (i.e. lack of sufficiently small bubbles in the plant cells) was the main cause for poor recovery of very fine Pd (< 10 µm) in the plant. The plant operated with MIBC as frother at about 12 g/t of solid feed, equivalent to 5-6 ppm added in solution. The data for D_{32} and S_b as a function of J_g are presented in Figure 6.4, on which the current model using MIBC parameters is also projected. The 2003 plant data are seen to be a very good fit to the model data for 5 ppm MIBC.

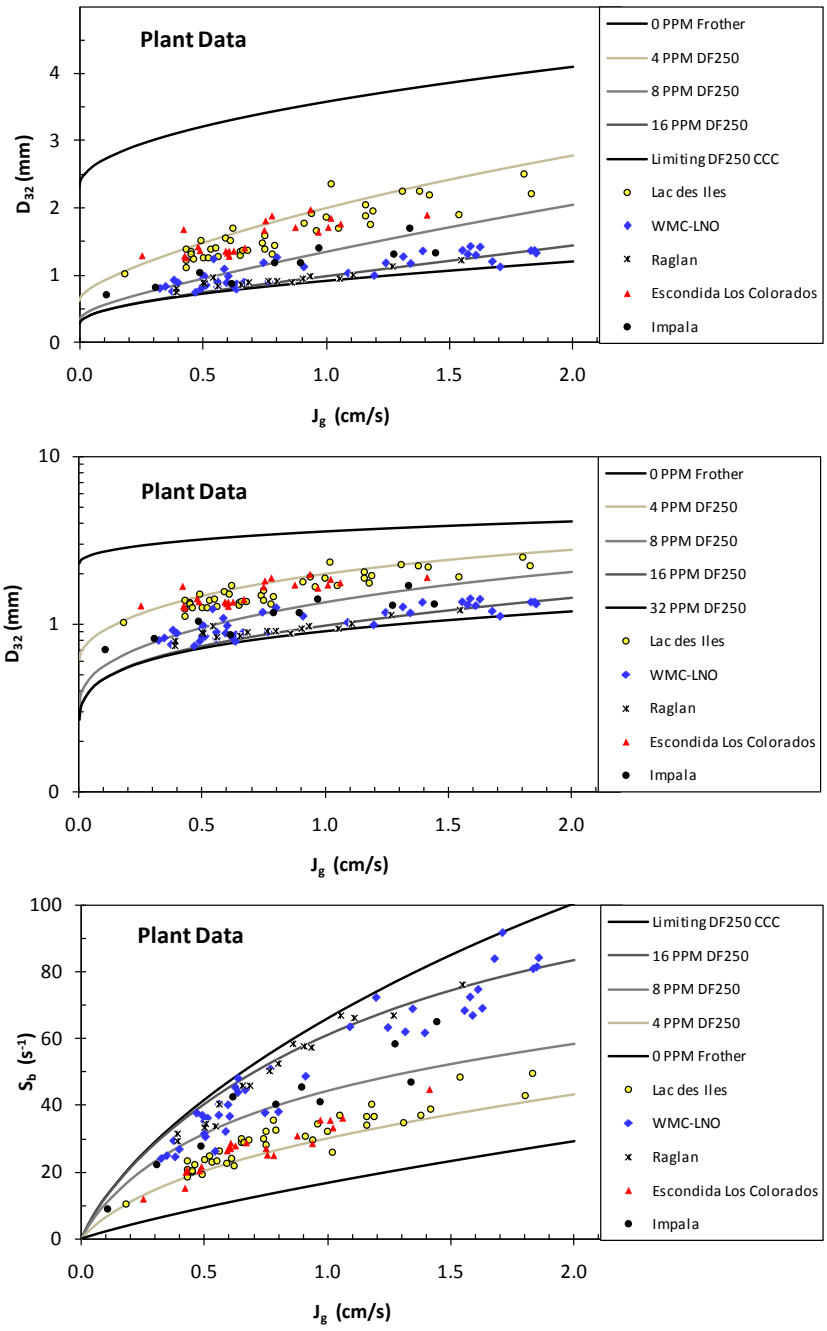

Figure 6.3 Comparison of D_{32} and S_b for five operating plants with the 2-phase model using DowFroth 250 parameters

In the 2005 follow-up study, an initial set of tests was conducted and confirmed the plant J_g-D_{32} relationship using MIBC was still the same as in 2003 (evident in Figure 6.4). A blended alcohol-polyglycol frother was then added to the same cells in an attempt to reduce D_{32} size

to that achieved in the 2003 pilot plant. The results, as shown in the figure, indicate the stronger, blended frother successfully reduced the D_{32} to the pilot plant values and significantly increased the S_b. Hernandez-Aguilar et al (2006) reported that recovery of minus 10 µm Pd increased from below 20% to over 60% as a result of achieving the smaller bubble size and correspondingly higher S_b. This example illustrates the usefulness of the model as a "roadmap" for benchmarking operating practice, and as an indicator of the potential for improvement.

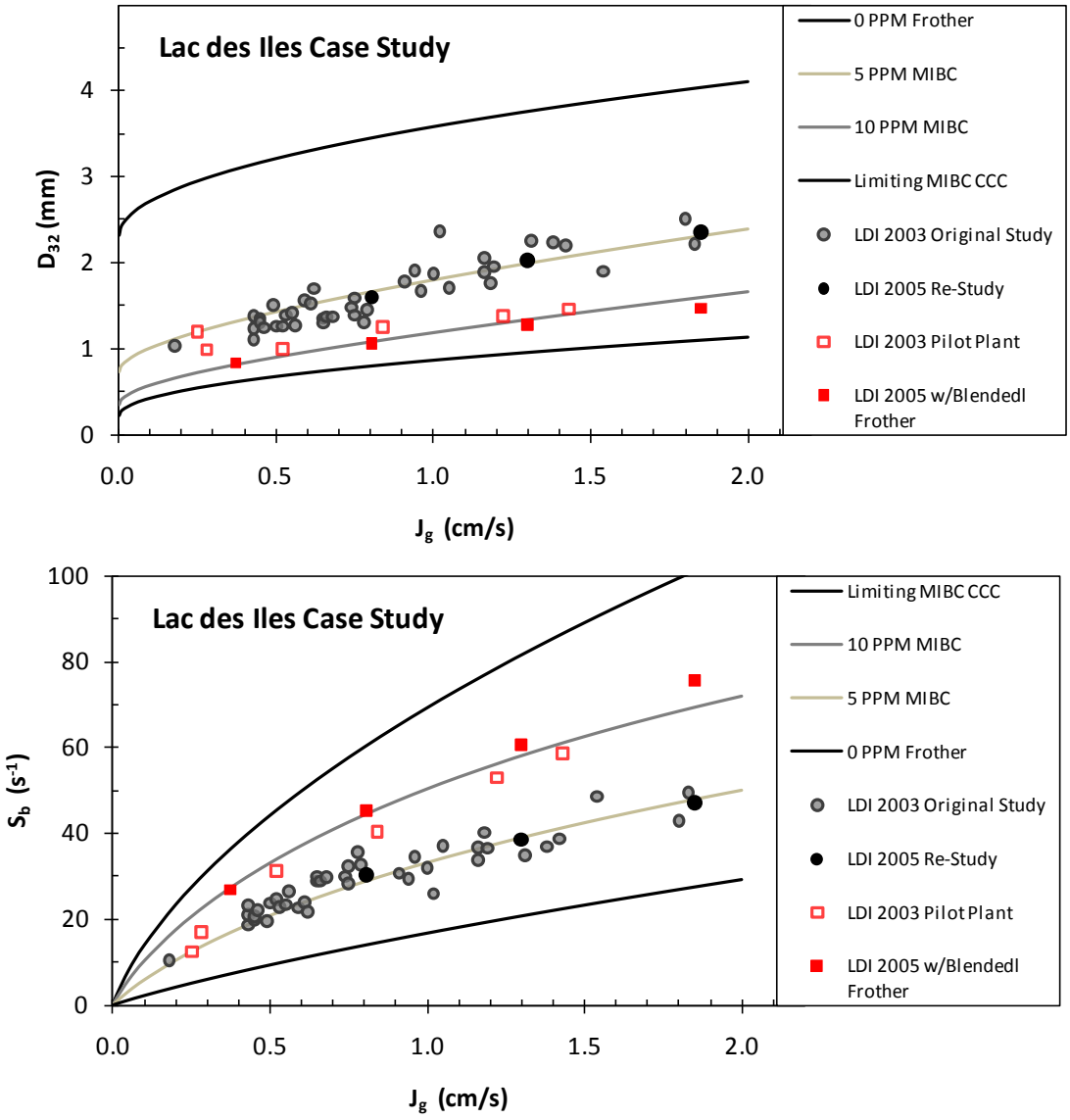

Figure 6.4 D_{32} (upper plot) and S_b (lower plot) as a function of J_g for the Lac des Iles case study. Note that the addition of a blended alcohol-polyglycol frother (2005 study) permitted the results to match the 2003 pilot plant results

6.4 Using the Model to Predict the Effect of Altitude and Viscosity

As noted, no specific references quantifying the effect of altitude or viscosity effects on the flotation performance of forced-air mechanical flotation cells could be located. However, the model can be used to investigate the impact on flotation performance of typical changes by assuming that a change in bubble size will produce a proportional (inverse) effect on S_b and hence mineral flotation rate constant, k (recall Equation 1.6), everything else being held constant. A simple flotation recovery model was constructed assuming perfect mixing for each cell and the same individual cell recovery. The base condition assumed individual cell retention time of 4 min, a rate constant k=0.15 min^{-1}, and a limiting recovery of 90%. For a bank of eight (8) cells this model predicts a cumulative mineral recovery approaching 88%.

The base case D_{32} is assumed to be 1 mm, the altitude is sea level and the viscosity is that for water at 20 ^{o}C, so factors f_g and f_v are both equal to 1. The altitude effect of interest is that for an operation at 4500 m, the upper range for current plants. The viscosity effect of interest is that for water viscosity at 5 ^{o}C, representative of a typical summer-winter fluctuation (a 15 ^{o}C change) in plant process water temperature in a Canadian or non-tropical location. The bubble size model predicts, using Equation 5.4, a D_{32} increase to 1.08 mm for an altitude of 4500 m, and hence a rate constant decrease to 0.139 min^{-1}. The 0.5% loss in recovery can be more than recouped by the addition of one additional flotation cell as illustrated in Figure 6.5. For the case of water viscosity increase at 5 ^{o}C, using Equation 5.3, the D_{32} increases to 1.38 mm resulting in a rate constant decrease to 0.109 min^{-1}, and a corresponding recovery loss of 2.4%. This substantial impact on flotation recovery can be recouped by the addition of 3 flotation cells for a total of 11 from the base case of 8. The significant impact of temperature effects yielding higher flotation rate constants at increased summer pulp temperatures has been experienced by the author at his own copper-zinc operation where it was often possible to shut down an entire row of cells during peak summer temperatures. The D_{32} model has been used to demonstrate that altitude effects on flotation recovery can be expected to be minimal, while the impact of pulp (i.e. water) viscosity changes (due, for example, to summer-winter temperature fluctuations) can be substantial, and need to be accounted for during plant operation and at the circuit design stage.

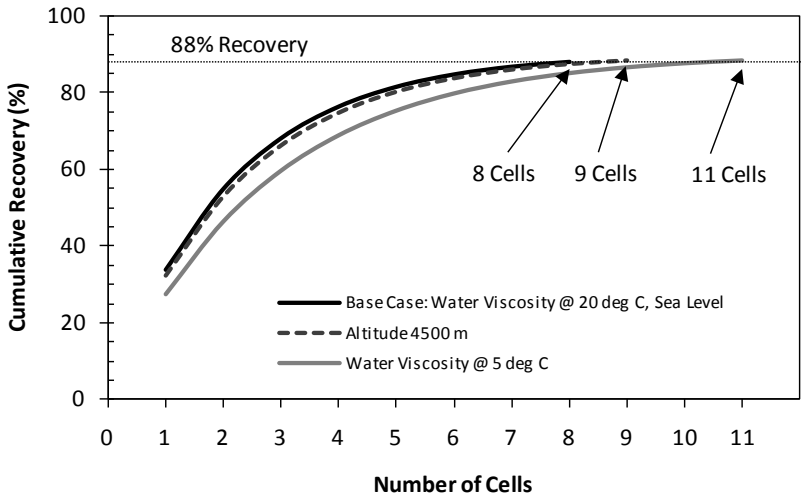

Figure 6.5 Comparing the D_{32} model-predicted effect on cumulative flotation recovery of altitude (at 4500 m) and viscosity (at 5 ^{o}C) to the base case at sea level and 20 ^{o}C. The effect of altitude can be mitigated by the addition of one cell (to 9) and that of viscosity by the addition of three cells (to 11) from the base case of eight (8) cells

6.5 Model Predictions

In order to better understand the differences between tested frother types, the D_{32} model was used to produce families of curves for D_{32} and S_b for varying frother addition and J_g. These are presented in Figures 6.6 and 6.7 and reveal useful information regarding frother behaviour. From Figure 6.6 one sees that the limiting bubble size will clearly increase with increasing J_g while S_b also increases. If very small bubbles are important in the process (e.g. fine particle recovery) then, clearly, understanding the trade-off between D_{32} and S_b becomes important.

The S_b curves of Figure 6.6 also provide important information about identifying optimum frother concentration. It would not be desirable, under most operating circumstances, to target a concentration on the steeper portion of the curve since small changes in concentration would significantly impact D_{32} and S_b, and hence particle recovery. A more suitable operating target would be just above where the S_b versus J_g curve changes slope and flattens, somewhat in excess of the CCC95 value, about +20% by estimate. The higher the J_g value, the higher the required frother concentration to reach this less sensitive region. Figure 6.7, showing D_{32} (left plots) and S_b (right plots) as a function of J_g, indicate that he frother type has a strong bearing on the maximum S_b that can be achieved; those with a lower limiting bubble size, such as Pentanol, having an S_b approaching 120 s^{-1} at J_g = 2 cm/s compared to 100 s^{-1} for DowFroth 250. The impact of different frother type is more clearly indicated in Figure 6.8 for the selected conditions of J_g = 1cm/s (upper plots), and limiting CCC levels of frother concentration (lower plots), for Pentanol, DowFroth 250 and F-150 (MIBC and F-140 being similar to DowFroth 250). Although higher concentrations of the lighter alcohol Pentanol are required for the same bubble size reduction effect, it also affords

an opportunity for achieving higher S_b and smaller D_{32}, both potentially important for improving particle recovery. These results help explain the success of some blended frothers combining larger proportions of alcohols with smaller proportions of polyglycols that result in small bubbles, high S_b and stable froth (Cappuccitti and Nesset, 2010).

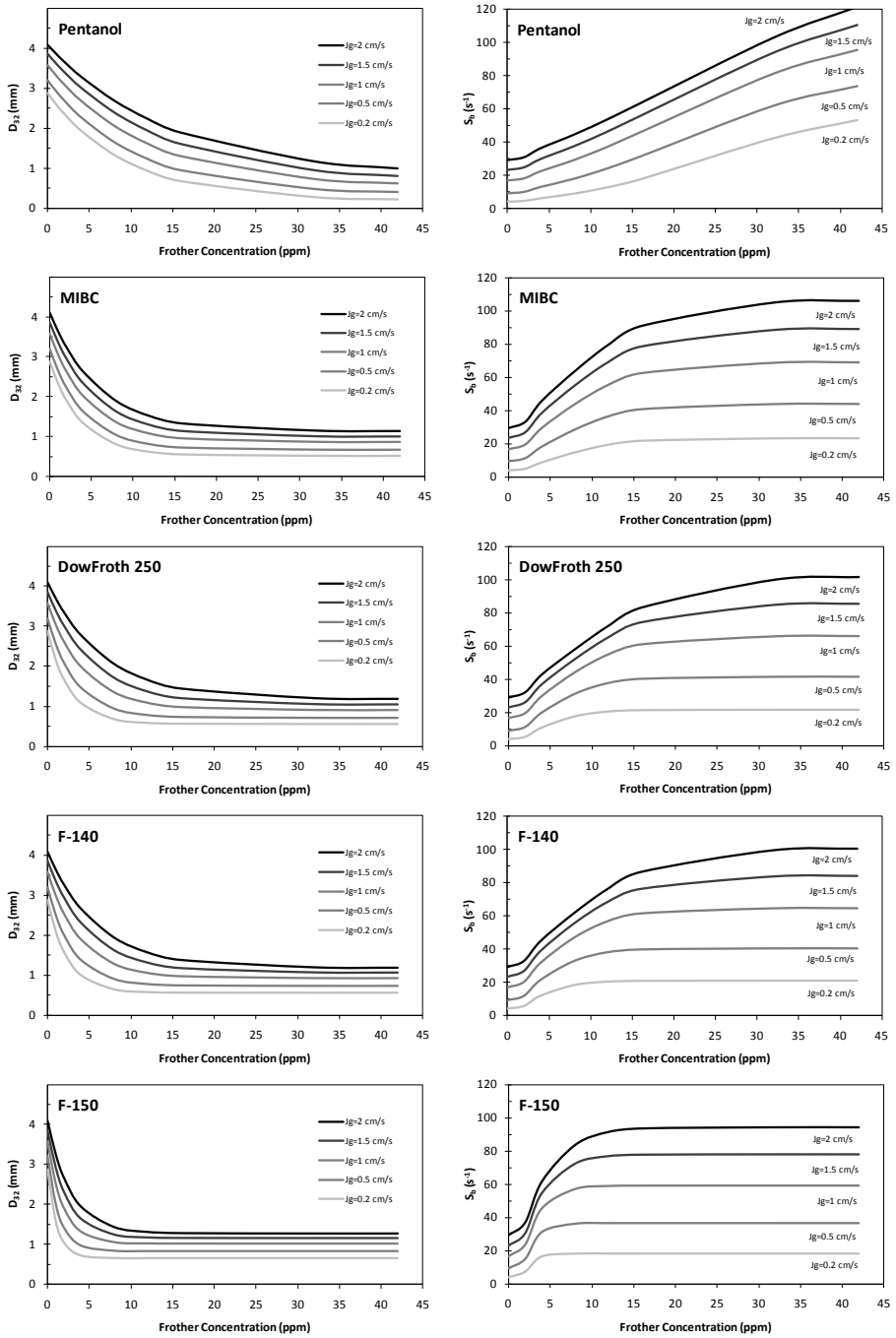

Figure 6.6 Model predictions for D_{32} (left plots) and S_b (right plots) at various J_g as a function of frother addition level

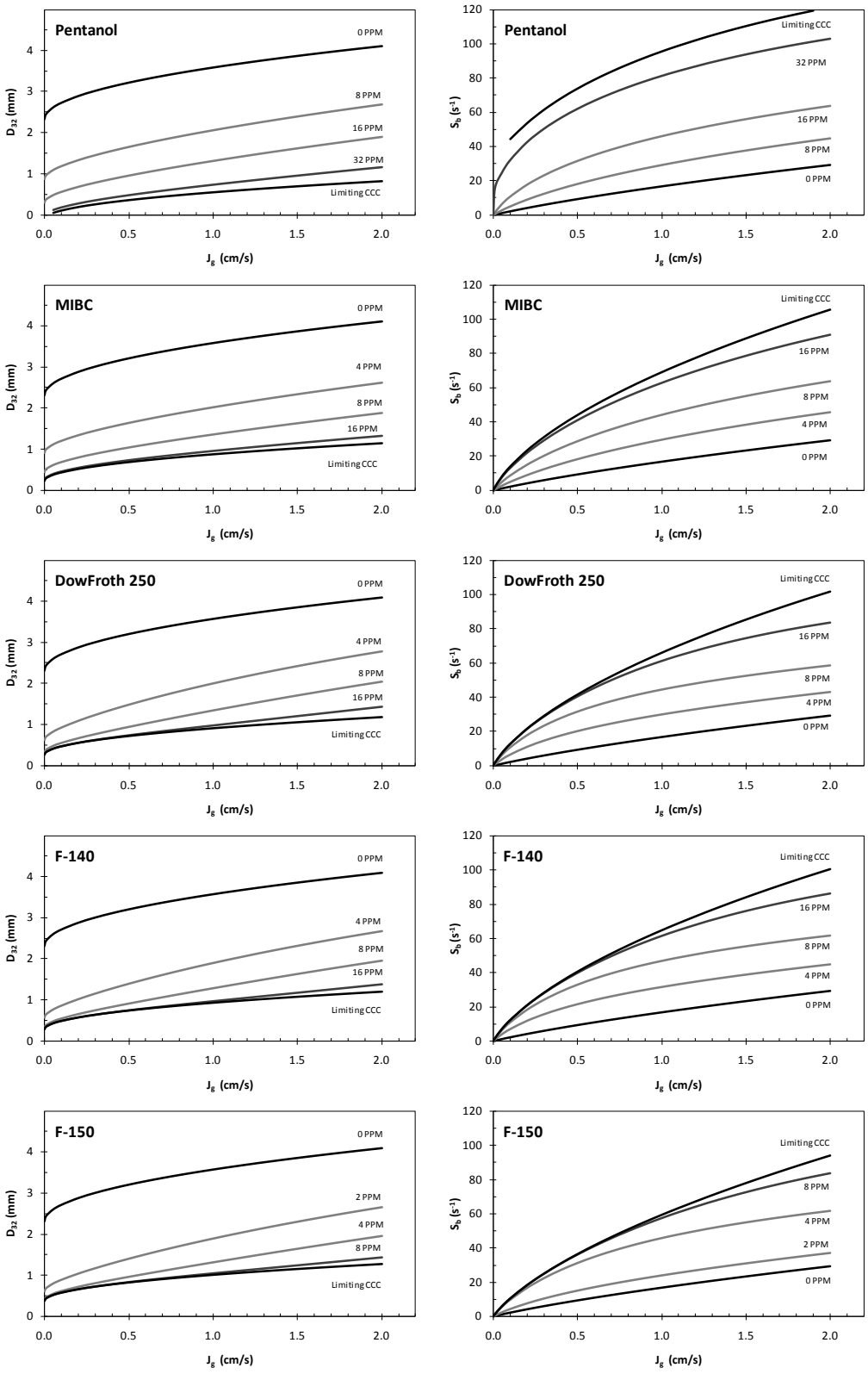

Figure 6.7 Model predictions for D_{32} (left plots) and S_b (right plots) at various frother addition levels (ppm) as a function of J_g. Note that the limiting CCC values differ for each frother type

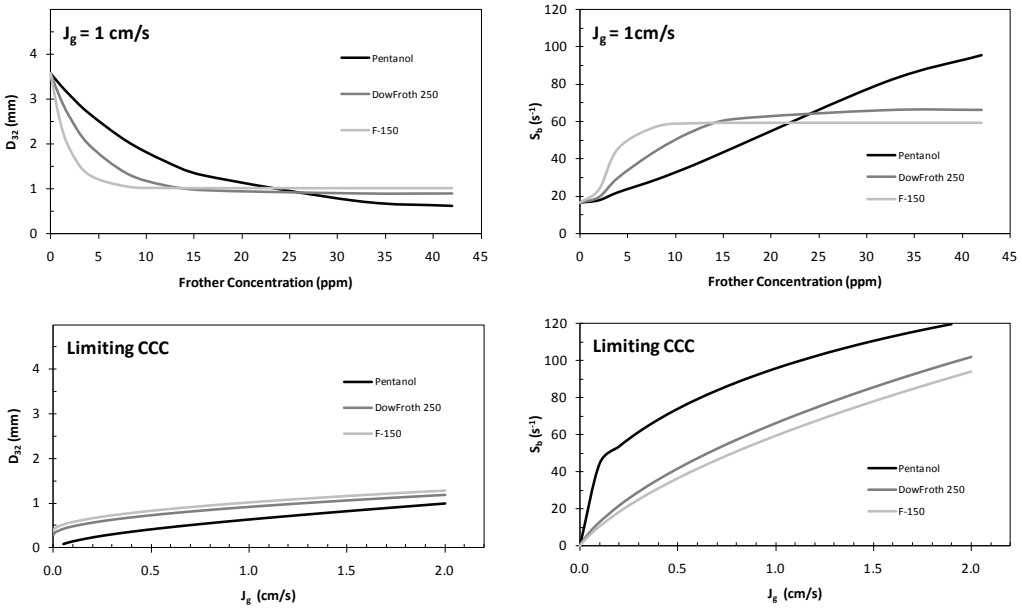

Figure 6.8 Selected plots demonstrating the difference in D_{32} and S_b versus frother addition (upper plots) for a J_g of 1 cm/s. The lower plots show selected predictions for D_{32} and S_b as a function of J_g for the limiting CCC condition. These curves illustrate the difference between three of the frothers tested (Note that MIBC and F-140 are similar to DowFroth 250)

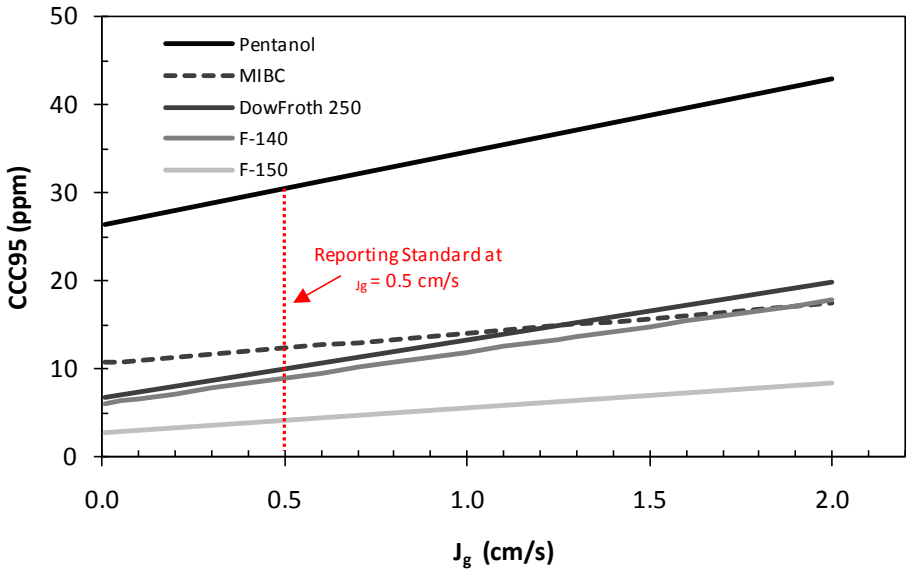

Figure 6.9 Variation in CCC95 with J_g for the five frothers tested. CCC95 values are reported for J_g = 0.5 cm/s

Inherent in the D_{32} model, and a significant factor in the curves shown in Figures 6.6, 6.7 and 6.8, is the revelation through this work that a frother's CCC, and its more practical manifestation the CCC95, depends significantly on the J_g value. Figure 6.9 has been prepared to show how the CCC95 varies with J_g for each frother. MIBC, DowFroth 250 and F-140 show similar values, although MIBC has a lesser slope resulting in higher CCC95 than DowFroth at J_g below 1 cm/s and higher for J_g above 1.5 cm/s. This work has established a norm for reporting J_g at a standard value of J_g = 0.5 cm/s. The details were given in Section 5.2 and Equations 5.11 for DowFroth 250, F-140 and F-150, and Equation 5.13 for Pentanol and MIBC.

This model validation section has demonstrated the practical and operational benefits available from even a 2-phase D_{32} model. The model was successfully correlated with the 3-phase industrial data from five different operating sites using an "equivalent" DowFroth 250 "roadmap" of D_{32} and S_b versus J_g, showing similar slopes and data ranges to the model. The Lac des Iles palladium case study provided an example of how such a roadmap can provide for immediate operational guidance and benefit. Note that a different set of "roadmap" curves will result for each frother type (Figure 6.7) since only the CCC0 curve is independent of type. For a specific plant the appropriate frother should be plotted. Comparisons can be made between plants using the "equivalent" DowFroth 250 approach as presented in Figure 6.3.

CHAPTER 7: Discussion of Results

Considerable discussion of results has been provided within individual chapters, however, there remain some important aspects of the work that would benefit from additional commentary. These have been divided into appropriate sections.

The choice of the Metso RCS™ flotation cell proved to be particularly fortuitous. The shelf baffle, located approximately half-way up the wall of the tank, provided for distinct turbulent and quiescent zones as indicated in the top plot of Figure 7.1. The resulting measurements were therefore truly representative of the bubble size distribution, superficial gas velocity (J_g), and, hence, bubble surface area flux (S_b), exiting the pulp (in this case, water) phase. The large size of the cell, 700 liters of water, compared to those of other researchers who have tested on smaller volumes of, typically, 10 to 250 liters, also enhances the relevancy of this work to the task of modeling the bubble size that drives S_b. Within a smaller volume and without baffles to aid in distinctly separating turbulent and quiescent zones, the measurements could include a portion of the bubble population not exiting the pulp zone, but returning to the impeller region. Measurement of what is occurring in the highly turbulent impeller and near impeller regions is also important to understanding flotation behaviour (the processes of particle-bubble collision, attachment and detachment, Schubert, 2008), however, that analysis was not the objective of this work.

D_{32} and the hydrodynamic conditions in the impeller/stator region

One of the findings of this work (Figure 4.12) is that D_{32} is largely unaffected by increased impeller tip speed across the range of 4.6 to 9.2 m/s, representing the industrial operating range, and an 8-fold increase in power intensity. This may seem at odds with other researchers (Gorain et al, 1999; O'Connor et al, 1990; Grau and Heiskanen, 2005) who have claimed that increased power intensity through increased impeller speed results in decreased bubble size (typically the D_{32}). Closer examination of Figure 4.12 does show that at below 4.6 m/s the D_{32} starts to increase and there is, arguably, a very slight downward slope to the data above 4.6 m/s, however for practical considerations the relationship can be considered flat. That others were finding a stronger D_{32} versus impeller speed relationship than here and a possible influence by the turbulent zone, prompted a follow-up test using a longer sampling tube to reach this zone. Figure 7.1(bottom) shows that with a 34 cm extension on the bubble viewer sampling tube, the region immediately adjacent to the impeller could be sampled. Since radial and tangential fluid velocities in this region are far greater than vertical ones, the end of the tube was cut at a 45^o angle and rotated to face the direction of maximum velocity. A flat end on the tube was also tested. The results are shown in the bottom plot of Figure 7.1 and are compared to the standard location results for J_g = 1 cm/s and DowFroth 250 at 10 ppm (non-coalescing condition). In addition to being considerably smaller in the turbulent region, there is also a distinct decrease in D_{32} with increasing impeller speed, resembling the trend found by others. The conclusion to be drawn is that the bubble population is distinctly different, and finer, in the turbulent region compared to the quiescent region and coalescence is not the reason. The smaller bubbles

are likely caught in the fluid streamlines and circulate through the impeller/stator region thus shifting the BSD to a finer size. Increasing the impeller speed increases the local fluid velocity (i.e. the pumping rate through the impeller) tending to trap a higher proportion of smaller bubbles in the streamlines. The fact that the BSD in the quiescent zone does not significantly change, while it does in the turbulent region, suggests that the BSD being created does not change with increasing impeller speed either, since steady state conditions must be respected across the creation, turbulent and quiescent zones.

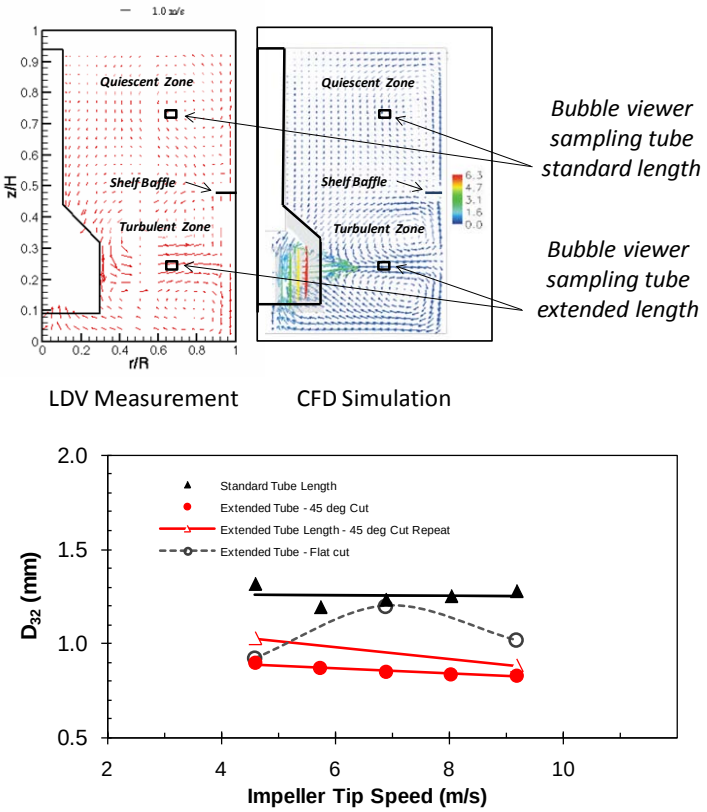

Figure 7.1 Comparison of D_{32} versus impeller tip speed measured with the standard length BV sampling tube (quiescent zone) and the extended length tube (turbulent zone). Note the extended length tube was tested with both a 45° angle end-cut (facing the radial and tangential flow) and a flat end-cut. (conditions: 10 ppm DowFroth 250, J_g = 1 cm/s)

The explanation offered helps sort out why some researches find a D_{32}-impeller speed dependence while others do not. Grau and Heiskanen (2005) reported $D_{32} \alpha N^{-0.55}$ and $N^{-0.41}$ for J_g of 0.7 and 1.3 cm/s for measurements on a (relatively small) 50 liter laboratory cell covering the range of 2 to 7 m/s tip speed. Subsequently, Grau and Laskowski (2006) reported a less dependent relationship for measurements at J_g = 1 cm/s, also under non-coalescing conditions, on a larger 265 liter cell where the measurement position was well above the impeller in the quiescent zone. In fact, for tip speeds above 4.7 m/s their data show virtually flat curves for both D_{32} and D_{10} that closely resemble the results obtained in this work. Subsequent communication with the manufacturer, Outotec, found that they now regard there to be no significant effect of impeller speed on D_{32} across this range

(Grönstrand, 2007, 2010). In a study on galena kinetics as a function of impeller speed for 8.5 m^3 plant cells, Grano (2005) concluded that bubble size did not change over the range 5.4 to 6.2 m/s tip speed based on no measured change in water recovery rates. On closer examination, the D_{32} measurements of Gorain et al (1999) as a function of impeller speed (Equation 2.9) were not taken solely in the area at the top of the cell beneath the froth, but were made throughout the test-cell volume (top, middle and near-bottom) and then averaged to provide the calculation of S_b. There does appear, therefore, sufficient evidence in the literature, arguably under-reported, that support the finding here that D_{32} remains effectively constant over the operating range 4.6 – 9.2 m/s when measured sufficiently away from the influence of the turbulent impeller region. Those reporting a stronger impeller speed-D_{32} relationship were, in fact, measuring in regions of higher turbulence, often because measurements were made in smaller cells. The findings of this work also show these conclusions apply across the spectrum of coalescing (0 ppm frother) to non-coalescing (approaching the CCC) conditions.

The fact that the bubble measure of interest, the D_{32}, does not change appreciably over an 8-fold increase in power intensity representing a range of impeller N_{Re} (2.3 to 6.1 x 10^5) that is well within the turbulent region, merits some discussion. The classical analysis of Hinze (1955) and others based on a Weber number approach and a balance between disruptive (turbulent, inertial) and stabilizing (surface tension) forces, and showing $D_{32} \alpha [P/V_L]^{-0.4}$ would appear not to apply for any of the cases (coalescing to non-coalescing) investigated here. Note that individual bubble N_{Re}, (4 x 10^3 to 3 x 10^4), assuming 1-3 mm spheres moving relative to water in a non-turbulent free-stream (i.e. up-stream) moving at the impeller tip speed, would also be well into the turbulent region thus having a constant drag coefficient. The N_{Re} is the ratio of inertial to viscous forces and in the fully turbulent N_{Re} region there is no additional contribution of surface friction to the total drag force (i.e. the drag coefficient remains constant). Under these conditions the additional drag force with increasing velocity comes solely from the drag associated with the pressure drop across the object (Massey, 1975). As a result, the drag force is proportional to the square of the relative velocity with no effect of viscosity as long as the flow regime remains fully turbulent. What this work has revealed is that D_{32} is quite significantly dependent on viscosity, $D_{32} \alpha [\mu/\mu_{20}]^{0.776}$, and is not affected by increased velocity of the impeller. In fact, this is the reverse of what would be expected if the disruptive force responsible for bubble size change was related to the fluid drag force and the turbulent conditions suggested by the impeller N_{Re}. Several possible explanations come to mind: first, that the hydrodynamic conditions existing within the air/water mixture of the rotating impeller/stator region are different from those of classic non-turbulent free-stream (i.e. upstream of the object) analysis; or second, that the disruptive force causing bubble break-up is not the classical one related to kinetic energy dissipation. Given that in this work no specific testing was performed to sort this out, definitive conclusions are difficult to reach, although a few comments and some discussion are in order. It has been noted that the drag coefficient on a sphere is markedly reduced (to below 0.1) in the presence of significant free-stream turbulence (Moradian et al, 2009) and that this reduction in the drag coefficient increases significantly with increasing free-stream turbulence. The influence of the size of the turbulence (*integral length scale*) relative to the

sphere diameter is also noted to be a significant factor by Moradian et al. A decreasing drag coefficient as bubble N_{Re} increases would effectively reduce the influence of velocity and increase the importance of viscosity (as a component of drag). The bubble N_{Re}'s appear to be in the right range, 10^3 to 10^4, for this to be the case. Given the observed significant effect of fluid viscosity on D_{32} it is suggested that the friction component of the fluid drag force is still playing a role in bubble break-up.

It has also been noted that the drag coefficient on individual bubbles will decrease significantly in a bubble swarm (Simonette et al, 2007) and that this reduction is strongly influenced by increasing void fraction (i.e. gas hold-up). The power versus impeller speed measurements in the aerated cell (reported in Section 3.3) suggest a void fraction of 35 to 50% in the impeller/stator region for J_g 0.5 to 1 cm/s under non-coalescing conditions (10 ppm DowFroth 250) and 20 to 35% at 0 ppm frother. In summary, the combination of high free-stream turbulence, high void fraction, and bubble N_{Re} in the 10^3 to 10^4 range, suggest that the hydrodynamic conditions prevailing in the impeller/stator region may well match the requirements for a reduced bubble drag coefficient that decreases with increasing impeller speed. The result would be a (disruptive) bubble drag force, and hence a D_{32}, with less dependence on velocity (impeller speed) and an increased dependence on viscosity.

The effect of frother concentration

The incorporation of an exponential decay function (Equation 4.1) and the $ppm/CCC95$ parameter to model the effect of frother concentration on D_{32} is a powerful development of this work and one that enabled the modeling to proceed in a straightforward manner. It also raises the question "is this the expected frother-addition versus D_{32} relationship?" Alves et al (2002) and Finch et al (2008) have introduced arguments that bubble break-up in the presence of surfactants is the result of surface tension gradients (non-steady state) caused by differences in surfactant concentration that occur across the bubble surface as it is swept by the moving fluid. Such gradients, it is argued, result in uneven surface forces that promote growth of perturbations on the bubble surface resulting in break-up under the turbulent conditions at bubble generation. An obvious question is "why does an initial and very small addition of surfactant have the largest effect on bubble size reduction?"

Measuring frother concentration on the bubble surface *in-situ* is a difficult proposition so suggested mechanisms are difficult to validate. Some researchers have made measurements on bubbles blown in air (Gelinas et al, 2005b; Finch et al, 2008) and inferred behaviour in the pulp. Recently, Zhang et al (2009b) studied frother behaviour and water recovery in a continuous mini-cell (5.5 liters) set-up using four commercially available frothers; MIBC, DowFroth 250, FX160-05 and F-150; the latter 2 (being from the polyglycol family of frothers) supplied by Flottec and having molecular weights of 207 and 425 respectively. They presented data showing the concentration measured in both the pulp and froth phases at increasing levels of frother addition to the closed-loop system (i.e. continuous recirculation of all water and hence frother back to the cell). Their results are presented in Figure 7.2 and show that for very low frother addition levels to the system,

resulting concentration in the froth is very high, decreasing until a minimum is reached and then increasing again, mirroring the total addition to the system. These data were re-worked by the author and afforded an opportunity to study the effect of concentration difference between the froth and the pulp (i.e. water), and consequently the effect on D_{32}. The froth depth in these tests was only a few cm and so, it can be argued, the concentration in the froth, C_{Froth}, is representative of the concentration at and near the bubble air-water interface, $C_{Interface}$. $C_{Interface}$ can be very different from that in the bulk solution, C_{Bulk}, as noted in Figure 7.2. An estimate of the concentration gradient across this layer is therefore possible; represented by either $C_{Froth} - C_{Bulk}$, or the ratio C_{Froth}/C_{Bulk}, both being measures of the difference. These plots are show in Figure 7.3 and both demonstrate exponential-type decays reaching limiting values for higher additions of frother to the system.

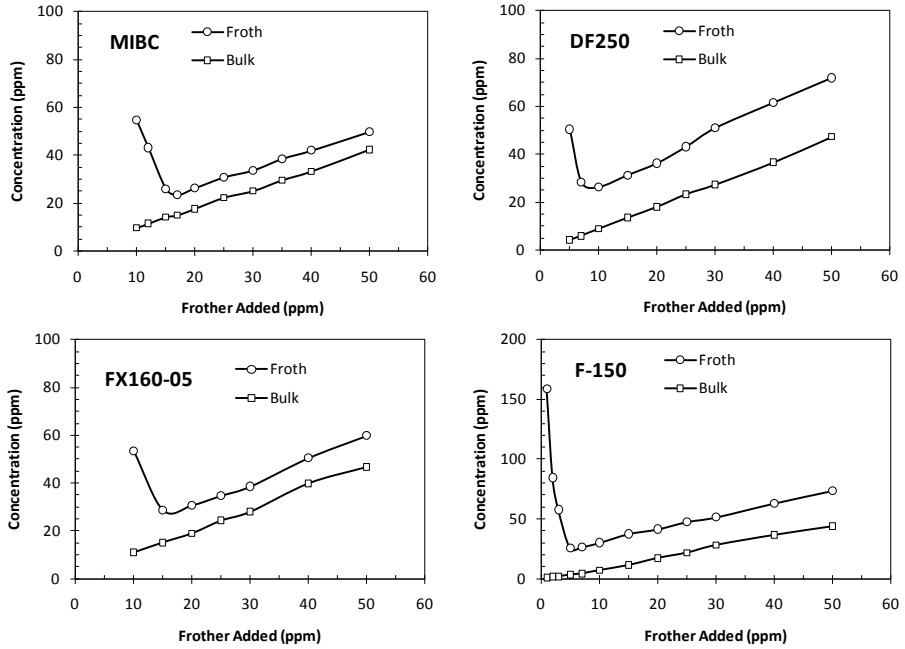

Figure 7.2 Frother partition curves between bulk and froth phases (from Zhang et al, 2009)

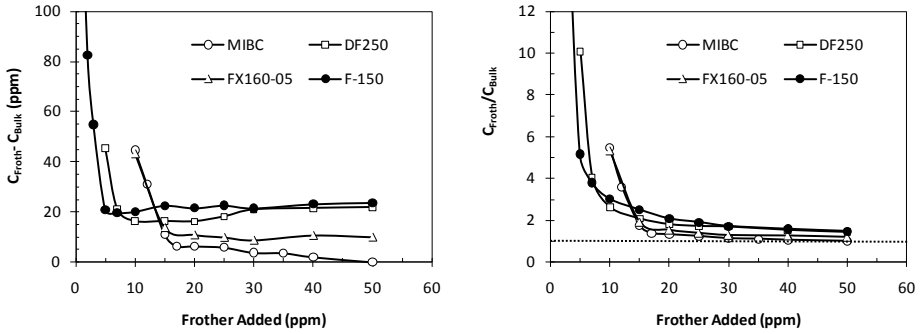

Figure 7.3 Two ways of plotting concentration gradient, $C_{Froth} - C_{Bulk}$ (left) and C_{Froth}/C_{Bulk} (right) for data of Zhang et al (Fig 7.2). Both exhibit an exponentially decreasing relationship

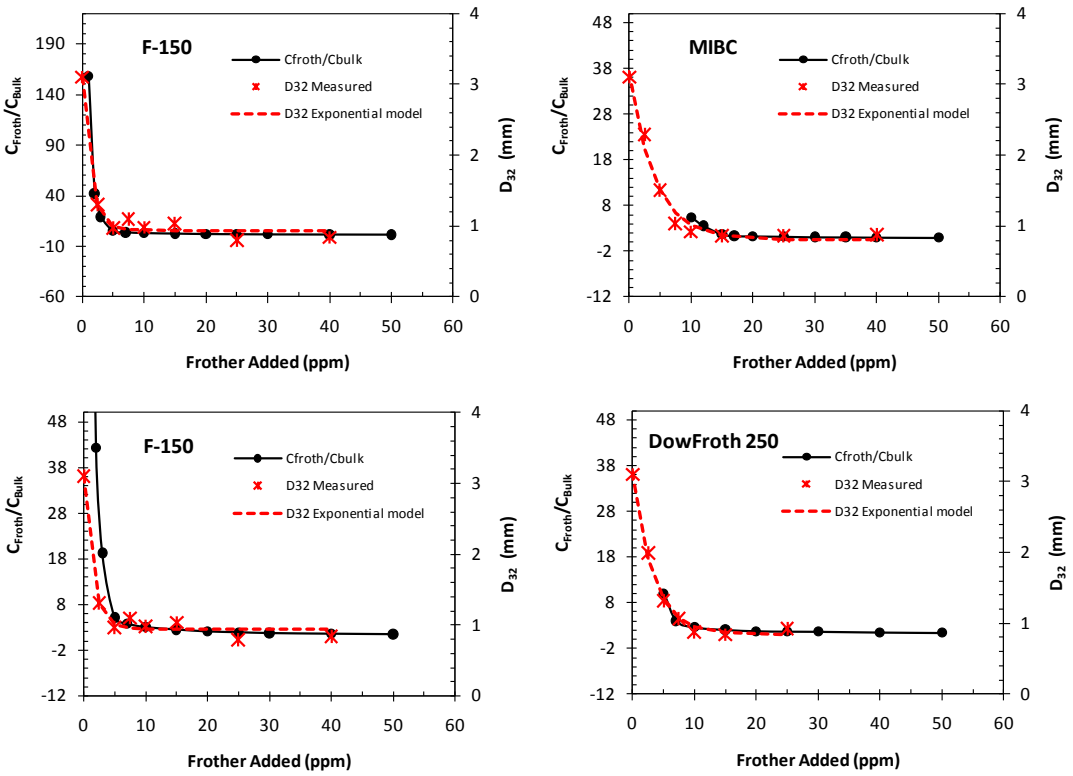

Figure 7.4 Plots showing similar exponentially decreasing relationships versus added frother for D_{32} data of this work and the C_{Froth}/C_{Bulk} ratio from results of Zhang et al

A comparison can be made between D_{32} versus added frother as reported earlier in this thesis (Section 4.1) and the reworked data of Zhang et al shown here. Figure 7.4 plots the C_{Froth}/C_{Bulk} ratio on the left ordinate axis and D_{32} on the right axis for the three frothers that were common to both studies. The scale of the left axis was chosen so as to compare curve shapes (bottom left, and top and bottom right plots have the same scale). The C_{Froth}/C_{Bulk} and D_{32} curves show similar exponential decay relationships as a function of added system frother, strongly suggesting that the frother concentration gradient between the bulk solution and the bubble interface is the driving force contributing to bubble size reduction. If one follows through on the initial premise that C_{Froth} is a representative substitute for $C_{Interface}$, in these tests then, mathematically, this can be expressed as;

$$\left[-\frac{dD_{32}}{dC}\right] \propto f\left\{\frac{C_{Frot\ h}}{C_{Bulk}}\right\} \propto f'\left\{\frac{C_{Interface}}{C_{Bulk}}\right\} \qquad 7.1$$

where C is the added concentration of frother in the system and f and f' are some functions.

Equation 7.1 expresses the notion that the concentration gradient between the bulk solution and the bubble interface is the key driver of bubble size reduction, and that the region of highest concentration gradient, $C_{Interface}/C_{Bulk}$, occurring at lowest frother addition, has the

largest impact on bubble size reduction. The comparison suggests that the maximum concentration/surface tension gradients that can occur on the bubble surface are proportional to this concentration gradient between the bulk solution and the bubble interface. It would appear to confirm, as Alves et al (2002) and Finch et al (2008) have suggested, that bubble break-up by frother is driven by surface tension gradients at the interface, and that these gradients are created by the primary driver suggested as being the concentration difference between the bulk solution and the bubble interface layer. Exploring the reasons why the largest value for $C_{Interface}/C_{Bulk}$ occurs at the lowest bulk concentrations would be an obvious area for continued investigation. This analysis also suggests a potentially simpler and faster method for determining the CCC95 (or CCC) of a frother based on measuring differences in bulk solution and froth concentration rather than by measuring D_{32} directly.

The use of CCC95

In their work on developing the CCC concept for characterizing frothers, Cho and Laskowski (2002), Laskowski (2003) and Grau and Laskowski (2006) employed a graphical technique, later simplified by an Excel routine, to determine the CCC value at the intersection of two straight lines defining the initial slope and limiting slope of the D_{32} versus frother concentration curves. The CCCX method developed in this work, curve fitting to an exponential relationship, is seen as an easier and more flexible method that allows for the ready determination of any desired CCCX value. This approach is an extension of work by Cunningham (2006). The CCC95 values determined by this method are very similar to the CCC values of Laskowski as seen for MIBC and DowFroth 250 in Table 7.1. For reporting purposes they can be considered as equivalent since Laskowski's CCC values fall within the 95% confidence interval of ±2.1 ppm established here for CCC95. The use of a simple exponential relationship for modeling the D_{32}-concentration behaviour has also permitted the incorporation of frother concentration into the D_{32} model in a straightforward manner. Laskowski (2003) concluded that the CCC is a unique property of a frother and unaffected by the J_g value used for its determination. This work has shown this not to be the case, in fact, CCC95 increases with J_g in a linear manner. The relationship has been well-defined for DowFroth 250 (Equation 5.11) and with two points for MIBC (at J_g values of 0.5 and 1 cm/s) (Equation 5.13). Clearly, more testing is needed to better define the $CCC95$-J_g relationship for the full suite of frothers but for the modeling reported here, the polyglycols were assigned the DowFroth 250 relationship, and the alcohols the MIBC relationship, based on the analysis of confidence limits presented in Section 5.2. This work has made the case for adopting CCC95 values measured at J_g of 0.5 cm/s as the standard measure for reporting of CCC95 and calibrating the equations.

The limiting D_{32} values have also been shown to depend on the frother type using CCC95 values at J_g=0.5 (Equation 5.12); those having a higher value (e.g. Pentanol) yielding a smaller (minimum) D_{32}. This has implications for the maximum S_b that is achievable and is therefore an important consideration in frother selection. Interestingly, a close examination of Laskowski's 2003 data does reveal both of these dependencies but he chose to ignore them, likely attributing the differences to measurement error.

An interesting development of the work on characterizing frother CCC95 values was the realization that an apparent (linear) relationship exists between CCC95 values and a frother's HLB to molecular weight (MW) ratio (Figure 4.3). HLB, the *hydrophile-lipophile balance*, is an empirical measure relating to the solubility of a frother (Rao and Leja, 2004). The solubility is governed by the proportional contributions of hydrophile (that which mixes with water) and lipophile (that which does not mix with water, literally *fat-loving*) groups in the molecule. The HLB number is a measure of the net contribution of the two groups to the solubility of the overall molecule in water. A low HLB number implies non-polar groups are dominant, therefore, lower solubility. On the opposite, higher HLB is consistent with higher solubility because the polar groups are stronger. For example, MIBC has an HLB of 6.1, lower than DowFroth 250 at 7.8, which corresponds to the lower solubility of MIBC. No reference could be found for the use of the ratio HLB/MW, although both Laskowski (2003) and Pugh (2007) note the importance of the HLB in frother characterization. The HLB/MW is seen as a method for normalizing frother solubility on a molar basis, essentially the hydrophobic strength per unit of molecular weight.

Table 7.1 Frother data for tests by Grau and Laskowski (2006), Nesset (2006) and Nesset et al (2010). Values reported are for J_g = 0.5 cm/s
(* refers to 1 and 2 $-C_3H_6$ groups respectively)

Surfactant	***MW***	***HLB***	***HLB/MW***	***CCC,CCC95***
Nesset (2006)				
DF250 (PG)	264.37	7.8	0.0295	10.06
F150 (PG)	425	7.83	0.0184	4.23
Pentanol (A)	88	6.52	0.0741	30.47
MIBC (A)	102	6.1	0.05981	12.37
Nesset et al (2010)				
DF250 (PG)	264.37	7.8	0.0295	9.93
F150 (PG)	425	7.83	0.0184	5.99
Pentanol (A)	88	6.52	0.0741	23.72
MIBC (A)	102	6.1	0.05981	10.54
Grau & Laskowski (2006)				
PO1* (PG)	90.12	8.3	0.0921	46.8
PO2* (PG)	148.12	8.15	0.0550	25.1
DF200 (PG)	206.29	8	0.0388	17.3
DF250 (PG)	264.37	7.8	0.0295	9.1
DF1012 (PG)	397.95	7.5	0.0188	6.6
MIBC (A)	102.18	6.1	0.0597	11.2
HEX (A)	102.20	6.00	0.0587	8.07
DEMPH (A)	248.4	6.6	0.0266	3.23
DEH (A)	190.3	6.7	0.0352	5.90
MPDEH (A)	248.4	6.6	0.0266	3.73

PG = Polyglycols, A = Alcohol Measurements at J_g = 0.5 cm/s

As a further examination of the concept that CCC95 is dependent on HLB/MW, data from Grau and Laskowski (2006) was assembled (Table 7.1) along with the data from the current work (Nesset, performed in 2006) and some follow-up testing by the author and McGill

colleagues (Nesset, Zhang and Rao performed in 2010), are also included in the table (reported values are for J_g = 0.5 cm/s). The frothers are organized into polyglycol and alcohol groups and plotted in Figure 7.5. Note that the 2010 CCC95 value for Pentanol is significantly lower than determined in 2006; 23.7 ppm versus 30.5 ppm, and corrects what was suspected (and noted earlier) of being a poor data point. The results show that a strong linear correlation for the polyglycols exists; having an R^2 value of 0.99 for the nine data points representing seven different frothers. The case for the alcohols is not as clear representing eight points, but it appears they fall on a different curve from the polyglycols and apparently not a linear one. Further testing of frothers has been initiated to better define the relationships for a broader range of alcohol groups, including isomers. The significance of the finding, if substantiated, is profound as it means that CCC95 values can be predicted for a frother from its molecular structure alone (molecular weight and HLB number). Furthermore, since the CCC95 value forms the basis for the chemical characterization of a frother, it would mean the entire model prediction for D_{32} and S_b could be established by knowing its molecular structure. Also needing to be determined is the contribution of blended frothers, i.e. is it simply a summation of the individual component frothers.

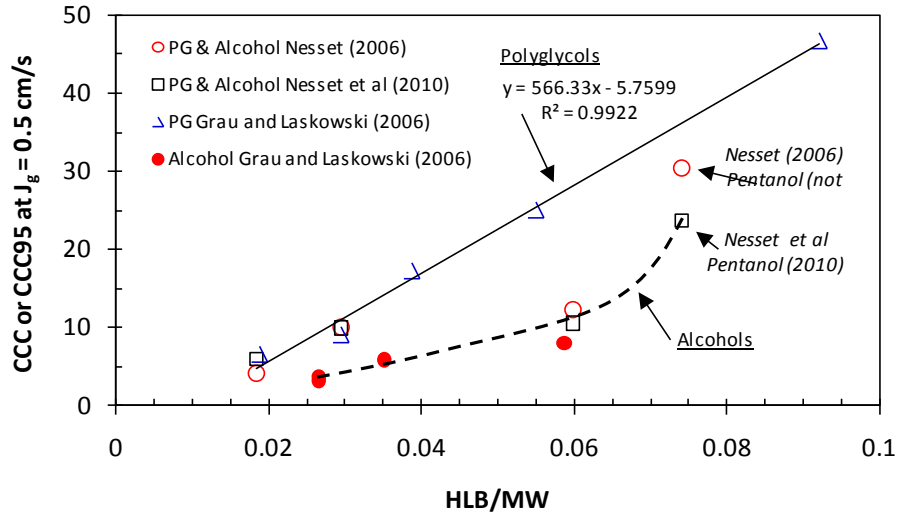

Figure 7.5 HLB/MW values versus CCC or CCC95 (measured at J_g = 0.5 cm/s) for the data of Grau and Laskowski (2006), Nesset (measured 2006) and Nesset et al (measured 2010)

Measurement correction factors

The McGill bubble viewer (BV) correction factor, developed in Section 3.4 (and Appendix B) and expressed in Equation 3.13, predicts a correction of 0.808 be applied to the measured D_{32} if no frother is present in the bubble viewer or the cell (i.e. the X in CCCX is 0). This is a sizeable correction and one that has a significant impact on the D_{32} model itself since it affects the a_0 term in Equation 5.1 directly. This zero frother correction also affects the determination of CCC95 values (i.e. they become significantly larger) since CCC95 represents 95% reduction in the a_0 term., All D_{32} data obtained (on the Metso cell subsequent to this thesis work) for 0 ppm frother in the cell was gathered. Of the total of 41

results, 31 points involved frother addition to the bubble viewer resulting in a non-coalescing condition, while ten had no frother added to the BV. The ratio of D_{32} with and without frother in the BV was 0.789, with a 95% CI of ±0.031, statistically indistinguishable from the 0.8083 value obtained using Equation 3.13 for CCCX when X=0 ppm. This serves to help confirm the validity of the correction factor equation. The BV correction factor is likely most applicable for use with the McGill device (and similar devices) and could change if a much longer, or shorter, sampling tube was employed, or a different material of construction was used. This has not been tested. Others (Grau and Heiskanen, 2005) have developed modified versions of the McGill BV that continuously remove the air entering the BV thus enabling the use of frother in the BV to produce non-coalescing conditions without the release of BV water/frother into the cell itself. Both methods, either that of Grau and Heiskanen or the correction factor method introduced here, are useful for measurements in smaller volume cells. The correction factor approach has the advantage of using whatever the concentration of frother is in the cell, particularly useful for laboratory work involving 2-phase systems if the concentration is known. Addition of frother to the BV is advantageous from the point of view of measurement precision (i.e. there is a larger standard deviation with 0 ppm frother added) and is clearly the preferred option for plant or large cell studies.

The overall equation for predicting D_{32} (Equation 5.5) introduces factors for simulated altitude (f_d) and viscosity (f_v) as well as a factor (f_l) to account for the dependence of limiting bubble size on frother type. Two, f_d and f_v, can be left at a value of 1 for general base-line conditions of sea level and 20 ^{o}C, and f_l can be set to 0 if no adjustment of the limiting bubble size is desired.

It is also recognized that the D_{32} model as developed, using the 0.7 m^3 of water in the Metso cell at essentially sea level conditions in Montreal (absolute pressure ≈ 1033 mm), and having a measurement location only 0.2 m below the froth and 0.25 m above the top of the impeller/stator, does not account for bubble expansion due to hydrostatic pressure changes in larger, deeper cells. This effect can be accounted for using the equations developed in Appendix A3 and from Gomez and Finch (2007). A fourth D_{32} factor to account for hydrostatic head, f_h, can be introduced as an additional multiplicative term in Equation 5.5. This term accounts for the decrease in hydrostatic pressure (Boyle's Law), and resulting increase in D_{32}, between the generation point as predicted by the model (P_{model}) located 0.25 m above the impeller/stator, and the reference point location ($P_{reference}$) beneath the froth where D_{32} and S_b calculations are usually of interest:

$$f_h = \sqrt[3]{\frac{P_{model}}{P_{reference}}} \qquad 7.2$$

For the example of a 130 m^3 cell, where the reference location of interest for D_{32} and S_b prediction is 0.5 m beneath the froth and is 3.75 m above the top of the impeller/stator (i.e. 3.75 m - 0.25 m = 3.5 m adjustment in hydrostatic pressure required), the correction factor to be applied to the predicted D_{32} would be of the order of 1.1, dependent on the bulk density of the pulp.

Density and viscosity effects

This work has concluded that a relatively weak relationship exists between D_{32} and the gas density ratio, $(\rho_o/\rho_g)^{0.132}$, as expressed in Equation 5.4. This is similar to the exponent of 0.16 found by Sridhar and Potter (1980), however, other elements of the Sridhar and Potter work relating to surface tension and power intensity do not agree with the current study. The work of Parthasarathy et al (1991) and later by Machon et al (1997) are supported by the current research showing that power intensity and surface tension have little effect on D_{32}. The lone reference to the effect of altitude on flotation results (Hales, 1998) in a self-aerated Wemco laboratory cell (note: may differ from this study on forced-air cells) concluded that there was no discernable effect on flotation recovery over a 4000 m altitude change.

Reference to the effect of viscosity on flotation recovery in the pulp is also very limited as noted previously. The link to flotation particle size P_{80} (= 80% cumulative passing size) of Gorain et al (1997) could be considered a viscosity effect and showed an exponent of 0.43, while the work of O'Connor et al (1990) yielded a D_{32}-viscosity link with an exponent of 0.26 for a coalescing system. The current work suggests a considerably stronger relationship may exist, having yielded D_{32} versus $(\mu/\mu_{20})^{0.776}$, and hence viscosity becomes an important design consideration for plants operating where pulp temperature fluctuations, very small particles or high % solids are present. As noted previously in the thesis, this work concerned itself with identifying the viscosity effect in the 2-phase system, recognizing that increasing solids content and smaller particle size will also impact fluid viscosity in a 3-phase system. The results of both Gorain et al (1997) and O'Connor et al (1990) suggest a weaker relationship for 3-phase system and that water viscosity on its own may be dominant.

The D_{32}-$J_g^{0.5}$ relationship

This relationship is the same as found by Sridhar and Potter (1980) and similar to the exponents of 0.4 (air-water) and 0.47 (solids-air-water) found by O'Connor et al (1990), but much stronger than found by Gorain et al (1997) who's work showed an equivalent exponent of 0.25, as did Finch and Dobby (1990) for spargers in flotation columns. A possible explanation for finding low-value exponents is that the Gorain and Finch models did not consider a non-zero bubble size at J_g = 0 cm/s (Equation 4.4). Including an intercept term is seen as a significant improvement of the current work over previous relationships and has introduced the notion of a "creation bubble size" at J_g = 0 cm/s (Nesset et al, 2006).

Does the 0.5 exponent, in fact, make sense? A simple thought experiment leads to part of the answer. Two extreme cases will be considered. If, as J_g is increased, the number of bubbles created remains the same (i.e. only the individual bubble volume increases) then the relationship will be $D_{32} \propto J_g$ and the exponent is unity. Alternatively, if the bubble size remains the same and only the number of bubbles increases, then the exponent is zero. The intermediate value obtained of 0.5 suggests that there is approximately proportional increase in both the number and size of bubbles as J_g is increased. An exponent closer to zero would suggest the bubble size increases significantly less in proportion to the number of bubbles created (this could, in fact, be the case for porous spargers as per the Finch and Dobby relationship having an exponent of 0.25). The 0.5 exponent found in this work

represents an overall average fit to the data and there are data at low J_g (< 0.2 cm/s) for which a different (and somewhat smaller) exponent would yield a better fit, however, this is below the typical operating range for most plant equipment.

Water quality

A few comments are in order regarding the quality of water (Montreal tap water) used I the development of the D_{32} model. As noted, over time (typically several weeks or months) a difference was observed in the measured D_{32}, most notable at zero frother addition. This difference has been attributed to small changes in water quality as variations in the impurity levels in the tap water are quite likely, particularly during changes of season. Minute quantities of impurities can have surfactant-like behaviour on bubble size (Clift et al, 1978). Smaller D_{32}, at zero frother addition was noted during March-April testing compared to later spring and summer. This highlights a potential problem with any model development, or laboratory testing, using equipment that is too large to fill with distilled or de-ionized water, so "slightly-contaminated" tap water must be contended with. Pure water however, would never be available as the zero frother condition at operating sites regardless, so the question remains as to the most appropriate water to use for model development. Observations of the D_{32} values reported for this work at zero ppm frother has found the values to be mid-range between those reported by others such as Grau and Heiskanen (2002, 2003, 2005) and Laskowski (2003).

Final comments

Overall, the D_{32} model developed in this work is seen as filling an important role linking key operating variables to prediction of both bubble size (D_{32}) and bubble surface area flux (S_b), and the all-important k-S_b relationship. There have been no comprehensive D_{32} models available to date for forced-air mechanical flotation machines (or any flotation machine type). Those relationships that exist are for systems that are either not entirely appropriate for flotation (such as stirred tank reactors or bioreactors), or suffered from issues of scale having developed relationships on laboratory sized cells. A major strength of this work is the use of a sufficiently large cell (700 liters) in which the quiescent zone of interest could clearly be studied with minimal influence from the near-impeller turbulent zone. Although the system investigated was the 2-phase air-water system, comparison to a wide range in plant data suggests that it has good applicability to 3-phase systems, at the least an appropriate starting framework. The suggestion is that for most plant systems the effect of solids may be secondary, or partly included within the viscosity parameter. The model has provided a framework and an approach that can be used for further refinement of the relationships between D_{32}, S_b and the key operating variables. One obvious outcome would be to move the equipment to a plant environment and "re-calibrate the parameters" in the context of a 3-phase, air-water-solids system. Researchers and modelers should also find the model developed here to be a useful addition to their arsenal given that, to-date, they have had to resort to using constant values for D_{32} or rely on rudimentary relationships. One obvious development would be the incorporation of this work, in some fashion, into the JKSimFloat™ model of flotation that currently uses the empirical model of Gorain et al (1997). This has

been shown to have shortcomings in the relationships for gas rate, impeller speed, viscosity and no means of accounting for frother type or concentration. The incorporation of frother type and concentration into the D_{32} model, and the apparent ability to link frother type through CCC95 directly to the HLB/MW parameter, essentially to the molecular structure, are seen as major advancements over anything currently available. Since frother has the greatest impact on bubble size, this is a powerful development indeed.

CHAPTER 8: Conclusions and Claims to Original Research

8.1 Conclusions

This thesis has addressed the development of a mathematical expression for predicting the Sauter bubble size, the D_{32}, for forced-air mechanical flotation machines. The D_{32} is a key metric in flotation, a bubble-surface-area-dependent process, since it relates gas volume delivered to the total bubble surface area for a distribution of bubbles. Through the relationship $S_b=6J_g/D_{32}$ the results also serve as a model for prediction of the bubble surface area flux S_b. The selected variables for study were the key ones (manipulated and situational) impacting the process; frother type and concentration, superficial gas velocity, impeller rotational speed, viscosity and gas density (simulating altitude). The model was validated by comparison of predicted D_{32} and S_b to measured values from five plants worldwide. The main conclusions from this work are the following:

1. There currently exists no single mathematical expression (i.e. model) for predicting D_{32} in mechanical flotation machines from the key process variables, either in the chemical engineering or mineral processing literature. This is seen as a significant shortcoming given the importance of flotation over the past 100 years in successfully securing metal production from large, complex and often low-grade ore deposits. This work has produced such a model for the 2-phase gas-water system and validated the results on the 3-phase system with plant data from 5 operating sites.
2. The most significant variable in terms of impact on D_{32} is the frother concentration. The effect of concentration (ppm) for different frother types has been shown to be the same once "normalized" by the introduced parameter $ppm/CCC95$, based on the concept of the CCC (critical coalescence concentration) introduced by Laskowski (2003). CCC95 is equivalent to Lakowski's CCC, but an easier parameter to determine and incorporate into mathematical expressions. An exponential-decay relationship utilizing the $ppm/CCC95$ parameter has been shown to well represent the effect of increasing frother concentration on D_{32}. An argument is advanced (based on a parallel study) that the ratio (or gradient) of frother concentration between the bulk solution and the bubble-water interface is the driver behind bubble size reduction by frother addition. This ratio is highest at low bulk concentrations of frother below the CCC.
3. CCC95 for a polyglycol-based frother appears to be uniquely determined from knowledge of its HLB (hydrophile-lipophile balance) and molecular weight (MW) through the HLB/MW ratio. A different relationship using the HLB/MW ratio may also apply for alcohol-based frothers. The effect of any frother on D_{32} and S_b, can therefore be determined directly from knowledge of its molecular structure.
4. There is an interaction between the superficial gas velocity, J_g, and the CCC95 of a frother, so that CCC95 values need to be specified at a particular value of J_g. As a convention, reporting CCC95 values at J_g = 0.5 cm/s has been proposed. Although CCC95 increases with increasing J_g, the relationship differs for polyglycol and alcohol-type frothers, with polyglycols having a stronger dependency.

5. D_{32} is dependent on $J_g^{0.5}$ with a non-zero value for D_{32} at J_g = 0 cm/s (a notional "creation size"). The square-root dependency suggests an approximately proportional increase in both the bubble size and number of bubbles created as J_g is increased.
6. The limiting bubble size at increasing frother concentration is also influenced by the frother CCC95 (or CCC), and therefore in turn, the HLB/MW ratio; higher values of CCC95 produce a smaller limiting bubble size. This has significant implications for frother selection when small bubbles or high bubble surface area flux, S_b, are desired for the process.
7. The effect of impeller tip speed on D_{32} over the industrial operating range of 4.6 to 9.2 m/s is minimal and therefore is not included in the final D_{32} model. The finding is valid for both coalescing and non-coalescing conditions. This agrees with some of the literature data but not all. The discrepancy is explained by noting that some studies have been conducted on small-volume cells or with bubble size measured in the highly turbulent region close to the impeller. Given that a key gas dispersion parameter is the bubble surface area flux (S_b) exiting the pulp zone, the argument is made that D_{32} should properly be measured in the quiescent zone at this location when used to calculate S_b. The Metso RCS™ cell used in this work was of a design, and hence afforded D_{32} measurement, with distinct separation of turbulent and quiescent zones.
8. The effect of viscosity was established by temperature variation of the water in the test cell, covering the range of 4 to 40 ^oC, and showed that liquid viscosity has a significant impact on bubble size. The D_{32} increases proportionally as $(\mu/\mu_{20\,^oC})^{0.776}$, a finding that highlights the importance of accounting for viscosity effects if, for example, large process temperature fluctuations or deviation from design/test conditions are expected.
9. The effect of altitude was simulated by varying the gas density of an air-helium mixture feeding a 5.5 liter Denver laboratory cell and showed a relatively small impact of density on bubble size for the practical range of altitude variation 0 to 5,000 m. The D_{32} was found to increase proportionally as $(\rho_o/\rho_g)^{0.132}$, taken to apply to forced-air mechanical cells. This relationship may not apply to self-aerating cells. The projected impact on flotation kinetics at 4500 m versus sea level is small, of the order of 1/2% recovery loss for a bank of eight flotation cells.
10. Conclusions 7 and 8 indicate that while impeller speed is not a factor in determining D_{32}, fluid viscosity is. The impeller N_{Re}, being greater than 10^5, well into the turbulent range, would appear not to be the determining hydrodynamic parameter for D_{32} since that would imply no effect of viscosity and a drag force dependency on velocity squared. A case is made that the bubble N_{Re}, being 10^3 to 10^4 in the high free-stream turbulence and high gas holdup region of the impeller/stator, is the hydrodynamic measure of significance. The literature shows that bubbles in bubble swarms under these conditions have a significantly reduced drag coefficient that decreases with increasing turbulence resulting in less effect of velocity and more effect of viscosity on the resulting (disruptive) drag force on a bubble. This interpretation better matches the observed results in this work.

11. A useful and practical development of the D_{32} model is the S_b- J_g "roadmap" that can be used to benchmark plant performance, and suggest the potential for improvement. The excellent agreement with plant data presented here also suggests that the 2-phase model is an appropriate model for 3-phase systems, albeit that some additional validation and calibration work is likely needed. It also suggests that the effect on D_{32} of solids of the size and volumetric concentrations in most plants is a secondary effect; in fact, it may largely be covered by the viscosity term already included.
12. The overall D_{32} model developed here has been shown to be sufficiently robust across a wide range of operating conditions, and with sufficient precision, to be of significant benefit to those requiring D_{32} and S_b estimates for modeling, as well as those involved in process design and operation looking for ways to improve plant performance.

8.2 Claims to Original Research

- A true measure of the bubble size leaving the quiescent region of the pulp zone was determined with minimal influence of the strong recirculation within the impeller region. This unique approach was made possible by the selection of a sufficiently large cell (700 liters) *having an internal shelf-baffle* that permitted the distinct separation of turbulent (near impeller) and quiescent (near froth layer) zones. As a result, the calculated key bubble surface area flux parameter (S_b) that links to flotation kinetics is also a true measure of what exits the pulp zone. By extension, this has also permitted a true measure of the D_{32} and S_b created in the impeller/stator region.
- Development of the first comprehensive mathematical expression for prediction of D_{32} for mechanical, forced-air flotation machines. By comprehensive it is meant that the key operating variables of frother type and concentration, gas rate, viscosity and altitude (gas density) have been accounted for. Surprisingly, impeller speed (power intensity) was not a significant factor. The model has been developed within the 2-phase air-water system but appears to be applicable for the 3-phase system, i.e. including solids. Some calibration within the 3-phase system will likely be required.
- The mathematical incorporation of frother type and concentration into the D_{32} model using the newly developed approach of $ppm/CCC95$ and the HLB/MW ratio to characterize frothers.
- Establishing the effect on D_{32} of i) viscosity, by varying the water temperature, and ii) simulating altitude, by testing gas mixtures (air and helium) of varying density.
- Development of a method for correcting measured D_{32} when the frother concentration in the bubble viewer is the same as that in the cell, often the case in laboratory studies when contamination by water from the bubble viewer chamber into the cell must be avoided.

8.3 Contributions to Knowledge

- A single mathematical expression has been developed and validated for prediction of D_{32} from key process variables for forced-air mechanical flotation machines in a 2-phase (air-water) system. By extension, the same model can be used for prediction of the bubble surface area flux, S_b. The model is suitable for calibration in a 3-phase (air-water-solids) flotation plant environment, but fits plant data well using the current parameters established for the 2-phase system.
- The D_{32} model equations are used to provide a "roadmap", or method for benchmarking plant performance in terms of S_b versus J_g behaviour. This is seen as a powerful tool for process optimization as illustrated with the Lac des Iles case study.
- The CCCX and, specifically, CCC95 concepts using an exponential decay relationship and normalized frother concentration, $ppm/CCC95$, to characterize the effects of frother type and concentration on D_{32}. This exponential decay relationship for D_{32} versus frother concentration is shown to be linked to the ratio between frother concentrations at the bubble/water interface and in the bulk solution ($C_{interface}/C_{bulk}$), thus demonstrating that the largest impact on bubble size reduction occurs when this ratio (i.e. concentration gradient) is at its highest. The $CCC95$ parameter is equivalent to Laskowski's CCC value but is easier to accommodate mathematically in a model.
- The importance of the HLB/MW ratio for prediction of $CCC95$ for polyglycol-type frothers; i.e. frother effect on bubble size reduction can be predicted from molecular structure. The link appears likely to extend to alcohol-type frothers also, although the current data are limited.
- A postulation is offered regarding the hydrodynamic conditions that exist in the impeller/stator region to explain the dependence of D_{32} on viscosity but not on impeller velocity (power intensity). Bubble swarms of individual bubble diameter 1 - 3 mm, having (laminar) free-stream N_{Re} in the 10^3-10^4 range, are subjected to high free-stream turbulence and high gas-holdup that significantly reduce the drag coefficient and hence the (disruptive) drag force on individual bubbles. This effectively places the bubbles within a hydrodynamic regime where the drag coefficient is no longer constant, and where viscosity effects are significant and relative velocity effects are much less so.

8.4 Recommendations

- Confirm the D_{32} model in a plant environment (i.e. 3-phase system) by running at various frother concentrations between 0 ppm (coalescing) and beyond the CCC (non-coalescing) across a broad range of J_g. Ideally, the same Metso unit could be used
- Re-test the limiting bubble size, D_l, for a wider selection of frothers, particularly alcohol-type frothers that appear to produce smaller bubble size, and hence higher S_b, than polyglycol frothers

- Explore an alternative method for calculating the $CCC95$ value of a frother based on measuring the ratio of frother concentration in froth and bulk (i.e. pulp) phases. Such a method is potentially faster and easier than the current method involving direct measurement of the BSD and calculation of D_{32}, and avoids the issue of maintaining non-coalescing conditions in the bubble viewer or correcting the measured D_{32}.
- Extend and confirm the HLB/MW parameter as a predictor for $CCC95$ to cover a broader range of polyglycols and alcohol-type frothers
- Continue to examine the relationship between frother concentration in the bulk solution and at the bubble-water interface, $C_{interface}/C_{bulk}$, and why the highest ratio produces the largest effect on bubble size reduction
- Explore the feasibility of incorporating the D_{32} model into simulation software such as JKSimFloat™

REFERENC**ES**

Al Taweel, AM, Cheng, YH, 1995, Effect of surface tension on gas/liquid contacting in a mechanically-agitated tank with stator, Trans Inst Chem Eng Research Design, Vol 73 (A6), pp 654-660

Alves, SS, Maia, CI, Vasconcelos, JMT, Serralheiro, AJ, 2002, Bubble size in aerated stirred tanks, Chem Eng J, Vol 89, pp109-117

Anfruns, JP, Kitchener, JA, 1976, Flotation machines, A. M. Gaudin Memorial Volume (Ed. MC Fuerstenau), SME of AIME, Vol 2, pp 625-637

Arbiter, N, Steininger, J, 1965, Hydrodynamics of flotation machines, Mineral Processing (Ed. E Roberts), Pergammon (New York), pp 595-608

Arbiter, N, Harris, CC, Yap, RF, 1976, The air flow number in flotation machine scale-up, Int J Miner Process, Vol 3, pp 257-280

Arbiter, N, 1999, Development and scale-up of large flotation cells, Advances in Flotation Technology (eds. Parekh, BK, Miller, JD, (SME), pp 345-352

Azgomi, F, Gomez, CO, Finch, JA, 2009, Frother persistence: A measure using gas holdup, Minerals Engineering, Vol 22, pp 874-878

Banisi, S, Finch JA, 1994, Reconciliation of bubble size estimation methods using drift flux analysis, Minerals Engineering, Vol 7 (12), pp 1555-1560

Bailey, M, Gomez, CO, Finch, JA, 2005, Development and application of an image analysis method for wide bubble size distributions, Minerals Engineering, Vol 18, pp 1214-1221

Calderbank, PH, 1958, The interfacial area in gas-liquid contacting with mechanical agitation, Trans Instrum Chem Eng, Vol 36, pp 443-463

Cappuccitti, F, 2007, President Flottec Inc, Personal communication

Cappuccitti, F, Nesset, JE, 2010, Frother and collector effects on flotation cell hydrodynamics and their implication on circuit performance, Proceedings 42nd Annual Meeting Canadian Mineral Processors, pp 39-54

Cho, YS, Laskowski, JS, 2002, Effect of flotation frothers on bubble size and foam stability, Int Journal Mineral Processing, Vol 64, pp 69-80

Cilliers, JJ, 2007, The froth in column flotation, Froth Flotation: A Century of Innovation (Eds. Fuerstenau, MC, Jameson, G, Yoon, RH) SME Publications, pp 708-729

Clift, R, Grace, JR, Weber, ME, 1978, Bubbles, Drops and Particles, Academic Press (NY)

Coleman, RG, Urtubia, HE, Alexander, DJ, 2006, A comparison of BHP-Billiton's Minera Escondida concentrators, Proceedings 38th Annual Meeting Canadian Mineral Processors (CIM), pp 349-370

Cooper, M, Scott, D, Dahlke, R, Finch, JA, Gomez, CO, 2004, Impact of air distribution profile on banks in a Zn cleaning circuit, CIM Bull, October 2004, Paper 13 (6 pages)

Cunningham, R, 2006, Comments on methods used in determining the CCC, Internal Report (McGill University), 5 pages

Dahlke, R, Gomez, CO, Finch, JA, 2005, Determining operating range of a flotation cell from gas holdup vs. gas rate, Minerals Engineering, Vol 18 (9), pp 977-980

Deglon, DA, Egya-Mensah, D, Franzidis, JP, 2000, Review of hydrodynamics and gas dispersion in flotation cells on South African platinum concentrators, Minerals Engineering, Vol13 (3), pp 235-244

Delprat, GD, 1904, Australian Patent No 763662, June 28

Dobby, GS, Finch, JA, 1986, Particle collection in columns – gas rate and bubble size effects, Can Metall Quart, Vol 25 (1), pp 9-13

Doucet, JS, Gomez, CO, Finch, JA, 2006, A first step towards gas dispersion management: Manipulation of gas distribution in flotation circuits, Proceedings 38th Annual Meeting Canadian Mineral Processors (CIM), pp 423-436

Elmore, FE, 1898, British Patent 21 948, 18 October

Everson, RJ, 1885, U.S. Patent 348,157, Aug 29

Fallenius, K, 1976, Outokumpu flotation machines, AM Gaudin Memorial Volume (Ed. MC Fuerstenau) (SME), Vol. 2, pp 838-861

Finch, JA, Dobby, GS, 1990, Column Flotation, (Pergamon Press)(Oxford)

Finch, JA, Gélinas, S, Moyo, P, 2006, Frother-related research at McGill University, Minerals Engineering, Vol 19 (6-8), pp 726-733

Finch, JA, Nesset, JE, Acuna, C, 2008, Role of frother on bubble production and behaviour in flotation, Minerals Engineering, Vol 21, pp 949-957

Foreman, D, 2010, FL Smidth Ltd, personal communication

Froment, A, 1902 British Patent 12 778, 4 June

Fuerstenau, DW, 2007, A century of developments in the chemistry of flotation processing, Froth Flotation: A Century of Innovation (Eds. Fuerstenau, MC, Jameson, G, Yoon, RH) (SME Publications), pp 3-64

Gélinas, S, Finch, JA, 2005, Colorimetric determination of common industrial frothers, Minerals Engineering, Vol 18 (2), pp 263-266

Gélinas, S, Gouet-Kaplan, M, Finch, JA, 2005b, Comparative real-time characterization of frother-bubble thin films, Colloid and Interface Science, Vol 291, pp187-191

Gomez, CO, Finch, JA, 2002, Gas dispersion measurements in flotation machines, CIM Bulletin, Vol 95 (1066), pp 73-78

Gomez, CO, Cortes-Lopez, F, Finch, JA, 2003, Industrial testing of a gas holdup sensor for flotation systems, Minerals Engineering, Vol 16, pp 493-501

Gomez, CO, Acuña, CA, Girgin, EH, Finch, JA, 2006, Bubble distributions in laboratory flotation machines: Measurement and evolution with increasing gas velocity, Proceedings of the International Mineral Processing Congress, (Istanbul), pp 579-586

Gomez, CO, Finch, JA, 2007, Gas dispersion measurements in flotation cells, Int J Miner Process, Vol 84, pp 51–58

Gorain, BK, Franzidis, JP, Manlapig, EV, 1997, Studies on impeller type, impeller speed, and air flow rate in an industrial scale flotation cell - Part 4: Effects of bubble surface area flux on flotation kinetics, Minerals Engineering, Vol 10 (4), pp 367-379

Gorain, BK, Franzidis, JP, Manlapig, EV, 1999, The empirical prediction of bubble surface area flux in mechanical flotation cells, Minerals Engineering, Vol 12 (3), pp 309-322

Grano, S, 2006, Effect of impeller rotational speed on the size dependent flotation rate of galena in full scale plant cells , Minerals Engineering, Vol 19, pp 1307-1318

Grau, RA, Heiskanen, K, 2002, Visual technique for measuring bubble size in flotation machines, Minerals Engineering, Vol 15, pp 507-513

Grau, RA, Heiskanen, K, 2003, Gas dispersion measurements in a flotation cell, Minerals Engineering, Vol 16, pp 1081-1089

Grau, RA, Heiskanen, K, 2005, Bubble size distribution in laboratory scale flotation cells, Minerals Engineering, Vol 18, pp 1164-1172

Grau, RA, Laskowski, JS, Heiskanen, K, 2005, Effect of frothers on bubble size, Inter Journal Mineral Processing, Vol 76, pp 225-233

Grau, RA, Laskowski, JS, 2006, Role of frothers in bubble generation and coalescence in a mechanical flotation cell, Can Journal of Chemical Engineering, Vol 84, pp 170-182

Grönstrand, S, Niitti, T, 2007, Flotation enters its second century with higher intensity and bigger capacity, Proceedings Mineral Processing Conference (Mineral Teknik) (February 6-7, 2007), Luleå, Sweden, 13 pages

Grönstrand, S, 2010, personal e-mail communication

Gupta, A, Yan, DS, 2006, Mineral Processing Design and Operations: An Introduction, (Elsevier) (Amsterdam), p 559

Hales, ML, 1998, The effect of altitude on aeration of a lab model Wemco Smart Cell™ flotation machine, Baker Process, Baker Hughes Report

Harbort, G, Schwarz, S, Characterisation measurements in industrial flotation cells, Flotation Plant Optimisation (Ed. CJ Greet), 2010, AusIMM (Carlton, Australia), pp 95-106

Harris, CC, 1976, Flotation machines, AM Gaudin Memorial Volume, Vol 2, (Ed. MC Fuerstenau), (SME), pp 753-815

Harris, MC, Runge, KC, Whiten, WJ, Morrison, RD, 2002. JKSimFloat as a practical tool for flotation process design and optimization, Proceedings of the SME Mineral Processing Plant Design, Practice and Control Conference (SME), Vancouver, pp 461-478

Heiskanen, K, 2000, On the relationship between flotation rate and bubble surface area flux, Minerals Engineering, Vol 13 (2), pp 141-149

Herbst, JA, Harris, MC, 2007, modeling and simulation of industrial flotation processes, Froth Flotation: A Century of Innovation (Eds. Fuerstenau, MC, Jameson, G, Yoon, RH) (SME Publications), pp 757-777

Hernandez, H, Gomez, CO, Finch, JA, 2003, Gas dispersion and de-Inking in a flotation column, Minerals Engineering, Vol 16 (6), pp 739-744

Hernandez-Aguilar, JR, Gomez, CO, Finch, JA, 2002, A technique for the direct measurement of bubble size distribution in industrial flotation cells, Proceedings 34th Annual Meeting Canadian Mineral Processors (CIM), pp 389-402

Hernandez-Aguilar, JR, Coleman, RG, Gomez, CO, Finch, JA, 2004, A comparison between capillary and imaging techniques for sizing bubbles in flotation systems, Minerals Engineering, Vol 17, pp 53-61

Hernandez-Aguilar, JR, Finch, JA, 2005, Validation of bubble sizes obtained with incoherent imaging on a sloped viewing window, Chemical Engineering Science, Vol 60, pp 3323-3336

Hernandez-Aguilar, JR, Rao, SR, Finch, JA, 2005b, Testing the k-Sb relationship at the micro-scale. Minerals Engineering, Vol 18, pp 591-598

Hernandez-Aguilar, JR, Thorpe, R, Martin, CJ, 2006, Experiences in using gas dispersion measurements to understand and modify metallurgical performance, Proceedings 38th Annual Meeting Canadian Mineral Processors (CIM), pp 387-402

Hinze, JO, 1955, Fundamentals of the hydrodynamic mechanism of splitting in dispersion processes, AIChE J, Vol 1(3), pp 289-295

Hoover, TJ, 1914, Concentrating Ores by Flotation, 2nd Edition, The Mining Magazine (London)

Jameson, GJ, Nam, S, Moo Young, M, 1977, Physical factors affecting recovery rates in flotation, Minerals Sci Eng, Vol 9(3), pp 103-118

Jameson, GJ, Allum, P, 1984, A survey of bubble sizes in industrial flotation cells, Report to Australian Mineral Industries Research Association Ltd.

Kelly, EG, Spottiswood, DJ, 1982, Introduction to Mineral Processing, (J. Wiley and Sons), pp 27-29

King, RP, 1972, Flotation research work of the N.I.M research group and the Department of Chemical Engineering, University of Natal, J. South Afr. Inst. Min. and Metall., Vol 72 (4), pp 135-145

King, RP, 1973, A computer programme for the simulation of the performance of a flotation plant, (South African) National Institute of Metallurgy Research Report (Revised), No. 1436, p 10

Koh, PTL, Manickam, M, Schwarz, MP, 2000, CFD simulation of bubble-particle collisions in mineral flotation cells, Minerals Engineering, Vol 13(14-15), pp 1455-1463

Koh, PTL, Schwarz, MP, 2001, CFD modeling of the Svedala flotation cell hydrodynamics, CSIRO Minerals Report No. 1786

Koh, PTL, Schwarz, MP, 2004, P780 CFD modeling of Metso Minerals flotation cell, FinalReport to AMIRA International, CSIRO Minerals Report No. DMR 2428

Koh, PTL, Schwarz, MP, 2007, CFD model of a self-aerating flotation cell, Int J Miner Process, Vol 85, pp 16-24

Kolmogorov, AN, 1949, On the breakage of drops in a turbulent flow, Dokl Akad Navk SSSR, Vol66, pp 825-828

Laist, F, 1933, History of reverberatory smelting in Montana, Copper Metallurgy 1933, AIME Vol 106 , pp 23-87

Laplante, AR, Toguri, JM, Smith, HW, 1983, The effect of air flow rate o the kinetics of flotation. Part 1: The transfer of material from the slurry to the froth, Int J Min Process, Vol 11, pp 203-219

Laskowski, JS, 1993, Frothers and flotation froth, Min Proc And Extractive Metal Review, Vol 12, pp 61-89

Laskowski, JS, 1998, Frothers and frothing, Frothers in Flotation II (Eds. JS Laskowski and ET Woodburn) (Gordon and Breach), pp 1-50

Laskowski, JS, 2003, Fundamental properties of flotation frothers, Proceedings of the 22nd International Mineral Processing Congress (Cape Town), pp 788-797,

Lynch, AJ, Watt, JS, Finch, JA, Harbort, GE, 2007, History of flotation technology, Froth Flotation: A Century of Innovation (Eds. Fuerstenau, MC, Jameson, G, Yoon, RH) (SME Publication), pp 65-91

Machon, V, Pacek, AW, Nienow, AW, 1997, Bubble sizes in electrolyte and alcohol solutions in a turbulent stirred vessel, Trans Instrum Chem Eng, Vol 75(A), pp 339-348

Martinez-Bazan, C, Montanes, JL, Lasheras, JC, 2000, Bubble size distribution resulting from the break-up of an air cavity injected into a turbulent water jet, Physics of Fluids, Vol 12 (1), pp 145-148

Massey, BA, 1975, Mechanics of Fluids (van Nostrand Reinhold) (London)

Menghetti, D, 2005, Invention and innovation in the Australian non-ferrous mining industry: Whose technology?, Australian Economic History Review, Vol 45 (2), pp 201-219

Moradian, N, Ting, DSK, Cheng, S, 2009, The effects of freestream turbulence on the drag coefficient of a sphere, Experimental Thermal and Fluid Science, Vol 33, pp 460–471

Mouat, J, 1996, The development of the flotation process: technological change and the genesis of modern mining, 1898–1911, Australian Economic History Review, Vol 36, pp 3–31

Nesset, JE, Gomez CO, Finch JA, Hernandez-Aguilar, JR, DiFeo, A, 2005, The use of gas dispersion measurements to improve flotation performance, Proceedings 37th Annual Meeting of the Canadian Mineral Processors (CIM), pp 401-421

Nesset, JE, Hernandez-Aguilar, JR, Acuña, C, Gomez, CO, Finch, JA, 2006, Some gas dispersion characteristics of mechanical flotation machines, Minerals Engineering, Vol19 (6-8), pp 807-815

Nesset, JE, Finch, JA, Gomez, CO, 2007, Operating variables affecting bubble size in forced-air mechanical flotation machines, AusIMM, Proceedings of the 9th Mill Operators Conference, pp 55-65

Nonaka, M, Inoue, T, Imaizumi, T, 1982, A microhydrodynamic flotation model and its application to the flotation process, Proceedings of the 14th International Mineral Processing Congress (Toronto), Vol. III, pp 9.1-9.19

O'Connor, CT, Randall, EW, Goodall, CM, 1990, Measurement of the effects of physical and chemical variables on bubble size, Int Jour Min Proc, Vol 28, pp 139-149

Oldshue, JY, Fluid Mixing Technology, 1983, (Chemical Engineering McGraw-Hill) (NY)

Parthasarathy, R, Jameson, GJ, Ahmed, NM, 1991, Bubble break-up in stirred vessels predicting the Sauter mean diameter, Trans I Chem Eng, Vol 69(A), pp 295-301

Pogorely, AD, 1962, Limits of the use of the kinetic equation proposed by K.F. Beloglazov , Invest Uysskikh Ucheb. Zavendenii. Tsvetn. Metall., Vol 5, pp 33-50

Pugh, RJ, 2007, The physics and chemistry of frothers, Froth Flotation: A Century of Innovation (Eds. Fuerstenau, MC, Jameson, G, Yoon, RH) (SME Publications), pp 259-281

Pyecha, J, Sims, S, Lacouture, B, Hope, G, Stradling, A, 2006, valuation of a Microcell™ sparger in the Red Dog column flotation cells, Minerals Engineering, Vol 19 (6-8), pp 748-757

Quinn, JJ, Kracht, Gomez, CO, Gagnon, C, Finch, JA, 2007, Comparing the effect of salts and frother (MIBC) on gas dispersion and froth properties, Minerals Engineering, Vol 20, pp 1296-1302

Randall, EW, Goodall, CM, Fairlamb, PM, Dold, PL, O'Connor, CT, 1989, A method for measuring the sizes of bubbles in two and three-phase systems, Journal of Physics E: Scientific Instruments, Vol 22, pp 827-833

Reay, D, Ratcliff, GA, 1975, Removal of fine particles from water by dispersed air flotation: effects of bubble size and particle size on collection efficiency, Can J. Chem Eng, Vol 53(10), pp 178-185

Rao, SR, Leja J, 2004, Surface Chemistry of Froth Flotation Volume II, (Kluwer Academic Publishers) (New York), pp 663-666

Rickard, TA, 1916, The Flotation Process,(Mining and Scientific Press) (San Francisco), 364 pages

Sawant, SB, Joshi, JB, Pangarkar, VG, Mhaskar, RD, 1981, Mass transfer and hydrodynamic characteristics of the Denver type flotation cells, Chem Eng J, Vol 21, pp 11-19

Schubert, H, 2008, On the optimization of hydrodynamics in fine particle flotation, Minerals Engineering, Vol 21, pp 930-936

Simonnet, M, Gentric, C, Olmos, E, Midoux, N, 2007, Experimental determination of the drag coefficient in a swarm of bubbles, Chemical Engineering Science, Vol 62, pp 858 – 866

Sridhar, T, Potter, OE, 1980, Interfacial areas in gas-liquid stirred vessels, Chem Eng Sci, Vol 35, pp 683-691

Sulman, HL, Kirkpatrick-Picard, HF, Ballot, J, 1906, British Patent No 835120, Nov 6

Taggart, AF, 1954, Handbook of Mineral Processing, (Wiley) (NY), pp 12-78 to12-82

Wilkinson, PM, van Dierendonck, L, 1990, Pressure and gas density effects on bubble break-up and gas hold-up in bubble columns, Chem Eng Sci, Vol 45, pp 2309-2315

Wills, BA, Napier-Munn, TJ, Wills' Mineral Processing Technology, 2007, 7th Edition, (Elsevier) (Amsterdam), pp 276-277

Wraith, AM., Li, R, Harris, R, 1995, Gas bubble volume in a narrow slot nozzle in a liquid, Chem Eng Sci, Vol 50(6), pp 1057-1058

Xu, M, Finch, JA, 1989, Effect of sparger surface area on bubble diameter in flotation columns, Can Metall Q, Vol 28(1), pp 1-6

Xu, M, Finch, JA, Uribe-Salas, A, 1991, Maximum gas and bubble surface area rates in flotation columns, Int J Miner Process, Vol 32, pp 233-250

Yianatos, JB, Bergh, LG, Condori, P, Aguilera, J, 2001, Hydrodynamic and metallurgical characterization of industrial flotation banks for control purposes. Minerals Engineering, Vol 14(9), pp 1033–1046

Zhang, W, Kolahdoozan, M, Nesset, JE, Finch, JA, 2009, Use of frother for sampling-with-imaging bubble sizing technique, Minerals Engineering, Vol 22, pp 513-515

Zhang, W, Nesset, JE, Finch, JA, 2009b, Water recovery and bubble surface area flux, Proceedings of the 7th UBC-McGill-UA International Symposium on Fundamentals of Mineral Processing (Eds. Gomez, CO, Nesset, JE, Rao, SR), (MetSoc Publication) (CIM), pp 155-168

Zhu, Y, Nguyen, B, Wu, J, Shepherd, IC, 2001, CSIRO Minerals Report No. DBCE DOC 01/309 (Melbourne)

APPENDIX A: Gas Dispersion Measurements and Correction Factors
(Adapted from the McGill Manual on Gas Dispersion Measurements. Courtesy of Dr. C.O. Gomez)

The three McGill sensors rely on collection of bubbles by natural buoyancy in a sampling tube, either to make direct measurements in the tube (gas holdup) or to transport bubbles to the measurement location (gas velocity and bubble size).

A.1 Gas Velocity Sensor

The gas velocity sensor is based on the collection of bubbles from the pulp zone into a vertical tube partially immersed in the cell below the froth. The collected bubbles rise until they reach the liquid surface and burst. If the tube is closed at the top, the gas accumulates, pressure increases, and the slurry (and any froth layer) is pushed down the tube. The rate of descent is related to the superficial gas velocity and can be monitored by the rate of increase in pressure.

The sensor is constructed around a piece of PVC plastic tube positioned vertically and fitted at the top with two outlets (Figure A.1). One outlet is connected to a pressure transmitter to continuously monitor gas pressure and the other houses a manual globe valve. Electronics and software have been developed to collect, digitize and register the signal from the pressure transmitter (Wika, model 8367656) using serial communication.

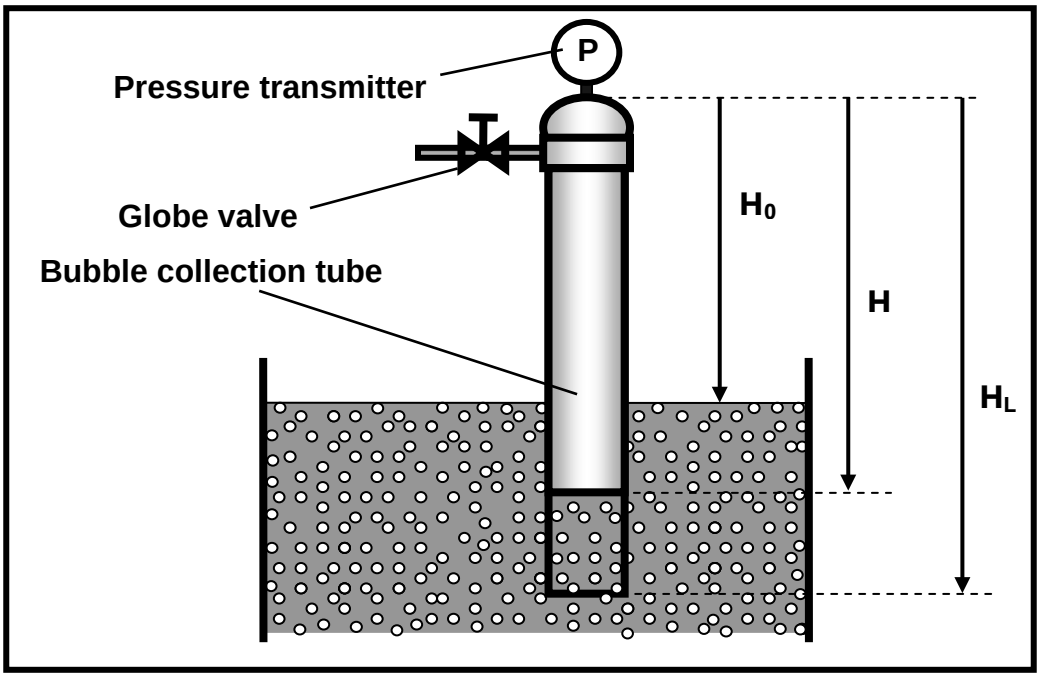

Figure A.1 Schematic diagram of gas velocity sensor indicating construction details, installation, and relevant dimensions

When the sensor is in position with the valve open, gauge pressure is zero. Once the valve is closed, gas accumulates, and pressure increases at a rate proportional to the gas flow into the tube (Figure A.2). When slurry is fully displaced from the tube the pressure reaches a constant value (related to the bulk density and level of the aerated slurry in the flotation cell). The superficial gas velocity J_g is calculated from the slope of the pressure-time curve (dP/dt) obtained between the valve opening and the tube filling completely.

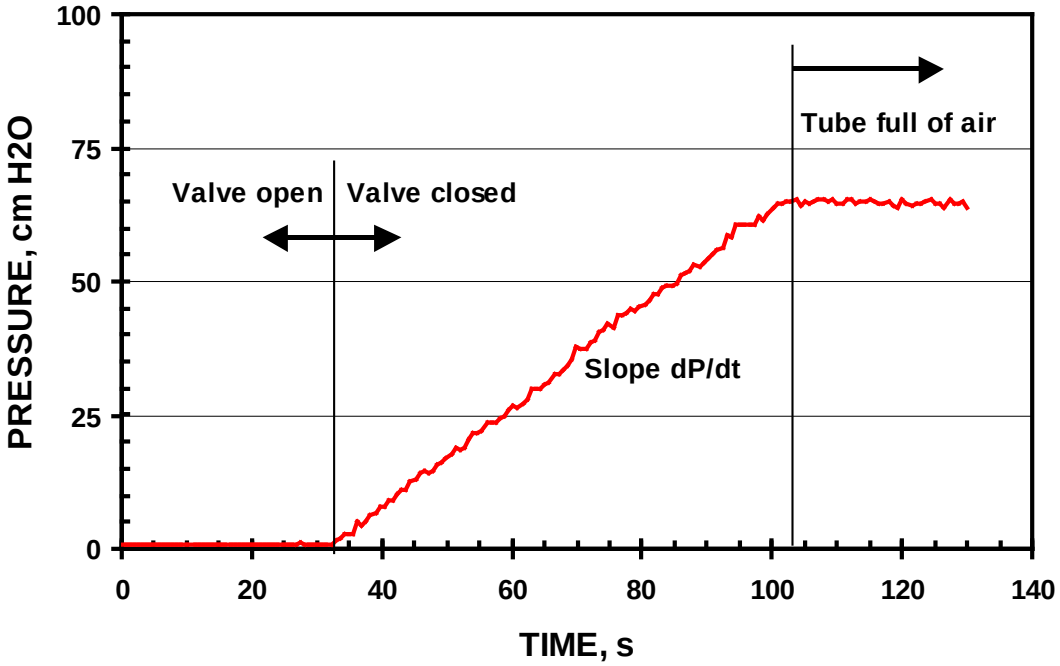

Figure A.2 Pressure vs. time curve collected during gas velocity measurement

The expression to calculate superficial gas velocity J_g (Equation A.1) is obtained from a mass balance applied to a vessel with variable volume and pressure (i.e., the top fraction of the tube filled with gas). Gas pressure and volume are related through the ideal gas equation and gas pressure is considered at all times in equilibrium with the hydrostatic pressure of the aerated pulp column.

$$J_g = \frac{1033 + \rho_b H_L}{\rho_b [1033 + \rho_b (H_L - H_o)]} \frac{dP}{dt} \qquad \text{A.1}$$

The calculation depends on the geometry of the sensor, the aerated-pulp bulk density, and the accumulated air pressure, which changes as the tube fills with the gas. Equation A.1 was derived for a constant mass flow of gas entering the tube at the local hydrostatic pressure and the accumulated gas pressure existing when the pulp level in the tube is at half the distance between H_O and H_L. The slope dP/dt is measured in cm of H_2O/s, lengths of the total tube H_L and the distance from the top to the pulp interface H_P (defined during installation) are measured in cm, the bulk density of the aerated pulp (ρ_b) in g/cm^3, and the value for the atmospheric pressure (P_{atm}) is 1033 cm of H_2O. The bulk density can be

determined by collecting a second pressure measurement at a different depth. By including a second tube (with its bottom end normally immersed closer to the pulp/froth interface, the bulk density can be calculated from the pressure difference measured after both tubes fill with gas (both reporting a constant pressure), knowing the distance between the two tubes bottom ends. The software includes an option to perform all these calculations automatically on-line once distances have been defined.

A.2 Gas Holdup Sensor

The gas holdup sensor is based on Maxwell's equation that relates the concentration of a non-conducting dispersed phase to the conductivities of the continuous phase and the dispersion. In our situation air bubbles constitute the dispersed phase, hence the gas concentration (gas holdup $\boldsymbol{\varepsilon}_g$) can be calculated knowing the conductivities of the dispersion (bubbles plus pulp) k_d and the continuous phase (pulp) k_p:

$$\varepsilon_g = \frac{1 - k_d/k_p}{1 + 0.5\, k_d/k_p} \qquad \text{A.2}$$

To meet the model requirements, an approach based on the use of two so-called flow conductivity cells, an open and a syphon cell, is utilized (Figure A.3). A flow conductivity cell in this context is defined as one that allows a fluid to flow through while the conductance is being measured.

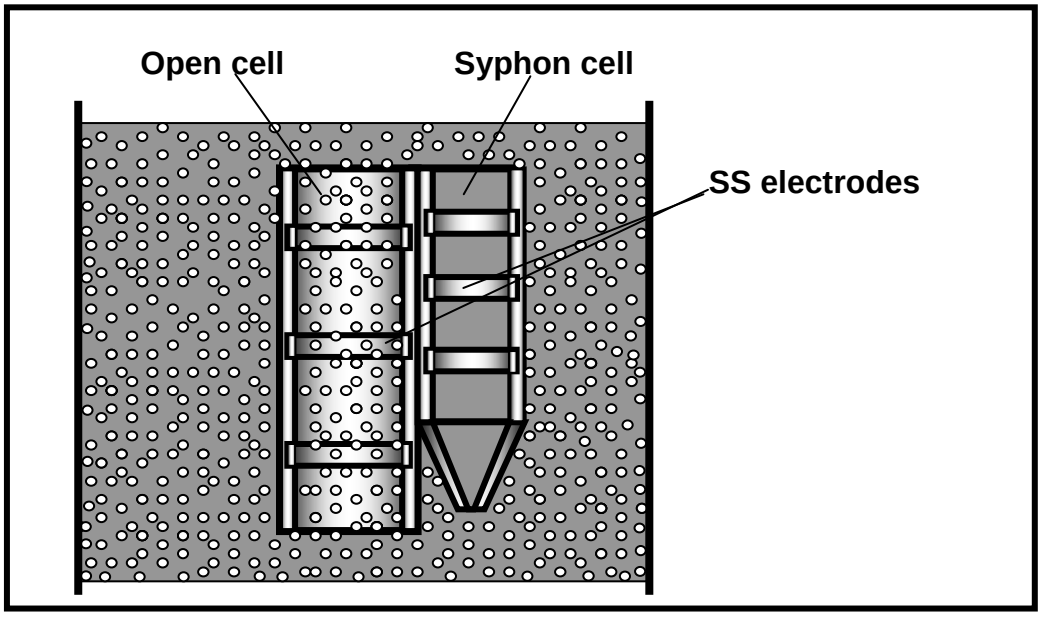

Figure A.3 Schematic diagram of gas holdup sensor showing construction details and functioning of the two flow conductivity cells

The open cell measures the conductivity of the dispersion, while the syphon cell measures the conductivity of the pulp, which requires the exclusion of bubbles. The open cell is a vertical cylinder open at both ends to allow a relatively free flow of bubbles and pulp. The syphon cell is a vertical cylinder with a conical bottom ending in a small orifice. The exclusion of bubbles is achieved because the orifice hinders entry of the ascending bubbles and, consequently, the cell contents develop a higher density than the dispersion outside the cell. This causes the cell contents to flow out through the orifice, and be replenished by pulp from the top. A steady state is reached when the pressure head at the orifice is the same as that outside the cell, achieved when a velocity in the cell that exactly compensates the hydrostatic pressure difference. This flow of pulp through the orifice completes the exclusion of bubbles from the syphon cell. Successful operation requires that the pulp velocity entering the top of the cell be lower than the terminal velocity of the smallest size bubble present in the system, otherwise bubbles would be entrained into the cell. Design criteria for the syphon cell have been established.

The sensor measures continuously the conductance in the two cells immersed in the pulp zone using a two-channel conductivity meter. This unit provides two 4-20 mA loops that can be programmed to deliver the conductivities, their ratio, or directly the gas holdup, which facilitates integration of the sensor with plant PLC systems. Typical signals collected in plant and corresponding gas holdup are displayed in Figure A.4.

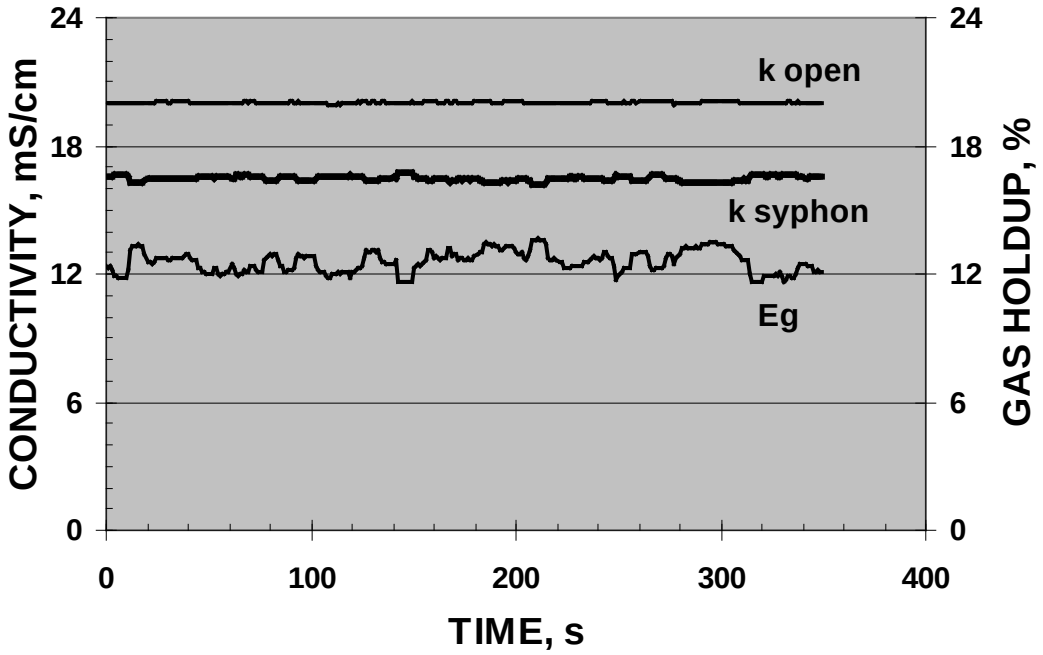

Figure A.4 Typical conductivity signals and calculated gas holdup

A.3 Technique for Measuring Bubble Size Distribution

To measure bubble size distributions bubbles are collected via a tube and directed into a viewing area where they are exposed under pre-set lighting conditions to be imaged using a digital video camera. Images, transferred into a computer, are automatically processed using a commercial software package (Northern Eclipse v 6.0 from Empix Imaging).

Although collection and imaging of bubbles has been used for many years, our set-up introduces some unique features that significantly improve image quality. As collected bubbles rise into the viewing area, they encounter an inclined window and spread into a single layer as they slide up (Figure A.5). The inclined window introduces two major beneficial effects on image quality: bubble overlap is reduced and the plane of focus is unambiguous. Employing back illumination renders the bubble image as a black circle with a clear center; bubble edge discrimination is very precise under these conditions. The quality of the images enables bubble sizing at rates exceeding 1000 bubbles per hour, depending on the magnification. Selection of magnification is a compromise between having many bubbles in an image (low magnification), and increased accuracy by reducing the size of a pixel (high magnification) (images are normally collected at a 1024x768 pixel density).

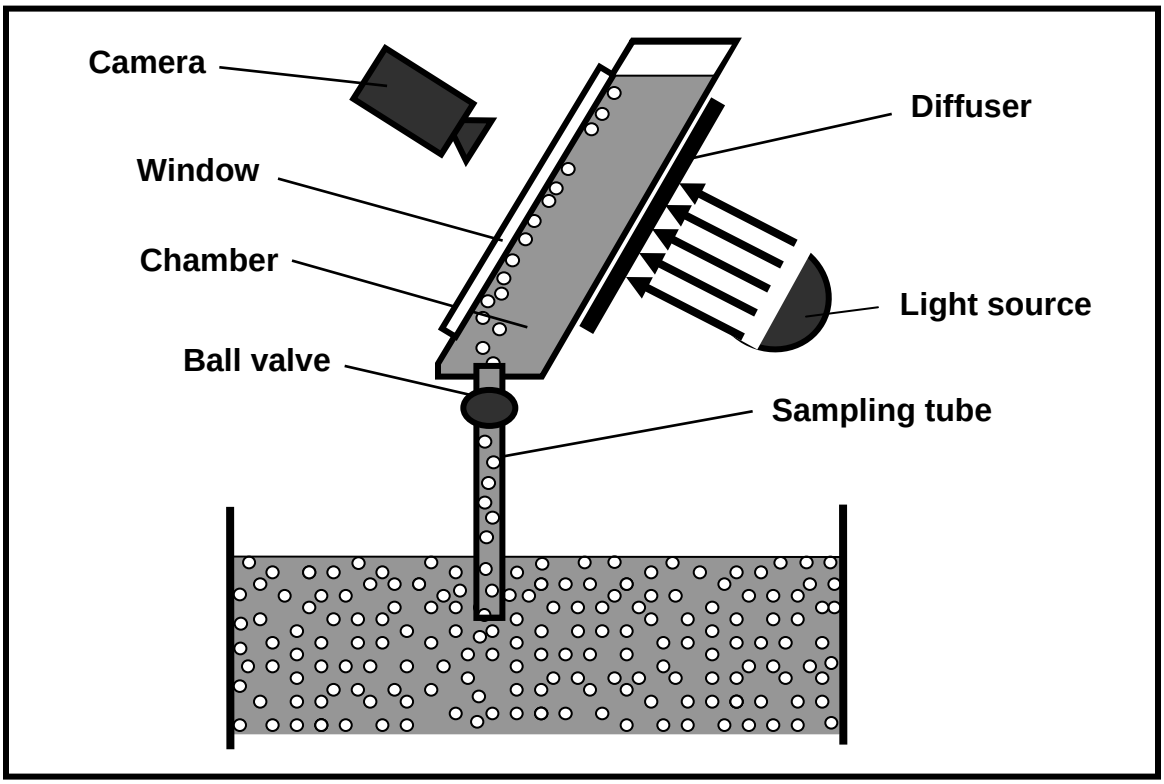

Figure A.5 Components used in the collection and exposing of bubbles to measure bubble size distributions

Unlike the gas velocity and gas holdup sensors, that once installed produce results, the present technique to measure bubble size requires a series of labor-intensive steps. In addition to the transfer and processing of images, the collection of images requires, for every measurement:

- Cleaning viewing chamber (and in particular, the inclined window) from particles,
- Filling the chamber with water (normally containing frother to prevent bubble coalescence),
- Sealing the viewing chamber gas-tight,
- Focusing the camera lens on a standard object fixed to the inside of the window,
- Opening the ball valve in the sampling tube to equilibrate pressure and to establish a flow of rising bubbles, and
- Recording for several minutes (normally until the water in the viewing chamber becomes too cloudy with particles released from bursting bubbles at the top of the chamber)

To facilitate plant work, the camera, light source, viewing chamber and sampling tube are mounted on an aluminum structure to make a single unit.

A.4 Sensor Installation

Because the volume of a mass of gas depends on its pressure and temperature, gas dispersion measurements will be affected by the location and geometry of the sensors during the measurements. In general, the conditions existing at the measurement point are not the same as those prevailing within the cell at the bubble collection point and corrections are necessary. In bubble size determination, for example, diameters are measured from images of bubbles exposed in the bubble viewer (which operates under vacuum); bubbles are larger than their sizes in the cell. A similar situation occurs with the measurement of gas velocity where a volume of gas is accumulated under variable pressure at conditions different from those existing at the location where bubbles enter the tube. Corrections to different conditions are not a problem for bubble size and gas velocity, as Boyle's law can be applied to account for gas expansion or contraction resulting from different pressures, given that air behaves as an ideal gas at the conditions under which flotation proceeds. In the case of the gas holdup however, correction to conditions different from those at the measurement point are not simple, and no method to correct the effect of pressure on the gas holdup resulting from the flow of a swarm of different diameter bubbles has been proposed in the literature.

The installation of the gas dispersion sensors during cell characterization exercises is crucial and requires careful documenting to be effective (Figure A.6). In our experience, the following protocol provides information compatible with efforts to compare cell performance in different banks, circuits and plants. As gas holdup cannot be corrected, this sensor needs to be located at the point where information is sought (reference line in Figure A.6). To have the three sensors collecting the same bubbles, the tubes for the gas velocity sensor and bubble viewer are immersed to the same depth as the bottom end of the gas holdup sensor open cell. Bulk density, measured with two tubes reaching different depths, is required for the dispersion at the top of the cell (above the gas velocity sensor tube). Therefore, one is installed at the same depth as the other sampling tubes while the second at no more than 1 ft below the interface (a minimum distance H_{BD} of 0.5 m between the immersed lengths of the two tubes is recommended).

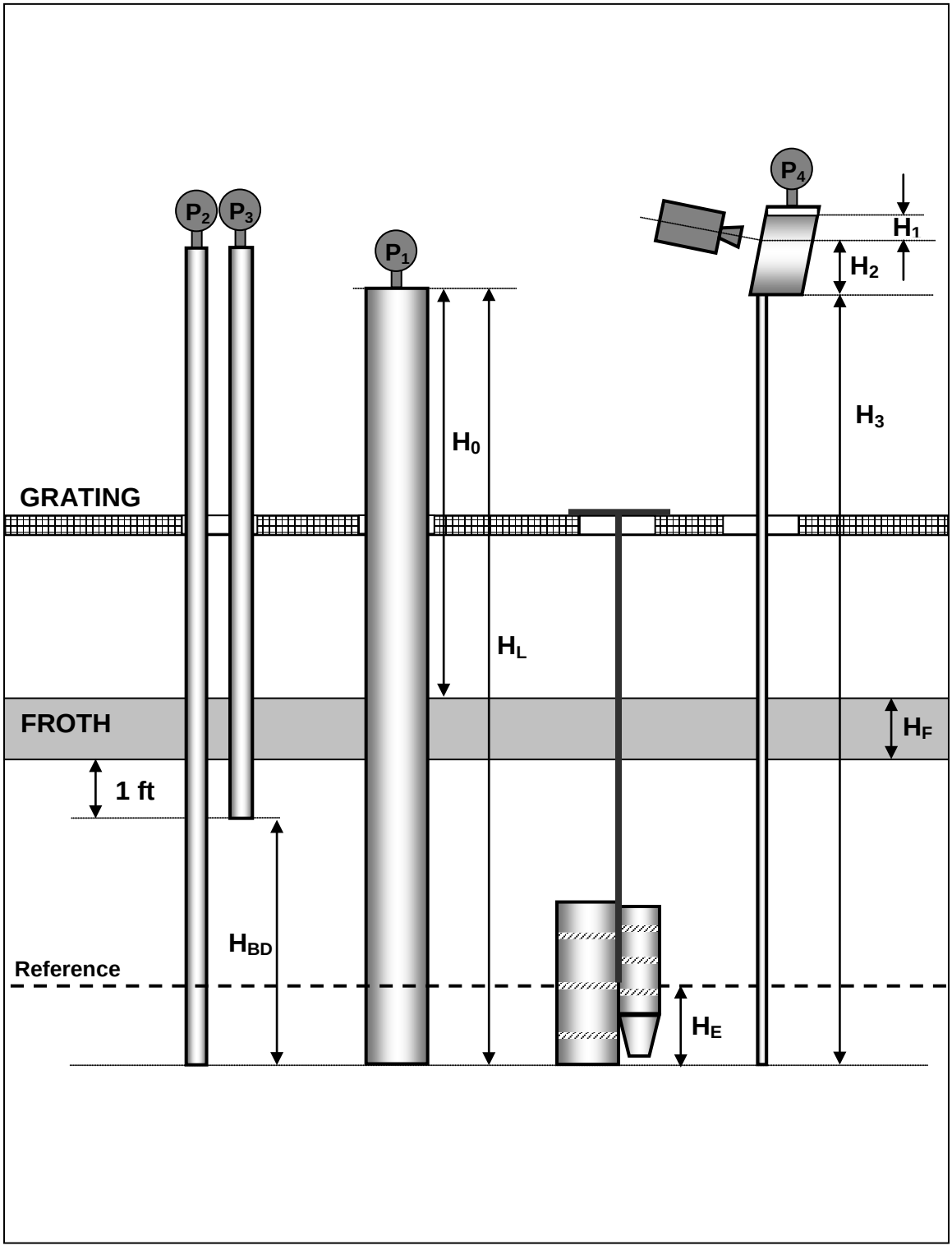

Figure A.6 Location of the different sensors and relevant lengths and distances for calculation of gas dispersion parameters

A.5 Correcting Gas Dispersion Measurements

Location of the sensors defines measurement conditions for the gas dispersion parameters. An installation and operation protocol for the three sensors is an adequate response to the non-homogeneity of gas dispersion in industrial cells; positioning the bubble sampling tubes at the same radial and axial location expose those to the same bubble population. This section describes the basis of the procedure followed by McGill, the information required to correct measurements for data interpretation purposes, and the equations used which are proposed for distances H measured in cm and manometric pressures P reported in cm H_2O.

Sensors should be operated through the same sampling port (radial position), and installation as described in Figure A.6 is strongly recommended. The reference location (position of the middle ring of the open cell of the gas holdup sensor) is carefully selected considering that this will be the only depth where the three gas dispersion parameters will be known. The reason for selecting this location as reference arises from our current inability to calculate changes of gas holdup from one depth to another. The conductivity in the open cell is measured using an arrangement of three equidistant rings flush mounted to the cell cylindrical walls; the sample volume involved in the measurement is that in between the two extreme rings. It is considered that the location of the middle ring is best to associate the measurement to a given depth. Gas holdup is then calculated utilizing Maxwell's equation (Equation A.2) for averages of the specific conductivity k vs. time data for both the open and syphon cells.

Gas velocity is estimated from the slope dP/dt and bulk density ρ_B (both calculated from pressure vs. time data) using Equation A.1. The value obtained with this equation corresponds to the superficial gas velocity of the bubbles entering the tube at a depth ($H_L - H_0$). Values of H_L (total length of tube) and H_0 (length of tube above the cell lip) are required in each case.

To correct the measured gas velocity to a different location (different hydrostatic pressure), a derivation of Boyle's law is used. To calculate, for example, gas velocity from the measurement (J_{g1}) to the reference (J_{g2}) conditions illustrated in Figure A.6 the following equation is used:

$$J_{g2} = J_{g1} \frac{P_{abs1}}{P_{abs2}} = J_{g1} \frac{1033 + P_2}{1033 + P_2 - \rho_b H_E} \qquad \text{A.3}$$

Bulk density is measured by using two separate tubes of different length (H_{BD}) installed as illustrated in Figure A.6. These two tubes are permanently maintained full of air; therefore, pressures P_2 and P_3 correspond to the hydrostatic pressure at the depths reached by these tubes; the average bulk density for the dispersion between depths selected for the two bulk density tubes is calculated from:

$$\rho_b = \frac{P_2 - P_3}{H_{BD}} \qquad \text{A.4}$$

In the case of bubble size, images are collected under vacuum (at a distance H_1 from the gas-liquid interface in the bubble viewer), where the absolute pressure is the atmospheric plus P_4 (a negative pressure) and plus the hydrostatic pressure of a water column of height

H_1. To correct bubble sizes to the collection point the pressure P_4 needs to be measured, and in the absence of proper instrumentation, estimated from equalizing two hydrostatic absolute pressures at the measuring depth: that from the water column inside the bubble viewer and collection tube to that of the pulp and froth column in the cell:

$$P_{atm} + P_4 + \rho_w(H_1 + H_2 + H_3) = P_{atm} + \rho_b(H_L - H_0 - H_F) + \rho_f H_F \qquad \text{A.5}$$

The manometric component of the right hand side of Equation A.5 is actually P_2, pressure measured to obtain the bulk density; therefore, with distances H_1, H_2, and H_3 the vacuum pressure P_4 can be accurately calculated:

$$P_4 = P_2 - \rho_w(H_1 + H_2 + H_3) \qquad \text{A.6}$$

Once P_4 is known, measured bubble sizes d_1 can be corrected to reference conditions (d_2) using the following equation also derived from Boyle's law:

$$d_2 = d_1 \sqrt[3]{\frac{P_{abs1}}{P_{abs2}}} = d_1 \sqrt[3]{\frac{1033 + P_4 + \rho_w H_1}{1033 + P_2 - \rho_b H_E}} \qquad \text{A.7}$$

Although the volume of gases is also affected by temperature, no corrections for this concept are normally applied because gas temperature differences not large enough to have a significant effect on volume have been measured. However, if large temperature differences are detected between the gas in the pulp, and that accumulated during Jg measurement or that in the bubble being imaged, then a temperature correction in Equations A.1, A.3 and A.6 has to be considered. Even in the case of uniform gas temperature, pulp temperatures should be consistently measured in case that results from cells in different banks, circuits and plants need to be compared or related.

APPENDIX B: Method for Correcting Initial D_{32} and CCCX Measurements

(This section details the calculations required for establishing corrected D_{32} and CCCX values from initial CCCX values for Correction Factor for Bubble Coalescence in Bubble Viewer found in Section 3.4)

B.1 Methodology for Establishing Correction Factors (CF's)

Step 1

The bases for the method are the Bubble Viewer (BV) tests for different frother levels CCCX, that assume the same frother concentration in both float cell and BV. D_{32} correction factors (CF's) are established from these tests for each level of CCCX. The "problem" occurs once initial CF's are determined and initial bubble sizes adjusted; the initial CCC values used to determine the CF's also change. An iterative procedure is required

Step 2

Since the CF's are based on CCCX values and not the actual ppm, each ppm needs to be converted to CCCX by using the appropriate CCC95 value for that frother and J_g, and the b parameter from the All Data model for D_{32}. The CF is obtained from the CF equation (Equation 3.13) based on the CCCX level for that test.

Step 3

The corrected set of D_{32} values are then used to recalculate revised parameter values for each frother D_{32} model and new CCC95 values for each frother

Step 4

The revised CCC95 values are then used to produce a new All Data Model which can be compared to the previous All Data model to check for convergence. This produces a revised set of D_l, a and b values for the All Data Model.

Step 5

Return to Step 1 to establish a revised equation for the D_{32} CF's since the initial CCCX values have changed. The actual CF values remain the same, however, the corresponding CCCX values (as established in the BV tests based on initial assumptions of the All Data Model) need to be revised to reflect the new All Data Model. Once these have been established, a new equation is fitted for the CF's and is used to correct the original bubble size data as the process is repeated returning to Step 2.

Step 6

Steps 2 to 5 are repeated until there is convergence in consecutive iterations for the parameters in the All Data Model and the CCC95 values. In this data set convergence took

2 revisions beyond the initial first round of calculations. The final All Data Model and CF-CCCX relationship are valid for all frothers where the CCC95 is known.

Procedure for a new data set of uncorrected D_{32}'s

In this case one can assume that he CF equation and the All Data Model apply. One needs to determine valid CCC95 values for the frother in use. There are 2 options;

1) Use pre-determined values of CCC95 if they are available.

2) Perform tests to establish the CCC95 (from D_{32} versus ppm frother-added curves) or determine from HLB/MW data

For Option 2 the initial calculation will be on uncorrected D_{32} values. This will establish an initial CCC95 value and hence CCCX values from which CF's for these initial D_{32} values can be found from Equation 3.13. These revised values will be used to recalculate a revised CCC95 from which a new set of CCCX's and CF's are calculated. The process iterates until the CCC95 values converge. Typically the final revised CCC95 values will be 15-20% greater than the initial values.

B.2 Developing the Equation for Revised CCCX from Initial CCCX

Derivation of the revised CCCX from the initial CCCX used in the determination of the D_{32} correction factor from initial, unadjusted data is developed here. Since each iteration (described above) results in a new value for CCC95, a set of new CCCX values also results for each iteration, since these are determined from CCC95 values according to;

$$CCCX = 100 \cdot \left[1 - \exp\left(-b\frac{PPM}{CCC95}\right)\right] \qquad \text{B.1}$$

where b is the decay constant from the All Data D_{32} model.

Premise: the ppm levels of frother (in this case DowFroth 250) are the same regardless of the CCCX value, which does change as the CCC95 changes. Based on the same ppm values one can therefore equate two versions of Equation B.1, one side for initial data using the subscript "o" and the other side for revised data having no subscripts:

$$\left(\frac{CCC95_o}{b_o}\right) \cdot ln\left(1 - \frac{CCCX_o}{100}\right) = \left(\frac{CCC95}{b}\right) \cdot ln\left(1 - \frac{CCCX}{100}\right) \qquad \text{B.2}$$

Or, simplified to;

$$BlnC = AlnD \qquad \text{B.3}$$

which becomes;

$$lnC^B = lnD^A \qquad \text{B.4}$$

Taking the exponential of both sides and re-arranging yields:

$$D = C^{B/A} \quad \text{B.5}$$

Substituting back for A, B, C and D from Equation B.2, and re-arranging, yields;

$$CCCX = 100\left\{1 - (1 - \frac{CCCX_o}{100})^e\right\} \quad \text{B.6}$$

where e, the exponent, is given by:

$$e = \frac{b \cdot CCC95_o}{b_o \cdot CCC95} \quad \text{B.7}$$

The values of $CCC95$ and b are those determined from the final iteration once convergence has been achieved. Figure 3.24, in the body of the thesis, represents Equation B.6 and was used to produce the final D_{32} correction factors versus CCCX show in Figure 3.25. For the case of the Bubble Viewer experiments to develop the correction factors:

$$e = \frac{b \cdot CCC95_o}{b_o \cdot CCC95} = \frac{(2.995) \cdot (8.35)}{(3.071) \cdot (10.06)} \quad = 0.8096 \quad \text{B.8}$$

This value of e applies to tests using DowFroth 250, however once established, the D_{32} correction factors as presented in Figure 3.25 are universally applicable to all frother types.

APPENDIX C: Experimental Data for the Laboratory Studies

(Presented on a CD)